

Lecture Notes in Civil Engineering

Magd Abdel Wahab *Editor*

Proceedings of the 1st International Conference on Numerical Modelling in Engineering

Volume 1 Numerical Modelling in Civil
Engineering, NME 2018, 28–29 August 2018,
Ghent University, Belgium

 Springer

Lecture Notes in Civil Engineering

Volume 20

Series editors

Marco di Prisco, Politecnico di Milano, Milano, Italy

Sheng-Hong Chen, School of Water Resources and Hydropower Engineering,
Wuhan University, Wuhan, China

Giovanni Solari, University of Genoa, Genova, Italy

Ioannis Vayas, National Technical University of Athens, Athens, Greece

Lecture Notes in Civil Engineering (LNCE) publishes the latest developments in Civil Engineering - quickly, informally and in top quality. Though original research reported in proceedings and post-proceedings represents the core of LNCE, edited volumes of exceptionally high quality and interest may also be considered for publication. Volumes published in LNCE embrace all aspects and subfields of, as well as new challenges in, Civil Engineering. Topics in the series include:

- Construction and Structural Mechanics
- Building Materials
- Concrete, Steel and Timber Structures
- Geotechnical Engineering
- Earthquake Engineering
- Coastal Engineering
- Hydraulics, Hydrology and Water Resources Engineering
- Environmental Engineering and Sustainability
- Structural Health and Monitoring
- Surveying and Geographical Information Systems
- Heating, Ventilation and Air Conditioning (HVAC)
- Transportation and Traffic
- Risk Analysis
- Safety and Security

To submit a proposal or request further information, please contact the appropriate Springer Editor:

- Mr. Pierpaolo Riva at pierpaolo.riva@springer.com (Europe and Americas);
- Ms. Swati Meherishi at swati.meherishi@springer.com (India);
- Ms. Li Shen at li.shen@springer.com (China);
- Dr. Loyola D'Silva at loyola.dsilva@springer.com (Southeast Asia and Australia/NZ).

More information about this series at <http://www.springer.com/series/15087>

Magd Abdel Wahab
Editor

Proceedings of the 1st International Conference on Numerical Modelling in Engineering

Volume 1 Numerical Modelling in Civil
Engineering, NME 2018, 28–29 August 2018,
Ghent University, Belgium

 Springer

المنارة للاستشارات

Editor

Magd Abdel Wahab
Faculty of Engineering and Architecture
Ghent University, Laboratory Soete
Ghent, Belgium

ISSN 2366-2557

ISSN 2366-2565 (electronic)

Lecture Notes in Civil Engineering

ISBN 978-981-13-2404-8

ISBN 978-981-13-2405-5 (eBook)

<https://doi.org/10.1007/978-981-13-2405-5>

Library of Congress Control Number: 2018952641

© Springer Nature Singapore Pte Ltd. 2019, corrected publication 2019

This work is subject to copyright. All rights are reserved by the Publisher, whether the whole or part of the material is concerned, specifically the rights of translation, reprinting, reuse of illustrations, recitation, broadcasting, reproduction on microfilms or in any other physical way, and transmission or information storage and retrieval, electronic adaptation, computer software, or by similar or dissimilar methodology now known or hereafter developed.

The use of general descriptive names, registered names, trademarks, service marks, etc. in this publication does not imply, even in the absence of a specific statement, that such names are exempt from the relevant protective laws and regulations and therefore free for general use.

The publisher, the authors and the editors are safe to assume that the advice and information in this book are believed to be true and accurate at the date of publication. Neither the publisher nor the authors or the editors give a warranty, express or implied, with respect to the material contained herein or for any errors or omissions that may have been made. The publisher remains neutral with regard to jurisdictional claims in published maps and institutional affiliations.

This Springer imprint is published by the registered company Springer Nature Singapore Pte Ltd.
The registered company address is: 152 Beach Road, #21-01/04 Gateway East, Singapore 189721, Singapore

المنارة للاستشارات

Preface

This volume contains the proceedings of the 1st International Conference on Numerical Modelling in Engineering: Volume 1 Numerical Modelling in Civil Engineering. Numerical Modelling in Engineering NME 2018 is the 1st NME conference and is held in the city of Ghent, Belgium, during the period 28–29 August 2018.

The overall objective of the conference is to bring together international scientists and engineers in academia and industry in fields related to advanced numerical techniques, such as FEM, BEM, IGA, and their applications to a wide range of engineering disciplines. The conference covers industrial engineering applications of numerical simulations to Civil Engineering, Aerospace Engineering, Materials Engineering, Mechanical Engineering, Electronics, Electrical Engineering, Biomedical Engineering, etc. The presentations of NME 2018 are divided into three main sessions, namely (1) Civil Engineering, (2) Electrical Engineering and (3) Mechanical and Materials Engineering.

The organising committee is grateful to keynote speaker, Professor René de Borst, The Centenary Professor of Civil Engineering, University of Sheffield, UK, for his keynote speech entitled ‘Computational Modelling of Fracture in Fluid-Saturated Porous Media’.

Special thanks to members of the Scientific Committee of NME 2018 for reviewing the articles published in this volume and for judging their scientific merits. Based on the comments of reviewers and the scientific merits of the submitted manuscripts, the articles were accepted for publication in the conference proceedings and for presentation at the conference venue. The accepted papers are of a very high scientific quality and contribute to advancement of knowledge in all research topics relevant to NME conference.

Finally, the organising committee would like to thank all authors, who have contributed to this volume and to those who have presented their research work at the conference venue in Ghent.

Magd Abdel Wahab
Chairman of NME 2018

Organization

Organising Committee

Chairman

Magd Abdel Wahab Laboratory Soete, Ghent University, Belgium

International Scientific Committee

S. Abdullah	Universiti Kebangsaan Malaysia, Malaysia
H. T. Ali	University of Bristol, UK
A. San-Blas	Miguel Hernández University of Elche, Spain
A. Cheknane	Amar Telidji University of Laghouat, Algeria
S. Bordas	University of Luxembourg
A. Caggiano	Technische Universität Darmstadt, Germany
I. Hilmy	International Islamic University Malaysia
S. Khatir	Ghent University, Belgium
M. Kwiatkowski	AGH University of Science and Technology, Poland
N. S. Mahjoub	Institut Préparatoire aux Etudes d'Ingénieurs de Monastir, Tunisia
G. Minafo	University of Palermo, Italy
N.-A. Noda	Kyushu Institute of Technology, Japan
K. Oda	Oita University, Japan
P. Phung Van	Ghent University, Belgium
R. V. Prakash	Indian Institute of Technology, India
T. Rabczuk	Bauhaus University Weimar, Germany
A. Rudawska	Lublin University of Technology, Poland
V. Silberschmidt	Loughborough University, UK
J. Santos	University of Madeira, Portugal
J. Toribio	University of Salamanca, Spain

L. V. Tran	Sejong University, South Korea
L. Vanegas Useche	Universidad Tecnológica de Pereira, Colombia
C. Wang	Liaocheng University, China
H.-N. Xuan	Hutech University, Vietnam
T. Yue	Ghent University, Belgium
C. Zhou	Nanjing University of Aeronautics and Astronautics, China
Y.-L. Zhou	National University of Singapore
X. Zhuang	Leibniz Universität Hannover, Germany

Contents

Numerical Geometry Optimization and Modelling of Insulation Filled Masonry Blocks	1
Balázs Nagy	
Stochastic Finite Element Analysis of Nonlinear Beam on Winkler-Pasternack Foundation	14
Seguini Meriem and Nedjar Djamel	
Thermal-Mechanical Coupled Behavior of Sliding Bearings for Seismic Isolation	30
Masaru Kikuchi and Ken Ishii	
Behaviour of Adjacent Ground and Existing Tunnel According to Locations of Pile Loading	44
Suk-Min Kong, Dong-Wook Oh, and Yong-Joo Lee	
A Numerical Approach to an Interface Damage Model Under Cyclic Loading	54
Roman Vodička and Katarína Krajníková	
Numerical Simulations of Precast Thin-Walled Concrete Blocks Forming Coastal Structure	67
Bao-Loi Dang, Hau Nguyen Ngoc, Hung Nguyen-Xuan, Hoang Duc Thao, and Magd Abdel Wahab	
Numerical Study of Heat and Moisture Transfers for Validation on Bio-Based Building Materials and Walls	81
T. Alioua, B. Agoudjil, and A. Boudenne	
Modelling Load-Transmission Mechanisms in Axially Loaded RC Columns Retrofitted with Steel Jackets	90
Giovanni Minafò, Alfio Francesco Siciliano, and Marinella Fossetti	

Three-Dimensional Analysis of an Innovative Hollow Concrete Block of Interlocking Revetment	112
Hau Nguyen-Ngoc, Bao-Loi Dang, Hung Nguyen-Xuan, Hoang Duc Thao, and Magd Abdel Wahab	
Effects of Construction Sequence on Reinforced Concrete Building Analysis	123
Mutlu Secer and Tolga Arslan	
A Six-Variable Quasi-3D Model for Static Analysis of Laminated Composite Plates Using Isogeometric Analysis	135
Loc V. Tran, Magd Abdel Wahab, and Jarkko Niiranen	
The Rock Failure Behavior Analysis in Rock Cutting Using Finite Element Analysis	143
Weiji Liu, Xiaohua Zhu, Yunlai Zhou, Quanmin Liu, and Magd Abdel Wahab	
Coupled Thermal and Mechanical Analysis of Composite Cross Sections During Concrete Hydration Using Mathematical Optimization Strategies	150
Marcel Helmrich, Christopher Taube, and Guido Morgenthal	
Topology Optimization of an Interlocking Revetment Block	165
Hau Nguyen-Ngoc, Bao-Loi Dang, Hung Nguyen-Xuan, Hoang Duc Thao, and Magd Abdel Wahab	
Damage Detection in Simply Supported Beam Using Transmissibility and Auto-Associative Neural Network	177
Huong Duong Nguyen, Tien Thanh Bui, Guido De Roeck, and Magd Abdel Wahab	
A Coupled SPH-FEM for Fluid-Structures Interaction Problem with Free-Surface and Revetment Slope Thin-Walled Structures	187
P. Truong-Thi, Hung Nguyen-Xuan, and Magd Abdel Wahab	
Incompressible Fluid Computation Based on Polygonal Finite Element	202
T. Vu-Huu, C. Le-Thanh, Hung Nguyen-Xuan, and Magd Abdel Wahab	
Investigation of Inclined Wellbore Stability Using Numerical Analysis	213
Weiji Liu, Xiaohua Zhu, Yunlai Zhou, Xiangning Zhang, and Magd Abdel Wahab	
Size-Dependent Analysis for FG-CNTRC Nanoplates Based on Refined Plate Theory and Modified Couple Stress	225
Cuong-Le Thanh, T. Vu-Huu, P. Phung-Van, Hung Nguyen-Xuan, and Magd Abdel Wahab	

Numerical Modelling of the Thermo-Mechanical Behavior of Concrete Arch Dams During the First Filling of the Reservoir	238
Noemi Schclar Leitão and Eloísa Castilho	
System Identification Based on Vibration Testing of a Steel I-Beam . . .	254
Viet Long Ho, Ngoc Hoa Tran, Guido De Roeck, Tien Thanh Bui, and Magd Abdel Wahab	
Numerical Calibration of a Simplified Model for FRP Confinement of Columns	269
Marinella Fossetti, Alfio Francesco Siciliano, Francesco Basone, and Giovanni Minafò	
Correction to: Damage Detection in Simply Supported Beam Using Transmissibility and Auto-Associative Neural Network	E1
Huong Duong Nguyen, Tien Thanh Bui, Guido De Roeck, and Magd Abdel Wahab	
Author Index	291



Numerical Geometry Optimization and Modelling of Insulation Filled Masonry Blocks

Balázs Nagy^(✉)

Budapest University of Technology and Economics,
Műegyetem rakpart 3, Budapest 1111, Hungary
nagy.balazs@epito.bme.hu

Abstract. Due to current energy performance requirements, masonry block producers developed thermal insulation filled masonry blocks to achieve lower thermal transmittance. However, the internal structural geometry of these blocks remained simple: producers mostly using only large rectangular hollows to fill with different insulating materials, such as mineral wool, polystyrene or expanded perlite. Manufacturers did not address the optimization of the internal geometry of the insulation filled masonry blocks before. In this study, a new masonry design approach is presented using finite element method and conjugated heat and moisture transfer analysis with derivative-free shape optimization of the internal structural geometry of an existing masonry block to get the best possible hygrothermal performance from the blocks. In the paper, the optimization process is presented through the results of mineral wool filled blocks, which gave combined parallelogram and trapezoidal shaped internal geometries depending on the bounds of the optimization. The study showed that the masonry products designed by optimization have lower thermal transmittance than the reference value. Using the presented optimization method in designing masonry blocks leads to more energy efficient structures using the same or even less materials, without increase of producing cost.

Keywords: Heat and moisture transfer · Derivative-free optimization
Masonry construction

1 Introduction

In the 19th century, ceramic bricks became one of the most popular building materials of industrial and commercial building. In the 20th century, new masonry products were developed, such as perforated fired clay bricks. The hollows in the masonry bricks reduced the amount of clay needed to manufacture the blocks, and also improved the thermal performance. Hollow bricks are lighter, therefore it is easier to handle, and usually used in single-wall constructions with finishes applied inside and outside. Comprehensive researches of hollow or filled masonry blocks started in Europe in the 1960s. In the 1970s, after the oil crisis the development of bricks occurred in two directions. The manufacturers started increasing the size of the holes, therefore decreasing the mass, as well as increasing the size of blocks to make the construction

process more efficient and applying more porous material with smaller thickness [1]. In case of perforated bricks, the location and geometry of holes have an effect on the thermal performance. For example a K-shaped zigzag design results in a longer route for the heat transfer, therefore increases the thermal resistance of the masonry block (see Fig. 1 left side).



Fig. 1. Modern unfilled- (left) and mineral wool filled (right) masonry blocks

Nowadays, the energy performance requirements are more and more rigorous, and a simple wall construction usually needs additional external thermal insulation, if the building block is not extremely thick and well optimized. Building block manufacturers addressed the problem, that people rather buy smaller blocks and insulate it from the external side, than buy thicker, heavier and more expensive bricks. Therefore manufacturers increase the thermal resistance of masonry blocks with different insulation fillers in the holes. If the holes are wider than 4 mm, since air can move in empty holes, most of solid insulating materials have lower thermal conductivities than the moving air's equivalent value. However, due to manufacturability, the internal shapes of filled holes are simplified to rectangles. In the past few years, insulating fillers were improved, and some manufacturer started filling smaller designed hole geometry as well (5–10 mm thick gaps). The thermal properties of insulation fillers are almost similar to air regarding that thickness, therefore no significant improvement can be achieved comparing to applying smaller well designed empty holes. In the past few years researchers started investigating the thermal and hygrothermal behaviour of hollow and filled ceramic masonry blocks with different fillers and geometries [1–10]. The topological optimization of internal geometry of building blocks was presented by Sousa et al. [11], who used genetic algorithms, and lightweight concrete blocks were optimized by minimizing their thermal transmittance by determining the optimum values of a finite number of parameters that define the position, the size and the spacing of the holes within the block. The holes are assumed to be rectangular and arranged in a regular mesh, either aligned or staggered. After their work, Bruggi and Taliercio [12] presented a topology optimization approach of the internal geometry of masonry blocks, resulted in non-trivial brick layouts. These layouts depended strongly on the design constraints, and most of the result cases are hardly constructible because the

walls between holes are too thin, or the internal holes are too narrow in some places to fill them with additional thermal insulations. Topological optimization is used mainly early in the design phase, when lots of analyses are needed and the final design is not yet constrained by any parameters. In this paper, the shape of the insulation filler in the masonry block is optimized based on an initial geometry using derivative-free optimization process. The objective is to minimize the thermal transmittance of masonry blocks by minimizing the inward heat flux through the internal surface. Heat flux is determined by numerical hygrothermal simulations.

2 Hygrothermal Modelling and Optimization

2.1 Optimized Insulation Filled Masonry Block Model

The optimized masonry block geometry is based on the mineral wool filled Porotherm 26-50 W.i. Object Plan of Wienerberger (see Fig. 2). The thickness of the block is 26 cm, it contains four rows with 40 mm thick and 68 or 114 mm wide rectangular shaped mineral wool insulated holes. Between insulation filled holes, horizontally there are 18 mm thick, and vertically there are 20 mm thick ceramic walls. The block is 50 cm long and 24.9 cm high, i.e. this block is twice as long as the usual masonry blocks in the market. This special masonry block is usually used in footings of buildings, and it is selected for research because of its special structure (4 filled holes in each of the 4 rows). The geometry is shown in Fig. 2. The simulation model was simplified by neglecting the fader and groove connection on the sides.

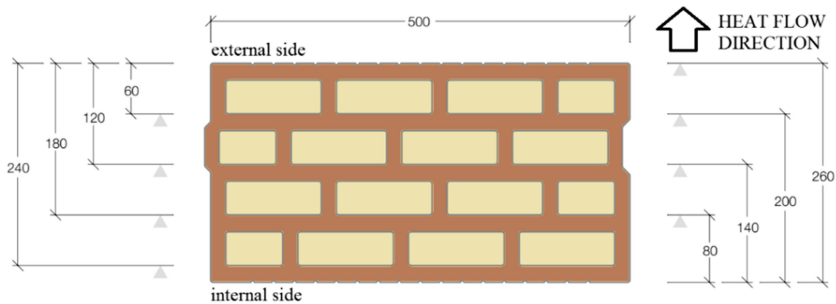


Fig. 2. Selected masonry block geometry based on [13]

2.2 Conjugated Heat and Moisture Transfer

In this research, the physics of steady-state conjugated heat and moisture transport in porous media was considered in 2D space. The partial differential equations (PDE) based on Künzel [14] were solved by using Comsol Multiphysics finite element

method (FEM) software [15] which is validated by both MSZ EN ISO 10211 [16] and MSZ EN 15026 [17]. The PDE for steady-state heat transfer is the following:

$$\nabla \cdot \mathbf{q} = Q \quad (1)$$

$$\mathbf{q} = -d_z(\lambda_{eff} \cdot \nabla \cdot \mathbf{T} + L_v \cdot \delta_p \cdot \nabla \cdot (\phi \cdot p_{sat})) \quad (2)$$

where ∇ is nabla vectorial differential operator, \mathbf{q} is heat flux [W/m^2], Q is heat source [W/m^3], λ_{eff} is temperature and moisture dependent effective thermal conductivity [W/mK], T is temperature [K], L_v is latent heat of evaporation of water [J/kg], δ_p is vapour permeability [g/msPa], ϕ is relative humidity [-] and p_{sat} is the saturation pressure of water vapour [Pa]. The PDE for moisture transfer is the following:

$$\nabla \cdot \mathbf{g} = G \quad (3)$$

$$\mathbf{g} = -d_z(\xi \cdot D_w \cdot \nabla \cdot \phi + \delta_p \cdot \nabla \cdot (\phi \cdot p_{sat})) \quad (4)$$

$$\xi = \frac{\partial w}{\partial \phi} \quad (6)$$

where \mathbf{g} is moisture flux [$\text{kg}/\text{m}^2\text{s}$], G is moisture source [$\text{kg}/\text{m}^3\text{s}$], ξ is differential moisture capacity [kg/m^3], D_w is moisture diffusivity [m^2/s] and w is the moisture content [kg/m^3] according to the hygroscopic sorption isotherms of the materials.

2.3 Boundary Conditions and Material Properties

The boundary conditions for adiabatic boundary (Eq. 5) and for heat flux (Eq. 6) are the following:

$$-\mathbf{n} \cdot \mathbf{q}_0 = 0 \quad (5)$$

$$-\mathbf{n} \cdot \mathbf{q}_0 = h_s(T_{air} - T) \quad (6)$$

where \mathbf{q}_0 is the inward heat flux [W/m^2], h_s is the heat transfer coefficient [$\text{W}/\text{m}^2\text{K}$] according to MSZ EN ISO 6946 [18]. T_{air} is internal air temperature in steady-state conditions set to 20 °C, and the external temperature set to 4 °C, which is the average seasonal temperature in a standard heating season in Hungary according to [19].

The moisture transfer boundary conditions are the following:

$$-\mathbf{n} \cdot d_z \mathbf{g}_0 = 0 \quad (8)$$

$$-\mathbf{n} \cdot d_z \mathbf{g}_0 = \beta_p(\phi_{air} \cdot p_{sat}(T_{air}) - \phi \cdot p_{sat}(T)) \quad (9)$$

where β_p is the moisture transfer coefficient [s/m] set to $7.69 \cdot 10^{-8}$ s/m on the internal and $25 \cdot 10^{-8}$ s/m on the external surface. ϕ is the relative humidity, internal boundary condition was set to 0.4 and externally 0.8 was used.

Material properties (fired clay, mineral wool and insulating plaster) used during conjugated heat and moisture transfer simulations were set by using WUFI PRO software's material property database [20]. Temperature and moisture dependency of all hygrothermal material properties, such as thermal conductivity, vapour resistance factor, and moisture diffusivity were included in the material models.

2.4 Derivative-Free Optimization

Comsol Multiphysics is capable of constrained gradient-free or gradient-based optimization processes, the process showed in Fig. 3. Gradient-free optimization can find the constrained design variables that have the minimal (or maximal) objective function without knowing the gradient of the objective function. It should be used, when the objective function and/or the constraints are scalar and non-differentiable, and in case of geometry optimization, which needs re-meshing. The disadvantage of the gradient-free methods is that the number of variables could increase the optimization time exponentially. In this case, searching for an optimum internal geometry needs re-meshing in each optimization step, therefore gradient-free methods are only possible options.

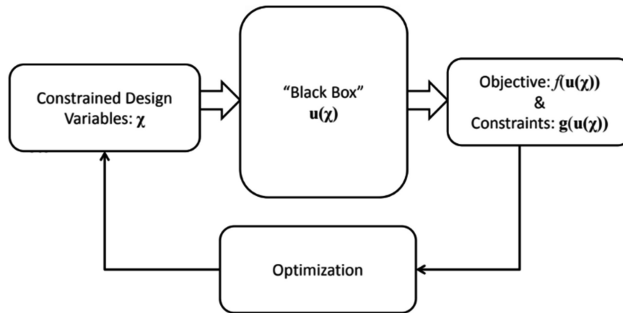


Fig. 3. Schematic description of the optimization process [21]

There are several different gradient-free solvers available, such as Monte-Carlo method, which randomly chooses the design variables between the given bounds, and evaluates the results; however, with this method, the global optimum can be found only with very dense statistical sampling, resulting in long optimization time. 1st order approximate gradient methods are Nelder-Mead [22] and constrained optimization by linear approximation (COBYLA) [23] methods. Both can take the constraints into consideration. Nelder-Mead method is constructing a simplex and improves the worst point, while COBYLA constructs a linear approximant, by using a unique linear polynomial, to the objective function. Powell [24] presented, that Nelder-Mead algorithm can find the least value of a function incorrectly in case of convex objective function. In this study, gradient-free optimization method called COBYLA was used.

The goal was to minimize the solution, and the objective function was the inward heat flux from the internal surface of the plastered masonry block. The variables were the horizontal dimensions of the insulation filled holes (Fig. 4), while the thickness of the insulations were constant 40 mm, assuming that the MW insulation is cut from 40 mm thick boards. The simplified model had 20–20 mm insulating plaster on each side. There are 64 variables (A1 to H4) describing the lengths of the insulation fillers’ sides perpendicular to the heat source. However, these variables are set to be identical in patterns to reduce the number of variables to 8, because COBYLA optimization is reasonable only under 9 variables [23].

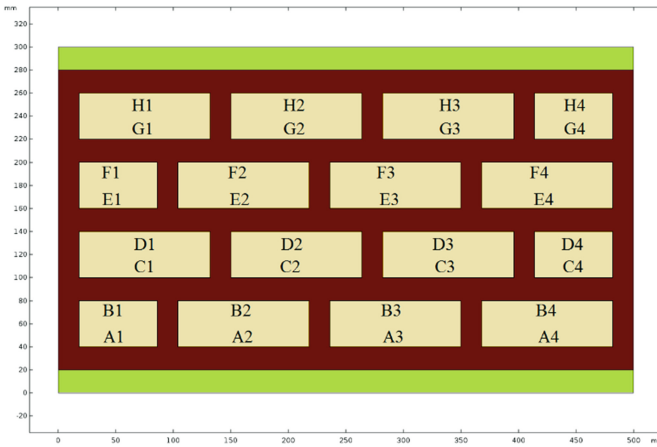


Fig. 4. Simplified masonry block geometry for optimization with marked variables

Table 1. Variables and bounds of the presented optimization cases

Case name	Variables	Bounds
1-ABAB	$A1 = C4 = E1 = G4, A2 = C3 = E2 = G3, A3 = C2 = E3 = G2, A4 = C1 = E4 = G1$ $B1 = D4 = F1 = H4, B2 = D3 = F2 = H3, B3 = D2 = F3 = H2, B4 = D1 = F4 = H1$	min: 40 max: 120
2-ABBA	$A1 = D4 = E1 = H4, A2 = D3 = E2 = H3, A3 = D2 = E3 = H2, A4 = D1 = E4 = H1$ $B1 = C4 = F1 = G4, B2 = C3 = F2 = G3, B3 = C2 = F3 = G2, B4 = C1 = F4 = G1,$	min: 40 max: 120
3-ABAB	$A1 = C4 = E1 = G4, A2 = C3 = E2 = G3, A3 = C2 = E3 = G2, A4 = C1 = E4 = G1$ $B1 = D4 = F1 = H4, B2 = D3 = F2 = H3, B3 = D2 = F3 = H2, B4 = D1 = F4 = H1$	min: 60 max: 180
4-ABBA	$A1 = D4 = E1 = H4, A2 = D3 = E2 = H3, A3 = D2 = E3 = H2, A4 = D1 = E4 = H1$ $B1 = C4 = F1 = G4, B2 = C3 = F2 = G3, B3 = C2 = F3 = G2, B4 = C1 = F4 = G1,$	min: 60 max: 180

The constraints were set to prevent the sum of the variables in one line of insulation, including the ceramic parts, from exceeding the width of the masonry block (500 mm); furthermore at least 18 mm thick ceramic part had to be horizontally between the edges of insulations. In first case the bounds were set to minimum 60 mm and maximum 120 mm, which is close to the original geometry (68 mm and 114 mm), and on the other cases, they were set to the minimum 60 mm and maximum 180 mm.

3 Results

3.1 Hygrothermal Results with the Initial Geometry

Before the optimization process, a steady-state conjugated heat and moisture transfer simulation with the initial geometry was performed. Only rectangular MW filled holes were in the initial geometry, the filled holes were either 68 mm × 40 mm or 114 mm × 40 mm. The finite element mesh consisted of 4518 triangle elements.

The hygrothermal simulation results are represented in Fig. 5. The temperature distribution and heat flux magnitudes in the masonry block shows that the ceramic structure, which is perpendicular to the internal (and external) side of the wall construction and parallel to the inward heat flux are the key in the hygrothermal evaluation of the blocks. Heat flux magnitudes are significantly larger in these parts of the blocks.

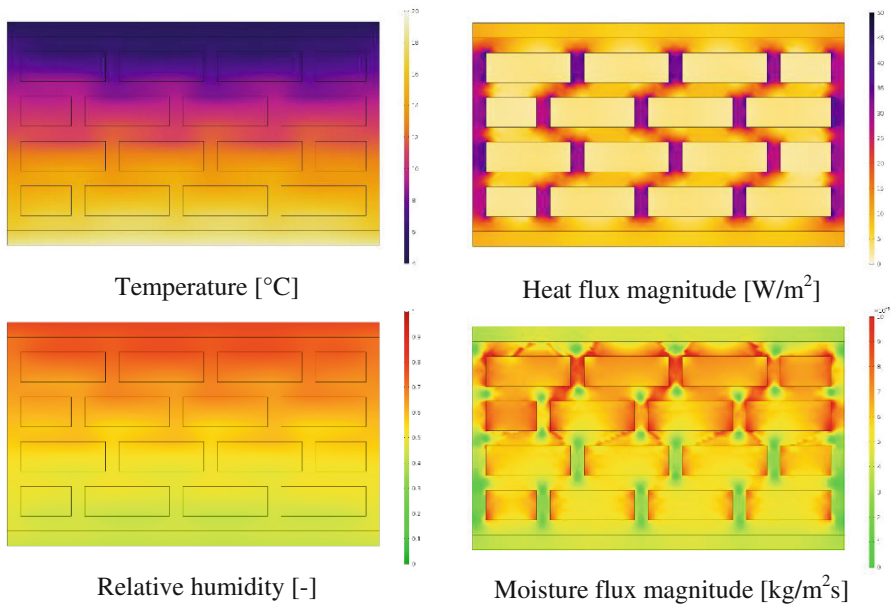


Fig. 5. Hygrothermal simulation results of MW filled masonry block with initial geometry

Relative humidity is between 40% and 80% in the construction. It is visible, that in the external sides of the insulation filler, higher relative humidity occurs than in the filler at the internal side. Fired clay is a capillary active material (it has significantly higher moisture diffusivity than mineral wool), but has also significantly higher vapour resistance factor, than mineral wool. The distribution of moisture flux magnitude shows an interesting pattern. Moisture flux is higher in the external insulation fillings and fired clay parts between them. Observing moisture flux magnitude rather than relative humidity, the moisture bridges (analogously with thermal bridges) are becoming much more visible. Moisture in materials increases their thermal conductivity.

Assuming heat transfer only, i.e. moisture transfer is neglected (see Fig. 6), the inward heat flux on the internal side of the insulating plaster applied on the masonry construction was 5.1835 W/m^2 , which equals to $0.32 \text{ W/m}^2\text{K}$ thermal transmittance. It is visible, that the heat flux magnitudes in the masonry block are significantly smaller. The model took the temperature dependence of thermal conductivities into consideration. The catalogue U-value of the masonry block is $0.29 \text{ W/m}^2\text{K}$ (where the geometry was not simplified, and declared thermal conductivities were considered without temperature dependency and the material properties presumably different due to the composition of the exact fired clay). When conjugated heat and moisture transfer simulation was performed, the inward heat flux was 7.3429 W/m^2 , which equals to $0.46 \text{ W/m}^2\text{K}$ thermal transmittance value. The average relative humidity in the masonry block was 58%. Considering not only thermal, but hygrothermal approach on the numerical simulation, the difference between results is more than 41%.

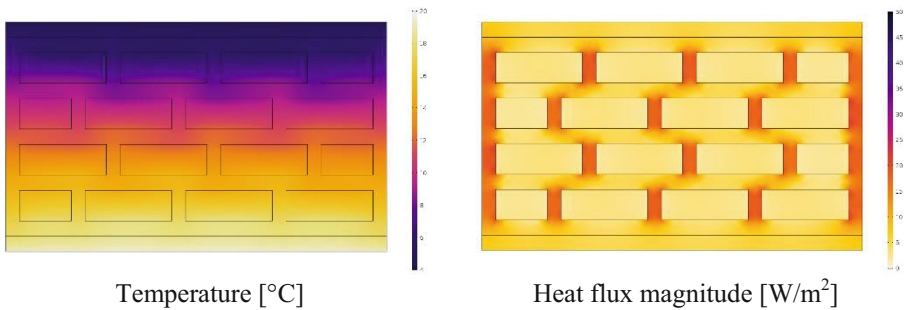


Fig. 6. Thermal simulation results of MW filled masonry block with initial geometry

3.2 Results of the Optimized Cases

In this paper, four optimization cases are presented with different optimization variables and bounds. Figures 7 and 8 show the results of the COBYLA optimization process, when the lowest bound was set to 40 mm and the highest bound was set to 120 mm. The internal geometry of the MW insulations in the masonry block is now trapezoid and parallelogram shape, depending on the variable set showed in Table 1. It is visible, that the highest heat flux magnitudes occur in the non-optimized edges of the masonry blocks, therefore it is also worth dealing with the optimization of this section in another

research. Case 2-ABBA has the lowest inward heat flux value, which equals to $U = 0.38 \text{ W/m}^2\text{K}$. Compared to the initial, non-optimized hygrothermal model, the optimization process achieved more than 17% reduction of U-value. Results of case 3-ABAB and Case 4-ABBA are shown in Figs. 9 and 10. In these optimization processes, the lowest bound was set to 60 mm, while the highest bound was increased to 180 mm. However, the shape of the internal structure of masonry block is similar to the previous optimized versions, but the angles and the filler geometry are changed. Comparing all the four cases, case 4-ABBA achieved the lowest inward heat flux value, resulting in $0.35 \text{ W/m}^2\text{K}$ thermal transmittance value. Therefore, the U-value of the masonry block was reduced by 24%.

Besides the main objective of decreasing the thermal transmittance of the masonry blocks, there is also visible difference in the heat flux and moisture flux magnitudes across the sections of the optimized blocks compared to the initial one. It is visible, that in the thinner internal ceramic parts between the insulation fillers, the heat flux is lower than in case of the initial simulation showed in Fig. 5. Nevertheless, the moisture flux magnitudes in the slanted ceramic internal structures are increased, especially in the outer side of the masonry blocks (these parts become thinner during the optimization); however, in the horizontal ceramic internal structures between the MW fillers are reduced.

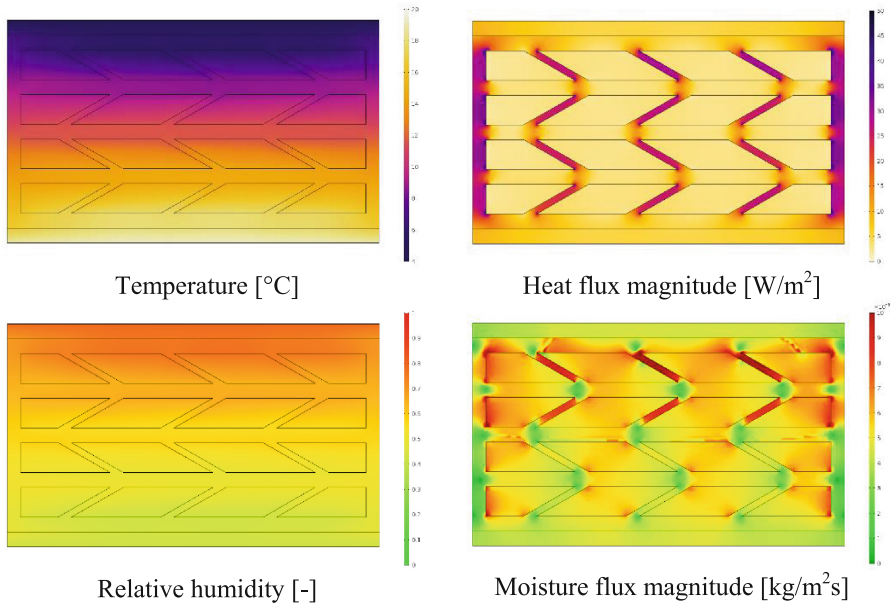


Fig. 7. Optimization results of model 1-ABAB, $q_0 = 6.1802 \text{ W/m}^2$

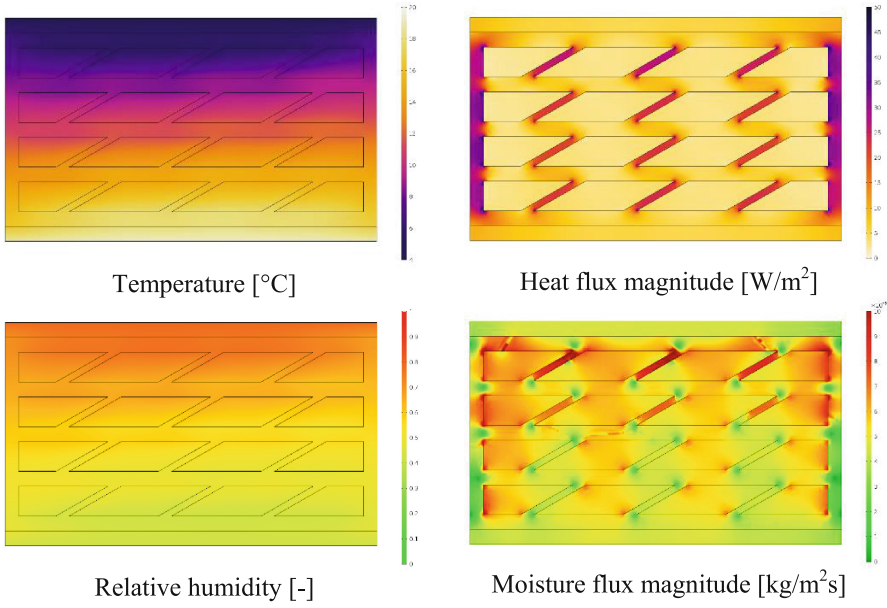


Fig. 8. Optimization results of model 2-ABBA, $q_0 = 6.0673 \text{ W/m}^2$

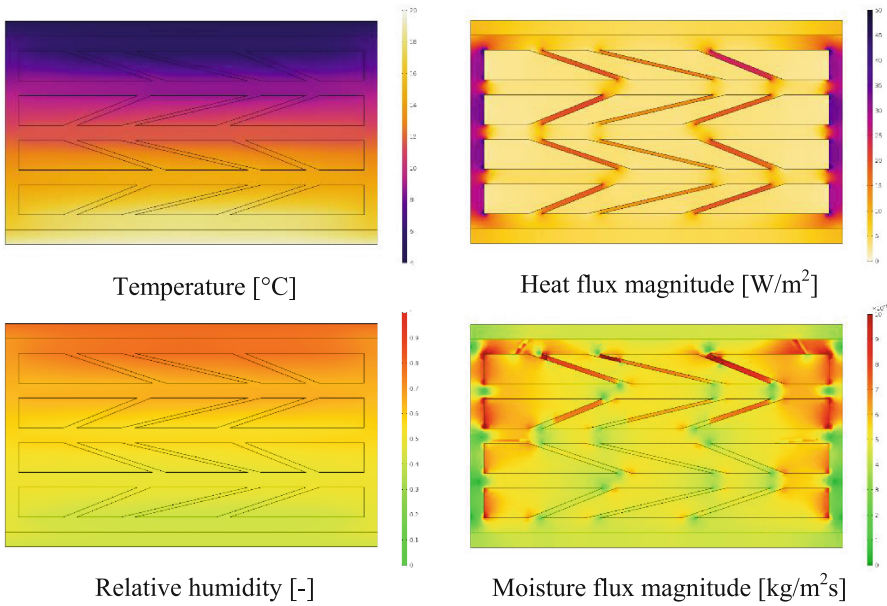


Fig. 9. Optimization results of model 3-ABAB, $q_0 = 5.6231 \text{ W/m}^2$

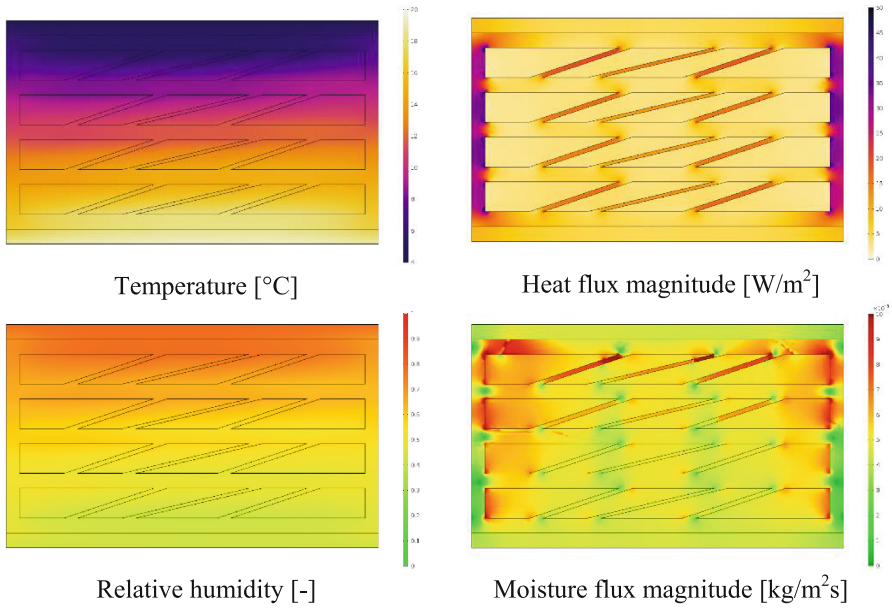


Fig. 10. Optimization results of model 4-ABBA, $q_0 = 5.5434 \text{ W/m}^2$

The above presented results demonstrated that COBYLA algorithm is applicable to obtain lower U-values of masonry blocks. Figure 11 shows how many steps of optimization process were needed to find the optimum. It is clearly visible, that the selection of the variables and bounds has impact on the process time and number of steps.

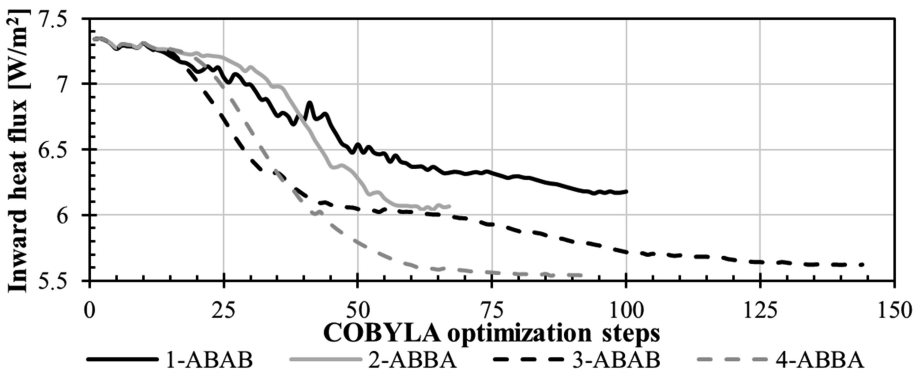


Fig. 11. Optimization process by using COBYLA

4 Conclusions

In the paper, derivative-free constrained optimization was performed on mineral wool filled ceramic masonry blocks with the aid of hygrothermal finite element simulations. The results showed that in case of the initial geometry, hygrothermal simulation resulted in 41% higher thermal transmittance, than thermal simulations, since moisture transfer and moisture dependent hygrothermal properties were taken into consideration. With the COBYLA internal geometry optimization of the insulation filler blocks with the selected bounds, 17% and 24% reduction was achieved, respectively. Proper selection of bounds probably can result in even higher reductions; however, the manufacturability of masonry blocks limits the boundaries of the optimization process. Applying the presented optimization method in masonry block design leads to more energy efficient structures, using the same or even less raw materials, without increasing the production cost.

References

1. Nagy, B., Tóth, E.: Hygrothermal behaviour of hollow and filled ceramic masonry blocks. In: RILEM Proceedings PRO, vol. 112, pp. 279–288 (2016)
2. Nagy, B., Orosz, M.: Optimized thermal performance design of filled ceramic masonry blocks. *Appl. Mech. Mater.* **797**, 174–181 (2015)
3. Zukowski, M., Haese, G.: Experimental and numerical investigation of a hollow brick filled with perlite insulation. *Energy Build.* **42**, 1402–1408 (2010)
4. Zach, J., Hroudova, J., Sedlmajer, M.: Study of hygrothermal behavior of advanced masonry components made with utilization of secondary raw materials. In: Proceedings of the 2nd Central European Symposium on Building Physics, pp. 169–174 (2013)
5. Kočí, J., Maděra, J., Jerman, M., Černý, R.: Effect of cavity filler on the effective thermal conductivity of hollow bricks: a computational analysis based on accurate input data. In: Proceedings of the 2nd Central European Symposium on Building Physics, pp. 635–639 (2013)
6. Pavlík, Y., Jerman, M., Trník, A., Kočí, V., Černý, R.: Effective thermal conductivity of hollow bricks with cavities filled by air and expanded polystyrene. *J. Build. Phys.* **37**, 436–448 (2014)
7. Setty, A.B.T.P., Shaik, S.: Investigation of dynamic thermal parameters of various insulation filled bricks exposed to periodic thermal variations for energy efficient stuffed bricks design. In: Proceedings of the 4th International High Performance Buildings Conference at Purdue, vol. 3416 (2016)
8. Zach, J., Novák, V.: Study of the use of vacuum insulation as integrated thermal insulation in ceramic masonry blocks. *Procedia Eng.* **151**, 206–2013 (2016)
9. Wernery, J., Ben-Ishai, A., Binder, B., Brunner, S.: Aerobrick – an aerogel-filled insulating brick. *Energy Procedia* **134**, 490–498 (2017)
10. Li, J., Meng, X., Gao, Y., Mao, W., Luo, T., Zhang, L.: Effect of the insulation materials filling on the thermal performance of sintered hollow bricks. *Case Stud. Therm. Eng.* **11**, 62–70 (2018)
11. Sousa, L.C., Castro, C.F., António, C.C., Sousa, H.: Topology optimisation of masonry units from the thermal point of view using a genetic algorithm. *Constr. Build. Mater.* **25**, 2254–2262 (2011)

12. Bruggi, M., Taliercio, A.: Design of masonry blocks with enhanced thermomechanical performances by topology optimization. *Constr. Build. Mater.* **48**, 424–433 (2013)
13. Wienerberger technical data and processing manual. <http://www.wienerberger.at>. Accessed 30 Mar 2018
14. Künzle, H.: Simultaneous Heat and Moisture Transport in Building Components. One and two-dimensional calculation using simple parameters, vol. 102. IRB Verlag (1995)
15. Comsol Multiphysics 5.3 Heat transfer module user's guide (2017)
16. MSZ EN ISO 6946:2017 Building components and building elements. Thermal resistance and thermal transmittance. Calculation methods (ISO 6946:2017). Hungarian Standards Institute (2017)
17. MSZ EN ISO 10211:2017 Thermal bridges in building construction. Heat flows and surface temperatures. Detailed calculations (ISO 10211:2017). Hungarian Standards Institute (2017)
18. MSZ EN 15026:2007 Hygrothermal performance of building components and building elements. Assessment of moisture transfer by numerical simulation. Hungarian Standards Institute (2007)
19. 7/2006 (V.24.) TNM decree on the Determination of the Energy Characteristics of Buildings. http://njt.hu/cgi_bin/njt_doc.cgi?docid=101820.352718. Accessed 30 Mar 2018
20. WUFI PRO database (2018)
21. Frei, W.: Optimization with COMSOL multiphysics. In: COMSOL Tokyo Conference 2014, Tokyo (2014)
22. Nelder, J.A., Mead, R.: A simplex method for function minimization. *Comput. J.* **7**(4), 308–313 (1965)
23. Powell, M.J.D.: A direct search optimization method that models the objective and constraint functions by linear interpolation. In: Gomez, S., Hennart, J.-P. (eds.) *Advances in Optimization and Numerical Analysis*, pp. 51–67. Kluwer Academic (1994)
24. Powell, M.J.D.: A view of algorithms for optimization without derivatives. Cambridge University Technical Report DAMTP (2007)



Stochastic Finite Element Analysis of Nonlinear Beam on Winkler-Pasternack Foundation

Seguini Meriem^(✉) and Nedjar Djamel

Faculty of Architecture and Civil Engineering, Department of Civil Engineering,
Laboratory of Mechanic of Structures and Stability of Constructions
LM2SC, University of Science and Technology of Oran Mohamed Boudiaf,
BP 1505, 3100 Oran, Algeria
seguinimeriem@yahoo.fr

Abstract. A new model of soil-structure is developed for the probabilistic finite element analysis of flexible beam resting on spatially random nonlinear soil where the Monte Carlo simulations have been used for this purpose. In fact, the present work deals with the evaluation of the effect of the randomness soil's parameters on the nonlinear response of beam resting on nonlinear Winkler-Pasternack foundation. The nonlinear equations of motion are derived using the von-Kármán's nonlinear strain-displacement relationships and have been solved by using the Newton-Raphson iteration method. In this study, the effects of large deflections, coefficient of subgrade reaction, shear deformation, type of foundation on the response of the beam are discussed and special attention is given to estimate the real behavior of the beam. A novelty in the analysis is that the heterogeneity of nonlinear soil is combined to the nonlinearity of beam by taking into account the shear effect where the soil's model's and the spatial variability of its parameters have a strong impact on the response of the structure.

Keywords: Soil-structure interaction · Finite element probabilistic analysis
Monte Carlo simulation · Nonlinear Winkler-Pasternack foundation
Geometric nonlinear beam · Shear deformation · Newton Raphson method

1 Introduction

The soil-structure interaction problems is significantly complex due to the nonlinear behavior of the beam and the soil and its heterogeneity. However, in the engineering practice the quantification of spatial variability of soil's characteristics effects at the beam behavior is of particular importance for structure design. In fact, several researches have been done on the beams resting on different type of foundations by neglecting the soil's heterogeneity [1–16]. Winkler [3] was the first who used the coefficient of subgrade reaction to represent the soil-beam interaction problems while Timoshenko [1] and Hetenyi [2] presented an analytical solution for beams on elastic foundation. Some researchers have developed the stiffness matrix of an elastic beam resting on foundation [17, 18]. The stiffness matrix of a beam with shear effect resting on elastic foundation has been also developed [19]. Other ones [20–23] analysed the

behaviour of beam resting on two-parameter elastic foundation. Moreover, there has been considerable research on Timoshenko beam resting on linear and nonlinear foundation and subjected to dynamic loads [24–26]. Several works [27–32] have been made in order to analyse the geometric nonlinear behaviour of structures (beam, pipe, catenary risers) resting on different type of foundations where Hosseini Kordkheili and Bahai [33] extended the same work of [27] for dynamic cases. The effect on the nonlinear behavior of the soil on the beam response has been also studied [34–37]. Furthermore, a series of papers appeared in the literature [42–55] where the effect of inherent random soil heterogeneity on beam response was assessed quantitatively and the heterogeneous soil characterized by its spatial properties (the mean, the coefficient of variation and the correlation length) is taken into account [38–41]. Grigoriu et al. [42] analysed the response of beam on Winkler random soil. Elachachi et al. [44, 45] developed a finite element models of soil-pipe interaction by using different models of soil in order to analyse the effect of the spatial variability of soil's characteristics on the behavior of the pipe by using the local average theory developed by Vanmarcke [46] while other researchers [47–49] have proposed to adopt probabilistic approaches in practical earthquake engineering applications. The influence of the nonlinear random soil characteristics on the behavior of the pipeline has also been studied [53] where the material nonlinear analysis of the soil was based on the elastic–perfectly plastic load–displacement relationship.

Seguini and Nedjar [54] carried out the geometric nonlinear analysis of the buried pipeline resting on variable Winkler foundation by using Euler-Bernoulli beam-Von Kármán theory combined to Vanmarcke method and Monte Carlo simulations. The nonlinear behavior of deep beam resting on nonlinear Winkler soil based on Von Kármán geometric non-linearity was also studied by Seguini and Nedjar [55]. In this reference, the soil is considered as heterogeneous and stochastic finite element method was used to quantify the effect of the spatial variability of soil characteristics on the beam response without taking into account the shear effect.

This study focuses on the shear deformation and heterogeneity soil problem. More specifically, the nonlinear analysis of supported Timoshenko beam on a Winkler-Pasternak foundation in Monte Carlo framework has been presented and discussed through applications of particular interest. The Von Kármán–Timoshenko formulation based on the assumptions of large deflections and moderate rotations of the beam is used. Moreover, the coefficient of subgrade reaction field has been simulated via local average subdivision and modelled as random field. The numerical applications are worked out to illustrate the efficiency, and wherever possible the accuracy and range of applications of the proposed method. Parametric studies are carried out to assess the effect of probabilistic characteristics of soil properties on the response of Timoshenko beam. Also, the difference between Euler-Bernoulli and Timoshenko beam theory is discussed. Results from the stochastic analysis are compared with corresponding results obtained by deterministic analysis. The present results are also compared with the previously published results to establish the validity of the present method and to obtain a more realistic behavior of the soil-beam interaction model.

2 Finite Element Theory for Deterministic Analysis

The problem considered in this study is investigated under the following assumptions: (i) the beam is based on Timoshenko-Von Kàrmàn theory and resting on Winkler-Pasternak foundations, (ii) the soil is considered as random field. However, to analyse the beam-soil interaction problem the total strain energy Ψ defined below is used.

$$\Psi = \Psi_1 + \Psi_2 \quad (1)$$

where Ψ_1 is the strain energy of the beam and Ψ_2 is the strain energy of the soil.

The polynomial displacement function, $w(x)$, is expressed as:

$$w(x) = [N_i]^t \cdot \{U\} \quad (2)$$

where $N_i, (i = 1, \dots, 4)$ is the vector composed of interpolation functions of Hermite type (Eq. 3) and U is the vector of nodal displacements of a one-beam element (Eq. 4).

$$\begin{cases} N_1(x) = 1 - 3\frac{x^2}{l^2} + 2\frac{x^3}{l^3}, & N_2(x) = x - 2\frac{x^2}{l} + \frac{x^3}{l^2} \\ N_3(x) = 3\frac{x^2}{l^2} - 2\frac{x^3}{l^3}, & N_4(x) = -\frac{x^2}{l} + \frac{x^3}{l^2} \end{cases} \quad (3)$$

$$\{U\} = \{w_1, \theta_1; w_2, \theta_2\} \quad (4)$$

2.1 Geometric Nonlinear Beam

Based on the basic hypothesis of Timoshenko theory, the axial displacement u and the transverse displacement w of the beam can be expressed by:

$$u_x(x, z) = u_0(x) + z\phi_x(x) \quad (5a)$$

$$u_z(x, z) = w_0(x) \quad (5b)$$

where u_0 and w_0 are the axial and the transverse displacements of any point of the neutral axis, ϕ_x is the rotation of the cross section. Due to the assumption of large displacement, the Von Kàrmàn nonlinear strains-displacements relationship [56] are defined as:

$$\varepsilon_x = \varepsilon_x^0 + z\varepsilon_x^1 \quad (6a)$$

$$\varepsilon_x^0 = \frac{\partial u_0(x)}{\partial x} + \frac{1}{2} \left(\frac{\partial w_0(x)}{\partial x} \right)^2 \quad (6b)$$

$$\varepsilon_x^1 = \frac{\partial \phi_x(x)}{\partial x} \quad (6c)$$

$$\gamma_{xz} = \frac{\partial w_0(x)}{\partial x} + \phi_x(x) \quad (6d)$$

ε_x and ε_x^0 are the longitudinal and the nonlinear strain respectively, ε_x^1 is the curvature of the beam element and γ_{xz} is the shear strain.

Using Hook's law, the internal axial force N_{xx} , the bending moment M_{xx} and the shear force Q_{xx} are determined by Reddy [56] as follows:

$$N_{xx} = A_{xx} \left[\frac{\partial u_0(x)}{\partial x} + \frac{1}{2} \left(\frac{\partial w_0(x)}{\partial x} \right)^2 \right] + B_{xx} \frac{\partial \phi_x(x)}{\partial x} \quad (7a)$$

$$M_{xx} = B_{xx} \left[\frac{\partial u_0(x)}{\partial x} + \frac{1}{2} \left(\frac{\partial w_0(x)}{\partial x} \right)^2 \right] + D_{xx} \frac{\partial \phi_x(x)}{\partial x} \quad (7b)$$

$$Q_{xx} = S_{xx} \left(\frac{\partial w_0(x)}{\partial x} + \phi_x(x) \right) \quad (7c)$$

Noting that A_{xx} , B_{xx} , D_{xx} are the extensional, extensional bending and flexural rigidity of the beam element respectively and S_{xx} is the shear stiffness. It can be defined as follows:

$$(A_{xx}, B_{xx}, D_{xx}) = \int_A E_b(z)(1, z, z^2) dA \quad (8a)$$

$$S_{xx} = K_{sb} \int_A G dA \quad (8b)$$

where $A_{xx} = E_b A$, $B_{xx} = 0$, $D_{xx} = E_b I_b$, $S_{xx} = K_{sb} \cdot G \cdot A$, the shear modulus $G = E/2(1 + \nu)$, and ν is the poisson ratio of the beam. The shear correction factor K_{sb} is equal to 5/6 [60].

The strain energy of Timoshenko beam can be written as:

$$\psi_1 = \frac{1}{2} \int_0^{le} (N_{xx} \varepsilon_x^0 + M_{xx} \varepsilon_x^1 + Q_{xx} \gamma_{xz}) dx \quad (9)$$

By substituting Eqs. (6a)–(7c) into Eq. (9), the strain energy of the beam takes the following form:

$$\psi_1 = \frac{1}{2} \int_0^{le} \left\{ E_b A \left[\frac{\partial u_0}{\partial x} + \frac{1}{2} \left(\frac{\partial w_0}{\partial x} \right)^2 \right]^2 + K_{sb} G A \left(\frac{\partial w_0}{\partial x} + \phi_x \right)^2 + E_b I_b \left(\frac{\partial \phi_x}{\partial x} \right)^2 \right\} dx \quad (10)$$

where the derivative of axial displacement $\frac{du_0}{dx}$ is assumed to be small, therefore it can be neglected and the Eq. (10) becomes:

$$\psi_1 = \frac{1}{2} \int_0^{le} \left\{ E_b A \left[\frac{1}{2} \left(\frac{\partial w_0}{\partial x} \right)^2 \right]^2 + K_{sb} GA \left(\frac{\partial w_0}{\partial x} + \varphi_x \right)^2 + E_b I_b \left(\frac{\partial \varphi_x}{\partial x} \right)^2 \right\} dx \quad (11)$$

$$\psi_1 = \frac{1}{2} \{U\}^t \left\{ \left[\frac{1}{2} E_b A \int_0^{le} \left(\frac{\partial w_0}{\partial x} \right)^2 \left(\frac{\partial N}{\partial x} \right) \left(\frac{\partial N}{\partial x} \right)^t dx \right] + \left[K_{sb} GA \int_0^{le} \left(\frac{\partial w_0}{\partial x} + \left(\frac{\partial N}{\partial x} \right) \left(\frac{\partial N}{\partial x} \right)^t \right)^2 dx \right] \right. \\ \left. + \left[E_b I_b \int_0^{le} \left(\frac{\partial^2 N}{\partial x^2} \right) \left(\frac{\partial^2 N}{\partial x^2} \right)^t dx \right] \right\} \{U\} \quad (12)$$

$$\psi_1 = \frac{1}{2} \{U\}^t [K_{bnl} + K_{bl}] \{U\} \quad (13)$$

$$K_T = K_{bl} + K_{bnl} \quad (14)$$

Noting that $[K_{bl}^e]$ and $[K_{bnl}^e]$ are respectively the linear and geometric nonlinear matrices of rigidity of the beam element.

2.2 Nonlinear Winkler-Pasternack Foundation

The strain energy of the soil Ψ_2 is defined as follows:

$$\Psi_2 = \frac{1}{2} \int_0^{le} p_e(x) \cdot w(x) dx \quad (15)$$

where $p_e(x)$ is the Winkler and Pasternak reaction related to the transverse displacement and rotation and it is expressed as follows:

$$p_e(x) = p_w(x) + p_p(x) \quad (16)$$

$$p_e(x) = k_w \cdot b \cdot w(x) - k_s \cdot b \cdot \frac{d^2 w}{dx^2} \quad (17)$$

Noting that b is the width of the beam, k_w and k_s are the coefficient of subgrade reaction of Winkler and Pasternak soil's respectively.

And by introducing Eq. (17) into Eq. (15), the energy of the soil is expressed as:

$$\Psi_2 = \frac{1}{2} \{U\}^t \left[k_w \cdot b \cdot \int_0^{le} N_i(x) N_j(x) dx + k_s \cdot b \int_0^{le} N'_i(x) N'_j(x) dx \right] \{U\} \quad (18)$$

The coefficient of soil's subgrade reaction k_w is considered constant for linear elastic soil. Thus for elastic nonlinear soil model, the coefficient k_w for an element e is [54]:

$$\begin{cases} p_w = k_w w_e & 0 \leq w_e \leq S_u \\ p_w = p_u & w_e > S_u \end{cases} \quad (19)$$

where S_u is the soil yield displacement and P_u is the ultimate subgrade reaction. The strain energy of the soil is expressed as:

$$\Psi_2 = \frac{1}{2} \{U\}^t [K_s] \{U\} \quad (20)$$

$[K_s]$ is the matrix of rigidity of the soil. Nevertheless, the total strain energy Ψ is written as follows:

$$\Psi = \frac{1}{2} \{U\}^t [K_e] \{U\} \quad (21)$$

Noting that $[K_e]$ is the elemental rigidity matrix and is expressed as:

$$[K_e] = [K_T] + [K_s] \quad (22)$$

$$[K_e(U)^i] \{U\}^{i+1} = \{F\} \quad (23)$$

$$\{U\}^{i+1} = \{U\}^i + \{\delta U\}^i \quad (24)$$

where F is defined for a distributed load respectively as:

$$\{F\} = \left\{ \begin{array}{c} \frac{q \cdot l_e}{2} \\ \frac{q \cdot l_e^2}{12} \\ \frac{q \cdot l_e}{2} \\ -\frac{q \cdot l_e^2}{12} \end{array} \right\} \quad (25)$$

Noting that the load increment δq^j and δP^j are used to update the distributed and concentrated loads respectively:

$$q^{j+1} = q^j + \delta q^j \quad (26a)$$

$$P^{j+1} = P^j + \delta P^j \quad (26b)$$

The incremental equation of equilibrium (23) is implemented by using the Matlab software and the Newton-Raphson iterative method [57–59] is introduced to solve it. The superscript j is used to denote the load step, the superscript i to denote the iterative cycle and the symbol δ to denote incremental quantities.

3 Spatial Variability Modelling

Due to the variety of soil's types and its layered profiles, the deterministic analysis is not enough to determine the real behavior of the structure. Therefore, in the present work the soil medium is divided into different layers by taking into consideration the correlation structures. In fact, the subgrade reaction coefficient's field has been simulated via local average subdivision method and characterized by a lognormal distribution with a fixed mean m_k , a variance σ_k^2 , various coefficients of variation and spatial correlation lengths structures (L_c , L_{cs}) which describe the distance over which the correlation between spatially random soil (Winkler and Pasternak) properties tends to disappear.

However, Vanmarcke [46] supposed that the mean and variance are constant throughout the entire soil field and gives an average value of the coefficient of subgrade reaction of each zone of the soil where the summation of all this zones averages values is equal to the average m_k . The local average of the coefficient of subgrade reaction k_{soil} is expressed as:

$$E[k_{soil}(D_i)] = m_k \quad (27)$$

and in each zone (i) of length D_i , the variance of k_{soil} is defined by:

$$Var[k_{soil}(D_i)] = \sigma_k^2 \gamma(D_i) \quad (28)$$

where $k_{soil} = k_w = k_s$ and $\gamma(D_i)$ is the variance function [54, 55] which depends on the spatial correlation function $\rho(x)$ and determined by Vanmarcke [46] as:

$$\gamma(D_i) = \frac{2}{D_i} \int_0^{D_i} \left(1 - \frac{x}{D_i}\right) \rho(x) dx \quad (29)$$

$$\text{with } \rho(\tau) = 1 - \frac{|\tau|}{L_c} \text{ for } |\tau| \leq L_c \quad (30)$$

by introducing Eq. (30) into Eq. (29), we obtain the variance function in a discrete formulation as follows:

$$\gamma(D_i) = \begin{cases} 1 - \frac{D_i}{3L_c} & \text{if } D_i \leq L_c \\ \frac{L_c}{D_i} \left(1 - \frac{L_c}{3D_i}\right) & \text{if } D_i > L_c \end{cases} \quad (31)$$

The local average subdivision method developed by Fenton and Vanmarcke [61] is then used to generate the random variable and compute the covariance matrix C_{ij} of the coefficient of soil's subgrade reaction. Each term of this matrix corresponds to the correlation between two zones (i) and (j) of length D_i and D_j respectively.

$$C_{ij} = Cov[k_{soil}(D_i), k_{soil}(D_j)] \tag{32}$$

$$C_{ij} = \frac{\sigma_k^2}{2} \left\{ (t-1)^2 \gamma [(t-1)D] - 2t^2 \gamma [t.D] + (t+1)^2 \gamma [(t+1)D] \right\} \tag{33}$$

where $t = |i - j|$ is the difference between two spatial zones (i) and (j) in absolute value with a same length (in our case $D = D_i = D_j$).

4 Numerical Study

A simply supported Timoshenko beam of length L , width b , thickness h , resting on nonlinear two-parameter foundation and subjected to a distributed load is shown in Fig. 1. In fact, for comparison reasons the deterministic and probabilistic properties of beam and soil are deduced from literature and resumed in Table 1 [54].

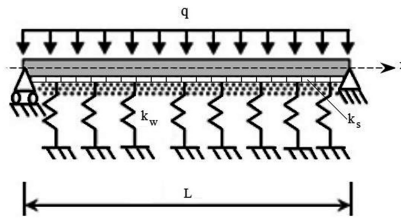


Fig. 1. Beam resting on two-parameter foundation and subjected to a uniform distributed load q

Table 1. Beam and Soil Properties [54].

Symbol	Parameters	Range of values	Unit
b	Width of beam	0.4	m
h	Height of beam	0.8	m
L	Length of beam	2,9	m
E_b	Beam Elastic Young modulus	25.106	kN/m ²
ν	Poisson ration of beam	0.15	(-)
k_w	Coefficient of Winkler soil's subgrade reaction	500, 10 ³ , 6000, 10 ⁴	kN/m ³
k_s	Coefficient of Pasternak soil's subgrade reaction	0, 100, 500, 600, 10 ³ , 6000	kN/m
S_u	Yield displacement of soil	1	mm
P_u	The ultimate subgrade reaction	2.5	kN/m ²
L_c	Correlation length of Winkler soil	0.5, 2, 4, 6, 8	m
L_{cs}	Correlation length of Pasternak soil	0.5, 2, 4, 6, 8	m
C_v	Coefficient of variation of soil	50, 70, 100	%
q	Applied load	25, 62.5	kN/m ²

On the basis of the hypothesis and numerical procedures presented in the previous sections, a Matlab program has been written and representative example has been studied to demonstrate the efficiency of the developed model. However, a stochastic nonlinear numerical modelling combined to Monte Carlo has been adopted in this study.

4.1 Effect of the Shear Deformation Beam

In order to assess the important effect of the shear deformation on the beam response, the obtained results from deterministic analysis were resumed in Table 2 and compared to those obtained by [54, 30]. In fact, from Table 2 it can be noted that the maximum deflection of the geometric nonlinear Timoshenko beam is smaller than the one obtained by using the Euler-Bernoulli theory [54] by about 1%. Therefore, from the finite element deterministic analysis it can conclude that the shear effect can not be neglected.

Table 2. Comparison of Maximum deflections, W_{max} of nonlinear beam (Timoshenko and Euler-Bernoulli) resting on linear soil).

	Present study (TBT)	Seguini et Nedjar [54] (EBT)	Al-Azzawi and Theeban [30]
W_{max} (m)	1.986×10^{-5}	1.997×10^{-5}	2.018×10^{-5}

4.2 Effect of the Variation of the Slenderness Ratio and Foundation Type on Timoshenko Beam Response

To demonstrate the important effect of the Winkler and Pasternak foundation on the response of the Timoshenko beam subjected to a distributed load $q = 62.5 \text{ kN/m}^2$, different slenderness ratio (L/h) have been taken into account.

The Winkler parameter k_w is chosen to be 500, 10^3 and 10^4 kN/m^3 and the stiffness of the shear layer k_s is chosen to be 0, 100, 500, 10^3 kN/m . From Fig. 2 it can be seen

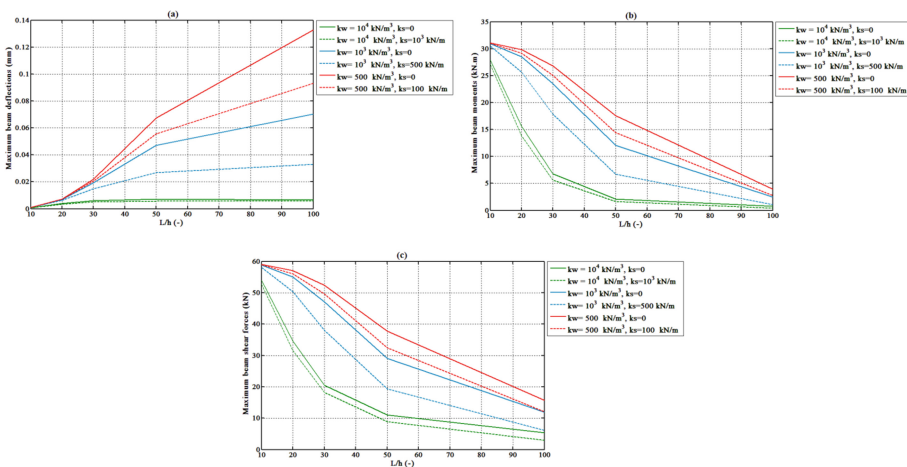


Fig. 2. Effect of the variation of soil's coefficient (k_w, k_s) and the slenderness ratio (L/h) on the response of the beam, (a) maximum deflection of the beam, (b) maximum bending moment of the beam, (c) maximum shear force of the beam.

that increases in the slenderness ratio (L/h) causes increases in the deflections and decreases in bending moment and shear force. It can also be observed that there is a difference in the deflection decrease for the higher coefficient of Winkler and Pasternak parameters foundations. However, these parameters play an important role on the nonlinear response of the beam. In fact when the height (h) of the beam is small and the soil is less stiff ($k_w = 500 \text{ kN/m}^3, k_s = 0$) the beam undergoes large deflections.

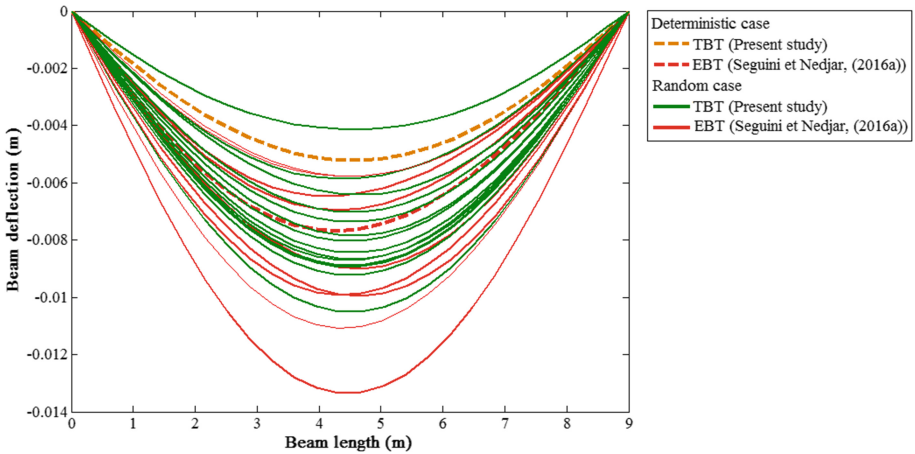


Fig. 3. Deflection of the Euler Bernoulli and Timoshenko beam under a distributed load using deterministic and probabilistic analysis.

4.3 Probabilistic Analysis for Nonlinear Beam Behavior

The effect of inherent random soil heterogeneity on the nonlinear behavior of the beam was assessed quantitatively. However, in this section a probabilistic approach based on the theory of local average of Vanmarcke [46] combined to Monte Carlo simulations was used, where the random field simulation is introduced into the nonlinear finite element modelling. Figure 3 shows the deflections obtained from the nonlinear deterministic and probabilistic analysis of the beam (Euler-Bernoulli and Timoshenko) resting on nonlinear Winkler foundation. For the deterministic analysis it is seen that when the geometric nonlinearity based on the Timoshenko theory, the maximum deflection is about 32% compared with the maximum deflection obtained by Seguini and Nedjar [54] while for the probabilistic analysis the percentage of difference of the maximum deflection obtained by Timoshenko theory (TBT) and Euler Bernoulli theory (EBT) [54] is about 21%. The Fig. 4 represents the cumulative functions of the maximum deflections of Euler-Bernoulli and Timoshenko beam (EBT, TBT) obtained from 1000 realizations of the coefficient of Winkler subgrade reaction k_w for $L_c = 6 \text{ m}$ and for different values of the coefficient of variation ($C_v = 50\%, 70\%$ and 100%).

In fact, according to Fig. 4 it can be observed that there is an increase in the maximum deflection of the Timoshenko beam with the increase of the coefficient of variation. It can also be observed that the shear coefficient has a great effect on the

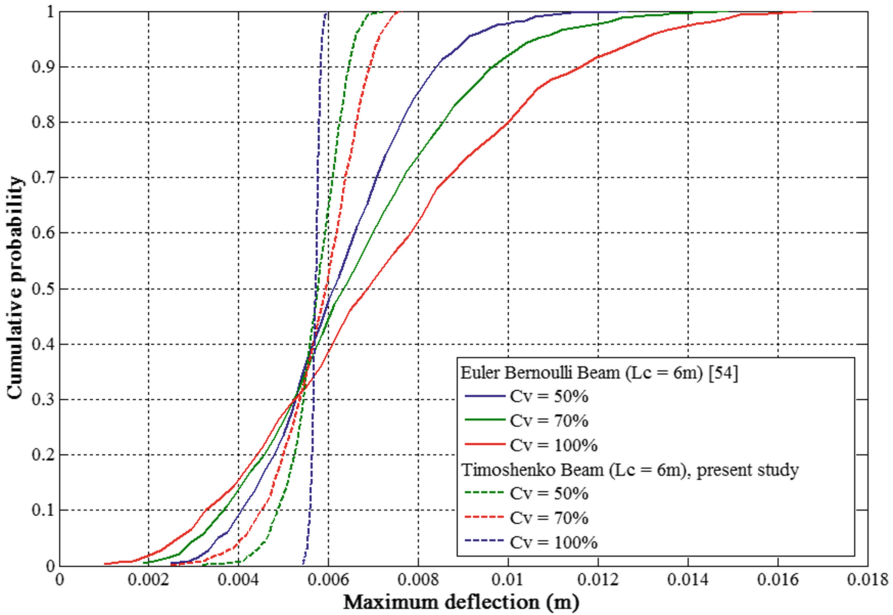


Fig. 4. Cumulative distribution functions for 1000 random realizations of maximum deflection of Euler-Bernoulli and Timoshenko beam with Cv variable and Lc = 6 m.

beam response and can be clearly seen in Table 3 by comparing the maximum deflection of the Euler and Timoshenko beams obtained from a probabilistic analysis with cumulative probability of 80%. In fact, from the results of the Table 3 it can be deduced that the percentage of difference of the maximum deflection of Euler-Bernoulli and Timoshenko beam (EBT, TBT) for Cv = 50%, 70% and 100% is respectively 25%, 29% and 34%.

Table 3. Maximum Euler-Bernoulli and Timoshenko beam deflections obtained by probabilistic analysis with a probability of 80% for different Cv (%) values.

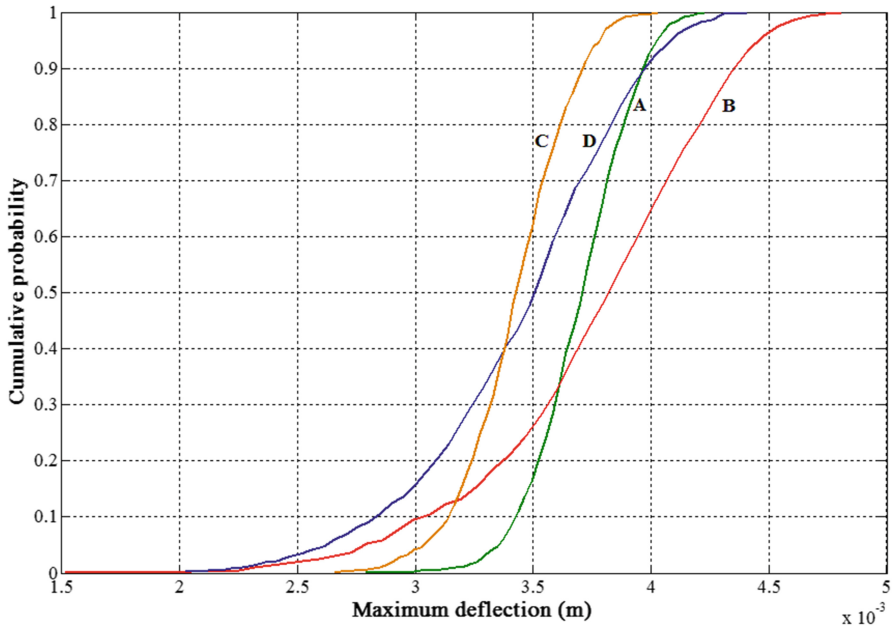
Maximum deflection (m) (Probabilistic analysis with Lc = 6 m)	Cv = 50%	Cv = 70%	Cv = 100%
Present study (TBT)	5.782×10^{-3}	6.227×10^{-3}	6.708×10^{-3}
Seguini and Nedjar (EBT) [54]	7.681×10^{-3}	8.796×10^{-3}	1.01×10^{-2}

4.4 Influence of the Coefficient of Variation and Foundation Type on the Beam Response

To show the evolution of the variation of the maximum deflection and the effect of foundation type and the shear deformation on the beam response, different values of k_w , k_s , L_c and L_{cs} (Table 4) have been chosen. From Fig. 5 it is can be deduced that the correlation length of Winkler coefficient seems to have more importance than the

Table 4. Values of k_w , k_s , L_c and L_{cs} .

	k_w (kN/m ³)	L_c (m)	k_s (kN/m)	L_{cs} (m)
Case A	6000	0.5	600	8
Case B	6000	8	600	0.5
Case C	6000	8	6000	0.5
Case D	6000	0.5	6000	8

**Fig. 5.** Cumulative distribution functions for the four different cases A-D presented in Table 4.

correlation length of the shear coefficient (case B compared to A) and it is also observed that it is not conservative when the shear effect is not taken into account (case B compared to C). In fact, the maximum deflection of the beam resting on Pasternak foundation obtained for a probability of 80% is less than the maximum deflection of the beam resting on Winkler foundation by about 10%. From Fig. 5 it can also be seen that the maximum deflection increases with the decrease of the coefficient of subgrade reaction. In fact, when the soil is less stiff, the beam undergoes large deflection (C compared to D).

5 Conclusion

Nonlinear behavior of a simply supported beam, undergoing moderate large deflections, subjected to a distributed load and resting on two parameter random soil has been investigated by using Timoshenko beam theory with the effect of the geometric nonlinearity. A stochastic finite element method has been used for the nonlinear analysis of beam-soil interaction. The nonlinear system of equations of motion is derived by using Von Kàrmàn hypothesis and resolved by using the Newthom-Raphson iterative method. The proposed model takes into account the coupling effects of shear deformations, geometric nonlinearity of the beam and the nonlinearity of random Winkler-Pasternak foundation where the validity of the proposed model was confirmed by comparison with the existing published models [33, 54]. Therefore the main conclusions that can be drawn from this study are:

- (i) Comparing the results obtained from the two theories (EBT and TBT), it can be noted that the deflection of the beam is significantly affected by the shear deformation where the used theory (TBT) is well suited for determine the real response of the beam.
- (ii) Modelling the Timoshenko beam on Winkler-Pasternak random foundation is more appropriate than modelling it as a Winkler foundation beam.
- (iii) The accuracy of the obtained results for the case of a deterministic analysis compared with those obtained from a probabilistic analysis is remarkable. In fact, the results indicate that the shear effect and the probabilistic analysis have an important role on the deflections of the beam.
- (iv) The coefficient of variation C_v and the correlation lengths have a significant effect on the nonlinear response of Timoshenko beam. Thus, the maximum deflection of a beam increased with an increase in the coefficient of variation and correlation lengths (L_c, L_{cs}). In fact, a random soil with higher values of coefficient of variation of different type foundations enable us to obtain a more realistic behavior of a beam. Therefore, the developed models yield very good predictions of the response of a deep beam resting on nonlinear soil where the Timoshenko beam theory must be used instead of Euler-Bernoulli beam theory and the shear layer effect hasn't to be neglected because of the effect of the shear stresses on the deformation.
- (v) Finally it is very important to consider the effect of the shear deformation, the spatial variability and the material nonlinearity of the soil when determining the nonlinear response of the structure (deep beam) to reduce risks, to optimize results and to provide a more realistic behavior of the beam.

References

1. Timoshenko, S.: Strength of Materials, Part II, Advanced Theory and Problems, 3rd edn. Van Nostrand, Princeton (1940)
2. Hetenyi, M.: Beams on elastic foundations. University of Michigan Press, Ann Arbor (1961)

3. Winkler, E.: Die Lehre von der Elasticitaet und Festigkeit [The theory of elasticity and strength]. Dominicus, Prag (1867)
4. Biot, A.M.: Bending of an infinite beam on an elastic foundation. *J. Appl. Mech. ASME* **4**, A1–A7 (1937)
5. Filonenko-Borodich, M.M.: A very simple model of an elastic foundation capable of spreading the load. *Sb Inst Inzh Transzheldorizdat*, vol. 53 (1945). (in Russian)
6. Pasternak, P.L.: On a new method of analysis of an elastic foundation by means of two foundation constants. *Gosudarstvennoe Izdatelstvo Literaturi po Stroitelstvu Arkhitekture*, Moscow, USSR (1954). (in Russian)
7. Kerr, A.D.: Elastic and viscoelastic foundation models. *J. Appl. Mech. Trans. ASME* **31**, 491–498 (1964)
8. Kerr, A.D.: A study of a new foundation model. *Acta Mech.* **1**, 135–147 (1965)
9. Vesic, A.B.: Bending of beams resting on isotropic elastic solid. *J. Eng. Mech. Div. ASCE* **87**, 35–53 (1961)
10. Vesic, A.B.: Beams on elastic subgrade and Winkler hypothesis. In: *Proceedings of the 5th International Conference on Soil Mechanics and Foundation Engineering*, Paris, vol. 1, pp 845–850 (1963)
11. Vlassov, V.L., Leontiev, N.H.: *Beams plates and shells on elastic foundations*. Fizmatgiz, Moscow (1966)
12. Vallabhan, C.V.G., Das, Y.C.: A parametric study of beams on elastic foundations. *J. Eng. Mech. ASCE* **114**(12), 2072–2082 (1987)
13. Vallabhan, C.V.G., Das, Y.C.: An improved model for beams on elastic foundations. In: *Proceedings of the ASME Pressure Vessel and Piping Conference*, Pittsburg (1988)
14. Vallabhan, C.V.G., Das, Y.C.: Modified Vlassov model for beams on elastic foundations. *J. Geotech. Eng. Mech. ASCE* **117**, 956–966 (1991)
15. Ma, X., Butterworth, J.W., Clifton, G.C.: Static analysis of an infinite beam resting on a tensionless Pasternak foundation. *Eur. J. Mech. A/Solids* **28**, 397–624 (2009)
16. Mo, Y., Ou, L., Zhong, H.: Vibration analysis of timoshenko beams on a nonlinear elastic foundation. *Tsinghua Sci. Technol.* **14**, 322–326 (2009)
17. Eisenberger, M., Yankelevsky, D.Z.: Exact stiffness matrix for beams on elastic foundation. *Comput. Struct.* **21**, 1355–1359 (1985)
18. Ting, B.Y., Mockry, E.F.: Beam on elastic foundation finite element. *J. Struct. Eng. ASCE* **110**(10), 2324–2339 (1984)
19. Aydogan, M.: Stifness-matrix formulation of beams with shear effect on elastic foundation. *J. Struct. Eng. ASCE* **121**(9), 1265–1270 (1995)
20. Zhaohua, F., Cook, D.R.: Beam elements on two-parameter elastic foundation. *J. Eng. Mech.* **109**(6), 1390–1402 (1983)
21. Nogami, T., O'Neil, M.W.: Beam on generalized two-parameter foundation. *J. Eng. Mech. ASCE* **111**(5), 664–679 (1985)
22. Eisenberger, M., Bielak, J.: Finite beams on infinite two-parameter elastic foundation. *Comput. Struct.* **42**, 661–664 (1992)
23. Eisenberger, M., Clastornik, J.: Beams on variable two-parameter elastic foundation. *J. Eng. Mech.* **113**, 1454–1466 (1987)
24. Wang, T.M., Stephens, J.E.: Natural frequencies of Timoshenko beams on Pasternak foundations. *J. Sound Vib.* **51**, 149–155 (1977)
25. Wang, T.M., Gagnon, L.W.: Vibrations of continuous Timoshenko beams on Winkler-Pasternak foundations. *J. Sound Vib.* **59**, 211–220 (1978)
26. Wang, C.M., Lam, K.Y., He, X.O.: Exact solution for Timoshenko beams on elastic foundation using Green's functions. *Mech. Struct. Mach.* **29**, 101–113 (1998)

27. Hosseini Kordkheili, S.A., Bahai, H.: Non-linear finite element analysis of flexible risers in presence of buoyancy force and seabed interaction boundary condition. *Arch. Appl. Mech.* **78**, 765–774 (2008)
28. Tsiatas, G.C.: Nonlinear analysis of non-uniform beams on nonlinear elastic Foundation. *Acta Mech.* **209**, 141–152 (2010)
29. Neto, A.G., Martins, C.A., Pimenta, P.M.: Static analysis of offshore risers with a geometrically-exact 3D beam model subjected to unilateral contact. *Comput. Mech.* **53**, 125–145 (2013)
30. Al-Azzawi, A.A., Theeban, D.M.: Large deflection of deep beams on elastic foundations. *J. Serb. Soc. Comput. Mech.* **4**, 88–101 (2010)
31. Al-Azzawi, A.A., Mahdy, H., Farhan, O.Sh.: Finite element analysis of deep beams on nonlinear elastic foundations. *J. Serb. Soc. Comput. Mech.* **4**, 13–42 (2010)
32. Al-Talaqany, D.M.: Large Deflection Deep Beams on Elastic Foundations. M.Sc. thesis, Faculty of Engineering, Nahrain University of Baghdad, Iraq (2007)
33. Hosseini Kordkheili, S.A., Bahai, H., Mirtaheeri, M.: An updated Lagrangian finite element formulation for large displacement dynamic analysis of three-dimensional flexible riser structures. *Ocean Eng.* **38**, 793–803 (2011)
34. Beaufait, J.P., Hoadley, W.: Analysis of elastic beams on nonlinear foundations. *Comput. Struct.* **12**, 669–676 (1980)
35. Cocchetti, G., di Prisco, C., Galli, A., Nova, R.: Soil–pipeline interaction along unstable slopes: a coupled three-dimensional approach. Part 1: theoretical formulation. *Can. Geotech. J.* **46**, 1289–1304 (2009)
36. Chen, H., Xu, S., Guo, H.: Nonlinear analysis of flexible and steel catenary risers with internal flow and seabed interaction effects. *J. Mar. Sci. Appl.* **10**, 156–162 (2011)
37. Yuan, F., Wang, L., Guo, Z., Xie, Y.: Analytical analysis of pipeline–soil interaction during J-lay on a plastic seabed with bearing resistance proportional to depth. *Appl. Ocean Res.* **36**, 60–68 (2012)
38. Phoon, K.K., Kulhawy, F.H.: Characterization of geotechnical variability. *Can. Geotech. J.* **36**, 612–624 (1999)
39. Phoon, K.K.: Reliability-based design of foundations for transmission line structures. Ph.D. thesis. Ithaca, Cornell University, New York (1995)
40. Jaksa, M.B.: The influence of spatial variability on the geotechnical design properties of a stiff, overconsolidated clay. Ph.D. thesis. University of Adelaide (1995)
41. Vanmarcke, E.H.: Probabilistic modeling of soil profiles. *J. Geotech. Eng. Div. ASCE* **103** (GT11), 1227–1246 (1977)
42. Grigoriu, M., Khater, M., O'Rourke, T.: Stochastic beams on elastic foundation. In: Proceedings of the Symposium, ASCE Convention in Denver, Colorado, pp. 96–106 (1985)
43. Griffiths, D.V., Paiboon, J., Huang, J., Fenton, G.A.: Numerical analysis of beams on random elastic foundations. In: Proceedings of the 9th International Congress on Numerical Methods in Engineering and Scientific Applications, Cimenics, pp. 19–25 (2008)
44. Elachachi, S.M., Breyse, D., Houy, L.: Longitudinal variability of soils and structural response of sewer networks. *Comput. Geotech.* **31**, 625–641 (2004)
45. Elachachi, S.M., Breyse, D., Benzeguir, H.: Soil spatial variability and structural reliability of buried networks subjected to earthquakes. *Comput. Methods Appl. Sci.* **22**, 111–127 (2011)
46. Vanmarcke, E.: *Random Fields: Analysis and Synthesis*. MIT Press, Cambridge (1983)
47. Nedjar, D., Bensafi, M., Elachachi, S.M., Hamane, M., Breyse, D.: Buried pipe response under seismic solicitation with soil–pipe interaction. In: Mestat (ed.) NUMGE Conference, pp. 1047–1053. ENPC/LCPC, Paris (2002)

48. Nedjar, D., Hamane, M., Bensafi, M., Elachachi, S.M., Breysse, D.: Seismic response analysis of pipes by a probabilistic approach. *Soil Dyn. Earthq. Eng.* **27**, 111–115 (2007)
49. Kholmyansky, M.L.: Dynamic soil-structure interaction considering random soil properties. In: 12th International Association for Computer Methods and Advances in Geomechanics (IACMAG), Goa, India, pp. 1–6, October 2008
50. Elachachi, S.M., Breysse, D., Denis, A.: Effect of soil spatial variability on reliability of rigid buried pipes. *Comput. Geotech.* **43**, 61–71 (2012)
51. Denis, A., Elachachi, S.M., Niandou, H.: Effects of longitudinal variability of soil on a continuous spread footing. *Eng. Geol.* **122**(3–4), 179–190 (2011)
52. Imanzadeh, S., Denis, A., Marache, A.: Simplified uncertainties analysis of continuous buried steel pipes on an elastic foundation in the presence of low stiffness zones. *Comput. Geotech.* **48**, 62–71 (2013)
53. Kazi Tani, N., Nedjar, D., Hamane, M.: Non-linear analysis of the behaviour of buried structures in random media. *Eur. J. Environ. Civil Eng.* **17**(9), 791–801 (2013)
54. Seguini, M., Nedjar, D.: Nonlinear finite element modeling of deep beam resting on linear and nonlinear random soil. *Int. J. Environ. Chem. Ecol. Geol. Geophys. Eng.* **10**(2), 134–141 (2016)
55. Seguini, M., Nedjar, D.: Modelling of soil-structure interaction behaviour: geometric nonlinearity of buried structures combined to spatial variability of soil. *Eur. J. Environ. Civil Eng.* **21**, 1217–1236 (2016). <https://doi.org/10.1080/19648189.2016.1153525>
56. Reddy, J.N.: *An Introduction to Nonlinear Finite Element Analysis*. Oxford University Press, Oxford (2004)
57. Bathe, K.J.: *Finite Element Procedures in Engineering Analysis*. Prentice-Hall, Englewood Cliffs (1982)
58. Crisfield, M.A.: *Non-Linear Finite Element Analysis of Solid and Structures*. Wiley, Chichester (1991)
59. Felippa, C.A.: *Lecture notes in nonlinear Finite element methods*. Center for Aerospace Structures, University of Colorado, Boulder, CO (1996)
60. Cowper, G.R.: The shear coefficient in Timoshenko's beam theory. *J. Appl. Mech.* **33**, 335–340 (1966)
61. Fenton, G.A., Vanmarcke, E.H.: Simulation of random fields via local average subdivision. *J. Eng. Mech.* **116**, 733–1749 (1990)



Thermal-Mechanical Coupled Behavior of Sliding Bearings for Seismic Isolation

Masaru Kikuchi^(✉) and Ken Ishii

Hokkaido University, Sapporo, Japan
mkiku@eng.hokudai.ac.jp

Abstract. In this paper, the authors focus on the thermal-mechanical coupled behavior of sliding bearings for seismic isolation. Sliding bearings are seismic isolation components which allow designers to develop longer-period isolation systems for structures. In Japan, long-period, long-duration ground motions have been of great concern since the 2011 Tohoku earthquake, when ground motions lasting more than five minutes were observed across a wide area. Such motions might induce numerous cyclic deformations in seismic isolation bearings. High-friction sliding bearings absorb seismic input energy and convert it to heat energy. Therefore, a large number of cyclic deformations might cause the performance of the sliding bearings to deteriorate due to an increase in the contact surface temperature of the sliding material and steel plates. The authors developed a numerical analysis model to account this thermal-mechanical coupled behavior of sliding bearings. The model combines thermal conductivity and seismic response analyses. The thermal and mechanical analytical procedures were both performed interactively by updating their parameters incrementally at each time step. Simulation of horizontal, two-dimensional cyclic loading tests of a scaled sliding bearing confirmed the validity of the model. Seismic response analyses using the model were conducted to evaluate the behavior of a seismically isolated building equipped with sliding bearings. The authors concluded that the thermal-mechanical coupled behavior should be considered in order to accurately predict the response of an isolated building with sliding bearings under long-duration ground motions.

Keywords: Seismic isolation · Sliding bearing · Cyclic deformation
Thermal conductivity analysis · Seismic response analysis

1 Introduction

Seismic isolation is the most effective technology for protecting building structures from being damaged by earthquakes. This protection is achieved by introducing flexible bearing supports at the foundation level that move the period of the structure away from the predominant period of the ground motions. Therefore, seismically isolated buildings can be understood as long-period structures [1]. A sliding bearing is a major type of seismic isolation device for building structures and is typically used with elastomeric isolation bearings. The mechanical characteristics of this device easily give a low fundamental frequency even to lightweight structures. It is also easily applicable underneath the foundation of columns supporting a low vertical load.

Moreover, even hysteretic damping is available due to sliding behavior with friction [2]. Because of these advantages, seismically isolated buildings with sliding bearings are increasingly being built [3].

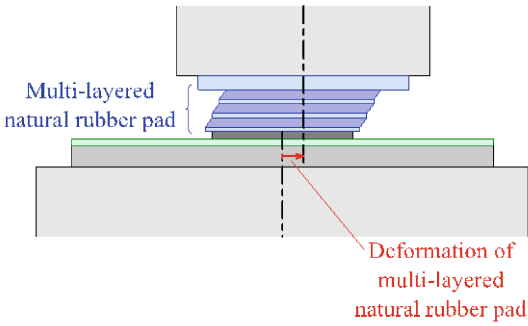
Long-period and long-duration ground motions have been a great concern since the 2011 Tohoku earthquake in Japan, when ground motions lasting more than five minutes were observed across a wide area. Previous research has predicted that a very large subduction earthquake in the Nankai and Tokai regions of Japan will produce similar long-duration strong ground shaking [4]. Such ground motions might induce numerous cyclic deformations in seismic isolation devices. Sliding bearings absorb seismic input energy and convert it to heat energy. A large number of cyclic deformations might cause the performance of the sliding bearings to deteriorate due to an increase in the contact surface temperature [5]. This phenomenon has been understood as thermal-mechanical coupled behavior. Since 2017, the Japanese Ministry of Land, Infrastructure, Transport and Tourism (MLIT) has obliged structural engineers to consider the impact due to long-period, long-duration ground motions to isolation devices for the design of seismically isolated buildings [4].

In this research, the authors focus on the thermal-mechanical coupled behavior of sliding bearings. First, cyclic loading tests of a scaled sliding bearing were conducted to understand the thermal-mechanical coupled behavior. Next, a numerical analysis model that considers the thermal-mechanical coupled behavior was constructed. Simulation analyses of the tests were conducted using the proposed model. The model was verified by comparing the analytical and experimental results. Finally, seismic response analyses of isolated buildings with sliding bearings were conducted to examine the influence of the cyclic deformations to the response of the building structures.

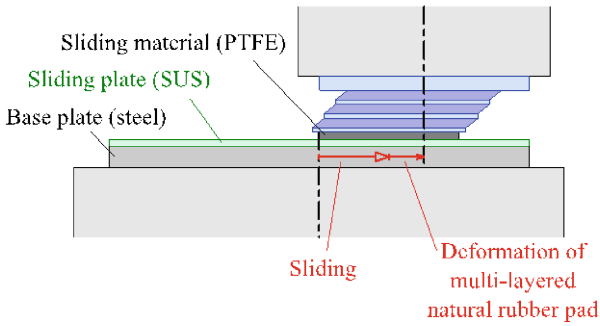
2 Bearing Tests

2.1 Concept of Sliding Bearing

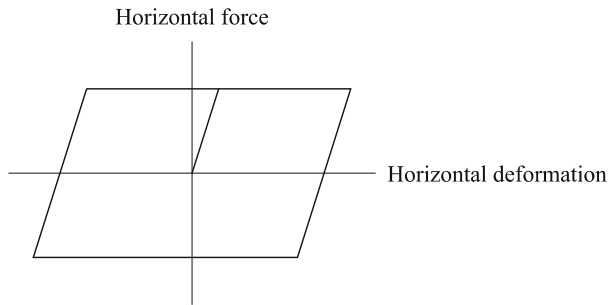
Figure 1 shows a sliding bearing with rubber pad. It consists of a multilayered natural rubber pad, sliding material, sliding plate, and base plate [6]. The sliding material is PTFE (Polytetrafluoroethylene). The material of the sliding plate and base plate is SUS and steel, respectively. There are two stages of deformation depending on the level of ground motions. Only the multi-layered natural rubber pad deforms when the shear force in the bearing is within the friction limit force in the case of a low-level earthquake (Fig. 1(a)). When the shear force reaches the friction limit force in the case of a high-level earthquake, the bearing starts sliding on the base plate (Fig. 1(b)). The shape of a typical hysteresis loop of deformation and force of the device shown in Fig. 1(c) is bilinear. The elastic stiffness is determined from the dimensions (thickness and cross section area) of the rubber pad, and the second stiffness is theoretically zero.



(a) Low-level earthquake



(b) High-level earthquake



(c) Typical hysteresis loop

Fig. 1. Concept of sliding bearing with rubber pad

2.2 Specimen

A scaled sliding bearing was used in the tests. It was manufactured by Oiles Corporation, Japan. The design of the bearing tested is shown in Fig. 2. The diameter of the rubber pad and sliding material was 120 mm and 100 mm, respectively. The multi-layered rubber pad consisted of six layers of 1.0-mm thick natural rubber sheets and 1.6-mm thick steel shims. The shear modulus of natural rubber was 0.784 MPa.

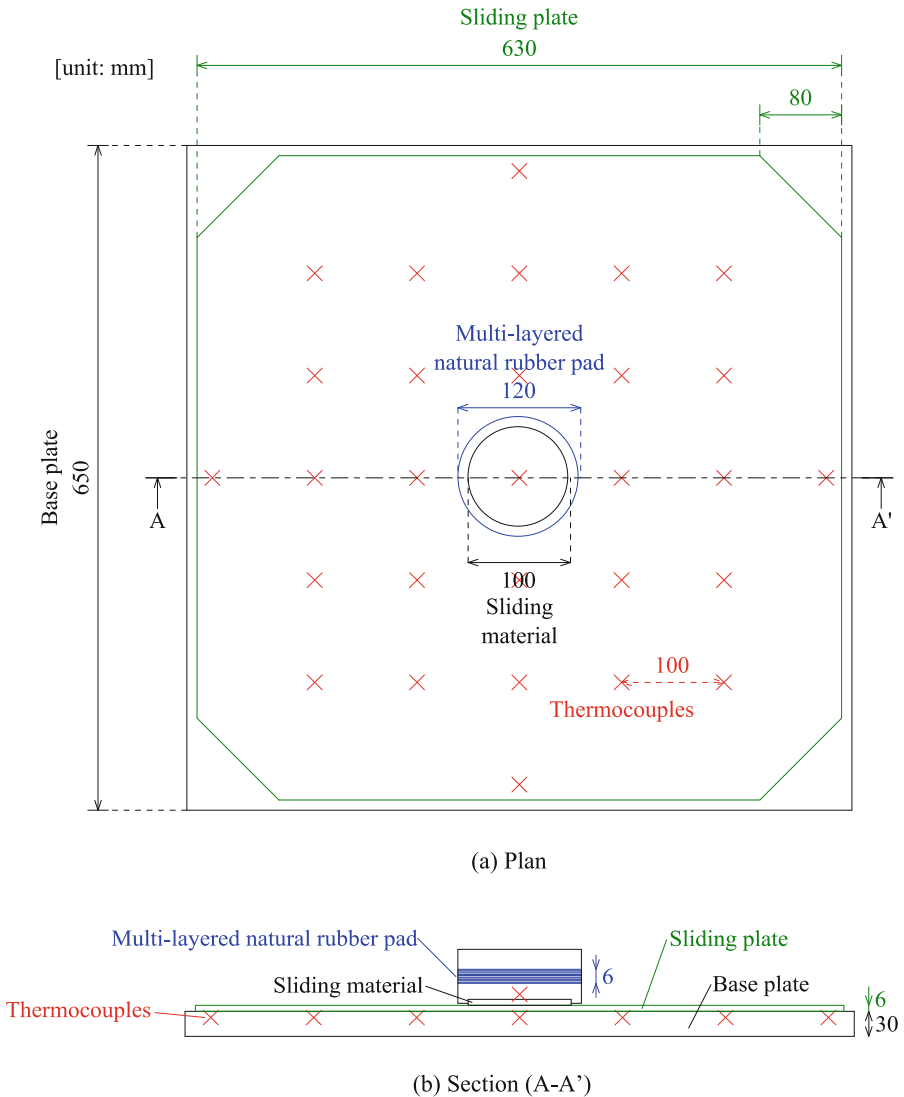


Fig. 2. Design of a sliding bearing used for the test

2.3 Test Program

Tests of the sliding bearing were conducted to investigate its mechanical characteristics under different horizontal displacement patterns and different levels of axial load. Three types of displacement patterns shown in Fig. 3 were examined. The test parameters are summarized in Table 1. The peak displacement in the longitudinal direction of each displacement pattern commonly increased to 50 mm, 100 mm, 150 mm, and 200 mm. Two levels of axial load, 136 kN and 203 kN, were applied, which corresponded to the design pressure of 17.3 MPa and 1.5 times that value, respectively. The loading frequency was 0.2 Hz, and the number of cycles was 10 for every test case. A total of 24 test cases were performed. The temperature was observed with thermocouples attached on the back side of the sliding plate. An interval time was introduced so that the temperature of the sliding plate dropped to 20 °C or lower.

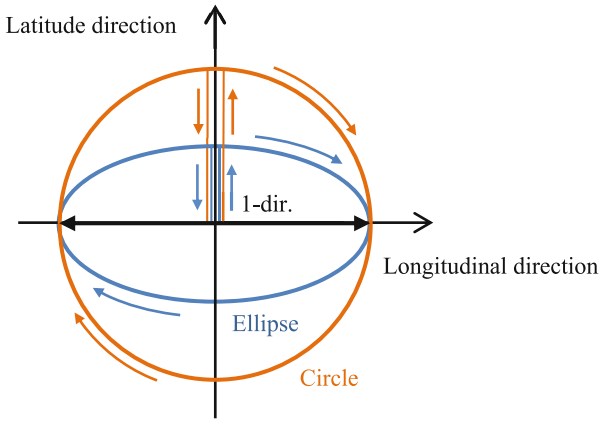


Fig. 3. Displacement patterns

Table 1. Test Parameters.

Displacement pattern	1-direction Ellipse (long.:lat. = 2:1) Circle
Peak longitudinal displacement [mm]	50, 100, 150, 200
Axial load [kN]	136, 203
Loading frequency [Hz]	0.2
Number of cycles	10

2.4 Test Results

The hysteresis loops in the longitudinal direction for three types of displacement patterns obtained in the tests of 200 mm peak displacement and 136 kN vertical load are shown in Fig. 4. The shape of the hysteresis loops varies depending on the

displacement pattern. Degradation of shear force during cyclic loading was commonly observed in every test. However, the peak shear forces are almost the same in every test. The performance recovered at the beginning of every test, although it deteriorated during cyclic loading. The time histories of the temperature of the sliding plate are shown in Fig. 5. In the 1-direction test (left graph in Fig. 5), the temperature rose to around 50 °C at the end of test and then dropped. These results imply that the performance degradation was caused by temperature rise, not by fatigue. Therefore, the thermal-mechanical coupled behavior should be considered for evaluating the performance of the sliding bearings.

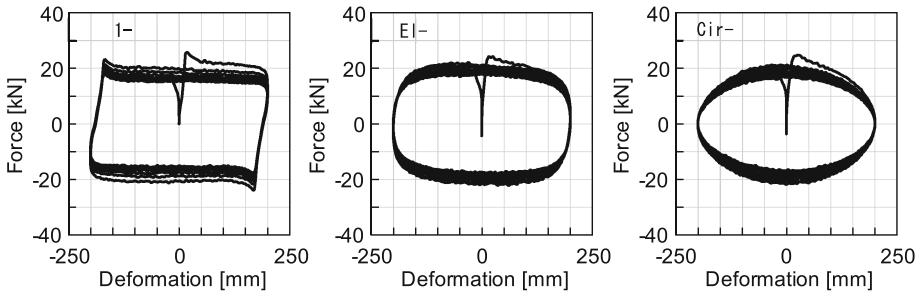


Fig. 4. Force-deformation relationship (longitudinal direction)

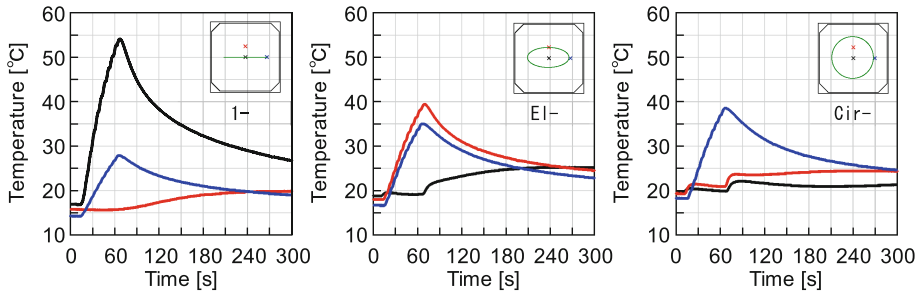


Fig. 5. Temperature measured in sliding plate

Figure 6(a) shows the relationship between the temperature measured on the back side of the sliding plate and the friction coefficient. The tendency that the friction coefficient decreases with temperature rise can be clearly seen. The manufacturer has specified Eq. (1) as an evaluation formula of the friction coefficient of this device [7]. This formula is expressed only in terms of the velocity and the vertical pressure in the bearing. Note that it does not involve the influence of temperature.

$$\mu_0 = (0.305 - 0.103e^{-0.019v}) \cdot \sigma^{-0.29} \quad (1)$$

where v is relative velocity between the sliding material and plate, and σ is vertical pressure in the sliding material.

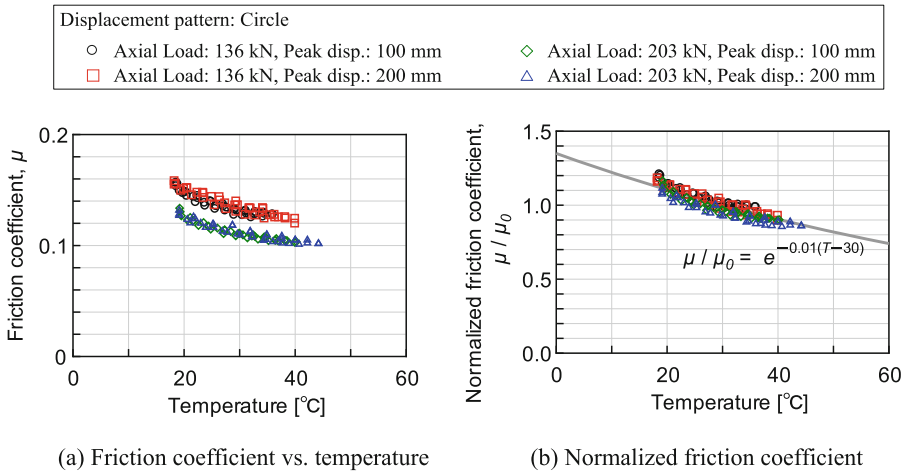


Fig. 6. Friction coefficient obtained from tests

Figure 6(b) shows the relationship between the temperature and the friction coefficient normalized by μ_0 . The identified line is also plotted in Fig. 6(b). This line gives the influence of the temperature on the friction coefficient. The authors will use Eq. (2) for the simulation analysis so that the influence of temperature can be taken into account. This equation was refined by modifying the identified line in Fig. 6(b) on the basis of the assumption that the temperature difference between the surface of the sliding plate and the temperature measurement point (back side of the plate) was 20 °C.

$$\mu = \mu_0 \cdot e^{-0.01(T-50)} \quad (2)$$

where T is the temperature of the sliding plate in contact with the center of the sliding material.

3 Numerical Analysis

3.1 Analysis Flow

The numerical analysis model consists of a thermal conductivity analysis and seismic response analysis. The model was implemented in the program OpenSees [8]. Both analyses are performed interactively by updating their parameters incrementally at each time step. Figure 7 shows a flowchart of the thermal-mechanical coupled analysis. This model was constructed by refining the existing model that the authors had previously developed for elastomeric seismic isolation bearings [9].

First, the mechanical properties of the sliding bearings are updated at a certain time step by use of Eq. (2) in which the temperature of the sliding plate was obtained at the previous analysis step. Then, seismic response analysis is conducted using the updated parameters. The hysteresis model shown in Fig. 1(c) is applied for the sliding bearing

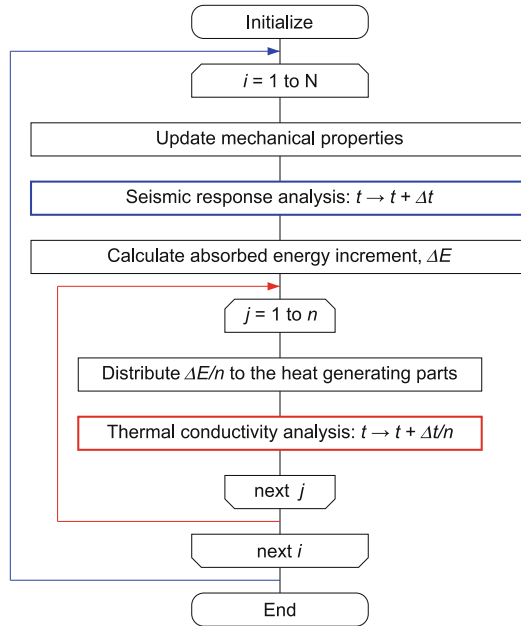


Fig. 7. Flowchart of thermal-mechanical coupled analysis

in the seismic response analysis. Accordingly, an energy increment absorbed by the sliding bearing, ΔE , is calculated at the end of the time increment. Next, ΔE is distributed to the surface of the sliding plate where the sliding material contacts, then thermal conductivity analysis is conducted. Note that the contact area of the sliding material to the surface of the sliding plate is updated in accordance with the movement and deformation of the rubber pad at each analysis step. Eventually, the temperature of the sliding plate for the next analysis step is obtained. These procedures are repeated by the end of the analysis steps.

A finite volume method was used for the thermal conductivity analysis. Figure 8 shows the three-dimensional analysis model for the sliding bearing used in the test. The cell thickness of the sliding plate (SUS) and the base plate (steel) was 2 mm and 5 mm, respectively. Each cell of the both plates measured 20 mm by 20 mm in the horizontal direction. The material constants used for the analysis are summarized in Table 2. The Newmark beta method was used for the seismic response analysis [10]. It has been widely used in numerical evaluation of the nonlinear dynamic response of structures as a method of numerical time integration. The constant average acceleration method ($\beta = 1/4$) was used as an option of the Newmark beta method in this paper.

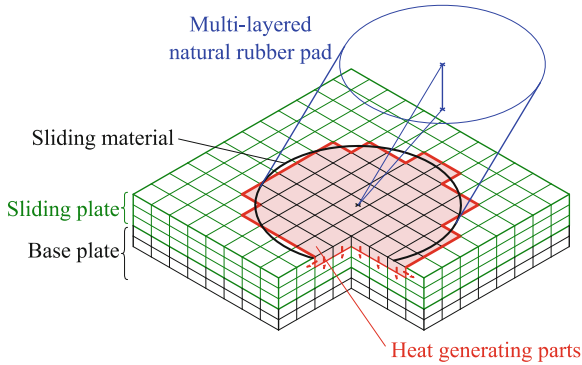


Fig. 8. Thermal conductivity analysis model for sliding bearing

Table 2. Material constants for thermal conductivity analysis.

Material	Thermal conductivity [W/(m·K)]	Density [g/cm ³]	Specific heat capacity [J/(g·K)]
SUS	16.0	7.93	0.500
Steel	59.0	7.86	0.473

3.2 Simulation Analysis

Simulation analysis was conducted for the cyclic loading tests described in the previous chapter. Time step intervals were 0.01 s and 0.002 s for the seismic response and the thermal conductivity analysis, respectively. Thus, five steps of the thermal conductivity analysis were carried out in one step of the seismic response analysis. The loading sequence was exactly the same as for the tests.

The analysis results are shown in Figs. 9 and 10. Comparing with Fig. 4 and Fig. 9, it is clearly seen that the analysis model can accurately predict the deterioration of the hysteresis loops due to cyclic loading in every displacement pattern. Comparing with Fig. 5 and Fig. 10, the temperature changes were also accurately predicted at every location in the sliding plate. These results verified that the analysis model captured the thermal-mechanical coupled behavior of the sliding bearing well.

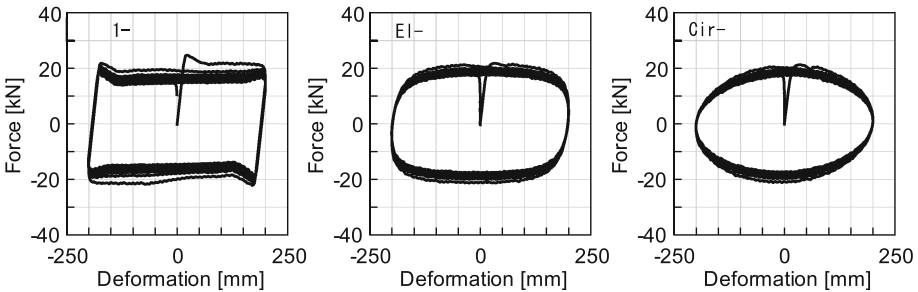


Fig. 9. Force-deformation relationship obtained from analysis (longitudinal direction)

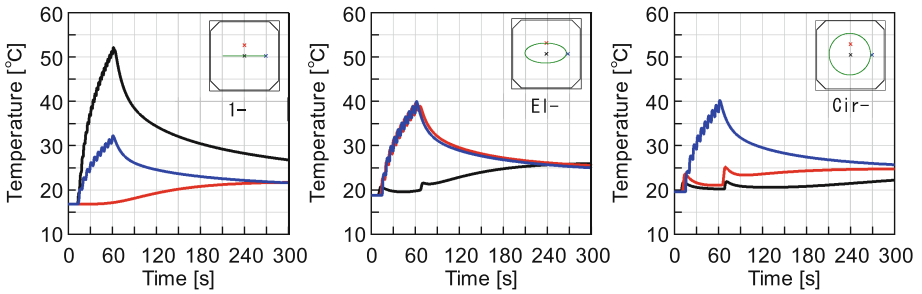


Fig. 10. Temperature of sliding plate obtained from analysis

4 Seismic Response Analysis

4.1 Structure Model

A 15-story reinforced concrete building model was used for the seismic response analysis. The model was as shown in Fig. 11. It was characterized as a typical seismically isolated condominium currently designed in Japan [3]. The structure consisted of six bays by one bay in the plan, with each bay measuring 6.5 m by 12.0 m. One isolation bearing was placed underneath each column for a total of 14 seismic isolation bearings. Those isolation bearings consisted of eight natural rubber bearings of 1,100 mm diameter and six sliding bearings of 1,100 mm diameter.

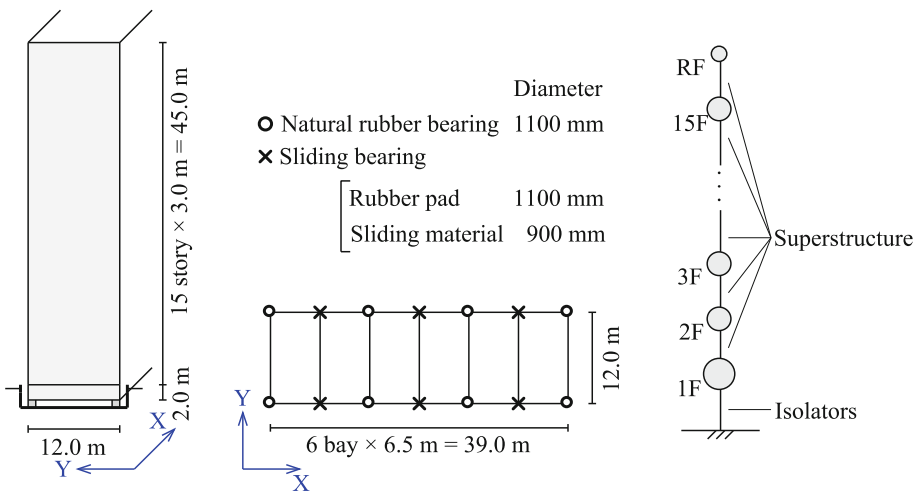


Fig. 11. Structure model

The structure was modeled as a 16-node MDOF system. The analysis dealt with only the X-direction of the building. The total mass of the superstructure was 11,443 tons. The superstructure was assumed to be elastic. The fundamental period was 1.23 s

when the base of the superstructure was fixed. Stiffness proportional damping was applied only to the superstructure. A damping ratio of 3% was defined for the fundamental period of the fixed-base structure.

4.2 Ground Motions

Two types of ground motions shown in Fig. 12 were used in the seismic response analysis. One is the El Centro N-S component observed during the Imperial Valley earthquake of May 18, 1940 in California, USA. This record has been widely used in the seismic design of buildings for a long time. The duration time is 40 s. The other was one of the ground motions provided by MLIT in Japan [4]. It had been developed for the purpose of reviewing the design of long-period structures such as tall buildings or seismically isolated buildings against huge subduction earthquakes. The location of this developed ground motion, OS1, is Osaka city. The duration time is much longer than that of the El Centro N-S component.

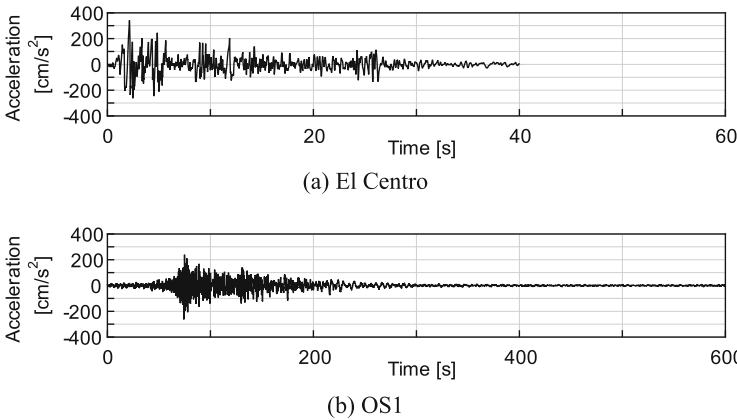


Fig. 12. Ground motions

4.3 Analysis Results

Four cases of seismic response analysis were conducted to evaluate the influence of the thermal-mechanical coupled behavior in the sliding bearings on seismic response values in the building structure. Analysis cases are summarized in Table 3.

Table 3. Analysis case.

Case	Ground motion	Thermal-mechanical coupled behavior in sliding bearings
1	El Centro	Not considered
2	El Centro	Considered
3	OS1	Not considered
4	OS1	Considered

Figures 13 and 14 show the seismic response analysis results that compare the peak response accelerations and displacements in the structure and hysteresis loops in isolation level. The response values obtained in Cases 1 and 2 for the El Centro input are similar (Fig. 13). The temperature in the sliding bearings increased only by 30°C in Case 2. The influence of thermal-mechanical coupled behavior in the sliding bearings does not appear so much under such a short-duration earthquake ground motion.

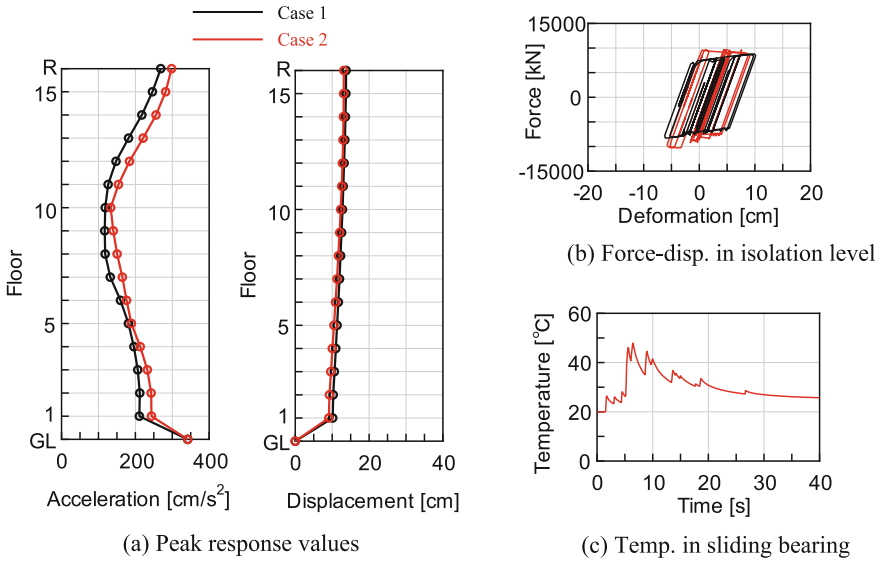


Fig. 13. Seismic response analysis result for El Centro input

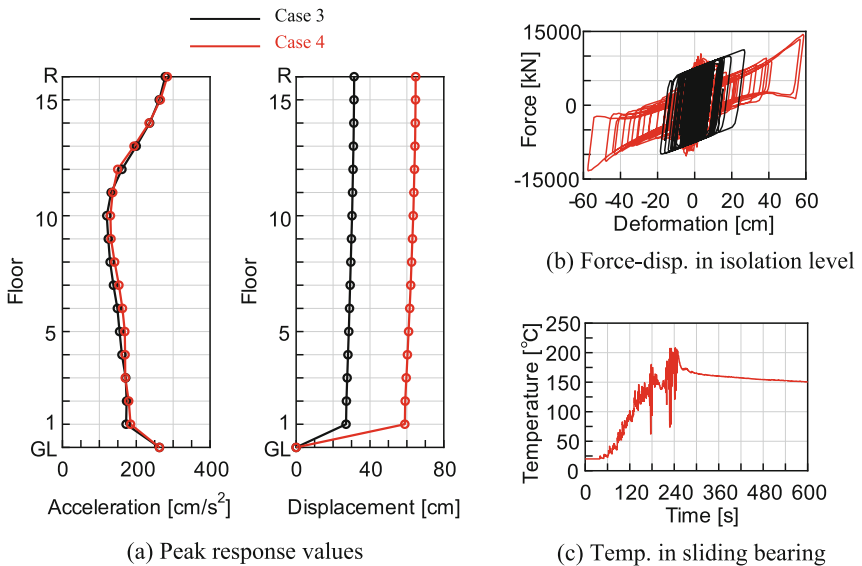


Fig. 14. Seismic response analysis result for OS1 input

However, the response values obtained in Cases 3 and 4 for the OS1 input are quite different (Fig. 14). The peak response displacements in Case 4 are approximately twice as large as those in Case 3, although the peak response accelerations are almost similar. The deterioration of the performance of the sliding bearings appeared very strongly in Case 4. The temperature in the sliding bearings increased by 200 °C, and the friction coefficient decreased from 0.17 to 0.03. These results suggest that the thermal-mechanical coupled behavior of seismic isolation devices should be considered, especially for long-duration earthquake ground motions.

5 Conclusion

In this research, the authors focused on the thermal-mechanical coupled behavior of sliding bearings for seismic isolation under long-duration ground motions. Sliding bearings are a major type of seismic isolation device for building structures. They have been widely used because of the advantage in which they can easily provide a low natural frequency to the building structures. Sliding bearings absorb seismic input energy and convert it to heat energy. Therefore, a large number of cyclic deformations significantly increases the temperature of the friction contact surface in the device. The temperature rise results in the deterioration of damping performance.

Cyclic loading tests of a scaled sliding bearing were conducted. The tests were performed with a varying displacement pattern, vertical pressure, and displacement amplitude. Degradation of the force during cyclic loading was commonly observed in every test. The friction coefficient decreased in accordance with the rising of the temperature of the sliding plate during the tests.

In order to consider such behavior, an analysis model was constructed by combining thermal conductivity and seismic response analysis procedures. The model was implemented in the program OpenSees. The validity of the model was demonstrated with analyses of the cyclic loading tests of the sliding bearing. The model captured the mechanical behaviors of the sliding bearings under cyclic loading well.

Seismic response analyses of an isolated building with sliding bearings were conducted using OpenSees. The influence of thermal-mechanical coupled behavior in the sliding bearings on the response values appeared strongly for the long-duration earthquake ground motion. It was concluded that the thermal-mechanical coupled behavior should be considered for evaluating the performance of the sliding bearings. The proposed model could be a useful numerical analysis tool for accurate seismic response analysis of seismically isolated structures equipped with sliding bearings.

Acknowledgements. This research was supported by the Taisei Foundation, Japan. The sliding bearing tests were conducted using the facilities of the Ashikaga Factory, Oiles Corporation, Japan. Dr. Frank McKenna of the University of California, Berkeley, assisted in the implementation of the numerical analysis model in the OpenSees program. The authors would like to express their gratitude for all of the financial support and assistance.

References

1. Kelly, J.M.: Earthquake-Resistant Design with Rubber, 2nd edn. Springer, London (1997)
2. Higashino, M., Okamoto, S.: Response Control and Seismic Isolation of Buildings. Taylor & Francis, Oxon (2006)
3. Architectural Institute of Japan: Design Recommendations for Seismically Isolated Buildings (2016). ISBN 978-4-8189-5000-9
4. Ministry of Land, Infrastructure, Transport and Tourism, Japan. http://www.mlit.go.jp/report/press/house05_hh_000620.html. Accessed 5 Feb 2018. (in Japanese)
5. Hibino, H., et al.: Safety verification of seismic isolation system using sliding bearings against long period earthquake motions. In: 15th World Conference of Earthquake Engineering, Lisbon, Portugal, Paper ID: 1377 (2012)
6. Oiles Corporation, Japan. <http://www.oiles.co.jp/en/menshin/building/menshin/products/ssr/>. Accessed 5 Feb 2018
7. Oiles Corporation, Japan, Technical report (2009). (in Japanese)
8. McKenna, F., Fenves, G., Scott, M.: Computer Program OpenSees, Open System for Earthquake Engineering Simulation, Pacific Earthquake Engineering Center, University of California, Berkeley, CA, USA. <http://opensees.berkeley.edu/>. Accessed 5 Feb 2018
9. Kikuchi, M., Ishii, K.: Thermal-mechanical coupled behavior of elastomeric isolation bearings under cyclic loadings. In: 15th European Conference on Earthquake Engineering. Thessaloniki, Greece (2018, in print)
10. Newmark, N.M.: A method of computation for structural dynamics. J. Eng. Mech. ASCE **85** (EM3), 67–94 (1954)



Behaviour of Adjacent Ground and Existing Tunnel According to Locations of Pile Loading

Suk-Min Kong , Dong-Wook Oh , and Yong-Joo Lee ^(✉) 

Department of Civil Engineering, Seoul National University of Science and Technology, 232 Gongneung-ro, Nowon-gu, Seoul 01811, Republic of Korea
ucesyjl@seoultech.ac.kr

Abstract. In densely developed urban areas, the use of underground space to provide necessary transportation and utility infrastructures (e.g., subway tunnels, water pipes, and electrical conduits) has increased. The number of deteriorating ground surface structures in need of reconstruction has concurrently increased. Oftentimes, underground structures continue to be used while the ground surface structures undergo repair. To ensure adequate safety above and below ground, the interactive behaviour between underground structures and the adjacent ground during ground surface reconstruction must be fully understood. In this study, the interactive behaviour between an underground tunnel structure and the adjacent ground was predicted using numerical analysis during reconstruction of a deteriorated ground surface structure. In this analysis, various pile loading locations were considered to determine the minimum pile-tunnel offsets for design. Study findings suggest a minimum vertical and horizontal offset between the pile and tunnel of 2.0 times the tunnel diameter to ensure safety.

Keywords: Adjacent ground · Existing tunnel · Locations of pile loading
Numerical analysis

1 Introduction

As densely developed urban land areas become saturated, the use of underground space to provide necessary transportation and utility infrastructures (e.g. subway tunnels, water pipes, electrical conduits) has increased. The number of deteriorating ground surface structures in need of reconstruction or repair has concurrently increased. Oftentimes, underground structures continue to be used while the ground surface structures undergo repair. To ensure adequate safety both above and below ground, the interactive behaviour between the underground structures and adjacent ground during reconstruction of the ground surface structures must be fully understood.

Various aspects of the underground structure-adjacent ground interaction have been previously studied. Mair and Williamson [1] compared the effects of point-bearing and friction piles using a case study analysis and found that a pile's surface friction decreased and increased when negative and positive relative displacements occurred, respectively, using numerical analysis.

Additional studies have considered adjacent ground effects during tunnel excavation. In a model test, Kong et al. [2] simulated a tunnel excavation below a pile using tunnel volume loss equipment and confirmed the pile and adjacent ground behaviour using close-range photogrammetry. Researchers found that as the vertical offset between the pile and tunnel decreased, the extent of adjacent ground settlement increased. In a similar study, Oh et al. [3] predicted the adjacent ground behaviour during tunnel excavation based on the number and spacing of piles using three-dimensional (3D) numerical analysis.

With the increased deterioration of ground surface structures, select studies have considered the interactive behaviour between existing underground structures and the adjacent ground during their reconstruction or repair. Using field measurement data, Dimitrios [4] analysed the pile loading effects on an underground tunnel operated by London Underground Limited (LUL) and the adjacent ground and recommended a minimum clearance of 3 and 15 m from the tunnel top for bored and driven piles, respectively. More recently, Prateep et al. [5] proposed a method for evaluating the pile loading effects on tunnel structures using numerical analysis.

Building upon this previous work, we investigated the effects of pile loading location on an underground tunnel structure and the adjacent ground during reconstruction of a deteriorated ground surface structure. Using two-dimensional (2D) numerical analysis, we considered 12 different cases using various vertical and horizontal pile-tunnel offsets to determine the minimum pile-tunnel offsets for design. The same material properties and dimensions defined for this numerical analysis will be used in a future model test.

2 Numerical Analysis

In this study, we used the PLAXIS 2D finite element software [6] to analyse the effects of pile loading location on an underground tunnel structure and the adjacent ground during reconstruction of a deteriorated ground surface structure. Figure 1 shows the pile, tunnel, and adjacent ground model and mesh used for numerical analysis.

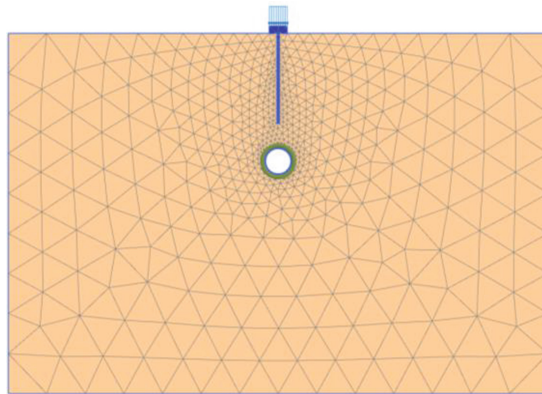


Fig. 1. Pile, tunnel, and adjacent ground model and mesh used for numerical analysis

In this numerical analysis, we defined the size of the adjacent ground as 1500×1000 mm (width \times height), the size of the tunnel as 70×2 mm (diameter \times thickness), and the size of each pile as 7×250 mm (width \times height). The model scale was 1/100, and a vertical allowable load of 0.015 kN/m² was applied to the pile cap based on recommendations by Oh and Lee [7].

Figure 2 shows the 12 different cases used to determine the minimum pile-tunnel offsets for design. These cases included vertical and horizontal pile-tunnel offsets of 1.0–3.0 D and 0.0–3.0 D, respectively, where D represents the tunnel diameter. The numbering scheme for the respective cases included a two-digit identifier. The first number corresponds to the vertical offset; Cases 1-X, 2-X, and 3-X correspond to vertical offsets of 1.0, 2.0, and 3.0 D, respectively. The second number corresponds to the horizontal offset; Cases X-1, X-2, X-3, and X-4 correspond to horizontal offsets of 0.0, 1.0, 2.0, and 3.0 D, respectively. Table 1 summarizes the input parameters used in this analysis for the soil material, tunnel, and pile based on recommendations by Das [8]. To reflect the soil behaviour, we applied the Mohr-Coulomb constitutive model for non-associated flow. To reflect the pile and tunnel behaviour, we applied linear-elastic models.

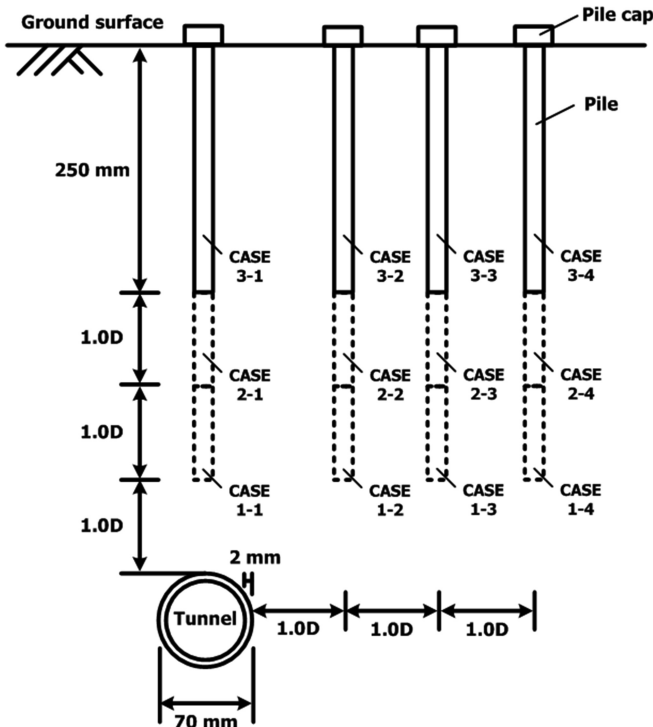


Fig. 2. Cases with various vertical and horizontal pile-existing tunnel offsets considered in this study (D: tunnel diameter)

Table 1. Input parameters for the soil material, tunnel, and pile [8]

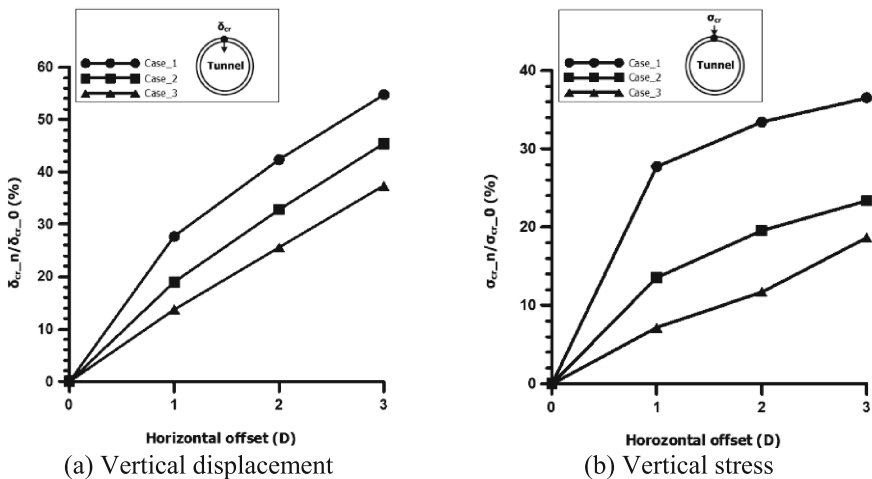
Parameter	Soil	Tunnel	Pile
Model	Mohr-Coulomb	Linear-elastic	Linear-elastic
γ (kN/m ³)	14.5	78	78
e	0.8	–	–
E (kN/m ²)	10,000	20,000,000	20,000,000
ν	0.3	0.25	0.25
c (kN/m ²)	0	–	–
Φ' (°)	27	–	–
R_{inter}	0.6	–	–

Note: γ = unit weight of soil, e = void ratio, E = Young's modulus, ν = Poisson's ratio, c = cohesion, Φ' = angle of shearing resistance, R_{inter} = interface factor

3 Results

The results of the numerical analysis were used to determine the minimum pile-tunnel offsets for design. Specifically, we considered the vertical displacement of and stress at the tunnel crown and the horizontal displacements and shear strains of the tunnel and adjacent ground based on various pile loading locations.

Figure 3(a) shows the predicted vertical displacement of the tunnel crown (expressed as a decreasing rate) based on the vertical and horizontal pile-tunnel offsets. When the horizontal offset was 0.0 D and greater than or equal to 1.0 D, the vertical displacement of the tunnel crown was δ_{cr-0} and δ_{cr-n} , respectively. As the vertical and horizontal pile-tunnel offsets increased, the vertical displacement of the tunnel crown decreased. Increasing the horizontal offset from 0.0 to 1.0 D decreased the vertical displacement by approximately 29%. For horizontal offsets greater than 2.0 D, the decreasing rate of vertical displacement gradually diminished.

**Fig. 3.** Predicted vertical displacement of and stress at the existing tunnel crown

Similarly, Fig. 3(b) shows the decreasing rate of vertical stress at the tunnel crown based on the vertical and horizontal pile-tunnel offsets. When the horizontal offset was 0.0 D and greater than or equal to 1.0 D, the vertical stress of the tunnel crown was σ_{cr-0} and σ_{cr-n} , respectively. As the vertical and horizontal pile-tunnel offsets increased, the vertical stress at the tunnel crown decreased. Increasing the horizontal offset from 0.0 to 1.0 D decreased the vertical stress by approximately 28%. For horizontal offsets greater than 2.0 D, the decreasing rate of vertical stress gradually diminished and approached a constant value.

Figures 4, 5 and 6 show the predicted horizontal displacements of the tunnel and adjacent ground based on various pile loading locations for vertical pile-tunnel offsets of 1.0 D, 2.0 D, and 3.0 D, respectively, with horizontal pile-tunnel offsets of 0.0–3.0 D. Irrespective of the vertical offset, a horizontal offset of 0.0 D produced symmetrical horizontal displacements to the left and right of the tunnel. As the horizontal offset increased and the pile moved to the right, horizontal displacements to the left of the tunnel increased (i.e. the horizontal displacement pattern was skewed left).

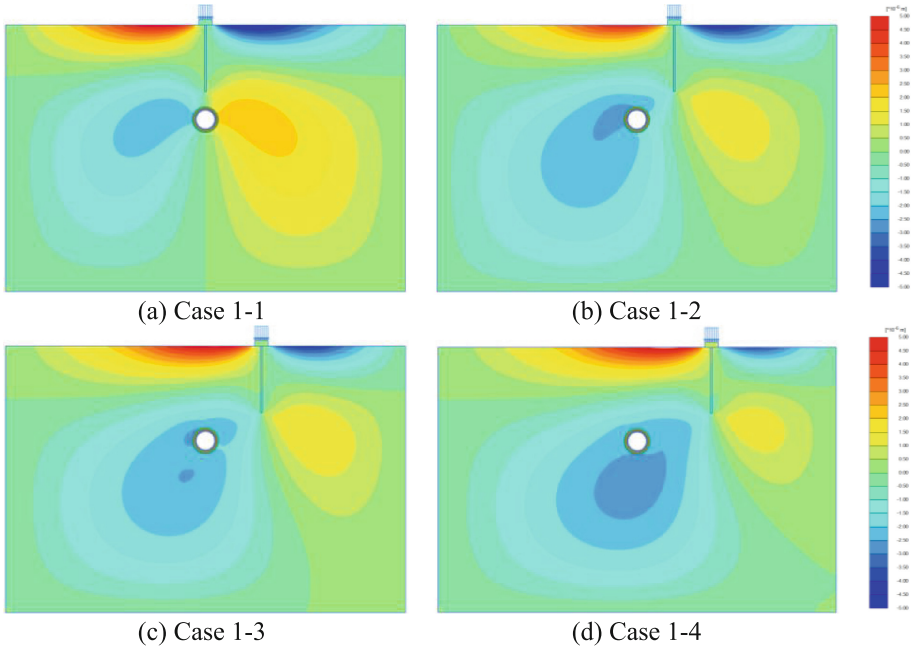


Fig. 4. Predicted horizontal displacements of the tunnel and adjacent ground for various pile loading locations (vertical offset = 1.0 D, horizontal offsets = 0.0–3.0 D)

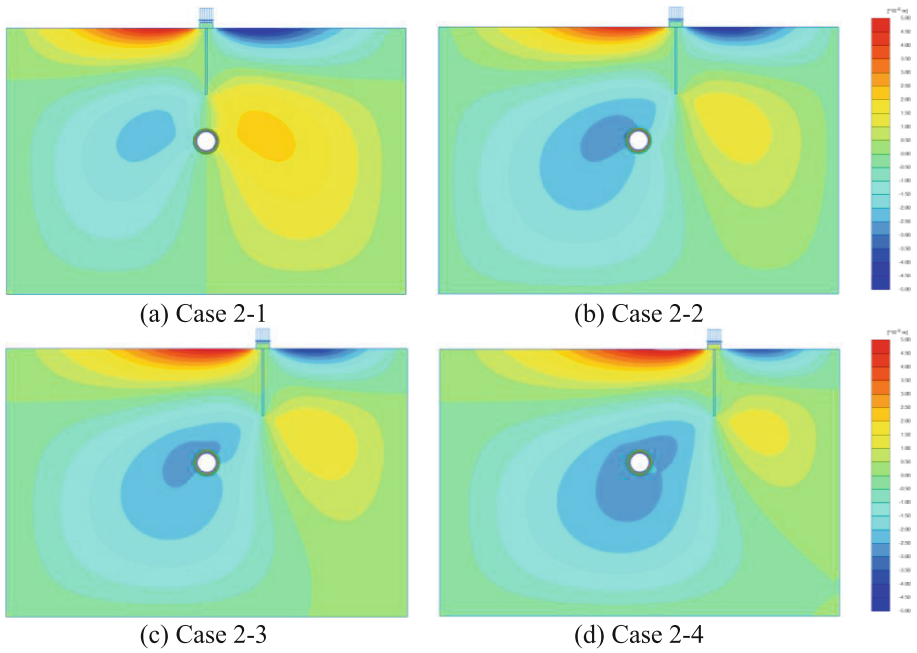


Fig. 5. Predicted horizontal displacements of the tunnel and adjacent ground for various pile loading locations (vertical offset = 2.0 D, horizontal offsets = 0.0–3.0 D)

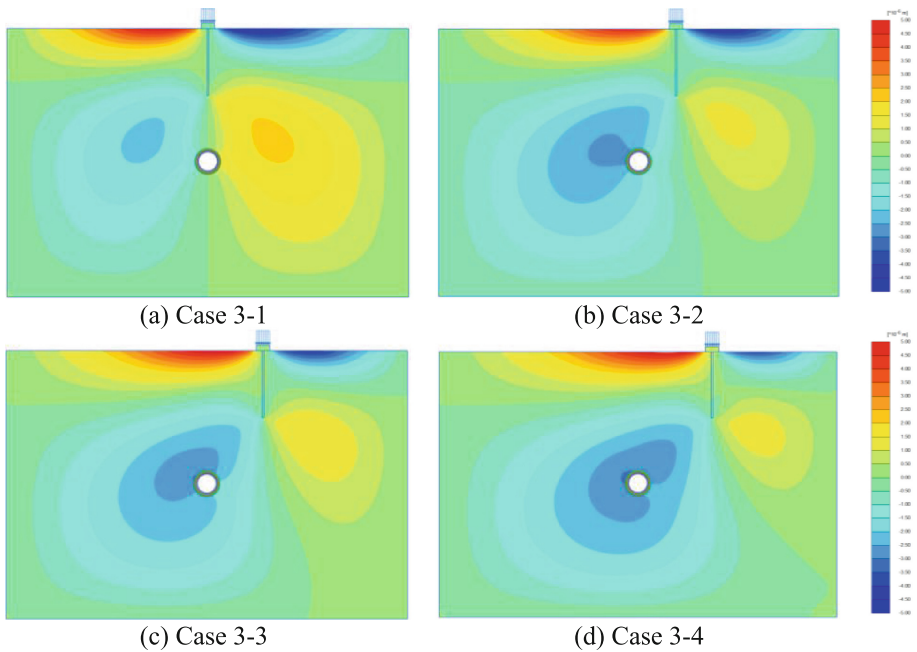


Fig. 6. Predicted horizontal displacements of the tunnel and adjacent ground for various pile loading locations (vertical offset = 3.0 D, horizontal offsets = 0.0–3.0 D)

Figures 7, 8 and 9 show the predicted shear strains of the tunnel and adjacent ground based on various pile loading locations for vertical pile-tunnel offsets of 1.0 D, 2.0 D, and 3.0 D, respectively, with horizontal pile-tunnel offsets of 0.0–3.0 D. When the horizontal offset was less than or equal to 1.0 D, shear strains at the pile tip were found to affect the tunnel; no effects were observed when the horizontal offset was greater than 2.0 D. Similarly, minimal shear strain effects were observed when the vertical offset was greater than 3.0 D, except when the horizontal offset was 0.0 D. These findings suggest minimum pile-tunnel vertical and horizontal offsets of 2.0 D to ensure safety.

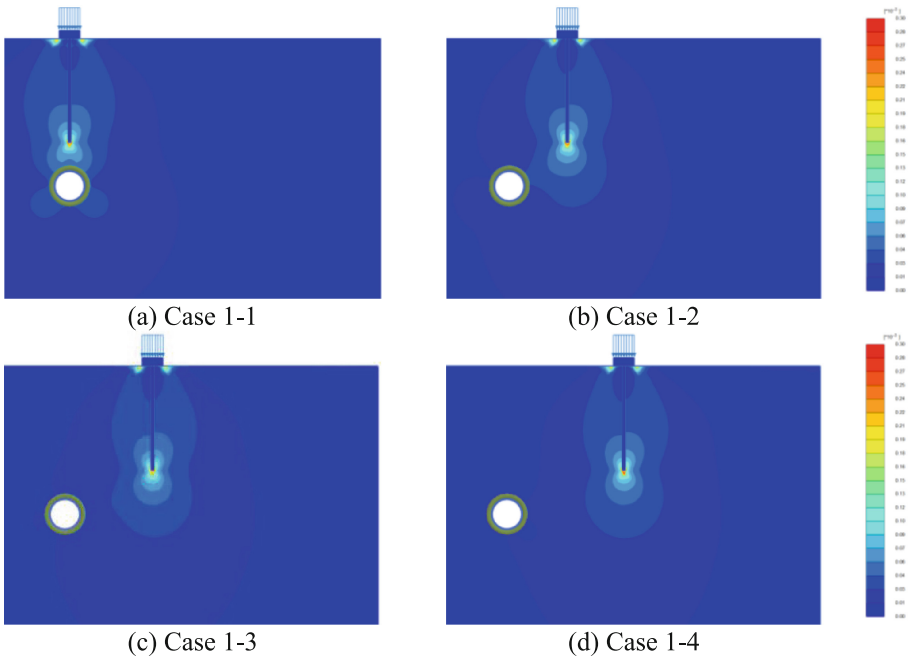


Fig. 7. Predicted shear strains of the tunnel and adjacent ground for various pile loading locations (vertical offset = 1.0 D, horizontal offsets = 0.0–3.0 D)

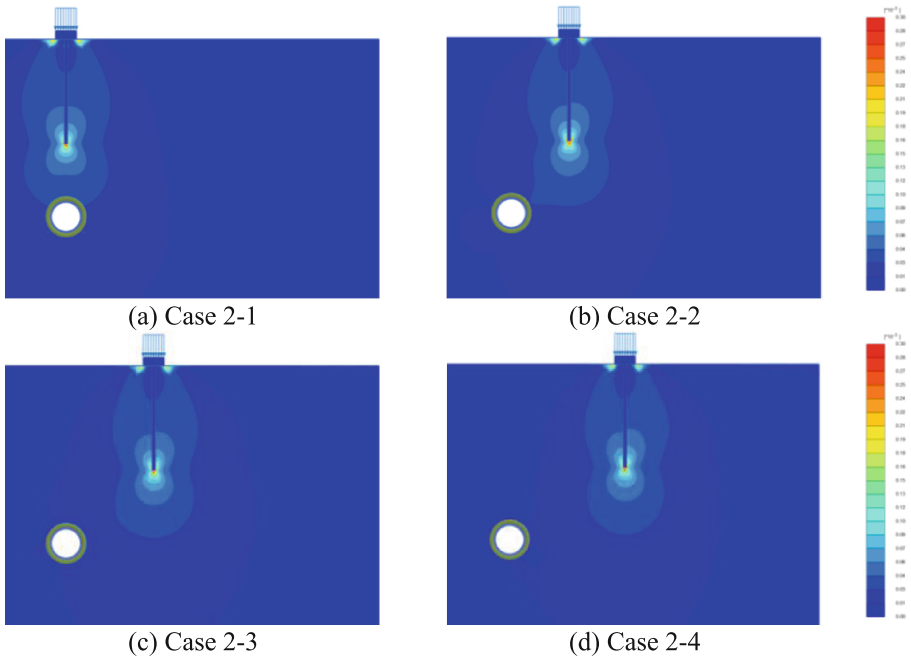


Fig. 8. Predicted shear strains of the tunnel and adjacent ground for various pile loading locations (vertical offset = 2.0 D, horizontal offsets = 0.0–3.0 D)

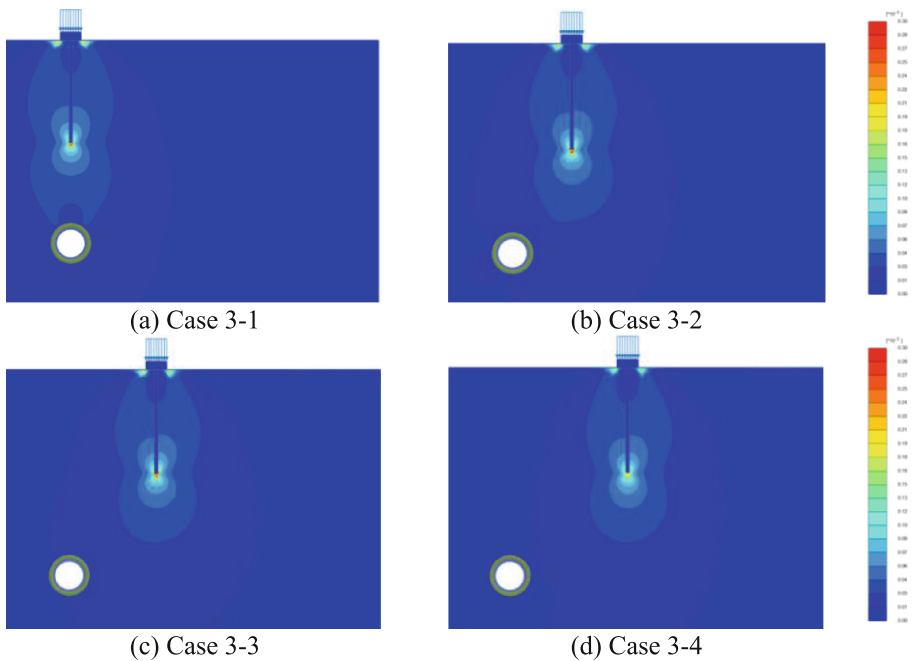


Fig. 9. Predicted shear strains of the tunnel and adjacent ground for various pile loading locations (vertical offset = 3.0 D, horizontal offsets = 0.0–3.0 D)

4 Conclusions

In this study, we investigated the effects of pile loading location on an underground tunnel structure and the adjacent ground during reconstruction of a deteriorated ground surface structure. Using 2D numerical analysis, we considered 12 different cases with vertical and horizontal offsets of 1.0–3.0 D and 0.0–3.0 D, respectively, to determine the minimum pile-tunnel offsets for design. Key findings from this study follow.

- As the vertical and horizontal pile-tunnel offsets increased, the vertical displacement of the tunnel crown decreased. Increasing the horizontal offset from 0.0 to 1.0 D decreased the vertical displacement by approximately 29%. For horizontal offsets greater than 2.0 D, the decreasing rate of vertical displacement gradually diminished.
- As the vertical and horizontal pile-tunnel offsets increased, the vertical stress at the tunnel crown decreased. Increasing the horizontal offset from 0.0 to 1.0 D decreased the vertical stress by approximately 28%. For horizontal offsets greater than 2.0 D, the decreasing rate of vertical stress gradually diminished and approached a constant value.
- Irrespective of the vertical offset, a horizontal offset of 0.0 D produced symmetrical horizontal displacements to the left and right of the tunnel. As the horizontal offset increased and the pile moved to the right, horizontal displacements to the left of the tunnel increased (i.e. the horizontal displacement pattern was skewed left).
- When the horizontal offset was less than or equal to 1.0 D, shear strains at the pile tip were found to affect the tunnel; no effects were observed when the horizontal offset was greater than 2.0 D. Similarly, minimal shear strain effects were observed when the vertical offset was greater than 3.0 D, except when the horizontal offset was 0.0 D.
- These collective findings suggest a minimum vertical and horizontal offset between the pile and tunnel of 2.0 D to ensure safety.

The results of this study substantially contribute to the state of knowledge regarding the effects of pile loading location on existing tunnel structures and the adjacent ground during reconstruction of deteriorated ground surface structures. Our research is of particular interest and use because of the enhanced theoretical understanding of pile loading location effects and the potential for direct improvements to reconstruction designs and methods it provides that will ultimately improve both above and below ground safety. Building upon this study's results, future efforts will include the conduct of a model test using the same material properties and dimensions defined for this study's numerical analysis.


Acknowledgments. This research was supported by the Basic Science and Engineering Research Program of the National Research Foundation of Korea (Project Number: NRF-2016R1A2B4013220).

References

1. Mair, R.J., Williamson, M.G.: The influence of tunnelling and deep excavation on piled foundations. In: Yoo, C., Park, S.-W., Kim, B., Ban, H. (eds.) Proceedings of the 8th International Symposium on Geotechnical Aspects of Underground Construction in Soft Ground. CRC Press, Boca Rotan, FL, pp. 21–30 (2014)
2. Kong, S.M., Jung, H.S., Lee, Y.J.: Investigation of ground behaviour adjacent to an embedded pile according to various tunnel volume losses. *Int. J. Geo-Eng.* **8**(5), 1–15 (2017)
3. Oh, D.W., Kong, S.M., Lee, H.G., Lee, J.H., Lee, Y.J.: Investigation of ground behaviour under pile-raft foundation applied vertical load due to tunnel excavation. In: Proceedings of the 19th International Society for Soil Mechanics and Geotechnical Engineering. ISSMGE, London, UK, pp. 1731–1735 (2017)
4. Dimitrios, S.: The response of full-scale pile and piled structures to tunnelling. Ph.D. thesis, University of Cambridge, UK (2005)
5. Prateep, L., Pornkasem, J., Pattaramon, J., Suchatvee, S.: Numerical investigation of tunnel deformation due to adjacent loaded pile and pile-soil-tunnel interaction. *Tunnel. Undergr. Space Technol.* **70**(1), 166–181 (2017)
6. PLAXIS (2016) 2D reference manual. PLAXIS, Delft, NL
7. Oh, D.W., Lee, Y.J.: Analysis of pile load distribution and ground behaviour depending on vertical offset between pile tip and tunnel crown in sand through laboratory model test. *J. Korean Tunnell. Undergr. Space Assoc.* **19**(3), 355–373 (2017)
8. Das, B.M.: Principles of Geotechnical Engineering, 7th edn. Cengage Learning, Boston, MA (2009)



A Numerical Approach to an Interface Damage Model Under Cyclic Loading

Roman Vodička^(✉)  and Katarína Krajníková 

Civil Engineering Faculty, Technical University of Košice,
Vysokoškolské 4, 042 00 Košice, Slovakia
{roman.vodicka,katarina.krajnikova}@tuke.sk

Abstract. A model for numerical analysis of interface damage is presented which leads to interface crack initiation and propagation in a multi-domain structure exposed to a cyclic loading. The proposed numerical approach is physically based on energy evolution, which includes stored elastic energy, energy of the external load and also dissipation due to damage. The solution evolution is approximated by a semi-implicit time stepping algorithm. In this algorithm, the variables in the energy functionals, related to deformation and damage, are separated in order to recursively solve the problem with respect to only one variable. The separation provides a variational structure to the solved problem followed by two separated minimisations in one time step. The variables of the elastic state are calculated by Symmetric Galerkin BEM which has the advantage that the minimisations, implemented by (sequential) quadratic programming solvers, can be performed only with respect to the interface displacement gap.

Keywords: Interface damage · Cohesive Zone Model · Fatigue life
Symmetric Galerkin Boundary Element Method
Quadratic Programming

1 Introduction

Numerical approaches for solving various civil engineering problems with rupturing interfaces are highly demanded. In this paper, we present a model for damage evolution under displacement or force loading with a constant amplitude which may cause total damage for the amplitudes substantially smaller than the load in pure uploading. The interface is supposed to be made of a very thin adhesive layer which may provide a stress-separation law as in a Cohesive Zone Model (CZM). The simulation of fatigue processes with CZM was introduced by their cyclic variant in [2, 7, 8], which includes a rate dependent damage evolution.

The present approach is physically based on energy evolution, which involves the stored elastic energy, energy of the external load and also dissipation due to damage. The dissipation potential has a rate dependent form with viscosity associated to damage, see also [6, 13]. The CZMs in the context of the energy

evolution were implemented in [15, 16]. In the present implementation, a viscous term was added to the energy dissipation in order to provide a model with hysteresis of damage which causes the unloading and reloading paths to be uncoincident. Other intentions with the model were to decrease transferable force with increasing damage and to keep the interface undamaged for low stresses.

Numerically, the solution evolution is approximated by a semi-implicit time stepping algorithm providing a variational structure to the solved problem by two recursively solved minimisations with respect to separated deformation and damage variables which was devised in [9, 12] and also described and used in the previous author’s works [15, 16, 18, 20]. Another numerical tools implemented in the model include the Symmetric Galerkin Boundary Element Method (SGBEM) [1, 14] with its multi-domain form of [17] to provide the displacement and stress solutions for the solids, and Quadratic Programming (QP) algorithms (possibly in a sequential modification) to calculate the solutions for energy minimisations in a variationally based approach [3, 4].

The paper is structured as follows. Section 2 describes the interface damage model and the relations which govern its evolution. Section 3 explains some aspects of the numerical solution and its particular implementation. Finally, Sect. 4 presents numerical results which demonstrate the properties of the model and reveal its characteristic response to cyclic loading.

2 Description of the Model

The model is based on evolution of energy. Let us therefore consider the energies which are taken into account in the model for two domains Ω^η , $\eta = A$, or B , bounded by the respective boundaries Γ^η as shown in Fig. 1. The common part of the boundaries (an interface) is denoted as $\Gamma_C = \Gamma^A \cap \Gamma^B$. Each of the boundaries is additionally split into disjoint parts according to boundary conditions: Γ_D^η where displacements are prescribed, Γ_N^η where tractions are given, i.e. $\Gamma^\eta = \overline{\Gamma_D^\eta} \cup \overline{\Gamma_N^\eta} \cup \overline{\Gamma_C}$. The normal and tangential vectors to the boundaries are denoted \mathbf{n}^η and \mathbf{s}^η , respectively.

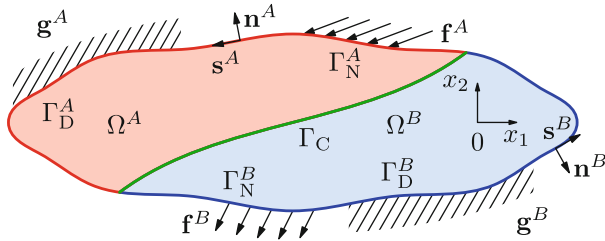


Fig. 1. A scheme of a two domain problem with one interface.



A state of the system is described by two variables: the displacement field \mathbf{u} and an internal variable ζ characterising the actual state of damage so that $\zeta = 1$ pertains to the initial undamaged state and $\zeta = 0$ means total damage (a crack). The stored energy functional is defined as

$$\mathcal{E}(t; \mathbf{u}, \zeta) = \begin{cases} \sum_{\eta=A,B} \int_{\Omega^\eta} \frac{1}{2} \mathbf{e}(\mathbf{u}^\eta) : \mathbf{C}^\eta : \mathbf{e}(\mathbf{u}^\eta) \, d\Omega \\ + \int_{\Gamma_C} \frac{1}{2} \left[k_n \Phi(\zeta) \llbracket \mathbf{u} \rrbracket_n^2 + k_s \Phi(\zeta) \llbracket \mathbf{u} \rrbracket_s^2 \right. \\ \quad \left. + k_g \left(\llbracket \mathbf{u} \rrbracket_n^- \right)^2 \right] \, d\Gamma \\ +\infty \end{cases} \quad \begin{array}{l} \text{if } \mathbf{u}^\eta = \mathbf{g}^\eta(t) \text{ on } \Gamma_D^\eta, \\ \text{and } 0 \leq \zeta \leq 1 \text{ on } \Gamma_C, \\ \text{otherwise,} \end{array} \quad (1)$$

where we have taken into account the bounds of the damage variable and where the admissible (time t dependent) displacement satisfies the boundary conditions on a part of boundary Γ_D^η . The fourth order tensor \mathbf{C}^η includes elastic constants for the domain Ω^η and \mathbf{e} is the small strain tensor. The interface integral defines dependence of the interface stiffnesses k_n and k_s , on the actual state of damage by the function $\Phi(\zeta)$ as in [15, 16]. The terms $\llbracket \cdot \rrbracket_n$ and $\llbracket \cdot \rrbracket_s$, respectively, are the normal and tangential relative displacements between opposite interface points, i.e. $\llbracket \mathbf{u} \rrbracket = \mathbf{u}^A - \mathbf{u}^B$ (superscripts A and B refer to the bodies adjacent to the interface from both its sides). The last term with $\llbracket \cdot \rrbracket_n^-$, denoting the negative part of the relative normal displacement, reflects the normal-compliance contact condition being understood as a reasonable approximation of Signorini contact conditions.

The potential energy of external forces (acting only along a part of the boundary denoted Γ_N^η) is given by the relation

$$\mathcal{F}(t, \mathbf{u}) = - \sum_{\eta=A,B} \int_{\Gamma_N^\eta} \mathbf{f}^\eta(t) \cdot \mathbf{u}^\eta \, d\Gamma, \quad (2)$$

where \mathbf{f}^η are the prescribed tractions on the part of boundary Γ_N^η .

The dissipated energy is introduced by the (pseudo) potential which reflects the rate-dependence and unidirectionality of the debonding process

$$\mathcal{R}(\dot{\zeta}) = \begin{cases} \int_{\Gamma_C} -\alpha_1 \dot{\zeta} + \frac{1}{2} \alpha_2 \dot{\zeta}^2 \, d\Gamma, & \text{if } \dot{\zeta} \leq 0, \\ +\infty & \text{otherwise,} \end{cases} \quad (3)$$

where α_1 is related to the instant of damage initiation and α_2 is visco-damage parameter which includes hysteresis into the damage evolution.

The relations which govern the evolution of solid elastic state and interface damage can be written in form of nonlinear variational inclusions with initial conditions

$$\begin{aligned} \partial_{\mathbf{u}} \mathcal{E}(t; \mathbf{u}, \zeta) + \partial_{\mathbf{u}} \mathcal{F}(t; \mathbf{u}) &\ni 0, & \mathbf{u}|_{t=0} &= \mathbf{u}_0, \\ \partial_{\zeta} \mathcal{R}(\dot{\zeta}) + \partial_{\zeta} \mathcal{E}(t; \mathbf{u}, \zeta) &\ni 0, & \zeta|_{t=0} &= \zeta_0, \end{aligned} \quad (4)$$

where ∂ denotes (partial) subdifferential of a convex non-smooth function which can be replaced by Gateaux differential if the functional is sufficiently smooth, as e.g. \mathcal{F} . The initial condition for damage is usually $\zeta_0 = 1$, pertaining to the undamaged state.

3 Numerical Solution and Computer Implementation

The numerical procedures proposed for the solution of the above problem consider the time discretisation and the spatial discretisation separately. The procedures are expressed only in terms of the boundary data as SGBEM is used to calculate elastic response of the solids.

Time Discretisation. The time discretisation scheme is defined by a semi-implicit algorithm with a fixed time step size τ such that the solution is obtained at the instants $t^k = k\tau$ for $k = 1, \dots, \frac{T}{\tau}$. In order to obtain such an algorithm from Eq. (4), the rates of damage are approximated by the finite difference $\dot{\zeta} \approx \frac{\zeta^k - \zeta^{k-1}}{\tau}$, where ζ^k denotes the solution at the instant t^k . The differentiation with respect to the rates can be replaced by the differentiation with respect to ζ^k , so that from Eqs. (4) we obtain

$$\partial_{\mathbf{u}^k} \mathcal{E}(t^k; \mathbf{u}^k, \zeta^{k-1}) + \partial_{\mathbf{u}^k} \mathcal{F}(t^k, \mathbf{u}^k) \ni 0, \quad (5a)$$

$$\tau \partial_{\zeta^k} \mathcal{R} \left(\frac{\zeta^k - \zeta^{k-1}}{\tau} \right) + \partial_{\zeta^k} \mathcal{E}(t^k; \mathbf{u}^k, \zeta^k) \ni 0, \quad (5b)$$

if we solve the inclusions separately in \mathbf{u} and ζ , respectively. Such a separation provides a variational structure to the solved problem, with two minimisations in each time step. First, the minimisation of

$$\mathcal{H}_{\mathbf{u}}^k(\mathbf{u}) = \mathcal{E}(t^k; \mathbf{u}, \zeta^{k-1}) + \mathcal{F}(t^k, \mathbf{u}) \quad (6a)$$

provides \mathbf{u}^k , and then the minimisation of

$$\mathcal{H}_{\zeta}^k(\zeta) = \mathcal{E}(t^k; \mathbf{u}^k, \zeta) + \tau \mathcal{R} \left(\frac{\zeta - \zeta^{k-1}}{\tau} \right) \quad (6b)$$

provides ζ^k .

Modification of Functionals Towards SGBEM. The role of the SGBEM in the present computational procedure is to provide a complete boundary-value solution from the given boundary data for each domain in order to calculate the elastic strain energy in these domains. Therefore, it is convenient to change the domain integral with \mathbf{u} in Eq. (6a) to boundary integrals. To do this, we define the linear mapping $S: (\mathbf{g}, \mathbf{f}, \mathbf{w}) \mapsto \mathbf{u}$ with \mathbf{u} being the weak solution to the transmission boundary value problem:

$$\operatorname{div}(\mathbf{C}^\eta \mathbf{e}(\mathbf{u}^\eta)) = 0 \quad \text{in } \Omega^\eta, \quad (7a)$$

$$\mathbf{u}^\eta = \mathbf{g}^\eta \quad \text{on } \Gamma_D^\eta, \quad (7b)$$

$$\mathbf{p}^\eta = \mathbf{f}^\eta \quad \text{with} \quad \mathbf{p}^\eta = (\mathbf{C}^\eta \mathbf{e}(\mathbf{u}^\eta)) \cdot \mathbf{n}^\eta \quad \text{on } \Gamma_N^\eta \quad (7c)$$

$$\left. \begin{array}{l} \llbracket \mathbf{u} \rrbracket = \mathbf{w} \\ \mathbf{p}^A + \mathbf{p}^B = 0 \end{array} \right\} \quad \text{on } \Gamma_C. \quad (7d)$$

The functional \mathcal{H}_u^k in Eq. (6a) is then converted to \mathcal{H}_w^k as

$$\begin{aligned} \mathcal{H}_w^k(\mathbf{w}) = & \sum_{\eta=A,B} \frac{1}{2} \int_{\Gamma_D^\eta} \mathbf{p}^\eta(\mathbf{g}(t^k), \mathbf{f}(t^k), \mathbf{w}) \cdot \mathbf{g}^\eta(t^k) \, d\Gamma \\ & - \sum_{\eta=A,B} \frac{1}{2} \int_{\Gamma_N^\eta} \mathbf{f}^\eta(t^k) \cdot \mathbf{u}^\eta(\mathbf{g}(t^k), \mathbf{f}(t^k), \mathbf{w}) \, d\Gamma \\ & + \int_{\Gamma_C} \frac{1}{2} \left[-\mathbf{p}^B(\mathbf{g}(t^k), \mathbf{f}(t^k), \mathbf{w}) \cdot \mathbf{w} + k_n \Phi(\zeta) w_n^2 + k_s \Phi(\zeta) w_s^2 + k_g (w_n^-)^2 \right] d\Gamma, \end{aligned} \quad (8)$$

where $\mathbf{u}^\eta(\mathbf{g}(t^k), \mathbf{f}(t^k), \mathbf{w})$ and $\mathbf{p}^\eta(\mathbf{g}(t^k), \mathbf{f}(t^k), \mathbf{w})$ denote the displacement and traction, respectively, resulting from Eq. (7) through the (generalised) Poincaré-Steklov operator as described in [19]. They are obtained by the SGBEM code supposing the displacement gap \mathbf{w} at Γ_C to be known from the used minimisation procedure in the same way as proposed and tested in [17, 19]. Once all the boundary data (displacements and tractions) are obtained from the solution of the SGBEM code, the pertinent energy functional in Eq. (8) can be calculated.

Remarks on the Minimisation Algorithms. The problem is numerically solved by recursive minimisation of the functionals (8) and (6b). In the former functional, we have quadratic functionals for whose minimisation quadratic programming algorithms are applied. The latter functional is generally a convex functional to which the QP algorithm is applied sequentially, however it remains quadratic if the function $\Phi(\zeta)$ is quadratic.

The functional (8) additionally contains a non-smooth term related to the normal contact term $(w_n^-)^2$, which can be replaced by a quadratic term v^2 introducing a new variable v satisfying additional constraints

$$v \geq 0, \quad v + w_n \geq 0. \quad (9)$$

This is classical trick, known also as a Mosco-type transformation, implemented also in [15, 19].

After the discretisation, all variables are approximated by the pertinent boundary element mesh introduced by SGBEM, see [14, 17]. The approximation formula can be written in the schematic form

$$\omega_h(x) = \sum_n N_n(x) \omega_n, \quad (10)$$

where ω can be \mathbf{u} , \mathbf{w} , \mathbf{p} , ζ , or v and ω_n are the nodal unknowns associated to the node x_n . In what follows, the nodal values ω_n are grouped into a column vector $\boldsymbol{\omega}$.

In minimisation of the functional (8) with the constraints (9), it is useful to reformulate the constraints as bound constraints. First, the constraint can be written in terms of the nodal variables as

$$\begin{pmatrix} 1 & 0 \\ 1 & 1 \end{pmatrix} \begin{pmatrix} \mathbf{v} \\ \mathbf{w}_n \end{pmatrix} \geq \begin{pmatrix} \mathbf{0} \\ \mathbf{0} \end{pmatrix}, \quad (11)$$

with the identity matrix \mathbf{I} .

The inequality is defined by a full rank matrix, therefore the following relation holds:

$$\begin{pmatrix} \mathbf{v} \\ \mathbf{w}_n \end{pmatrix} = \begin{pmatrix} 1 & 0 \\ -1 & 1 \end{pmatrix} \begin{pmatrix} \mathbf{y}_1 \\ \mathbf{y}_2 \end{pmatrix}, \quad \text{with} \quad \begin{pmatrix} \mathbf{y}_1 \\ \mathbf{y}_2 \end{pmatrix} \geq \begin{pmatrix} \mathbf{0} \\ \mathbf{0} \end{pmatrix}. \quad (12)$$

This implies the same number of bound constraints as provided by the more general conditions (11).

The functional (8) can be expressed after discretisation in a general matrix form as

$$\mathcal{H}_{\mathbf{w},h}^k(\mathbf{y}) = \frac{1}{2} \mathbf{y}^\top \mathbf{A}_h^k \mathbf{y} - (\mathbf{b}_h^k)^\top \mathbf{y} + \mathbf{c}_h^k, \quad \mathbf{y} \geq \mathbf{0}. \quad (13)$$

The constrained minimum obtained by a QP algorithm is denoted by \mathbf{y}^k .

Similarly, the discrete form of the functional (6b) can be written as

$$\mathcal{H}_{\zeta,h}^k(\boldsymbol{\zeta}) = \mathbf{K}_h(\boldsymbol{\zeta}) - (\mathbf{G}_h^k)^\top \boldsymbol{\zeta} + \mathbf{c}_h^k, \quad \mathbf{0} \leq \boldsymbol{\zeta} \leq \boldsymbol{\zeta}_h^{k-1}, \quad (14)$$

where the constraint guarantees unidirectionality of the damage process and also the bounds for the damage parameter. The function \mathbf{K}_h can be quadratic as the first term in (13), if Φ depends quadratically on ζ , otherwise, it is generally convex. Anyhow, the constrained minimum is denoted by $\boldsymbol{\zeta}^k$. In the general case, we apply the QP algorithm sequentially, see [15]. Therefore, we first approximate \mathbf{K}_h by a quadratic form using the Taylor polynomial

$$\mathbf{K}_h(\boldsymbol{\zeta}) \approx \mathbf{K}_h(\boldsymbol{\zeta}_0) + \mathbf{K}_h'^\top(\boldsymbol{\zeta}_0) (\boldsymbol{\zeta} - \boldsymbol{\zeta}_0) + \frac{1}{2} (\boldsymbol{\zeta} - \boldsymbol{\zeta}_0)^\top \mathbf{K}_h''(\boldsymbol{\zeta}_0) (\boldsymbol{\zeta} - \boldsymbol{\zeta}_0), \quad (15)$$

where $\boldsymbol{\zeta}_0$ is known. It should be noted that the second derivative is positive due to required convexity of the \mathbf{K}_h function.

The methods of QP can be implemented numerically by various algorithms. Here, we use Conjugate Gradient based algorithms with bound constraints [4]. The pertinent algorithms are not described explicitly as they can be found in the aforementioned reference.

Summing it up, in each time step k we first find \mathbf{y}_h^k by QP. Then we apply SQP by starting with $m = 1$ and putting $\boldsymbol{\zeta}_0 = \boldsymbol{\zeta}_h^{k-1}$ and iteratively find the minimum of $\mathcal{H}_{\zeta,h}^k(\zeta)$, the minimiser being denoted $\boldsymbol{\zeta}_m$ until a convergence criterion is met for $\boldsymbol{\zeta}_m$. Then, we put $\boldsymbol{\zeta}_h^k = \boldsymbol{\zeta}_m$. This we apply recursively up to prescribed time T .

4 A Beam Under a Cyclic Load

We use the model to find solutions for various amplitudes of the same load applied to the beam shown in Fig. 2, see also [15,16]. The model formulation is implemented in a MATLAB computer code.

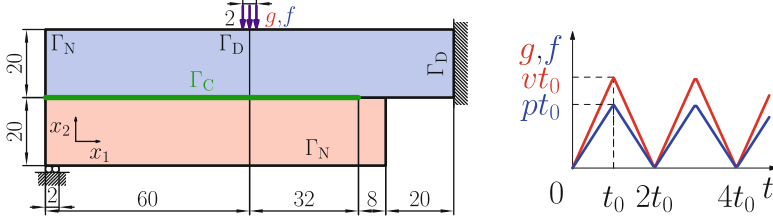


Fig. 2. The beam with its supports and time dependent displacement load.

The material properties of both layers in our example are: $E = 70$ GPa, $\nu = 0.35$. The beam is loaded either by a time dependent displacement load with the amplitude $g_m = vt_0$ or by a time dependent force load with the amplitude $f_m = pt_0$. It is also shown in Fig. 2, where $v = 1$ mm s⁻¹, $p = 2800$ MPa s⁻¹ and for t_0 are used various values. The characteristics of the interface needed for functionals in Eqs. 1 and 3 are $\alpha_1 = 1.01$ Jm⁻², $\alpha_2 = 100$ Jsm⁻², $k_g = 14$ TPam⁻¹, $k_n = 2k_s = 2$ TPam⁻¹ and $\Phi(\zeta) = 100\zeta/(101 - \zeta)$, cf. [16].

First, we intend to present how fast the crack length increases when it propagates. Table 1 summarises number of time steps $n_{a=10\text{mm}}$ needed to obtain a crack of length 10 mm (in the sense that ζ at the pertinent nodal point of the interface falls below 0.1) and number of time steps $n_{a=22\text{mm}}$ for which the condition is satisfied at the point 22 mm far from the end point. The used discretisation is uniform such that the boundary element mesh size (element length) is $h = 2$ mm and the pertinent time step is $\tau = 5$ ms. With given τ , the number of cycles ΔN which is needed to extend the crack from the length $a = 10$ mm to $a = 22$ mm is $\Delta N = \Delta n \cdot \tau / (2t_0)$. In fact, we had solved the problem until we reached a crack at least of the length $a = 30$ mm which is directly below the applied load.

Table 1. Number of time steps n_a to reach a crack length a , $\tau = 5$ ms: (a) displacement loading, (b) force loading.

(a)	t_0 [mm]	0.025	0.05	0.1	0.2	(b)	t_0 [mm]	0.025	0.05	0.1	0.2
	$n_{a=10\text{mm}}$	3494	788	186	44		$n_{a=10\text{mm}}$	3038	690	176	42
	$n_{a=22\text{mm}}$	6507	1522	372	107		$n_{a=22\text{mm}}$	4684	1030	257	52
	Δn	3013	734	186	63		Δn	1646	340	81	10



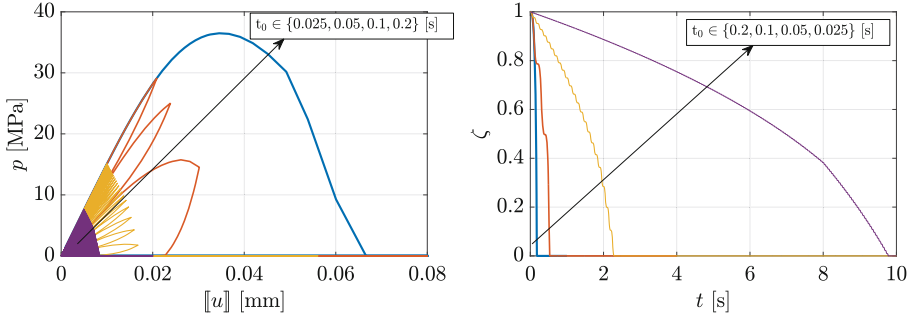


Fig. 3. The stress-displacement-gap relation (left) and evolution of ζ (right) for a near-to-the-end point of the interface $x_1 = 90$ mm, influence of the amplitude $g_m = vt_0$.

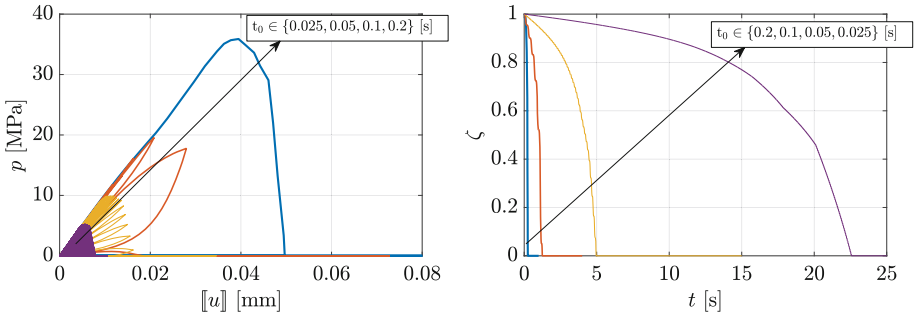


Fig. 4. The stress-displacement-gap relation (left) and evolution of ζ (right) for the point at $x_1 = 78$ mm, influence of the amplitude $g_m = vt_0$.

The data from Table 1 can be used to calculate the parameters of the crack-growth power law known for fatigue processes, see [5]. Linearised regression is used to obtain $\Delta a / \Delta N = 852.2 \cdot g_m^{2.872}$ ($R^2 = 0.9985$) for the displacement loading. Here, the amplitude g_m is applied instead of stress intensity factor used in the aforementioned Paris law. Similarly, the power relation for the force load reads $\Delta a / \Delta N = 2 \times 10^{-8} \cdot f_m^{3.4158}$ ($R^2 = 0.9965$), where the amplitude of the applied force is used as the independent variable.

The relations that can be checked at the interface where a crack propagates include traction-separation relation and evolution of damage. Both of them are shown in Figs. 3 and 4 for two distinct interface points which are, respectively: a point close to the end point of the interface where the damage (and subsequently crack) is initiated, and the point at the crack tip if $a = 14$ mm. These graphs pertain to the evolution under the displacement load. The graphs show how the interface stiffness is decreasing during the loading process. Also it can be observed, influenced by the neighbourhood of a particular point, that the decrease of the stress appears to be faster as the crack tip approaches that point. Also the decrease of the damage parameter is steeper in that case. The curves show the results for four different amplitudes of the load. The number of

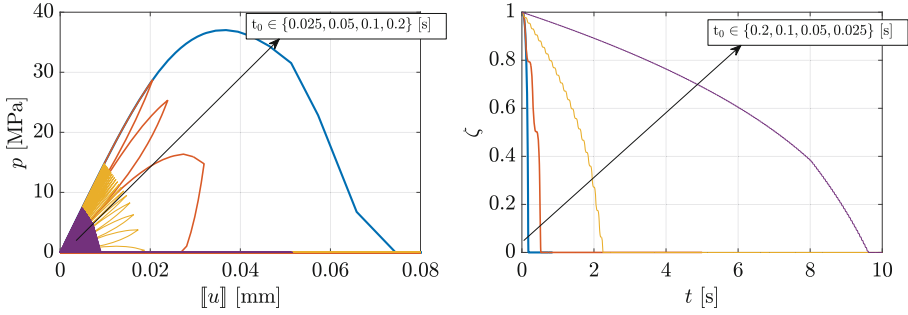


Fig. 5. The stress-displacement-gap relation (left) and evolution of ζ (right) for a near-to-the-end point at the interface $x_1 = 90$ mm, influence of the amplitude $f_m = pt_0$.

cycles to provoke total damage ($\zeta = 0$) at each point is different. In the case of the smallest amplitude, the cycles cannot be easily counted in these graphs due to their large number.

Similar graphs for the force load are shown in Figs. 5 and 6. The same points of the interface are used to obtain pertinent graphs. Compared to the previous case, the damage evolution is faster, especially in the interior of the interface where the applied force causes the interface stiffness and also overall stiffness of the structure (cf. Figs. 7 and 8) to decrease more steeply.

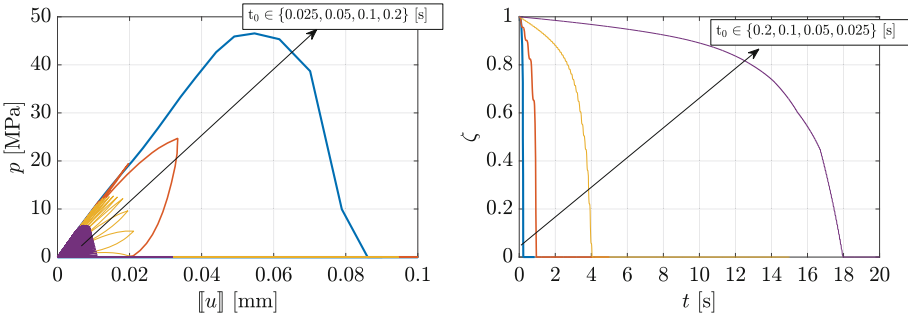
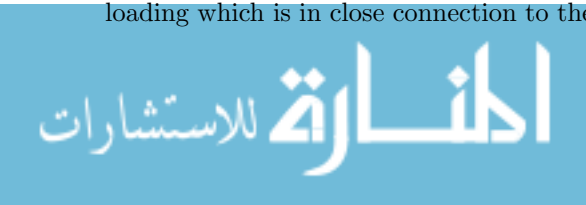


Fig. 6. The stress-displacement-gap relation (left) and evolution of ζ (right) for the point at $x_1 = 78$ mm, influence of the amplitude $f_m = pt_0$.

The overall response of the beam to both types of loading is documented by the stiffness K which relates the average force and average displacement applied or enforced at the same locus of load application in the middle of the upper layer top face. The responses for the same values of t_0 as used before are shown in Figs. 7 and 8 for displacement and force loading, respectively. As we expected and as we have already mentioned afore, the stiffness decreases faster for force loading which is in close connection to the faster crack propagation in this case.



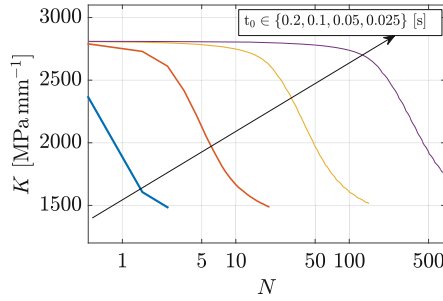


Fig. 7. The stiffness K of the beam considered as $p_g = Kg$, where p_g is the average traction at the prescribed displacement locus, influence of the amplitude $g_m = vt_0$.

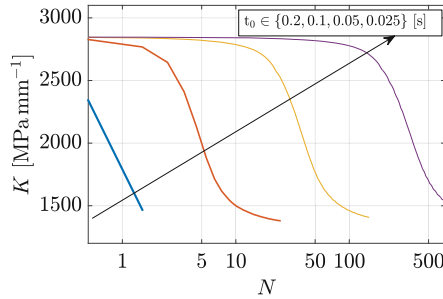


Fig. 8. The stiffness K of the beam considered as $f = Ku_f$, where u_f is the average displacement of the prescribed traction locus, influence of the amplitude $f_m = pt_0$.

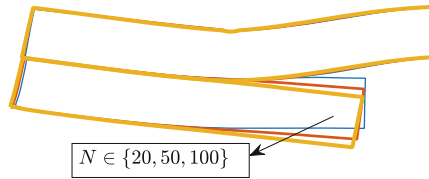


Fig. 9. The deformation of the beam (magnified 200 \times) at three instants of the displacement load, $t_0 = 0.05$ s.

Finally, the evolution of deformation is compared for both loading cases. Here, we used the results of one particular amplitude, namely that for $t_0 = 0.05$ s. Figure 9 shows the maximal displacements for the displacement load at three instants of loading after N cycles, where pertinent N s are displayed in the picture. The displacement type of loading causes that the deformation of the upper layer is more or less the same for all three instants, while the bottom layer deforms differently in the selected instants due to the evolving crack.

Similarly, Fig. 10 shows the maximal displacements for force loading at the same three instants after N cycles. The deformations of the upper beam are now

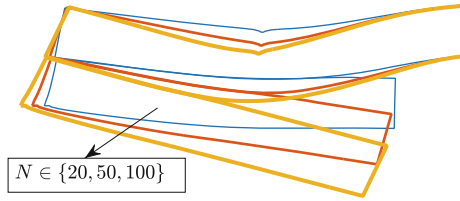


Fig. 10. The deformation of the beam (magnified 200×) at three instants of the force load, $t_0 = 0.05$ s.

increasing as the stiffness decreases due to increasing crack length. At the last used instant the stiffness would be approximately a half of the original one as the crack has extended to the left part of the beam, cf. also Fig. 8.

At the very end, we try to assess the convergence of the proposed numerical approach which may be analysed similarly to the models used e.g. in [10,11]. Therefore, in addition to the used discretisation characterised by the time step $\tau = 5$ ms and the mesh size $h = 2$ mm, we choose another two discretisations: the first one coarser with $\tau = 10$ ms, $h = 4$ mm, the other one finer with $\tau = 2.5$ ms, $h = 1$ mm. Figure 11 documents how the global stiffness K introduced for Fig. 7 changes with respect to the chosen discretisation in the case of $t_0 = 0.05$ s and displacement loading. The other graph in Fig. 11 shows locally at $x_1 = 78$ mm the evolution of ζ for the same discretisations and loadings. The same two graphs are provided for force loading in Fig. 12. Both comparisons provide an evidence of a tendency to a mesh-independent solution in these particular calculations, because the difference between the finer meshes is smaller than between the coarser ones, though in the case of force loading, the difference is almost invisible for the stiffness graphs.

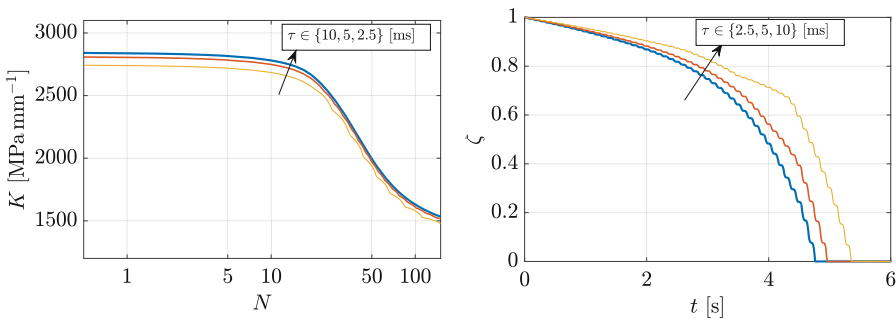


Fig. 11. An observation of convergence in the numerical data of three discretisations distinguished by the time step τ : a global structure characteristic – the stiffness K (left), and a local value of the state variable – the damage ζ at $x_1 = 78$ mm (right), displacement loading.



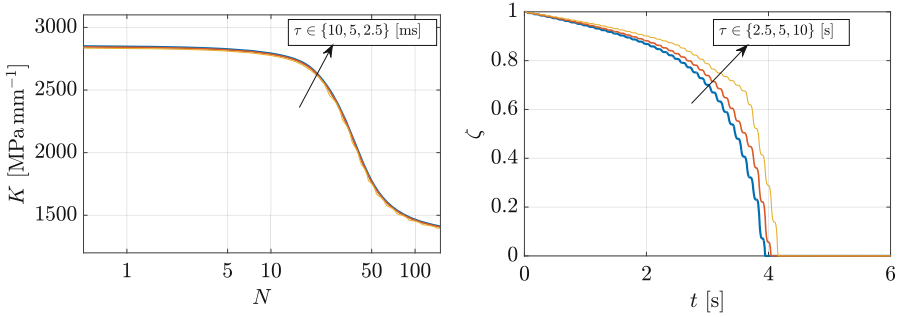


Fig. 12. An observation of convergence in the numerical data of three discretisations distinguished by the time step τ : a global structure characteristic – the stiffness K (left), and a local value of the state variable – the damage ζ at $x_1 = 78$ mm (right), force loading.

5 Conclusion

A model for solving interface damage previously presented in [15] was enhanced here by a kind of hysteresis in damage. The aim was to observe the model behaviour under cyclic loading. The presented results confirm that the model is capable to evolve the damage in the sense of fatigue life. From the computational point of view, to obtain the solution of a evolution problem semi-implicit time discretisation was implemented to obtain a variational structure of the numerical approximation model. The approximated model then utilises method of sequential quadratic programming with a space discretisation by SGBEM. The choice of the latter mentioned numerical technique enable to formulate the minimisation problems only in terms of interface variables such as displacement gap and interface damage, if all non linear processes in the model are accumulated only at the interface. Of course, there are many parameters in the model that should be appropriately set to follow satisfactorily some experimental results. Nevertheless, it might be expected that the proposed approach turns to be useful in practical engineering calculations.

Acknowledgement. Authors acknowledge support from the Slovak Ministry of Education by the grants VEGA 1/0078/16 and VEGA 1/0477/15.

References

1. Bonnet, M., Maier, G., Polizzotto, C.: Symmetric Galerkin boundary element method. *Appl. Mech. Rev.* **15**, 669–704 (1998)
2. Bouvard, J., Chaboche, J., Feyel, F., Gallerneau, F.: A cohesive zone model for fatigue and creep' fatigue crack growth in single crystal superalloys. *Int. J. Fatigue* **31**, 868–879 (2009)
3. Dostál, Z.: An optimal algorithm for bound and equality constrained quadratic programming problems with bounded spectrum. *Computing* **78**(4), 311–328 (2006)

4. Dostál, Z.: *Optimal Quadratic Programming Algorithms*. Springer Optimization and Its Applications, vol. 23. Springer, Berlin (2009)
5. París, P., Erdogan, F.: A critical analysis of crack propagation laws. *ASME J. Basic Eng.* **85**(4), 528–533 (1963)
6. Raous, M., Cangemi, L., Cocu, M.: A consistent model coupling adhesion, friction and unilateral contact. *Comput. Meth. Appl. Mech. Eng.* **177**(6), 383–399 (1999)
7. Roe, K., Siegmund, T.: An irreversible cohesive zone model for interface fatigue crack growth simulation. *Eng. Frac. Mech.* **70**, 209–232 (2003)
8. Roth, S., Hütter, G., Kuna, M.: Simulation of fatigue crack growth with a cyclic cohesive zone model. *Int. J. Frac.* **188**, 23–45 (2014)
9. Roubíček, T., Panagiotopoulos, C., Mantič, V.: Local-solution approach to quasistatic rate-independent mixed-mode delamination. *Math. Models Methods Appl. Sci.* **25**(7), 1337–1364 (2015). <https://doi.org/10.1142/S0218202515500347>. <http://www.scopus.com/inward/record.url?eid=2-s2.0-84928622466&partnerID=40&md5=4eb8c21f6e532de7f0675601e9fa786d>
10. Roubíček, T.: Adhesive contact of visco-elastic bodies and defect measures arising by vanishing viscosity. *SIAM J. Math. Anal.* **45**(1), 101–126 (2013). <https://doi.org/10.1137/12088286X>
11. Roubíček, T.: Maximally-dissipative local solutions to rate-independent systems and application to damage and delamination problems. *Nonlin. Anal., Th. Meth. Appl.* **113**, 33–50 (2015)
12. Roubíček, T., Panagiotopoulos, C., Mantič, V.: Quasistatic adhesive contact of visco-elastic bodies and its numerical treatment for very small viscosity. *Zeitschrift angew. Math. Mech.* **93**, 823–840 (2013)
13. Roubíček, T., Souček, O., Vodička, R.: A model of rupturing lithospheric faults with reoccurring earthquakes. *SIAM J. Appl. Math.* **73**(4), 1460–1488 (2013)
14. Sutherland, A., Paulino, G., Gray, L.: *The Symmetric Galerkin Boundary Element Method*. Springer, Berlin (2008)
15. Vodička, R.: A quasi-static interface damage model with cohesive cracks: SQP-SGBEM implementation. *Eng. Anal. Bound. Elem.* **62**, 123–140 (2016)
16. Vodička, R., Mantič, V.: An energy based formulation of a quasi-static interface damage model with a multilinear cohesive law. *Discrete Cont. Dynam. Syst.* **10**(6), 1539–1561 (2017)
17. Vodička, R., Mantič, V., París, F.: Symmetric variational formulation of BIE for domain decomposition problems in elasticity - an SGBEM approach for nonconforming discretizations of curved interfaces. *Comp. Model. Eng. Sci.* **17**(3), 173–203 (2007)
18. Vodička, R., Mantič, V., Roubíček, T.: Energetic versus maximally-dissipative local solutions of a quasi-static rate-independent mixed-mode delamination model. *Mechanica* **49**(12), 2933–296 (2014)
19. Vodička, R., Mantič, V., Roubíček, T.: Quasistatic normal-compliance contact problem of visco-elastic bodies with Coulomb friction implemented by QP and SGBEM. *J. Comp. Appl. Math.* **315**, 249–272 (2017)
20. Vodička, R., Roubíček, T., Mantič, V.: General-purpose model for various adhesive frictional contacts at small strains. *Interfaces and Free Boundaries* (2018, submitted)



Numerical Simulations of Precast Thin-Walled Concrete Blocks Forming Coastal Structure

Bao-Loi Dang^{1,2(✉)}, Hau Nguyen Ngoc^{1,3}, Hung Nguyen-Xuan⁴,
Hoang Duc Thao⁵, and Magd Abdel Wahab¹

¹ Laboratory Soete, Faculty of Engineering and Architecture,
Ghent University, Ghent, Belgium
BaoLoi.Dang@UGent.be

² Mien Trung University of Civil Engineering, Tuy Hoa, Vietnam

³ University of Science and Technology,

The University of Danang, Da Nang, Vietnam

⁴ Center for Interdisciplinary Research in Technology, HUTECH University,
Ho Chi Minh City, Vietnam

⁵ Ba Ria – Vung Tau Urban Sewerage and Development One Member Limited
Company (BUSADCO), Vung Tau, Vietnam

Abstract. Seawalls have been implemented for coastal protection for centuries. The gravity type vertical seawalls made of plain concrete is the most common one used widely because of its advantages such as competitive construction cost, little maintenance requirement, etc. In this work, a novel three dimensional precast thin-walled concrete block forming seawall has been simulated by using finite element software. Unlike the traditional gravity type seawalls, such as hollow block, is low self-weight structure and can be damaged under exceed load. Therefore, load-bearing capacity of block itself under wave attack is necessarily evaluated. Of course, stability of seawall structure against sliding, overturning or bearing capacity of soil foundation are important factors and should not be overlooked. Theoretical aspects and computational modelling procedures are presented in detail. ABAQUS commercial software is adopted for this study.

Keywords: Seawalls · Stress analysis · Thin-walled block
Finite element analysis

1 Introduction

Climate change have affected human life worldwide. Extremely events such as hurricane, flooding, melting ice sheet, etc. occurs more fluently. High-rise sea level is one of the most serious issues that induced coastline erosion phenomenon. Since then, millions of hectares of coastal land have been vanished [1]. Many attempts to preventing coastline from erosion have been made. Due to particular conditions, coastal protections such as breakwaters, seawalls, etc. have been employed [2].

For centuries, alongside physical models testing, a large number of numerical model for coastal structures has been conducted. This allows for more optimal and cost-efficient design of structures. Most of studies are related to solving hydrodynamic

performances of various type of sea waves and stability of coastal structures under different conditions [3–8]. Recently, a research on inter-locking concrete block forming revetment slope structure by using ABAQUS have been presented [9]. Researchers have proposed an effective tool for coastal design which can deal with various problems such as load-bearing capacity, contact problem and soil-structure interactions.

In this work, a novel thin-walled concrete block forming seawalls is analyzed using a commercial simulation software, i.e. ABAQUS [10]. Unlike the conventional concrete blocks forming seawalls owning massive self-weight, this new concrete block is similar to caisson-type component. A construction company in Vietnam, namely BUSADCO have developed and employed such type of seawall block [11]. This precast thin-walled structure may be damaged under repetitive loading, for instance inducing cracks or fretting fatigue. For this reason, analysis of its bearing capacity is very important. In this paper, stress analysis of novel thin-walled concrete block forming the toe of seawall structure as shown in Fig. 1 is considered.

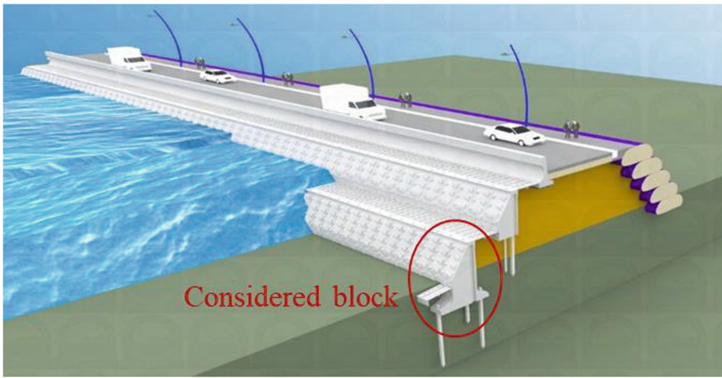


Fig. 1. Seawall structure proposed by BUSADCO.

The detail of novel block including geometric characteristic and material parameters will be provided in Sect. 2. Brief of seawalls design and computation-related are also discussed in this paper.

2 Computation-Related Details

2.1 Model of Novel Thin-Walled Concrete Seawall Block

The length of the block is 4.18 m, the width is 1.2 m, and the height is 5.0 m. The detail of thin-walled concrete block dimension proposed by BUSADCO is shown in Fig. 2. The unit in the given figure is in millimeter. Geometry of novel block has been simplified and modelled in ABAQUS as shown in Fig. 3. The mechanical properties of concrete used for thin-walled block are introduced in Table 1. In case of group of blocks analysis, the coefficient of friction between blocks is 0.3.

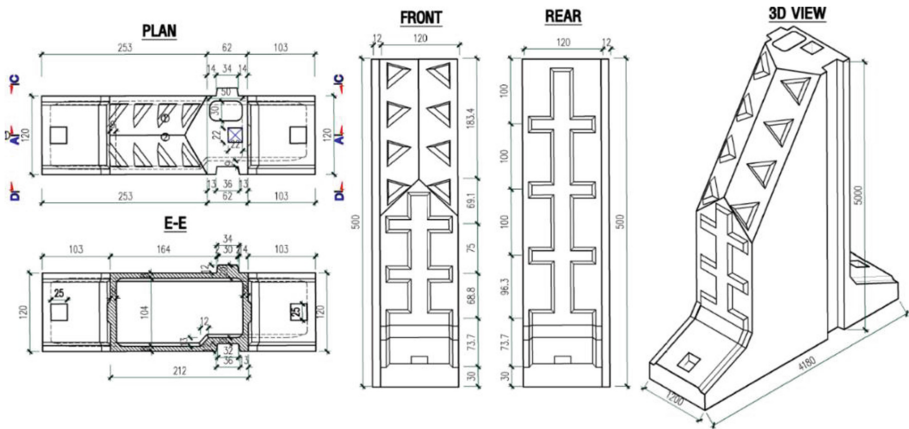


Fig. 2. Dimension of novel thin-walled block proposed by BUSADCO.

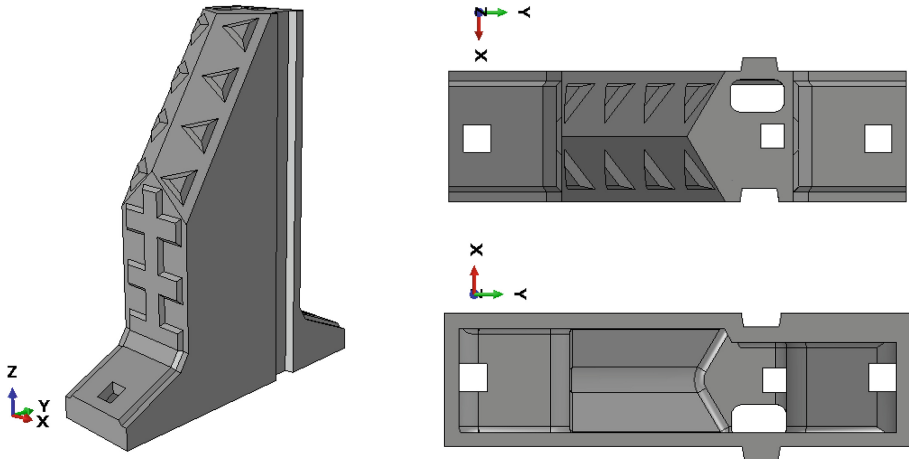


Fig. 3. Model hollow block in ABAQUS software.

Table 1. Mechanical properties of used materials

Parameters	Concrete	Backfill and sand fill	Natural soil	Sea water
Modulus of elasticity, MPa	20×10^3	20	—	—
Unit weight, kG/m ³	2300	2000	1630	1025
Poisson's ratio	0.2	0.3	—	—
Compressive strength, MPa	30	—	—	—
Tensile strength, MPa	2.4	—	—	—
Angle of internal friction, °	—	30	17	—

An in-situ volume of sand will be filled inside the hollow block. For sand fill inside the hollow block, linear elastic solid model is used. The material parameters of sand fill are also presented in Table 1. Interaction between sand fill and block are also considered as friction contact. The coefficient of friction between block and sand fill is 0.3.

To enhance the stability and bearing capacity of seawalls blocks, a supported-piles system is employed. In this work, however, supported-piles system is not defined in modelling. Instead, simpler boundary condition are applied at bottom of the blocks, for instance, horizontal movements are restricted and only vertical movement is allowed.

2.2 Loads Exerted on Seawall Consideration

2.2.1 Wave Pressure

Equivalent static pressure caused by sea wave is calculated based on Goda's formula for irregular waves modified to include impulsive forces from head on breaking waves and adapted to the geometry of the proposal seawall [12]. The detail of wave pressure calculating procedure is presented as follows (Fig. 4).

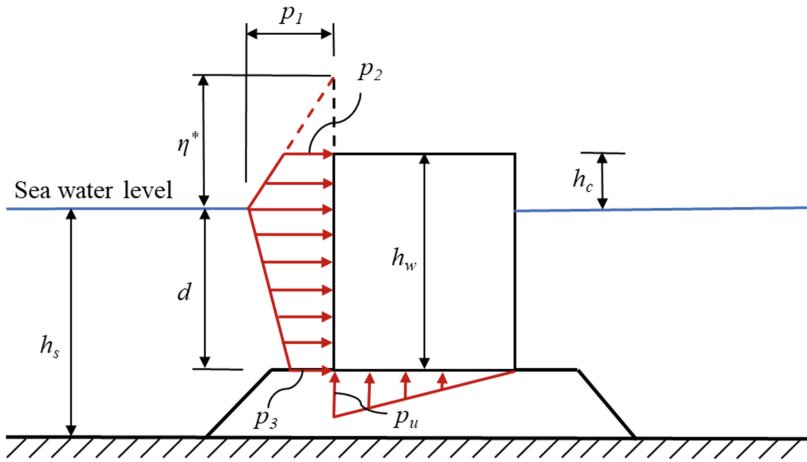


Fig. 4. Definition sketch for Goda's formula for wave induced pressure.

Pressures on front of vertical seawall at each position:

$$p_1 = 0.5(1 + \cos\beta)(\lambda_1\alpha_1 + \lambda_2\alpha^* \cos^2\beta)\rho_w g H_{design} \quad (1)$$

$$p_2 = \begin{cases} \left(1 - \frac{h_c}{\eta^*}\right)p_1 & \text{for } \eta^* > h_c \\ 0 & \text{for } \eta^* \leq h_c \end{cases} \quad (2)$$

$$p_3 = \alpha_3 p_1 \quad (3)$$

$$p_u = 0.5(1 + \cos\beta)\lambda_3\alpha_1\alpha_3\rho_w g H_{design} \quad (4)$$

where:

p_1, p_2, p_3 are wave pressure at design water level, wave/seawall crest height, and at base of seawall;

p_u is wave uplift pressure at base of seawall;

β is the angle of incidence of design waves;

H_{design} is design wave height;

η^* is wave crest height;

h_s is depth of structure toe;

h_w is overall height of structure;

h_c is height of structure above design water level;

d is water depth at toe of structure;

ρ_w is density of water;

g is gravity acceleration;

$\lambda_1, \lambda_2, \lambda_3$ are modified factor due on structure type;

$\alpha_1, \alpha_2, \alpha_3, \alpha^*$ are modified pressure coefficients.

In this work, the calculations are performed under wave action regarding to storm level 12 (highest design level) with parameters as: $H_{design} = 3.1$ m; $h_s = 4.25$ m; $\beta = 0$. The results of applied loads induced by sea wave are not shown in this paper.

2.2.2 Lateral Earth Pressure

In this study, we assume that displacement of gravity type seawall under external loads is very small, so that lateral at-rest earth pressure acting on seawall is considered. Let us consider a vertical wall retaining a backfill soil of a height H as shown in Fig. 5. The wall is not allowed to moving away or toward backfill soil. Therefore the lateral earth pressure acting on front vertical face of wall is regarded to at-rest lateral earth pressure, which can be calculated by using the following empirical equation [13]:

$$\sigma'_h = K_0 \sigma'_v \quad (5)$$

$$\sigma'_v = \gamma z \quad (6)$$

$$K_0 = 1 - \sin\varphi \quad (7)$$

where

γ is the unit weight of backfill soil,

z is the depth measured from the top surface of backfill to the toe of retaining wall,

φ is angle of internal friction of soil,

σ'_v is vertical geostatic stress,

K_0 is coefficient earth pressure at rest.

For inclined back of wall, the normal component of earth pressure is calculated as:

$$\sigma'_n = \sigma'_v (\sin^2\alpha + K_0 \cos^2\alpha) \quad (8)$$

where α is the back face inclination of wall.

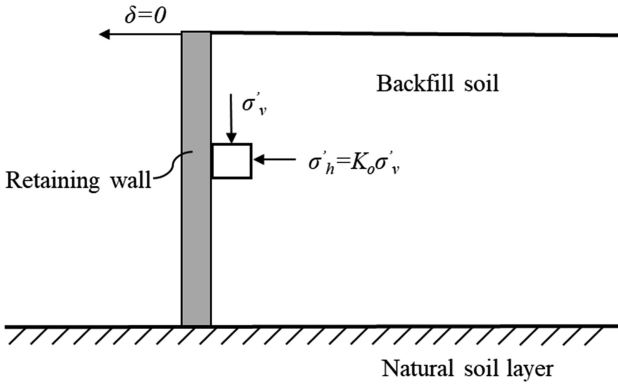


Fig. 5. At-rest earth pressure.

Figure 6 shows the schematic of seawall structure. It is seen that natural soil, backfill soil, and sand fill are below the design water level. As calculating at-rest earth pressure, buoyance unit weight of soils are used.

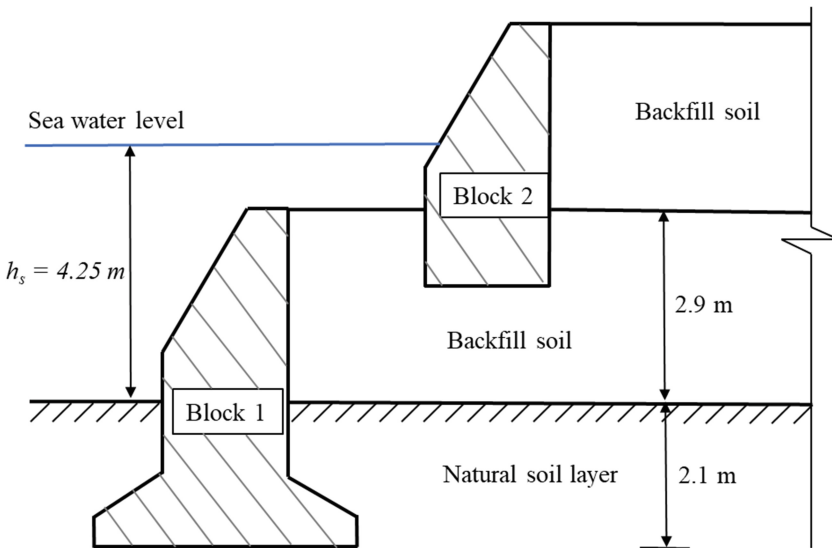


Fig. 6. Schematic of seawall structure.

2.3 Elastic Foundation

In this study, we assume that seawall blocks are placed above linear elastic soil foundation. The foundation pressures will act normal to surfaces on which they are applied. This is the easy way to define the effects of the soil under a structure, but convergence difficulties may arise with large-deformation problems.

The modulus of foundation is experimentally measured using plate load test [14] as:

$$k_z = p/S \quad (9)$$

where p is applied load on plate (force/length²); S is settlement of plate (length). In this study, the elastic foundation stiffness, k_z , is assumed to be 20000 kN/m²/m.

3 Results and Discussions

3.1 Single Block Analysis

To analyze load-bearing capacity of proposed hollow block for seawalls, a single block has been modelled. At-rest earth pressure and equivalent static wave load are applied on the front side and rear side of the block. Horizontal displacement of two remain sides of block according to x direction is restricted as shown in Fig. 7. Numerical simulation results are shown and discussed in details.

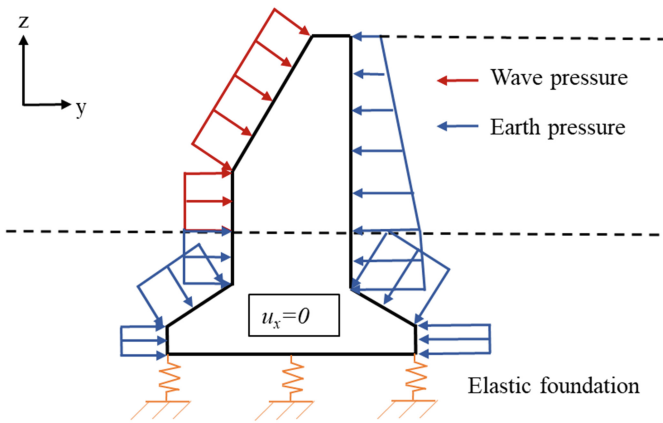


Fig. 7. Boundaries condition in case of single block analysis.

It is seen that under such loads and boundaries conditions, block tends to be bended along x axis. As a result, stress distribution is located around path-1 as shown in Fig. 8. For this reason, mesh density in this zone will be increased for improving accuracy of simulation results. Linear tetrahedral solid element is Effect of mesh density is reported in Table 2 and Fig. 9 as well.

Solid block, which means a dense block with the same outer face of hollow block and without holes inside representing for conventional designs. Empty space inside hollow block can be filled by using sand to improve mass properties. Figure 10 shows the deference between the two types of block in term of mass properties. Obviously, hollow block consumes much less concrete material than solid one.

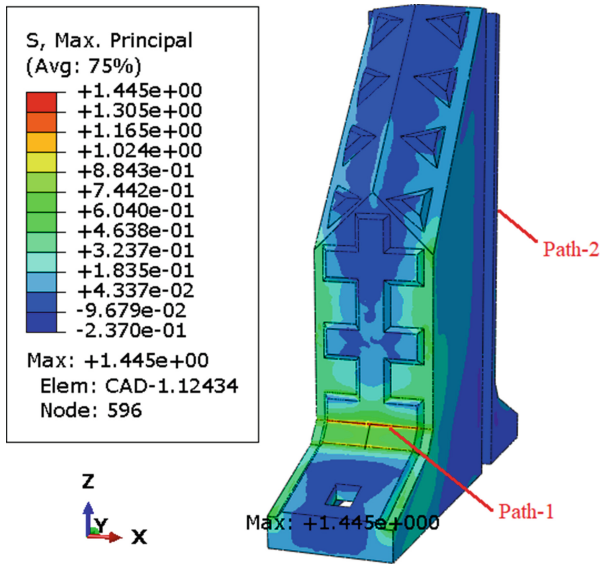


Fig. 8. Maximum principal stress distribution on single hollow block.

Table 2. Simulation results versus mesh density (at the left end-point of path-1)

Type of mesh	Number of elements	Number of nodes	Max. principal stress, MPa	% of difference
1	8635	2764	0.452	–
2	30822	8932	0.697	54.2
3	84698	20674	0.732	5.0
4	90586	46110	1.359	85.7
5	139240	56811	1.396	2.7
6	307047	92635	1.431	2.5
7	542838	139682	1.442	0.8
8	1113711	251769	1.453	0.8

Concrete is well-known as high compressive material but low tensile one. The novel block uses only concrete without reinforcement. For this reason, tensile load bearing capacity is crucial. In this simulation, maximum principal stress values will be considered to assesses tensile load bearing capacity of block.

Figure 11 shows the difference of maximum principal stress along path-1 for various type of block. It is obviously seen that values of maximum principal stresses on hollow block are much higher than ones on solid block. Maximum principal stresses, however, are still less than tensile strength of used concrete material. It is also seen that effect of sand fill to stress distribution is not significant.

Similarly, deformation of novel block is also greater than solid block as shown in Fig. 12. This figure shows the backward displacement according to y direction along

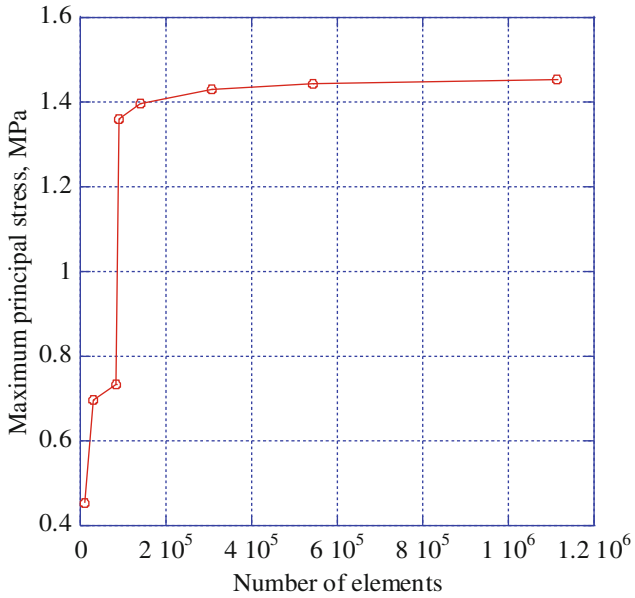


Fig. 9. Convergence of peak of principal stress at left end-point of path-1

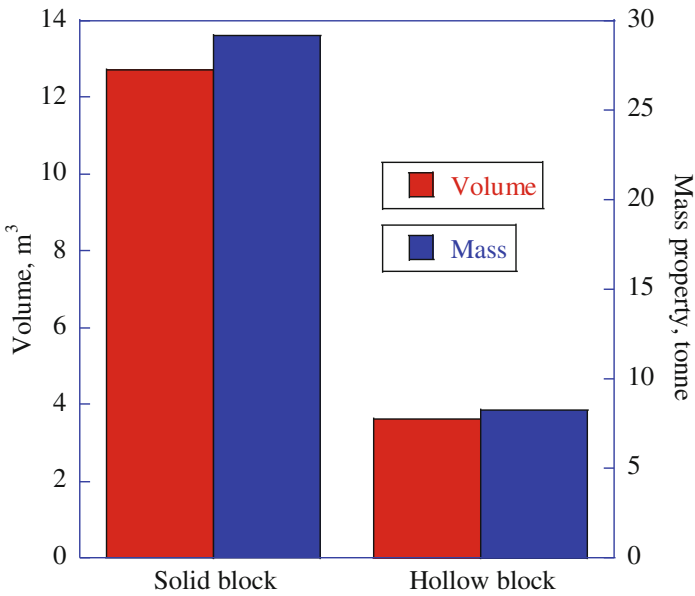


Fig. 10. Comparison of two models in term of mass properties

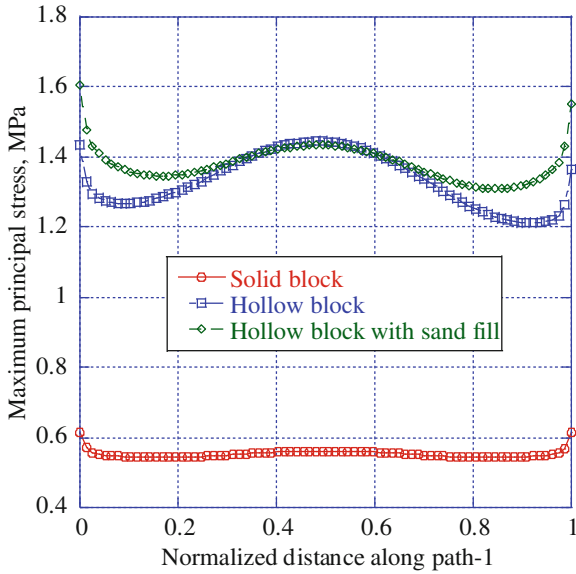


Fig. 11. Maximum principal stress along path-1 on single block.

path-2 on block. Presence of sand fill is highly affects deformation of hollow block, for instance, displacement of hollow block with sand fill and solid block is identical. However, in this simulation, sand fill is modelled as solid part, which is incorrect in practical.

3.2 Assemble Blocks Analysis

In this case, a group of three blocks is assembled for simulation as shown in Fig. 13. For similarity and reducing computational cost, sand fill inside hollow block is not considered. Contact pressures distribution for two models, e.g. solid block and hollow block model, are shown in Figs. 14 and 15, respectively.

It is seen that the contact area of the two models is very different. Due to the small deformation of solid block, contact area is distributed on large area with smaller magnitude of contact pressure. On the other hand, contact area on hollow block is nearby edges with higher magnitude of contact pressure.

Figure 16 shows the comparison between the two analysis cases, e.g. single block analysis and group of blocks analysis, in term of maximum principal stress along path-1. Stress in the middle of path-1 in case of assembled blocks analysis is slightly smaller than one in case of single block analysis.

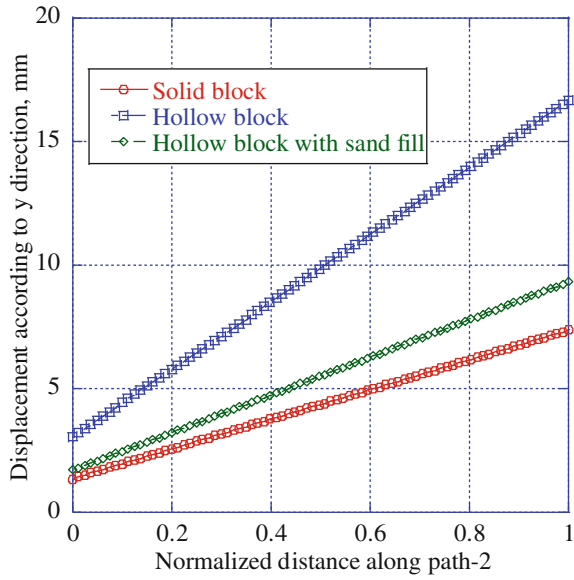


Fig. 12. Displacement according to y direction along path-2.

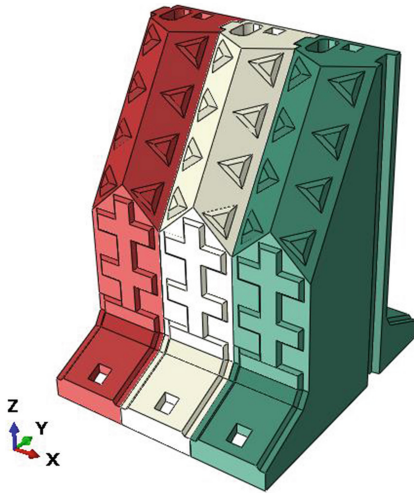


Fig. 13. Contact pressure in case of solid block.

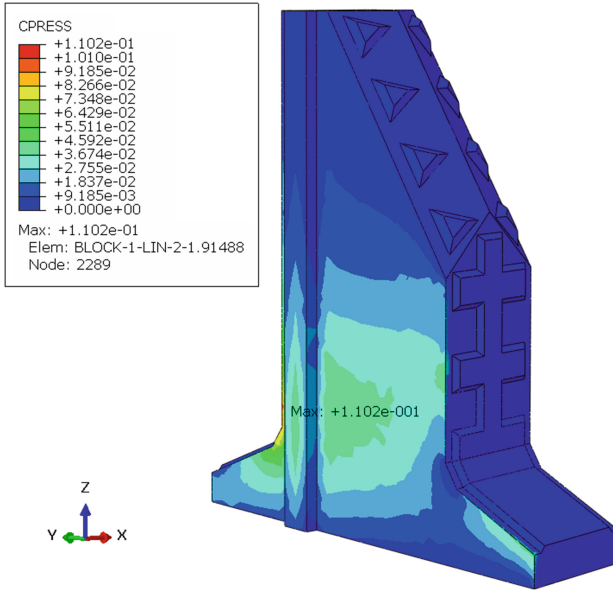


Fig. 14. Contact pressure distribution on the middle solid block

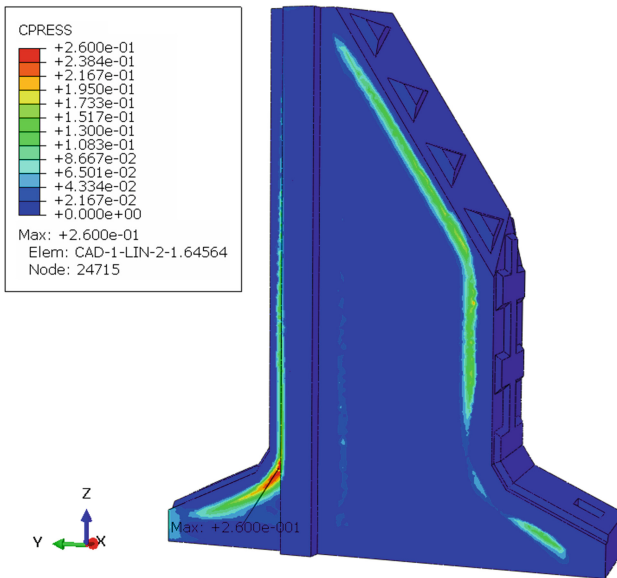


Fig. 15. Contact pressure distribution on middle hollow block

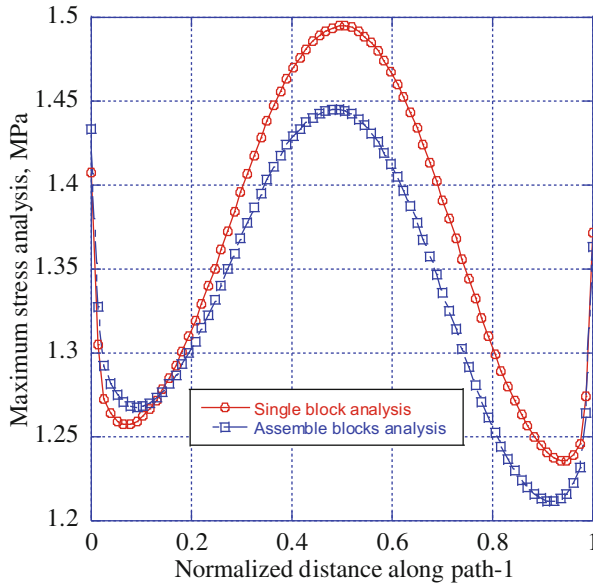


Fig. 16. Maximum principal stress along path-1 for two types of analysis

4 Conclusions

A novel design of concrete block forming seawalls has been studied using finite element method. Such thin-walled block consumes much less concrete material than the conventional one. With the appropriate geometry, however, proposed block exhibits load-bearing capacity quite well under certain load and boundaries condition. For instance, although stresses and deformation of hollow block are much greater compared to the solid block, they are still within the limit.

For future studies, there will be many problems need to be solved such as fluid-structure or soil-structure interactions, and stability of entire structure, etc. Additionally, other boundaries conditions can be applied to simulate a structure that is similar to the real application.

Acknowledgements. The authors acknowledge the financial support of VLIR-OUS TEAM Project, VN2017TEA454A103, ‘An innovative solution to protect Vietnamese coastal riverbanks from floods and erosion’, funded by the Flemish Government.



With the support of
THE BELGIAN
DEVELOPMENT COOPERATION



We would like to thank to Prof. Hung Nguyen-Dang for their helps in relevant research direction and materials. We also thank to BUSADCO for their kind cooperation.

References

1. Bengtsson, L.: The Earth's Cryosphere and Sea Level Change. Springer, New York (2012)
2. Thomas, R.S., Hall, B.: 5 - Seawall Structure—Overall Concept and Types, in Seawall Design, pp. 113–179. Butterworth-Heinemann (1992)
3. Guanache, R., Losada, I.J., Lara, J.L.: Numerical analysis of wave loads for coastal structure stability. *Coast. Eng.* **56**(5–6), 543–558 (2009)
4. Hajivalie, F., Bakhtiary, A.Y.: Numerical simulation of the interaction of a broken wave and a vertical breakwater. *Int. J. Civ. Eng.* **9**(1), 71–79 (2011)
5. Hur, D.S., Kim, C.H., Yoon, J.S.: Numerical study on the interaction among a nonlinear wave, composite breakwater and sandy seabed. *Coast. Eng.* **57**(10), 917–930 (2010)
6. Tofany, N., et al.: Numerical modeling of the hydrodynamics of standing wave and scouring in front of impermeable breakwaters with different steepnesses. *Ocean Eng.* **88**, 255–270 (2014)
7. Meringolo, D.D., Aristodemo, F., Veltri, P.: SPH numerical modeling of wave-perforated breakwater interaction. *Coast. Eng.* **101**, 48–68 (2015)
8. Didier, E., Martins, R., Neves, M.G.: Numerical and Experimental Modeling of Regular Wave Interacting with Composite Breakwater (2013)
9. Nguyen-Dang, H., Truong, P., Phan-Vu, D., Tran-Thanh, T.D., Le-Xuan, H.: Analysis of inter-locking blocks structure for coastal revetment using non-linear finite element analysis. In: National Fluid Mechanics Conference, Vietnam (2015)
10. Dassault Systèmes. ABAQUS/CAE user's manual: version 6.14
11. Ba Ria – Vung Tau Urban Sewerage and Development One Member Limited Company (BUSADCO). <http://busadco.com.vn>
12. Tanimoto, K., Takahashi, S.: Design and construction of caisson breakwaters - the Japanese experience. *Coast. Eng.* **22**(1–2), 57–77 (1994)
13. Jaky, J.: The coefficient of earth pressure at rest. *J. Soc. Hung. Archit. Eng.* **78**(22), 355–358 (1944)
14. Terzaghi, K.: Theoretical Soil Mechanics. i-xvii (2007)



Numerical Study of Heat and Moisture Transfers for Validation on Bio-Based Building Materials and Walls

T. Alioua^{1,2}, B. Agoudjil¹, and A. Boudenne²(✉)

¹ LPEA Laboratory, Batna 1 University, 05000 Batna, Algeria

² Universite Paris Est Creteil/Certes, 61 Avenue Du General De Gaulle, 94010 Creteil Cedex, France
boudenne@u-pec.fr

Abstract. In this work, we study the two most used mathematical models (Phillip & De Vries model and Kunzel's model) which describe heat and moisture transfers in porous building materials. These models were implemented in COMSOL Multiphysics and solved numerically with the finite elements method. To validate the representation of the physical phenomena made by the numerical models, results were compared with data obtained by Wufi using a concrete wall. The results indicate that values estimated by both models are relatively in good agreement with those obtained by Wufi especially for temperature, while in humidity variations an underestimation by Phillip and De Vries model was Highlighted. Consequently, results confirm the suitability of these models to be used in further studies in order to predict hygrothermal behaviors of bio-based building materials and walls under various thermal and hyric conditions at different scales.

Keywords: Mathematical models · Bio-based building materials
COMSOL · Simulation

Nomenclature

b	moisture supplement (%/%)
c_0	material specific heat at dry state (J/kgK)
c_l	liquid specific heat (J/kgK)
c_v	vapor specific heat (J/kgK)
$D_{l,\varphi}$	liquid transport coefficient under relative humidity gradient (kg/ms)
D_T	mass transport coefficient under thermal gradient (m^2/Ks)
$D_{T,v}$	vapor transport coefficient under thermal gradient (m^2/Ks)
$D_{T,l}$	liquid transport coefficient under thermal gradient (m^2/Ks)
D_w	mass transport coefficient under water content gradient (m^2/s)
$D_{w,v}$	vapor transport coefficient under water content gradient (m^2/s)
$D_{w,l}$	liquid transport coefficient under water content gradient (m^2/s)
G_Ω	vapor flux at the boundary surface (kg/m^2s)
h	convective heat transport coefficient (W/m^2K)
l_v	latent heat of vaporization (J/kg)
Q_Ω	heat flux at the boundary surface (W/m^2)

t	time (s)
T	temperature (K)
p_{sat}	vapor saturation pressure (Pa)
w	water content (kg/m^3)
β	water vapor transfer coefficient ($\text{kg}/\text{m}^2\text{sPa}$)
δ	water vapor permeability of the material (kg/msPa)
δ_a	water vapor permeability of air (kg/msPa)
ζ_φ	hygric capacity ($\text{kg}/\text{m}^3\%$)
λ	thermal conductivity (W/mK)
ρ_0	material density at dry state (kg/m^3)
ρ_l	liquid water density (kg/m^3)
φ	relative humidity (%)

Scripts

0	at dry state
amb	ambient
Ω	at boundaries

1 Introduction

The housing sector represents one of the major energy consumers, where thermal insulation and interior comfort can still be optimized. One of recent solutions that took a lot of attention is the use of new bio-based building materials. In the last decade, many experimental works were carried out to study their mechanical, thermal and hygric properties at material and wall scales [1–3]. In the same way, several models for predicting heat and mass transfers in porous building materials were developed and resolved with simulation programs such as SPARK [4], TRNSYS [5], DELPHIN [6] and Wufi. Phillip and De Vries [7] have developed a model basically for soil materials, this model took into account temperature gradients inside materials, it represents the origin of most new models, it was lately well studied and represented by Mendes *et al.* [8]. Kunzel *et al.* [9] have carried out a comprehensive parametric study of heat and mass transfers for the specific case of building materials, where his developed model was adopted by many works and gave satisfactory results [10–12]. In this work, we aim to validate Phillip & De Vries and Kunzel models by doing a confrontation against simulations performed on an already validated commercial simulation tool using a classic material, for a next work that will be dedicated to the use of these models for bio-based building materials.

2 Mathematical Models

2.1 Formulation of the Problem

Heat and moisture transfer models are developed starting from the concept of physical properties conservation. In porous media, it is familiar to adopt a number of assumptions such as considering the material to be isotropic. The material is in thermodynamic equilibrium with water and air which is considered as a mix of ideal gases. Moreover, radiative heat transfers and chemical reactions are neglected inside the material.

Based on these hypotheses, the final 1D equations system for Phillip and De Vries model is written as follows [8]:

$$\frac{\partial w}{\partial t} = \nabla(D_w \nabla w + D_T \nabla T) \quad (1)$$

$$(\rho_0 c_0 + c_l w) \frac{dT}{dt} = \nabla(\lambda \nabla T) + l_v \nabla(D_{w,v} \nabla w + D_T \nabla T) \quad (2)$$

Where driving potential are water content and temperature. Mass transport coefficients are expressed as follows (liquid transport under temperature gradient is usually neglected for this model [13]):

$$D_w = D_{w,v} + D_{w,l} = \delta P_{sat} \frac{d\varphi}{dw} = \frac{\delta P_{sat}}{\xi_\varphi} \quad (3)$$

$$D_T = D_{T,v} + D_{T,l} \approx D_{T,v} = \frac{\delta\varphi}{\rho_l} \frac{dP_{sat}}{dT} \quad (4)$$

In order to respect units, equations Eqs. (1, 2) were divided by ρ_l since water content used here is expressed in (kg/m^3).

Kunzel's model uses relative humidity instead of water content as a moisture driving potential, justifying this choice by the continuity of relative humidity at boundaries. Based on the same hypotheses, the 1D heat and mass conservation equations of this model are written as follows [9]:

$$\xi_\varphi \frac{d\varphi}{dt} = \nabla(\delta \nabla p_{sat} \varphi + D_{l,\varphi} \nabla \varphi) \quad (5)$$

$$(\rho_0 c_0 + c_l w) \frac{dT}{dt} = \nabla(\lambda \nabla T) - l_v \nabla(\delta \nabla p_{sat}) \quad (6)$$

2.2 Boundary Conditions

Boundary conditions considered in this study are the case of heat and mass fluxes at boundaries without taking into account other parameters (*i.e.* rain, radiation...).

Where heat and mass transport terms for each model are set equal to the following heat and mass fluxes respectively [9]:

$$Q_{\Omega} = h(T_{\Omega} - T_{amb}) \quad (7)$$

$$G_{\Omega} = \beta(P_{v,\Omega} - P_{v,amb}) \quad (8)$$

Where water vapor transfer coefficient is defined as:

$$\beta = 7.10^{-9}.h \quad (9)$$

3 Material Properties

In order to validate models for bio-based materials, a first validation is made against a known material which is concrete, chosen from Wufi data base. The concrete properties are highlighted in Table 1.

Table 1. Concrete properties

Property	Value
Dry density [kg/m ³]	2200
Porosity [m ³ /m ³]	0.18
Dry specific heat [J/kgK]	850
Moisture supplement of thermal conductivity [%/‰]	8
Vapor resistance factor [-]	92
Dry thermal conductivity at 10 °C [W/mK]	1.6

Where vapor resistance factor is equal to:

$$\mu = \frac{\delta}{\delta_a} \quad (10)$$

The thermal conductivity has been considered as a function of water content using the following expression [9]:

$$\lambda(w) = \lambda_0 \left(1 + b \cdot \frac{w}{\rho_0} \right) \quad (11)$$

Sorption curve describes the evolution of water content in the material when it reaches equilibrium state with the ambience at different values of relative humidity (Fig. 1), it was obtained for the studied concrete at ambient temperature (23 °C).

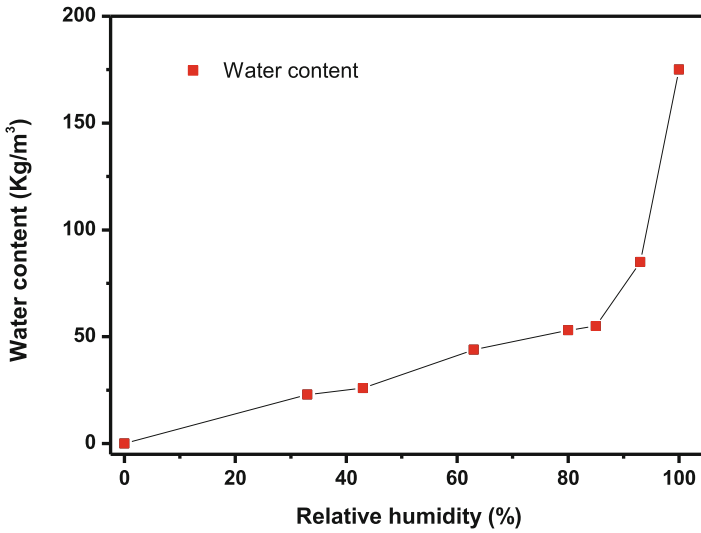


Fig. 1. Sorption isotherm of concrete

4 Numerical Resolution and Validation

4.1 Simulation Conditions

The two models, as well as the previously presented properties, were implemented in COMSOL Multiphysics, a powerful simulation tool and accurate equation systems solver using the finite elements method.

In order to verify the accuracy of our implementation and preform a first validation of the models, they were compared with simulation results obtained by Wufi, a simulation software for buildings based on Kunzel's model. This software was already validated against experimental data by the manufacturer and other works [14, 15].

A 15 cm thick wall was studied, where boundary conditions are set corresponding to Fig. 2 as follows:

- Left surface: heat and mass exchange with the outside
- Surfaces at the top and the bottom: thermal and mass insulation (zero fluxes)
- Right surface: constant ambient values of temperature and relative humidity.

Initial values were set as follows: $T = 23 \text{ }^\circ\text{C}$, $\varphi = 50\%$ (that corresponds to a water content value of $w_0 = 32.3 \text{ kg/m}^3$).

Two scenarios were applied to the left surface (exterior ambience) keeping the right side (interior ambience) fixed and unchanged in temperature and relative humidity

- Scenario one: temperature step from $23 \text{ }^\circ\text{C}$ to $40 \text{ }^\circ\text{C}$
- Scenario two: humidity step from 50% to 70% .

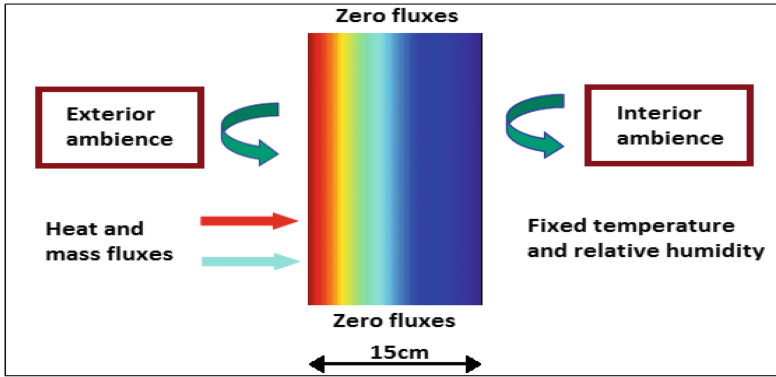


Fig. 2. Boundary conditions

4.2 Results

Figure 3 shows temperature variations as a function of time for three different depths (4.5, 8 and 11 cm from the external surface respectively) for a thermal excitation ranging from 23 °C to 42 °C. It is clearly seen that the temperature variations became stable after about $t = 1 \times 10^5$ s and reach 34.7 °C, 33.4 °C and 32.3 °C for depths 4.5, 8 and 11 cm respectively. As it can be also seen, good agreement was found whatever was the depth, which confirms the validity of using COMSOL with the Phillip & De Vries and Kunzel model to predict thermal behavior of walls.

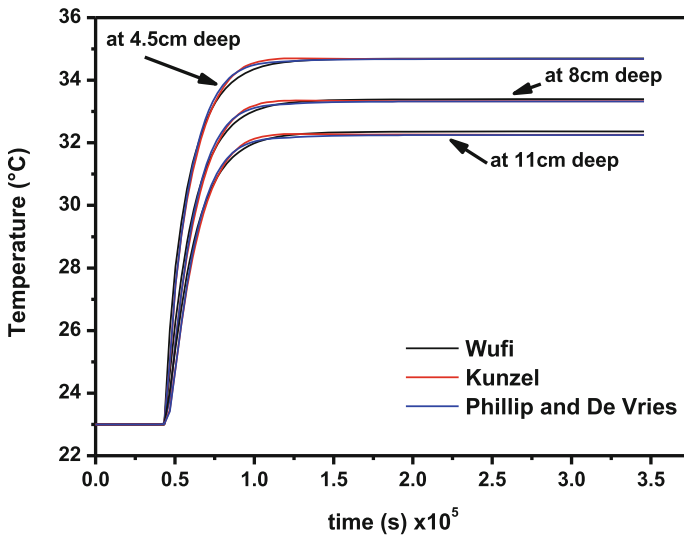


Fig. 3. Temperature variation in the wall at different depths

Figure 4 shows relative humidity variations as a function of time predicted by both models and Wufi for a humidity excitation range from 50% to 70%. Unlike to the temperature behavior, relative humidity variations take quite more long time to reach the steady state and especially the deeper points of the wall. For this reason, only the two points close to the external surface were considered. We notice a relatively close behavior of relative humidity variations in the wall between Kunzel's model and Wufi the several deeps. These variations reach about 63% at 0.5 cm deep and 54% at 1.5 cm deep. This is not the case for the Phillip and De Vries model that underestimates relative humidity variations compared with both Kunzel's model and Wufi. In fact, the values obtained by Phillip and De Vries model only indicate 58% and 50.5% of relative humidity at 0.5 cm and 1.5 cm deep of the wall respectively. This difference is probably related to the mass transfer coefficients since each model defines them differently.

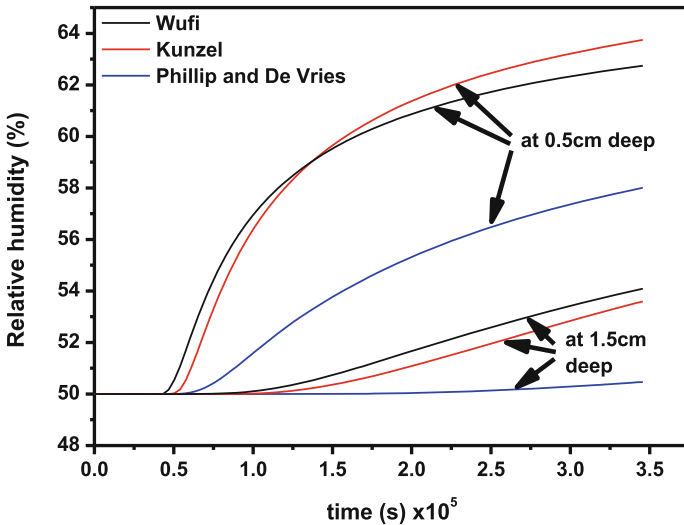


Fig. 4. Relative humidity variation in the wall at two depths

5 Conclusion

To validate hygrothermal mathematical models for walls based on porous building materials, a comparative study, of both thermal and hygric behaviors, has been carried out between the two most used mathematical models and a commercial building simulation software (Wufi). Heat and mass conservation equations were presented for each model as well as boundary conditions and properties of a known material listed in Wufi database. Equations systems implemented in COMSOL, were solved with the finite elements method and results were compared with temperature and humidity variations obtained by Wufi for the same conditions. Results gave a good agreement between COMSOL and Wufi especially for thermal transport, while it was noticed that

Phillip and De Vries model gives underestimations reaching a maximum of about 6% in relative humidity compared with Kunzel's model and Wufi. Consequently, in our future work, COMSOL with one of these models can be an efficient tool for studies on the hygrothermal performance of bio-based building materials, attention should be paid to moisture transfer, for the highlighted differences, which needs further comparisons with experimental data.

Acknowledgements. This research was conducted with financial support of PHC TASSILI Project 16MDU976.

References

1. Rahim, M., Douzane, O., Le, A.T., Promis, G., Laidoudi, B., Crigny, A., Langlet, T.: Characterization of flax lime and hemp lime concretes: Hygric properties and moisture buffer capacity. *Energy Build.* **88**, 91–99 (2015)
2. Haba, B., Agoudjil, B., Boudenne, A., Benzarti, K.: Hygric properties and thermal conductivity of a new insulation material for building based on date palm concrete. *Construct. Build. Mater.* **154**, 963–971 (2017)
3. Colinart, T., Lelièvre, D., Glouannec, P.: Experimental and numerical analysis of the transient hygrothermal behavior of multilayered hemp concrete wall. *Energy and Build.* **112**, 1–11 (2016)
4. Maalouf, C., Le, A.T., Umurigirwa, S.B., Lachi, M., Douzane, O.: Study of hygrothermal behaviour of a hemp concrete building envelope under summer conditions in France. *Energy Build.* **77**, 48–57 (2014)
5. Steeman, M., De Paepe, M., Janssens, A.: Impact of whole-building hygrothermal modelling on the assessment of indoor climate in a library building. *Build. Environ.* **45**(7), 1641–1652 (2010)
6. Tijskens, A., Janssen, H., Roels, S.: A simplified dynamic zone model for a probabilistic assessment of hygrothermal risks in building components. *Energy Procedia* **132**, 717–722 (2017)
7. Philip, J.R.: Evaporation, and moisture and heat fields in the soil. *J. Meteorol.* **14**(4), 354–366 (1957)
8. Mendes, N., Ridley, I., Lamberts, R., Philippi, P. C., Budag, K.: UMIDUS: a PC program for the prediction of heat and moisture transfer in porous building elements. In: *Building Simulation Conference–IBPSA*, vol. 99, pp. 277–283, September 1999
9. Kunzel, H.M.: *Simultaneous Heat and Moisture Transport in Building components: One- and Two-Dimensional Calculation Using Simple Parameters*. IRB-Verlag, Stuttgart (1995)
10. Bart, M., Moissette, S., Ait Oumeziane, Y., Lanos, C.: Transient hygrothermal modelling of coated hemp-concrete walls. *Eur. J. Environ. Civ. Eng.* **18**(8), 927–944 (2014)
11. Piot, A., Béjat, T., Jay, A., Bessette, L., Wurtz, E., Barnes-Davin, L.: Study of a hempcrete wall exposed to outdoor climate: Effects of the coating. *Constr. Build. Mater.* **139**, 540–550 (2017)
12. Evrard, A.: *Transient hygrothermal behaviour of lime-hemp materials*. Ph.D., Université Catholique De Louvain (2008)

13. Mendes, N., Winkelmann, F.C., Lamberts, R., Philippi, P.C.: Moisture effects on conduction loads. *Energy Build.* **35**(7), 631–644 (2003)
14. Künzel, H.M., Zirkelbach, D., Sedlbauer, K.: Predicting indoor temperature and humidity conditions including hygrothermal interactions with the building envelope. In: Proceedings of 1st International Conference on Sustainable Energy and Green Architecture, October, 2003
15. Hall, M.R., Allinson, D.: Transient numerical and physical modelling of temperature profile evolution in stabilised rammed earth walls. *Appl. Therm. Eng.* **30**(5), 433–441 (2010)



Modelling Load-Transmission Mechanisms in Axially Loaded RC Columns Retrofitted with Steel Jackets

Giovanni Minafò¹(✉), Alfio Francesco Siciliano²,
and Marinella Fossetti²

¹ Dipartimento di Ingegneria Civile, Ambientale, Aerospaziale,
dei Materiali DICAM, Università degli Studi di Palermo, Scuola Politecnica,
Viale delle Scienze Ed.8, 90128 Palermo, Italy

giovanni.minafo@unipa.it

² Università degli Studi di Enna “Kore”, Facoltà di Ingegneria e Architettura,
Cittadella Universitaria, 92100 Enna, Italy

Abstract. The use of steel jacketing technique is a common practice for retrofitting existing reinforced concrete (RC) columns, as it allows increasing load-carrying capacity and ductility of the member. When the external jacket has no end connections – i.e. the jacket is indirectly loaded- the load sustained by the column is transferred from the inner RC core to the external jacket through shear stresses along the contact surface. The assessment of this mechanism is quite complex, due to the marked non-linear behaviour of constituent materials and to the calibration of a proper shear stress-relative slip constitutive law of the concrete-to-steel interface.

In this paper, a step-by-step analytical approach is proposed to assess the load transfer mechanisms in steel jacketed RC columns loaded in compression. The model is able to predict slip and shear stresses along the core-to-jacket contact interface and then the load-carrying capacity of strengthened members. Shear stress-slip constitutive law on the interface is initially assumed linear and a suitable stress-strain constitutive model of confined concrete is considered. Yielding of steel angles is also taken into account into the process by assuming a bilinear law with strain hardening. The progressive damage of concrete is also considered by dividing the examined member in portions and splitting governing equations. Finally, comparisons are performed in order to validate the proposed procedure against experimental results available in the literature, showing good agreement.

Keywords: Steel jacketing · Interface · Indirectly loaded · Compression

1 Introduction

The adoption of external steel angles and battens for caging existing reinforced concrete (RC) columns is a widespread technique in engineering retrofitting applications. Structural performances of weak members are improved aiming to satisfy current safety requirements in terms of required load carrying capacity, ductility and stiffness. Steel

jackets are usually installed with two possible configurations: directly or indirectly loaded jacket [1], depending on the connection ensured between the external jacket and the slabs, and as a consequence on the different force transmission mechanisms that is activated. When the jacket is considered directly loaded, axial load is transferred to the external jacket through connections with slabs. In this way, the complete axial capacity can be fully exploited and the contribution of the steel angles to the capacity is directly related to their effective area. Consequently, from a design point of view, it should be the most convenient method for a retrofit intervention but however, constructive details of connections are difficult to be warranted and for this reason, most of technical codes allows the installation of the jacket only by indirect loading. In this last case, the steel angles has no-end connections, and a gap of few centimetres is left between the jacket and the top and bottom extremities of the column. The axial load acting on the column is then transferred to the jacket through shear stresses, which develop at the interface between the concrete surface and the steel of angles. This portion of axial load is not simple to be due to the involvement of several parameters, such as the geometry, the non linear constitutive laws of materials and interface and load conditions of the pillar. For these reasons, technical standards indicate to assess the efficiency of the technique only by considering confinement effects induced by the external jacket to the inner column [2], and consequently the contribution of jacket is neglected [3].

Several research works in the literature studied the structural efficiency of external RC or steel jackets, and the most investigated the case of jackets with pinned ends [4–6]. Differently, fewer studies are available on the case of indirectly loaded jackets.

With reference to steel jacketing, Adam et al. (2009) [7] presented a parametric study performed by non-linear finite element (FE) analysis, the latter carried out with the aim of analyzing the behaviour of RC columns strengthened by steel caging. Researchers modelled force transmission at steel-to-concrete interface via contact elements with Coulomb's friction and validated their models with experimental data of Gimenez et al. (2009) [8].

Badalamenti et al. (2010) [9] proposed an analytical model able to take into account the variation of confinement pressure as a function of the axial shortening. In this model, relative slip of the steel jacket is taken into account by limiting the confinement pressure to a maximum value, which depends by the friction coefficient. Belal et al. (2014) [10] tested seven RC columns with different steel jacket's configurations. Specimens were retrofitted with angles, channels or plates and they were indirectly loaded. Researchers found increases of the axial strength up to 20%, but their FE simulations overestimated the load-carrying capacity of jacketed specimens up to 58% of the experimentally recorded data.

A recent experimental study on the compressive behaviour of RC columns with indirectly loaded jackets was performed by Campione et al. (2017) [11]. Two series of RC columns with different concrete grade and retrofitted by steel jackets with no-end connections applied by mortar were tested under axial or eccentric compression. Tests have shown that the behaviour of retrofitted columns in terms of axial load vs. shortening curve was intermediate between the analytical prediction under the assumptions of only confinement and that of overall contribution of the external jacket. Based on obtained results, a fictitious constitutive law of the angles in compression was proposed, in which peak stress was calculated by considering the maximum load

transferred at interface under the assumption of Mohr-Coulomb friction model. Similarly, strain corresponding to peak stress of steel angles was set arbitrarily equal to strain corresponding to peak stress of concrete in compression.

Literature review highlights that mechanical-based analytical investigations are still missing in this field, and all previous studies proposed some analytical models based on simplified or empirical assumptions, or on more complex numerical solutions. In this work, the problem is investigated through an analytical model, which idealized the interaction of three plane elements connected by a non-linear interface. Closed form solution of the model is given under the assumption of elastic behaviour of constituent materials, allowing to make some considerations for low levels of axial shortening. Finally, a simplified version is proposed for RC members, accounting for the non-linear behaviour of concrete, by a piece-wise subdivision of the member in small portions, and considering a proper constitutive law of the concrete core and steel jacket in compression. Results achieved by proposed model are then compared with experimental data available in the literature, showing good agreement.

2 Elastic Analysis

The current case study refers to a model of column subjected to an uniform distribution of axial shortening δ , with an indirectly loaded jacket placed adjacently at the sides (Fig. 1). Assumptions are plane model and defined by two axes of symmetry, in which the half-length of the column is denoted as “ l ”. The column -layer c - is assumed to be made with a different material from the jacket (layer j), and the two layers are connected each other with an interface, which properties are defined in the following.

In this section, materials are assumed to behave linearly in compression with an indefinite strength limit, while moduli of elasticity are labelled as E_c and E_j for core and jacket respectively. Force is transferred between the two layers by means of an interface, the latter assumed to transfer only shear stresses τ on the basis of relative slip s between core and jacket. The constitutive law of the interface defines a relationship between τ and s , and it is here assumed as linear elastic with stiffness equal to K_t .

The differential form of equilibrium equation along x -axis of layer j is therefore written as

$$\frac{dN_j(x)}{dx} = p_x(x) \quad (1)$$

where $p_x(x)$ represents the distribution of shear forces transferred through the interface and N_j is the axial force in the jacket. As it is well-known, internal congruence allows relating normal strain ε to axial displacement u_j , and considering the hypothesis of linear elasticity, it can be written in the form

$$\varepsilon_j(x) = \frac{du_j(x)}{dx} = \frac{N_j(x)}{E_j \cdot A_j} \quad (2)$$

where A_j is the transverse area of the jacket.

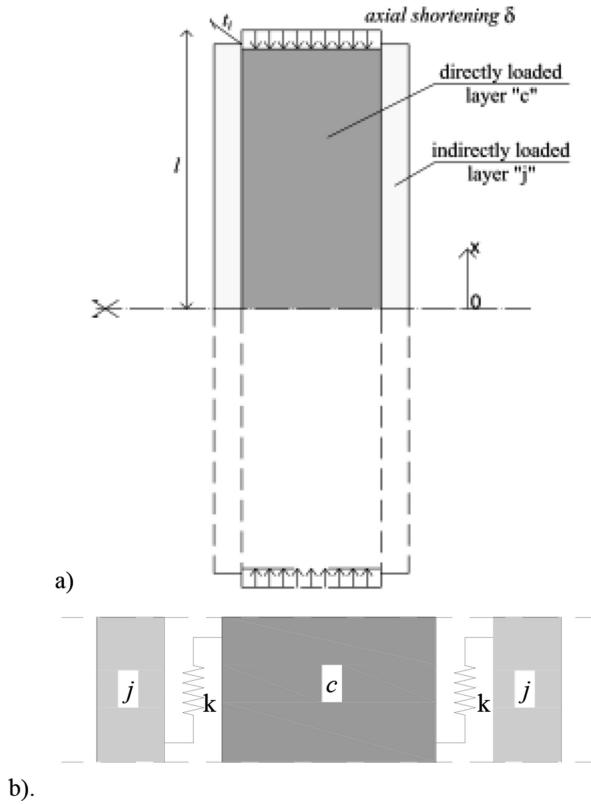


Fig. 1. Proposed model. (a) geometry; (b) interface scheme.

First order derivative of Eq. (2) and its introduction in Eq. (1) allows to write the following relationship

$$\frac{d^2 u_j(x)}{dx^2} = \frac{p_x(x)}{E_j \cdot A_j} \quad (3)$$

being E_j and A_j assumed to be constant along the column.

In general, shear forces along the interface are written as a function of relative slip between the two layers

$$p_x(x) = f(u_c(x) - u_j(x)) \quad (4)$$

And for the above mentioned hypothesis of linear pure brittle constitutive law of the interface, Eq. (4) is written as

$$p_x(x) = k_{tt} \cdot (u_c(x) - u_j(x)) \cdot t_i \quad (5)$$

where t_i is the thickness of the interface and k_{tt} is the interface stiffness.

The first governing equation is therefore obtained by substituting $p_x(x)$ expressed by Eq. (5) in Eq. (3)

$$\frac{d^2 u_j(x)}{dx^2} = -\frac{k_{tt}}{E_j \cdot A_j} \cdot (u_c(x) - u_j(x)) \cdot t_i \quad (6)$$

Similarly, equilibrium equation of the “c” layer can be easily written in the form

$$\frac{dN_c(x)}{dx} = -2 \cdot p_x(x) \quad (7)$$

And with the same substitutions performed for layer “j”, the second governing equation is written as it follows

$$\frac{d^2 u_c(x)}{dx^2} = \frac{2 \cdot k_{tt}}{E_j \cdot A_j} \cdot (u_c(x) - u_j(x)) \cdot t_i \quad (8)$$

Equations (6) and (8) represent a coupled system of two second order differential equations, governing the axial force transmission in an axially loaded column connected to an external jacket. This system can be rewritten by considering the following parameters

$$\begin{aligned} \beta_j &= \sqrt{\frac{k_{tt} \cdot t_i}{E_j \cdot A_j}} \\ \beta_c &= \sqrt{\frac{k_{tt} \cdot t_i}{E_c \cdot A_c}} \end{aligned} \quad (9a, b)$$

β_j and β_c represent the non-dimensional relative stiffness parameters between interface and jacket or core respectively, and they allow to rewrite Eqs. (6) and (8) as it follows

$$\begin{cases} \frac{d^2 u_j(x)}{dx^2} + \beta_j^2 \cdot (u_c(x) - u_j(x)) = 0 \\ \frac{d^2 u_c(x)}{dx^2} - 2\beta_c^2 \cdot (u_c(x) - u_j(x)) = 0 \end{cases} \quad (10a, b)$$

System (10a,b) can be usefully uncoupled for simplifying its solution. $u_c(x)$ can be expressed by Eq. (10a,b)

$$u_c(x) = u_j(x) - \frac{1}{\beta_j^2} \frac{d^2 u_j(x)}{dx^2} \quad (11)$$

which second order derivative is

$$\frac{d^2 u_c(x)}{dx^2} = \frac{d^2 u_j(x)}{dx^2} - \frac{1}{\beta_j^2} \frac{d^4 u_j(x)}{dx^4} \quad (12)$$

Therefore, Eq. (12) can be introduced in Eq. (10a,b) and the uncoupled form of system (10) is finally obtained by multiplying both sides for β_j^2 .

$$\frac{d^4 u_j(x)}{dx^4} - \beta_j^2 \cdot \frac{d^2 u_j(x)}{dx^2} \left(1 + 2 \frac{\beta_c^2}{\beta_j^2} \right) = 0 \quad (13)$$

Equation (13) rules the force transmission in the elastic system of a column with an external layer connected by an elastic interface. Involved parameters are related to the axial stiffness of column and jacket and to the shear stiffness of the interface. It is worth to note that when the interface is deformable ($\beta_j = \beta_c = 0$), Eq. (13) represents the classic governing equations of axial shortenings in an elastic axially loaded column.

The solution of this homogeneous fourth-order differential equation is written in the form

$$u_j(x) = c_1 \cdot \frac{e^{x\sqrt{2\beta_c^2 + \beta_j^2}}}{2\beta_c^2 + \beta_j^2} + c_2 \cdot \frac{e^{-x\sqrt{2\beta_c^2 + \beta_j^2}}}{2\beta_c^2 + \beta_j^2} + c_3 \cdot x + c_4 \quad (14)$$

where c_1 , c_2 , c_3 and c_4 are the unknown constants to be calculated on the basis of boundary conditions. It is observed that the function which describes the trend of axial shortening in the indirectly loaded jacket is a combination of exponential functions, amplified by the axial shortening δ of the core.

In order to solve the Cauchy problem, two compatibility conditions can be imposed with reference to the symmetry axis of the model ($x = 0$)

$$u_j(0) = 0 \quad (15a)$$

$$u_c(0) = \frac{d^2 u_j(x)}{dx^2} \Big|_{x=0} = 0 \quad (15b)$$

Similarly, compatibility equation at the top ($x = 1$) of the loaded layer provides:

$$u_c(1) = -\frac{1}{\beta_j^2} \frac{d^2 u_j(x)}{dx^2} \Big|_{x=1} = \delta \quad (15c)$$

Finally, equilibrium of the jacket is enforced in $x = 1$

$$N_j(1) = \frac{du_j(x)}{dx} \Big|_{x=1} = 0 \quad (15d)$$

Equation (15d) represent the system of equations to be solved for obtaining constants of Eq. (14) and solving the elastic problem. From the resolution of this system, expressions of constants can be found, and the expression of $u_j(x)$ holds

$$u_j(x) = \frac{\delta \cdot \beta_j^2 (x \cdot \eta \cdot \text{Cosh}(\eta l) - \text{Sinh}(\eta x))}{\beta_j^2 \cdot \eta l \cdot \text{Cosh}(\eta l) + 2\beta_c^2 \cdot \text{Sinh}(\eta l)} \quad (16)$$

where $\eta = \sqrt{2\beta_c^2 + \beta_j^2}$

Clearly, once that function $u_j(x)$ is calculated by Eqs. (14) and (16), the trend of axial shortening in the core $u_c(x)$ is evaluated by means of Eq. 11, leading to the following expression

$$u_c(x) = \frac{\delta \cdot (x \cdot \beta_j^2 \cdot \eta \cdot \text{Cosh}(\eta l) + 2\beta_c^2 \cdot \text{Sinh}(\eta x))}{\beta_j^2 \cdot \eta l \cdot \text{Cosh}(\eta l) + 2\beta_c^2 \cdot \text{Sinh}(\eta l)} \quad (17)$$

Finally, axial forces in each layer are evaluated by first order derivative of $u_c(x)$ and $u_j(x)$.

$$N_j(x) = E_j A_j \frac{\delta \cdot \beta_j^2 \eta \cdot (\text{Cosh}(\eta l) - \text{Cosh}(\eta x))}{l \cdot \beta_j^2 \eta \cdot \text{Cosh}(\eta l) + 2\beta_c^2 \cdot \text{Sinh}(\eta l)} \quad (18)$$

$$N_c(x) = E_c A_c \frac{\delta \cdot \eta \cdot (\beta_j^2 \cdot \text{Cosh}(\eta l) + 2\beta_c^2 \cdot \text{Cosh}(\eta x))}{l \cdot \beta_j^2 \eta \cdot \text{Cosh}(\eta l) + 2\beta_c^2 \cdot \text{Sinh}(\eta l)} \quad (19)$$

It is worth to observe that when $\beta_j \rightarrow 0$ (e.g. $K_{tt} = 0$), the axial force in the jacket is equal to zero, while that in the core approaches the constant value, valid for an elastic column with uniform section along its height and subjected to an axial shortening.

Figure 2 shows the results of the elastic analysis for $\beta_j = 0.00122474$ and $\beta_c = 0.00141421$, and assuming a normalised axial shortening equal to $\delta/l = 0.00001$. In particular, Fig. 2a plots the trend of the axial force in both layers as a function of the normalised abscissa x/l . It is observed as the application of an external jacket modifies the trend of the axial force, being the latter not constant along the member. $N_c(x)$ reaches its maximum value at the member extremities, while that in the jacket $N_j(x)$ is maximum at the middle. This is due to the absence of relative slippage for $x = 0$, which means that the two layers are rigidly connected in the middle section. The increase of relative slippage at the interface $s(x) = u_c(x) - u_j(x)$ (Fig. 2b) tends to unload the external jacket, up to the extremity sections, in which the jacket is totally unloaded and the force is sustained only by the core.

The trend of functions plotted in Fig. 2 respects the symmetry conditions of the model, being axial forces symmetric and slippage anti-symmetric. It is worth to observe as the trend of relative slippage is quasi-linear up to $x/l = \pm 0.5$, and over this point relative slip tends to be amplified up to its maximum value recorded for $x/l = \pm 1$. Obviously, due the assumption of linear elastic behaviour of the interface expressed by Eq. (5), shear stresses (Fig. 2c) tend to follow the trend of relative slip, and intensification in the range $0.5 < x/l < 1$ – or $-1 < x/l < -0.5$ for symmetry- is observed.

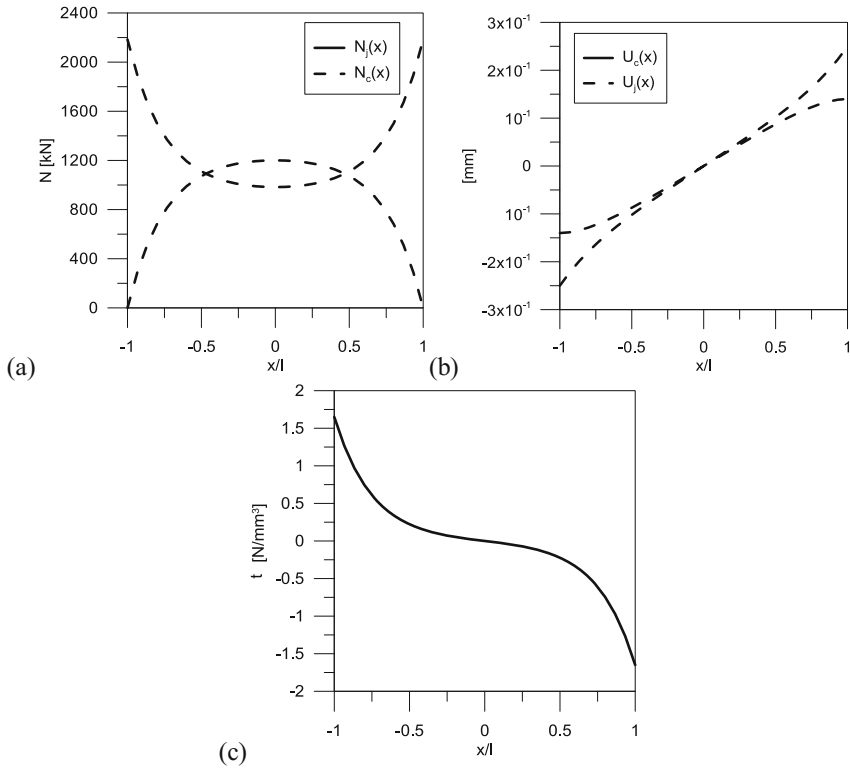


Fig. 2. Elastic solution. (a) Trend of axial force; (b) shortenings and relative slip at interface; (c) shear forces along the interface

This fact means that the most stressed parts of interface are those located at about one-fourth of the total length from the extremities of the column.

Figure 3 shows the trend of the maximum slippage $s_{\max} = u_c(l) - u_j(l)$ as a function of relative stiffness parameters β_c and β_j . Its value is normalised with respect to δ in order to obtain a non-dimensional representation. It is observed that s_{\max} is a non-linear function of β_j while it tends to be constant with β_c . This result highlights the fact that relative stiffness interface/racket is a key parameter. Therefore, aiming to minimize the maximum slippage, the requested shear stiffness of interface should increase as stiffer jacket are disposed. Obviously, when $\beta_j \rightarrow 0$, i.e. the stiffness of the interface is equal to zero or the axial stiffness of the jacket is very high, maximum slippage is equal to the imposed axial shortening of the core, which means that no force transmission occurs and the load is sustained only by the core.

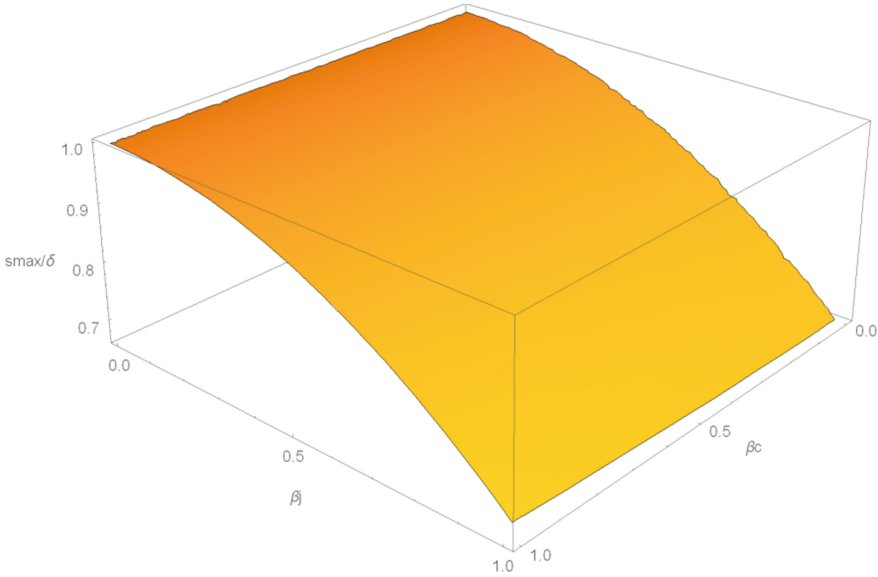


Fig. 3. Normalized maximum slip s_{\max}/δ as a function of β_j and β_c .

3 Application to RC Members: Assumptions and Constitutive Relationships

Aiming to extend the previously described model to RC columns, some assumptions are here made. In particular, the lateral expansion of the core is neglected and bending effect on the jacket is assumed to be negligible. Additionally, slippage between core and jacket is assumed to be zero in perpendicular direction to interface, which means that the interface is assumed to be rigid orthogonally to its plane.

Concerning the material's behaviour, it is well-known that an RC column is subjected to damage during a compressive loading process and consequently its behaviour is described by a non-linear constitutive law in compression. Hence, the linear elastic solution described previously cannot be applied, but it should consider the variation of the internal stiffness parameters. Therefore, in order to take into account the non-uniformity of concrete behaviour along the member, the previous geometric model is divided in "n" portions with equal length " Δ " (Fig. 4). Elastic modulus of constituent materials E_{ci} , E_{ji} and shear stiffness of the interface k_{ti} are assumed to be constant within each segment "i".

The elastic perfectly plastic law adopted for internal reinforcement, transverse and longitudinal rebars, is defined by means a yielding stress $f_{y,i}$, a Young's modulus $E_{s,i}$ and by ultimate axial strain $\varepsilon_{su,i}$. Instead, the constitutive law of the steel angles and battens is assumed to be plastic with linear hardening. The latter is characterized by a yielding stress $f_{y,e}$, Young's modulus $E_{s,e}$, ultimate axial strain $\varepsilon_{su,e}$ and hardening modulus E_{sh} .

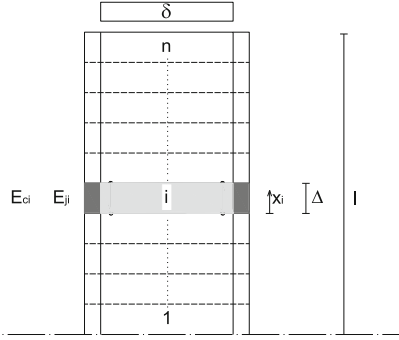


Fig. 4. Column subdivided in layers

The RC core, strengthened by steel angles and battens, is modelled through the confinement model proposed by Montuori and Piluso (2009) [4]. In this model, the volumetric ratio of steel battens and stirrups in the perpendicular directions of the cross section, ρ_x and ρ_y , are calculated as follows:

$$\rho_x = \frac{n_x A_{s,x} (b - 2c)}{s_s (b - 2c) (h - 2c)} + \frac{2A_{b,e} b}{s_b b h} \quad (20)$$

$$\rho_y = \frac{n_y A_{s,y} (h - 2c)}{s_s (b - 2c) (h - 2c)} + \frac{2A_{b,e} h}{s_b b h}$$

where $A_{s,x}$ and $A_{s,y}$ are the cross sections area of a stirrup arm in x and y directions; n_x and n_y are the respective numbers; b and h are the size of the cross section in x and y directions; s_s and s_b are the spacing of the stirrups and battens respectively; c is the size of the concrete cove and A_b is the cross section area of battens. There is no guarantee that yield stress of steel of battens is equal to that of stirrups. So, the volumetric ratio refers to an equivalent transverse area of the battens $A_{b,e}$, calculated as

$$A_{b,e} = A_b \frac{f_{y,e}}{f_{y,i}} \quad (21)$$

The lateral confinement pressures are calculated as follows:

$$f_{l,e,x} = k_e \cdot \rho_x \cdot f_{x,i} \quad (22)$$

$$f_{l,e,y} = k_e \cdot \rho_y \cdot f_{y,i}$$

being k_e a coefficient that quantifies the effectively confined area

$$k_e = \left[1 - \frac{s_b - \phi}{2(b - 2c)} \right] \cdot \left[1 - \frac{s_b - \phi}{2(h - 2c)} \right] \quad (23)$$

and ϕ is the diameter of the stirrups. The compressive response of confined concrete in compression is evaluated by the expression given by Mander et al. (1988) [12].

In particular, the cylindrical compressive strength of the confined concrete f_{cc} and the corresponding strain ε_{cc} are obtained as

$$f_{cc} = k \cdot f_c \quad (24)$$

$$\varepsilon_{cc} = \varepsilon_c \left[1 + 5 \left(\frac{f_{cc}}{f_c} - 1 \right) \right] \quad (25)$$

Where f_c is the cylindrical compressive strength of the unconfined concrete and ε_c is the corresponding strain. The constant k takes into account the shape of the cross section and is evaluated by means an abacus that can be found in [12]. According to this model, the ultimate stress of the confined concrete ε_{ccu} is calculated through the following expression:

$$\varepsilon_{ccu} = \varepsilon_{cu} + \frac{1,4\rho f_{y,i}}{f_{cc}} \varepsilon_{su,i} \quad (26)$$

Finally, the overall compressive response of confined concrete (see Fig. 5) is evaluated as follows:

$$\sigma_c = f_{cc} \frac{r \cdot \left(\frac{\varepsilon}{\varepsilon_{cc}} \right)}{r - 1 + \left(\frac{\varepsilon}{\varepsilon_{cc}} \right)^r} \quad (27)$$

With:

$$\begin{aligned} E_c &= 5000\sqrt{f_c} \quad [MPa] \\ E_{sec} &= \frac{f_{cc}}{\varepsilon_{cc}} \\ r &= \frac{E_c}{E_c - E_{sec}} \end{aligned} \quad (28)$$

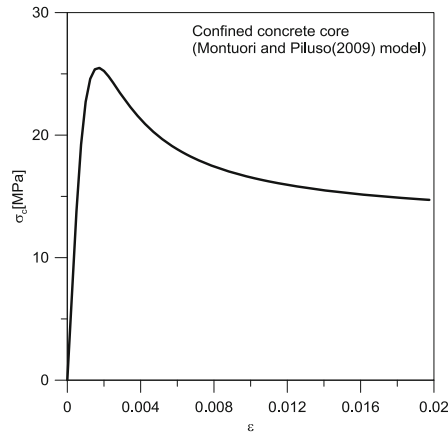


Fig. 5. Constitutive laws of confined concrete by Mander et al. (1988) [12]

Where E_{sec} and E_c are the secant and tangent elastic modulus of the confined concrete respectively.

The steel-concrete interface constitutive law is modelled through the model proposed by Chen and Teng (2001) [13]. According to this study, bi-linear relationship without hardening can be adopted expressed as

$$\begin{aligned}\tau &= k_{tt}s \quad \text{for } 0 \leq s \leq s_y \\ \tau &= \tau_r \quad \text{for } s_y \leq s \leq s_u\end{aligned}\quad (29)$$

where k_{tt} is the stiffness of the interface and s is the slippage between core and jacket.

4 Calculus Procedure and Practical Examples

In the proposed algorithm, the equations of the elastic analysis, provided in the previous chapters, are used into a step-by-step procedure. In each step, an axial shortening δ is imposed to the column's core and the compressive response of the jacket is obtained through different iterations.

Once half-column is divided in "n" portions with equal length " Δ ", the coordinates of all the column's pieces are defined within the following vectors:

$$\begin{aligned}\underline{x_c^{r,k}} &= [x_{c,1}^{r,k} \dots x_{c,i}^{r,k} \dots x_{c,n+1}^{r,k}]^T \\ \underline{x_j^{r,k}} &= [x_{j,1}^{r,k} \dots x_{j,i}^{r,k} \dots x_{j,n+1}^{r,k}]^T\end{aligned}\quad (30a, b)$$

The first term of the previous vectors is the origin of the reference system, while the apices "r" and "k" are the load step and the iteration respectively. At the first load step, the previous vectors contain the positions of the layers related to the undeformed column.

For each layer i , a constant value of stiffness can be assigned for the confined concrete, for jacket and for interface respectively. Hence, the constitutive laws of materials are divided into parts:

$$\begin{aligned}\underline{E_c} &= [E_{c,1} \dots E_{c,w} \dots E_{c,nc}]^T \\ \underline{E_j} &= [E_{j,1} \dots E_{j,w} \dots E_{j,ns}]^T \\ \underline{K} &= [K_1 \dots K_w \dots K_{nk}]^T\end{aligned}\quad (31a, b, c)$$

Where n_c , n_s and n_k are the parts in which the constitutive laws were divided, with reference to confined concrete, steel jacket and interface respectively. Previous vectors included the tangent stiffness moduli, defined as

$$\begin{aligned}
 E_{c,w} &= \frac{\sigma_{c,w+1} - \sigma_{c,w}}{\varepsilon_{c,w+1} - \varepsilon_{c,w}} \\
 E_{j,w} &= \frac{\sigma_{j,w+1} - \sigma_{j,w}}{\varepsilon_{j,w+1} - \varepsilon_{j,w}} \\
 K_w &= \frac{\tau_{w+1} - \tau_w}{s_{w+1} - s_w}
 \end{aligned} \tag{32a, b, c}$$

Each value of stiffness modulus matches an interval of axial strain of the core or jacket and an interval of relative slippage for the interface. After elastic solutions are known, it is possible to assign a stiffness value to each layer of the column.

$$\begin{aligned}
 \underline{E_c^{r,k}} &= \left[E_{c,1}^{r,k} \dots E_{c,i}^{r,k} \dots E_{c,n}^{r,k} \right]^T \\
 \underline{E_j^{r,k}} &= \left[E_{j,1}^{r,k} \dots E_{j,i}^{r,k} \dots E_{j,n}^{r,k} \right]^T \\
 \underline{K^{r,k}} &= \left[K_1^{r,k} \dots K_i^{r,k} \dots K_n^{r,k} \right]^T
 \end{aligned} \tag{33a, b, c}$$

It is worth noting that the stiffness values just assigned to each layer are function of the axial strain of the pieces of the core and the jacket, as well as relative slippage of the interface, which, in this stage, are not know. At this point, the relative stiffness parameters β_c e β_j , defined by Eqs. (9a,b), can be assigned to each pieces of the column and grouped into the following vectors:

$$\begin{aligned}
 \underline{\beta_j^{r,k}} &= \left[\beta_{j,1}^{r,k} \dots \beta_{j,i}^{r,k} \dots \beta_{j,n}^{r,k} \right]^T \\
 \underline{\beta_c^{r,k}} &= \left[\beta_{c,1}^{r,k} \dots \beta_{c,i}^{r,k} \dots \beta_{c,n}^{r,k} \right]^T
 \end{aligned} \tag{34a, b}$$

As stated above, the relative stiffness parameters and the positions of the ends out of the layers of column and jacket are obtained by means a step-by-step approach, in which each step needs different iterations. In particular, an axial shortening δ is assigned to the core of the jacketed column at the “r-th” analysis step and, at the “k-th” iteration of this step, a system of linear equations is solved.

The governing equation of axial shortening of the “i-th” jacket’s piece, introduced in Eqs. (14), is written taking into account of the variability of relative stiffness parameters:

$$\begin{aligned}
 u_{j,i}^{r,k}(x) &= c_{1,i} \cdot \frac{e^{x\sqrt{2\beta_{c,i}^{r,k} + \beta_{j,i}^{r,k}}}}{2\beta_{c,i}^{r,k} + \beta_{j,i}^{r,k}} + c_{2,i} \cdot \frac{e^{-x\sqrt{2\beta_{c,i}^{r,k} + \beta_{j,i}^{r,k}}}}{2\beta_{c,i}^{r,k} + \beta_{j,i}^{r,k}} + c_{3,i} \cdot x + c_{4,i} \\
 \left\{ x_{j,i}^{r,k} \leq x \leq x_{j,i+1}^{r,k}, i \in [1, n] \right\}
 \end{aligned} \tag{35}$$

Where $x_{j,i}^{r,k}$ and $x_{j,i+1}^{r,k}$ are ends out of the “i-th” jacket’s piece. Similarly, the axial shortening law in the core, presented in Eq. (11), can be written as follows

$$u_{c,i}^{r,k}(x) = u_{j,i}^{r,k}(x) - \frac{1}{\beta_{j,i}^{2r,k}} \frac{d^2 u_{j,i}^{r,k}(x)}{d^2 x} \quad (36)$$

$$\left\{ x_{c,i}^{r,k} \leq x \leq x_{c,i+1}^{r,k}, i \in [1, n] \right\}$$

where $x_{c,i}^{r,k}$ and $x_{c,i+1}^{r,k}$ are ends of the “i-th” core’s piece. The previous axial shortening laws in the core and in the jacket are defined on the layers of the jacket and core by means of four constants. The latter are calculated on the basis of boundary conditions for each column’s piece. In particular, four compatibility equations can be imposed on the contact surface between the two adjacent layers of the column

$$u_{j,i}^{r,k}(x_{j,i}^{r,k}) - u_{j,i+1}^{r,k}(x_{j,i}^{r,k}) = 0$$

$$E_{j,i}^{r,k} A_j \left. \frac{du_{j,i}^{r,k}(x)}{dx} \right|_{x=x_{j,i}^{r,k}} - E_{j,i+1}^{r,k} A_j \left. \frac{du_{j,i+1}^{r,k}(x)}{dx} \right|_{x=x_{j,i}^{r,k}} = 0 \quad (37a, b, c, d)$$

$$u_{c,i}^{r,k}(x_{c,i}^{r,k}) - u_{c,i+1}^{r,k}(x_{c,i+1}^{r,k}) = 0$$

$$E_{c,i}^{r,k} A_c \left. \frac{du_{c,i}^{r,k}(x)}{dx} \right|_{x=x_{c,i}^{r,k}} - E_{c,i+1}^{r,k} A_c \left. \frac{du_{c,i+1}^{r,k}(x)}{dx} \right|_{x=x_{c,i}^{r,k}} = 0$$

The following boundary conditions can be imposed at the origin of the reference system ($x = 0$)

$$u_{j,1}^{r,k}(0) = 0$$

$$u_{c,1}^{r,k}(0) = 0 \quad (37e, f)$$

In similar manner, two compatibility equations can be imposed on the loaded surface ($x = 1$):

$$E_{j,n}^{r,k} A_j \left. \frac{du_{j,n}^{r,k}(x)}{dx} \right|_{x=1} = 0 \quad (37g, h)$$

$$u_{c,n}^{r,k}(1) = \delta$$

Once that constants of integration are obtained by solving the previous system of Eqs. (37a,b,c,d), the updated position of the ends of all the column’s pieces can be calculated using Eqs. (35) and (36)

$$x_{c,i}^{r,k+1} = x_{c,i}^{r,k} + u_{c,i}^{r,k}(x_{c,i}^{r,k})$$

$$x_{j,i}^{r,k+1} = x_{j,i}^{r,k} + u_{j,i}^{r,k}(x_{j,i}^{r,k}) \quad (38a, b)$$

On the basis of vertical displacements, the length of each piece Δ is shortened and it can be expressed as

$$\begin{aligned}\Delta_{c,i}^{r,k+1} &= x_{c,i}^{r,k+1} - x_{c,i-1}^{r,k+1} \\ \Delta_{j,i}^{r,k+1} &= x_{j,i}^{r,k+1} - x_{j,i-1}^{r,k+1}\end{aligned}\quad (39a, b)$$

The lengths obtained are subsequently grouped in the following vectors:

$$\begin{aligned}\underline{\Delta}_c^{r,k+1} &= \left[\Delta_{c,1}^{r,k+1} \dots \Delta_{c,i}^{r,k+1} \dots \Delta_{c,n}^{r,k+1} \right]^T \\ \underline{\Delta}_j^{r,k+1} &= \left[\Delta_{j,1}^{r,k+1} \dots \Delta_{j,i}^{r,k+1} \dots \Delta_{j,n}^{r,k+1} \right]^T\end{aligned}\quad (40a, b)$$

The axial strain along each layer can be calculated as ratio between the shortening of each layer by the initial length

$$\begin{aligned}\varepsilon_{c,i}^{r,k+1} &= \frac{\Delta - \Delta_{c,i}^{r,k+1}}{\Delta} \\ \varepsilon_{j,i}^{r,k+1} &= \frac{\Delta - \Delta_{j,i}^{r,k+1}}{\Delta}\end{aligned}\quad (41a, b)$$

It is worth to note that the previous axial strains laws are justified by the hypothesis of linear trend of shortening along each piece. Once that axial strains are known by relations (41a,b), the updated values of stiffness moduli in the vectors (33a,b,c) are evaluated by means of vectors in Eqs. (31a,b,c). Axial forces in all core and jacket's layers are computed from these updated values of stiffness moduli, by evaluating the first order derivative of axial shortening laws

$$\begin{aligned}N_{c,i}^{r,k+1}(x) &= E_{c,i}^{r,k+1} A_j \frac{du_{c,i}^{r,k+1}(x)}{dx} \\ N_{j,i}^{r,k+1}(x) &= E_{j,i}^{r,k+1} A_j \frac{du_{j,i}^{r,k+1}(x)}{dx}\end{aligned}\quad (42a, b)$$

The shear stress at the interface of each layer is calculated by means of relative slippage between core and jacket

$$\tau_i^{r,k+1}(x) = k_i^{r,k+1} \left[u_{c,i}^{r,k+1}(x) - u_{j,i}^{r,k+1}(x) \right] \quad (43)$$

where the shear stiffness of the interface of each layer $k_i^{r,k+1}$ is updated through relative slippage between core and jacket. Afterwards, a successive iteration is carried out by solving the system (37a,b,c,d) on the basis the new values of stiffness moduli and the position of the ends of all the column's pieces (38a,b). The iterations of each load step concludes when the axial strain of each layer, between two successive iterations, is less than a selected tolerance

$$\begin{aligned} \left| \varepsilon_{c,i}^{r,k+1} \right| - \left| \varepsilon_{c,i}^{r,k} \right| < tol \\ \left| \varepsilon_{j,i}^{r,k+1} \right| - \left| \varepsilon_{j,i}^{r,k} \right| < tol \end{aligned} \tag{44a, b}$$

Furthermore, before proceeding to new load step, the equilibrium condition of the core is checked. In particular, the value provided by the equilibrium equation for each piece of the core must be close enough to zero, without exceeding a selected tolerance

$$\left[N_{c,i+1}^{r,k+1} \left(x_{c,i+1}^{r,k+1} \right) - N_{c,i}^{r,k+1} \left(x_{c,i}^{r,k+1} \right) \right] + 2 t \Delta_{c,i}^{r,k+1} \int_{x_{c,i}^{r,k+1}}^{x_{c,i+1}^{r,k+1}} \tau_i^{r,k+1}(x) dx < tol2 \tag{45}$$

where the second addend indicates the total shear force acting along the interface of a layer, while the first term is the difference between the axial forces acting to the end of the same.

The increments of displacement δ are stopped when the ultimate axial strain of the confined concrete is achieved into a generic portion of the column.

Three examples were carried out by applying the proposed algorithm. Example A refers to a square cross section with size b equal to 300 mm. The length of the column is $2l = 820$ mm, and its half-length l was partitioned in 6 layers. Thickness of the steel angles w_j is equal to 10 mm, the interface depth t is 200 mm and two values of interface stiffness k_{tt} , equal to 3.41 and 51.09 N/mm³, are considered.

In example B and C the side of the square cross section was $b = 400$ mm, the length of the column was $2l = 2500$ mm, and half-length l was divided in 25 layers. Interface stiffness k_{tt} is 4.44 N/mm³. In example B the interface depth t is 200 mm and three values of thickness of the steel angles w_j , equal to 20, 30 and 40 mm, were studied. Finally, in example C the width of steel angles is kept constant and equal to 30 mm, while three values of interface depth t , equal to 200, 300 and 400 mm, are examined.

All examples assumed concrete with cylinder compressive strength equal to 15 MPa, while yield strength and ultimate stress of the steel jacket is equal to 275 MPa and 430 MPa respectively. The elastic modulus of the steel jacket is equal to 210000 MPa and hardening modulus is equal to 5000 MPa.

Figure 6 shows the compressive response of the indirectly loaded column A compared with the two borderline cases of directly loaded jacket and confined RC core. The plot shows that the compressive behavior of the indirectly loaded column tends to the load-shortening curve of the directly loaded element when the interface stiffness increases due to the greater portion of load transferred by the core to the jacket. The latter concept is exposed more clearly in Fig. 7, which reports the trend of shear stress τ and axial force in the core N_c and in the jacket N_j achieved by proposed algorithm, for different values of interface stiffness. Furthermore, for each value of interface stiffness, the previous quantities are plotted for three different values of axial shortening δ/l , equal to 0.1%, 0.2% and 0.3%.

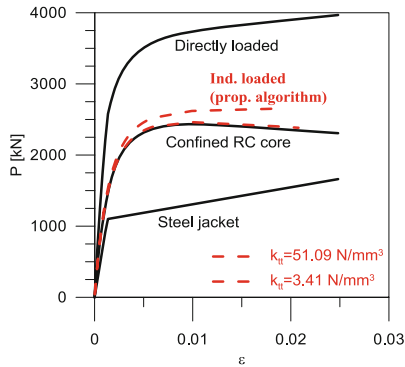


Fig. 6. Example A: compressive behavior of steel-jacketed columns with different interface stiffness k_{It}

It can be observed that shear stress tends to be more intensified at the extremities of the column not only when the interface stiffness increases, but even when the axial shortening δ increases. In fact, Fig. 7a shows that a greater shear stress is obtained at the extremity ($x/l = 1$) for all values of interface's stiffness, when shortening δ increases. Obviously, this last phenomenon is even more marked for greater values of interface's stiffness, as shown in Fig. 7a. In this case, for $\delta = 0.003 l$ and $k_{It} = 81.09 \text{ N/mm}^3$, the shear stress developed after an abscissa equal to $0.6 x/l$ tends to a substantial amplification. Consequently, higher interface shear stress induces lower axial force at the core's middle section and greater axial force at the jacket's center, as shown in Fig. 7b and c respectively. Moreover, it should be noted that the interface stiffness influences the axial strain of the column's pieces and consequently it influences the distribution of stiffness moduli along the column, as shown in Fig. 7d. In fact, the distribution of axial strain along the RC core is more uniform for lower interface's stiffness than that achieved by higher values of K_{It} . In this last case, the axial strains are intensified at the extremities and decrease at the center section.

The distributions of axial strain and shear stress along the column's length in examples B and C are also analysed as a function of the thickness w_j and depth of the steel angles. Figure 8 shows the trend of interface shear stress the axial strains, the stiffness moduli along the column's pieces and the load-shortening curves predicted by proposed analytical model for the example B. In this case, an increasing value of w_j has a negligible effect on the shear stress at the extremities but it influences slightly its distribution along the length of the column. This fact is shown in Fig. 8a, which plots the shear stress at a shortening δ equal to $0.222\% l$, i.e. an axial strain value that is close to that corresponding to peak stress of concrete. It is clear that greater axial shortenings of the RC core are expected for low values of thicknesses of the steel angles but this last parameter has a negligible influence on the trend of axial load, as shown in Fig. 8b.

As it reported in Fig. 8c, greater values of thickness w_j induce increasing axial strains at extremity of the column, so lower stiffness moduli. Conversely, lower axial strains at the center correspond to higher stiffness moduli in the central zone of the member. Accordingly, the ultimate shortening of the column strengthened with thicker

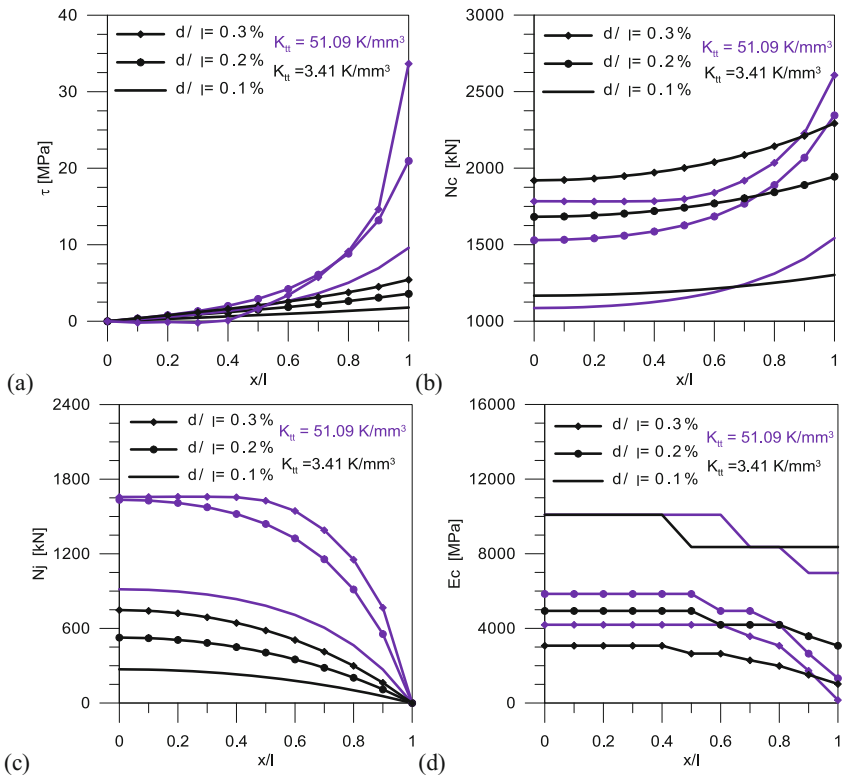


Fig. 7. Example A: algorithm predictions: (a) interface shear stress; (b) axial force in the core; (c) axial force in the jacket; (d) stiffness moduli along the column's pieces

steel angles is less than the same column reinforced with to less thick steel angles, as shown by the load-shortening curves plotted in Fig. 8d.

Figure 9 shows the trend of interface shear stress, axial strains, stiffness moduli along the column's pieces and the load-shortening curves predicted for the example C by the proposed analytical model, in which three values of depth t of the steel angles were adopted. In this case, lower interface shear stress are obtained for greater depth of the steel angles, due to the fact that the same load is distributed over a larger interface (Fig. 9a). Coherently, axial strains and stiffness moduli along the column are distributed as in the Example B. In fact, great values of depth t induce greater axial strains at the extremity and lower axial strains at the centre (Fig. 9b); on the contrary, great values of depth t induce lower stiffness moduli at the extremity and higher stiffness moduli at the centre (Fig. 9c).

As a consequence, the ultimate shortening of members with larger interface thickness tends to be lower, as shown in Fig. 9d.

Previous examples show that an intensification of the axial strains at the ends of the column can occur when increasing the interface stiffness, the thickness or the depth of the steel angles. This phenomenon leads on a reduction of the ultimate shortening

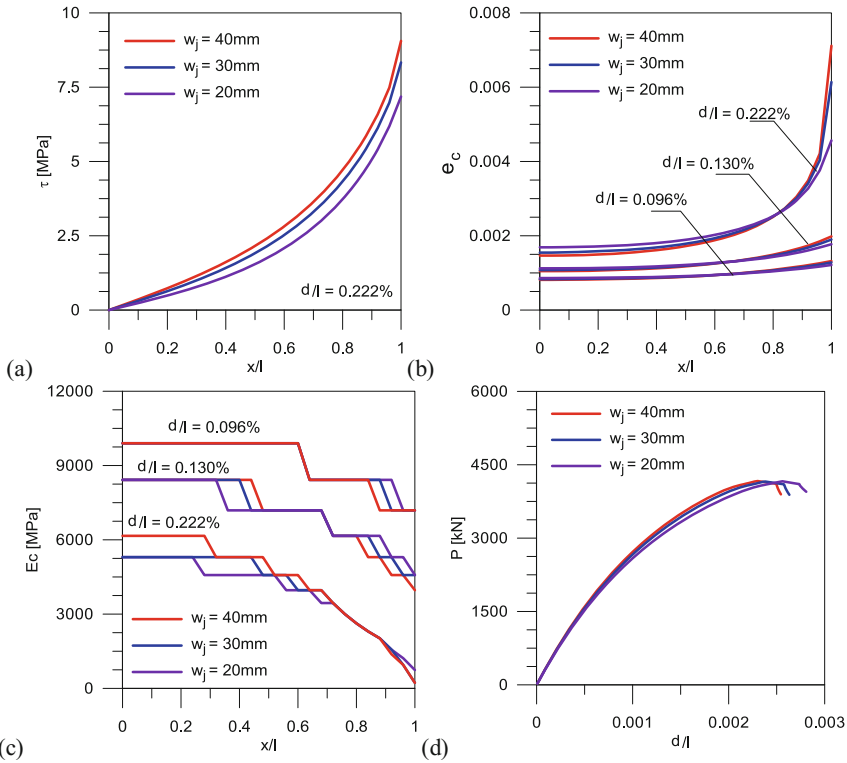


Fig. 8. Example B: algorithm predictions: (a) interface shear stress; (b) axial strains along the RC core; (c) stiffness moduli along the column’s pieces; (d) Normalized axial shortening vs. axial load curves

capacity of the column, making the latter more rigid. Nevertheless, rigid interface allows increasing the overall compressive response of the member, instead a deeper interface zone allows reducing shear stress keeping the axial capacity of the column unaltered.

5 Experimental Comparison

The validity of results carried out with the proposed analytical model is investigated through comparisons with experimental data published by Campione et al. (2017) [11]. This experiential campaign considered two columns with rectangular cross section with a size equal to 220×300 mm and length $2l = 810$ mm. The external jacket was constituted by four $50 \times 50 \times 5$ mm steel angles of grade S275; therefore, the parameters assumed in the algorithm were thickness of the jacket equal to $w_j = 5$ mm, interface depth $t = 200$ mm, $f_y = 275$ MPa, $f_{su} = 430$ MPa, $E_s = 210000$ MPa and $E_{sh} = 50000$ MPa. The two columns were created concrete of different compressive strength. In particular, the column “A” was made with concrete grade $f_c = 12,65$ MPa,

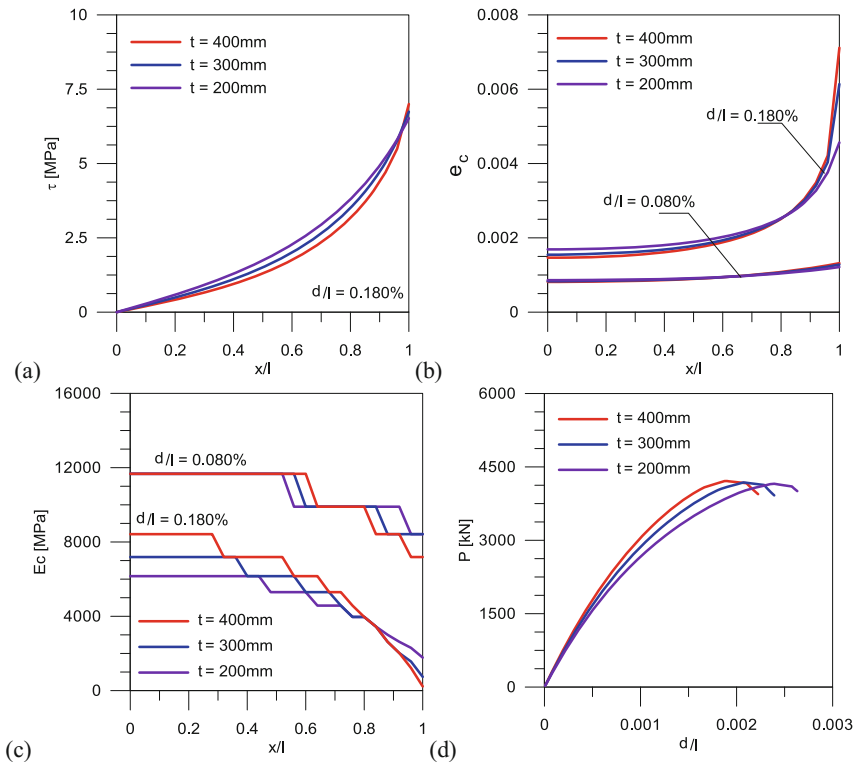


Fig. 9. Example C: algorithm predictions: (a) interface shear stress; (b) axial strains along the RC core; (c) stiffness moduli along the column's pieces; (d) Normalized axial shortening vs. axial load curves

instead, the concrete of the column “B” was grade $f_c = 24,00$ MPa. The value adopted for the interface stiffness was $K_{tt} = 10$ N/mm³ for both columns. The latter are divided in 15 layers, that is each layer of the columns is high 6,66% l .

Figure 10 shows the experimental-theoretical comparison. In particular, the axial strain-load curves of the specimens A and B [11] are compared with the analytical predictions achieved by the proposed algorithm. From the previous Fig. 10, it can be observed that the proposed model is able to predict the axial capacity and the initial stiffness. The latter is overestimated in the column A because of the high initial stiffness of the constitutive law adopted for only confined core. Furthermore, the algorithm manifest a good accuracy in predicting of the post-peak branch.

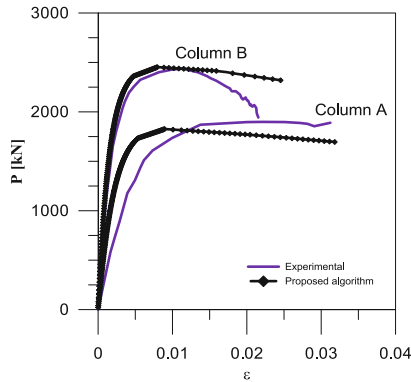


Fig. 10. Theoretical predictions of the proposed algorithm compared with experimental data published by Campione et al. (2017) [11]

6 Conclusions

An analytical algorithm for predicting the compressive response of RC columns jacketed with external steel angles without a specific connection at the end is presented in this paper. The proposed model is based on the closed form solution valid under the assumption of linear elastic behaviour of constituent materials. At this point, the non-linear compressive response of the concrete is taken into account partitioning the column into layers and within each portion, the elastic solution is assumed. So, the results obtained with this method have the advantage of are well supported by a mechanical approach and they are in good agreement with the experimental data available in the literature then, it can be concluded that the compressive response of steel jacketed columns can be reproduced successfully through the proposed algorithm. This method was used in three examples to explore the compressive response dependence by the interface stiffness, the thickness or the depth of the steel angles. It is clear that a more rigid interface increases the axial capacity of the column, but it is important to note that an increase of the previous parameters leads on to intensification of the axial strain at the extremities of the column and so the ultimate shortening is less. Furthermore, It was found that the axial capacity of the column does not change when the thickness or the depth of the steel angles increasing, but It is interesting that interface shear stress is less with a deeper interface.

References

1. Therrou, G.E., Elnashai, A.S.: Seismic retrofit schemes for RC structures and local–global consequences. *Prog. Struct. Engng Mater.* **8**, 1–15 (2006)
2. CEN (European Committee for Standardization): Design of composite steel and concrete structures. Part 1: General rules for buildings. Eurocode 4, Brussels, Belgium (2005a)

3. CEN (European Committee for Standardization): Design of structures for earthquake resistance. Part 1: General rules, seismic actions and rules for buildings. Eurocode 4, Brussels, Belgium (2005b)
4. Montuori, R., Piluso, V.: Reinforced concrete columns strengthened with angles and battens subjected to eccentric load. *Eng. Struct.* **31**(2), 539–550 (2009)
5. Nagaprasad, P., Sahoo, D.R., Rai, D.C.: Seismic strengthening of R.C. columns using external steel cage”. *Earthq. Eng. Struct. Dyn.* **38**(14), 1563–1586 (2009)
6. Tarabia, A.M., Albakry, H.F.: Strengthening of RC columns by steel angles and strips. *Alexandria Eng. J.* **53**(3), 615–626 (2014)
7. Adam, J.M., Ivorra, S., Pallarés, F.J., Giménez, E., Calderón, P.A.: Axially loaded RC columns strengthened by steel caging. Finite element modelling. *Constr. Build. Mater.* **23**(6), 2265–2276 (2009)
8. Giménez, E., Adam, J.M., Ivorra, S., Moragues, J.J., Calderón, P.A.: Full-scale testing of axially loaded RC columns strengthened by steel angles and strips. *Adv. Struct. Eng.* **12**(2), 169–181 (2009)
9. Badalamenti, V., Campione, G., Mangiavillano, M.L.: Simplified model for compressive behaviour of concrete columns strengthened with steel angles and strips. *J. Eng. Mech.* 230–238 (2010). [https://doi.org/10.1061/\(asce\)em.1943-7889.0000069](https://doi.org/10.1061/(asce)em.1943-7889.0000069)
10. Belal, M.F., Mohamed, H.M., Morad, S.A.: Behavior of reinforced concrete columns strengthened by steel jacket. *HBRC J.* **11**(2), 201–212 (2015)
11. Campione, G., Cavaleri, L., Di Trapani, F., Ferrotto, M.F.: Frictional effects in structural behavior of no-end-connected steel-jacketed RC columns: experimental results and new approaches to model numerical and analytical response. *J. Struct. Eng.* **143**(8), 04017070 (2017)
12. Mander, J.B., Priestley, M.J.N., Park, R.: Theoretical stress-strain model for confined concrete. *ASCE J. Struct. Eng.* **114**(8), 1804–1826 (1988)
13. Chen, J.F., Teng, J.G.: Anchorage strength models for FRP and steel plates bonded to concrete. *J. Struct. Eng.* **127**(7), 784–791 (2001)



Three-Dimensional Analysis of an Innovative Hollow Concrete Block of Interlocking Revetment

Hau Nguyen-Ngoc^{1,2(✉)}, Bao-Loi Dang^{1,4}, Hung Nguyen-Xuan³,
Hoang Duc Thao⁵, and Magd Abdel Wahab¹

¹ Laboratory Soete, Faculty of Engineering and Architecture,
Ghent University, Ghent, Belgium
Hau.NguyenNgoc@ugent.be

² Faculty of Water Resources Engineering, University of Science
and Technology, The University of Danang, Da Nang, Vietnam

³ Center for Interdisciplinary Research in Technology, Ho Chi Minh City
University of Technology (Hutech), Ho Chi Minh City, Vietnam

⁴ Mien Trung University of Civil Engineering, Tuy Hòa, Vietnam

⁵ Ba Ria – Vung Tau Urban Sewerage and Development One Member Limited
Company (BUSADCO), Vung Tau, Vietnam

Abstract. In this study, we investigate a new design of interlocking revetment that is constructed by precast hollow concrete blocks. The defense structure is to protect the estuary from complex water actions at a river mouth in Vietnam. The hollow concrete block of the structure is designed to be hollow inside for material saving and construction efficiency. Then, the block will be filled by sand onsite. However, the structure performance under the effects of external loads should be investigated since its design is the first time of implementation in coastline protecting system in Vietnam. The block is modeled in ANSYS 18.0 for the calculation of deformation and stresses induced by the action of wave on the block surfaces. The conventional finite element method is used for solving the unknowns of studied models. The investigated results are the displacements of the hollow concrete block in various directions and the equivalent von-Mises stress generated within the structure. The calculation also shows that there are some sharp points of the structure experiencing stress singularity, which should be considered in design.

Keywords: Hollow concrete block · ANSYS 18.0 · Displacements
Von-Mises stress · Stress singularity

1 Introduction

Sea defenses are well known as an effective solution to protect life, coastlines, embankments and artificial constructions from erosion and destruction of water actions like wave, storm, tsunami and so on. In which, protecting slope structures such as concrete sea dikes, seawalls, breakwaters, etc. are being used worldwide with great effectiveness. However, many structures have built for years or over different periods

so that they may not be able to resist the complex boundary conditions caused by climate change and rising sea level in recent years. Consequently, there are many damages of coastal defense system determining every year. They are caused by various reasons such as storm, erosion, flood or even insufficient structure analysis or insufficient geometry of defense construction.

Natural disasters, especially storm and tsunami, are the main reason that destroys not only life and facilities behind the protection structure but also the structure itself that supposed to resist hazard. The failure mechanism of those defense system (protected slope sea dikes and seawalls) during the tsunami is believed to be generated by local scour of revetments, which caused by frequent wave impacting on the structure and subsequent high flow velocity and turbulence at the toe [1–5]. In additionally, overturning was a very common damage that could be seen in failure mechanism of seawalls. It is well known that vertical walls are greatly affected by the acting of seaward and landward pressure, which should be in equivalent state when the structures are stable. However, the tsunami was able to destroyed this state by inducing scour at the toe, dynamic hydraulic force acting on the slopes, etc.

It is well known that revetments made of randomly placed concrete blocks such as Tetrapod, Dolos, Coreloc, Accropode, Ecopode, Xbloc, etc. can protect defense structures from wave attack efficiently. These units need to be very massive so that they can remain stable and have acceptable movement during the designed storm period. However, in the history of coastal structures, severe damages of interlocked concrete units were reported to be the main reasons in many cases of defense system failures [6]. Therefore, individual concrete unit's broken mechanism under different boundary conditions has been studied by researchers worldwide. The numerical simulation of three dimensional unreinforced Dolos under dynamic and extreme loading conditions was studied to investigate the fracture mechanism in FEMDEM (the combined finite-discrete element method) program [7]. The results have been compared with a study of Burcharth [8] and a report from monitoring at Crescent City [9] with great agreement. In the research of Latham et al. [10], the various types of concrete units are modelled to determine their stress behavior under the effects of wave attack and interaction of nearby blocks. It is noticeable that numerical calculation of three dimensional fracture model should use unstructured meshes for elements made of homogeneous isotropic quasi-brittle material in order to gain reasonable results [11].

Innovations in design of coastline defense structures as well as more reliable equations have been developing recent years [12–14]. In the study of Park et al. [12], the rubble mound armor made of layers of different size tetrapods with or without vertical wall on the crest are investigated. The authors concluded that, the wave discharges over the protected structure decreases with the increase in size of tetrapod in the case of no vertical wall. On the other hand, both parameters of vertical wall height and roughness of revetment highly affect the wave overtopping on the coastal structures. Besides, the paper recommended that under constant wave condition, the use of shorter vertical wall combine with large tetrapod would save cost with better performance. Yang et al. has carried out an experiment to study the failure mechanism of scaled model sea-dike caused by wave overtopping [13]. From the results, the authors suggested to design flat concrete revetment to protect gentle landward slope because

the failure overtopping rate is greatly influenced by armor layer material, the landward slope and the top-mounted wall.

In this study, the innovative concrete block is analyzed for the displacements and stress performance under the static load (wave load) acting on the block surface. The well-known ANSYS software [15] is used to analyze the block model using the finite element method (FEM). The concrete block is the new design for constructing interlocking revetment, which protects the slope of a coastal dike. Unlike Tetrapod, Dolos, etc. the new concrete block is not too heavy for construction and does not have concentrated stress corner, which usually experiences fracture failure. Yet they can connect each other forming the interlocking structure, which has already showed many advantages.

2 Studied Models

2.1 Theoretical Analysis

In this project, we investigate the new design of hollow concrete block of interlocking revetment. The defense structure is to protect the estuary from complex water actions at a river mouth in Vietnam. The precast hollow concrete block of the structure is designed to be hollow inside for material saving and construction efficiency. Then, the block will be filled by sand onsite. The shape and size of the concrete block is showed in Figs. 1 and 2a, b.

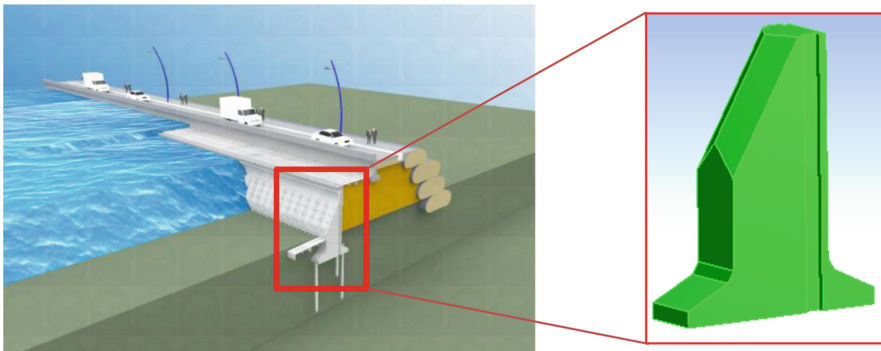


Fig. 1. Innovative interlocking revetment model and hollow concrete block.

The aim of the study is to calculate the behavior of the structure under static loading condition. The equivalent model of the hollow concrete block is showed in Fig. 2c, in which the bottom surface of the block is fixed. The objective is to investigate the performance of innovative block under the effect of wave force, which is equalized as a

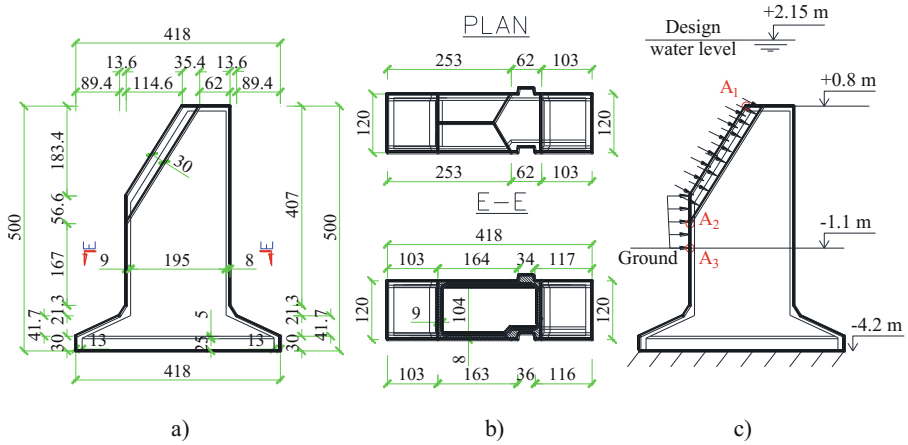


Fig. 2. Detail of innovative hollow concrete block: (a) Vertical section of the block, (b) Plan view and cross section of the block, (c) The equivalent model of the block from the real structure. Unit in cm.

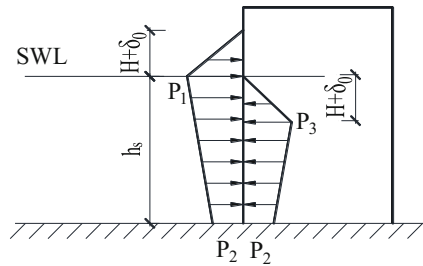


Fig. 3. Onward and backward wave force acting on a vertical wall.

various distribution load acting on the incline surface of the model. The wave force is determining based on the Sainflou’s formula [16] as following (see Fig. 3):

$$P_1 = (P_2 + \gamma_w h_s) \frac{H + \delta_0}{h_s + H + \delta_0} \tag{1}$$

$$P_2 = \frac{\gamma_w H}{\cosh(kh_s)} \tag{2}$$

$$P_3 = \gamma_w (H - \delta_0) \tag{3}$$

where H (m) is the wave height, $H = 3.1$ m.

g (m/s^2) is the gravity acceleration, $g = 9.81$ m/s^2 ;

h_s (m) is the water depth in front of the structure; $h_s = 4.25$ m.

γ_w (kg/m^3) is the weight density of sea water;
 $\gamma_w = 1.025 \text{ g} = 1.025 \times 9.81 = 10.055 \text{ kg/m}^3$.
 δ_o (m) takes the value of 0.1473 m.
 $k = 4\pi/L$; L (m)= 83.2 is the wavelength corresponding to the period of $T = 12.5 \text{ s}$
 Substituting those value into Eqs. (1) and (2) we get

$$P_1 = 29.6 \text{ kPa and } P_2 = 25.7 \text{ kPa} \tag{4}$$

Because the block is hollow and lies under water, the hydraulic pressures acting on the outside and inside of block surface offset from each other. Therefore, in the studied models, the hydraulic pressure is neglected. The pressures apply at points A_1 , A_2 and A_3 (see Fig. 2c) are:

$$P_{A1} \approx 28 \text{ kPa}; P_{A2} \approx P_{A3} \approx 26 \text{ kPa} \tag{5}$$

2.2 ANSYS Model

ANSYS 18.0 is used to model the block, which will be analyzed using the regular finite element method with tetrahedral meshes (element type Tet10). The dimensions of the hollow concrete block are showed in Fig. 2a, b. The block is a part of the interlocking revetment, which connects with two other elements on the sides. Therefore, in the model, the displacements of the side surfaces are restrained (see Fig. 4).

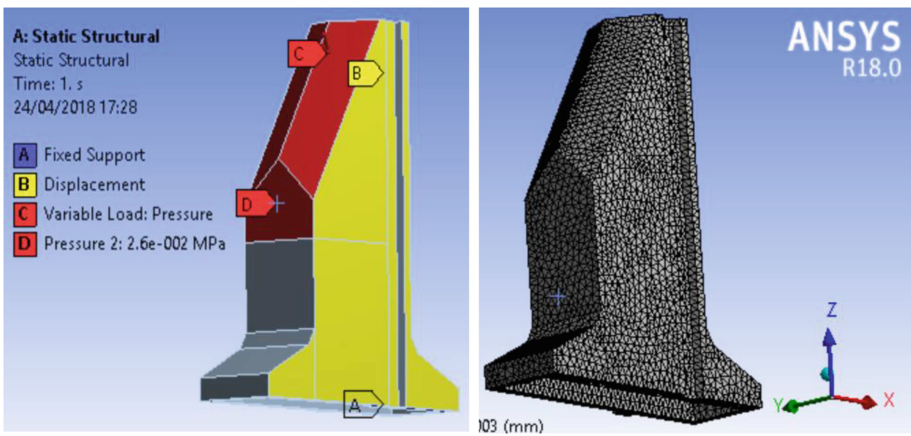


Fig. 4. Models of the blocks on ANSYS 18.0

The material of concrete has Young’s elastic modulus E of 30500 MPa and Poisson’s ratio ν of 0.2.

3 Results and Discussing

3.1 Results of the Full Model

The results determined in ANSYS include displacements on the main direction (X-Axis) and on the vertical direction (Z-Axis) and equivalent von-Mises stress. Figure 5 shows the convergence of the maximum displacement results according to the number of elements whereas Fig. 6 presents the maximum von-Mises stress of the model. It can be easily seen that, the displacements start to converge with a very low number of elements of around 50000. As presented in Table 1, the differences in percentage between the values of displacements after convergence are less than 0.10%. Therefore, the displacements of the block can be determined simply by just using the fine mesh of 10-node tetrahedral elements (type Tet10) in ANSYS.

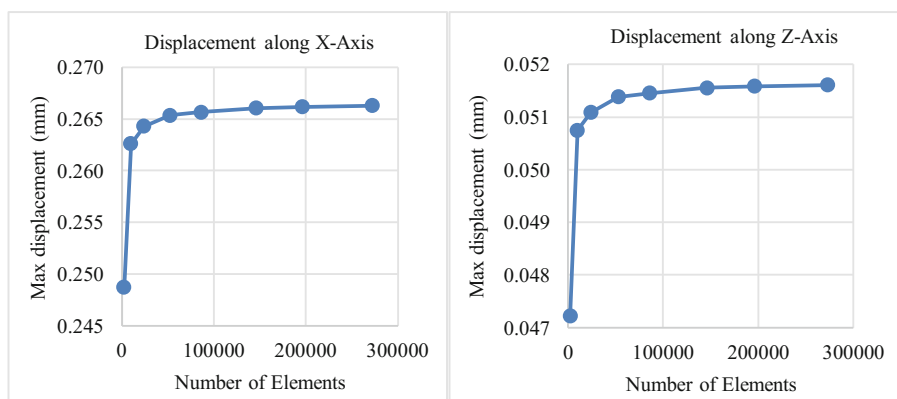


Fig. 5. Convergence of maximum displacement of the block: (a) X-direction displacement, (b) Z- direction displacement.

Table 1. Convergence values of displacements and von-Mises stress according to the number of elements and nodes.

Number of element	Number of nodes	Max displacement (mm)		Mises stress (MPa)	Percentage of difference (%)		
		X	Z		X	Z	Stress
2258	4438	0.249	0.047	1.165			
9900	18348	0.263	0.051	1.883	5.29	6.95	38.15
23915	44846	0.264	0.051	2.056	0.64	0.66	8.38
52766	94674	0.265	0.051	2.272	0.39	0.57	9.53
86124	147685	0.266	0.051	2.391	0.12	0.14	5.00
146291	241381	0.266	0.052	2.358	0.15	0.19	-1.43
196242	319582	0.266	0.052	2.476	0.05	0.07	4.79
272695	438754	0.266	0.052	2.685	0.05	0.04	7.79

However, the values in Table 1 and Fig. 6 show that the maximum von-Mises stress increase steadily with respect to the number of model's elements. In Fig. 7, the positions, where the maximum displacements and von-Mises stress take place, are presented. It should be noticed that the maximum equivalent stress occurs at the sharp corner of the block where meets the condition to experience stress singularity. Consequently, the stress of the block should be calculated at an appropriate location. Figure 8 shows an edge 1–2 as an example for an alternative way of analysis with the aim to avoid stress singularity.

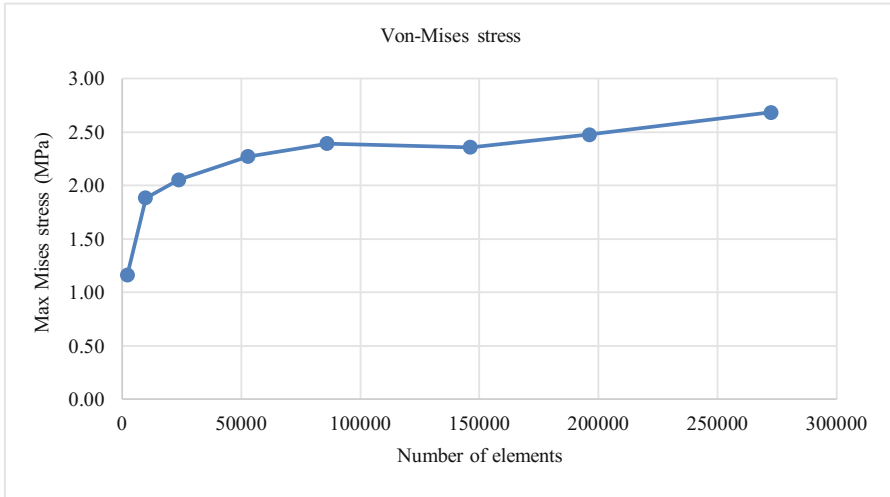


Fig. 6. Convergence of maximum equivalent von-Mises stress of the block.

3.2 Results of the Specific Edge

It can be seen from Figs. 9 and 10 that all the results of displacements and equivalent stress converge with respect to mesh refinement. Similar to the previous case, the displacements of the edge 1–2 converge quickly with small number of elements of around 50000. On the contrary to Fig. 6, the von-Mises stress does not increase infinity as the model refinement but converges with the same number of elements as for displacements. Finally, Figs. 11 and 12 present the analyzed results along the edge 1–2, which are considered as the exact values because they have been compared with the results of ABAQUS after checking the convergence. The model in ANSYS is meshed using about 270000 elements (440000 nodes) whereas in ABAQUS is about 370000 elements (580000 nodes) (Table 2).

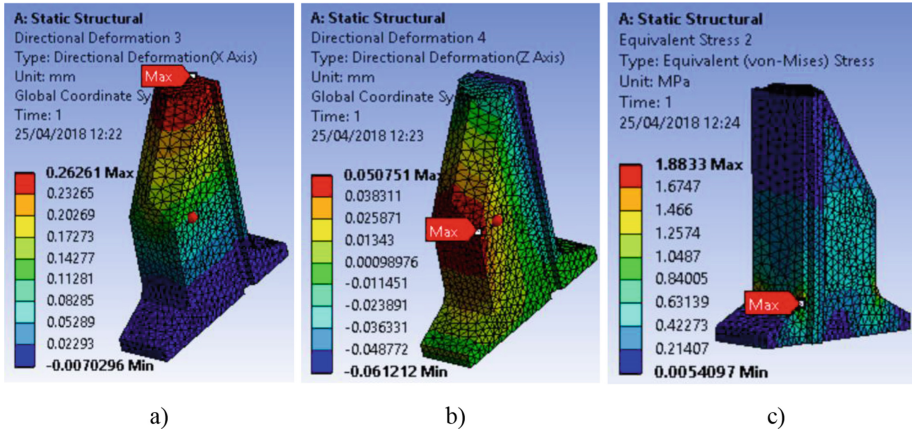


Fig. 7. Results are calculated in ANSYS with 9900 tetrahedral elements: (a) X-direction displacements, (b) Z-direction displacements, (c) von-Mises stress.

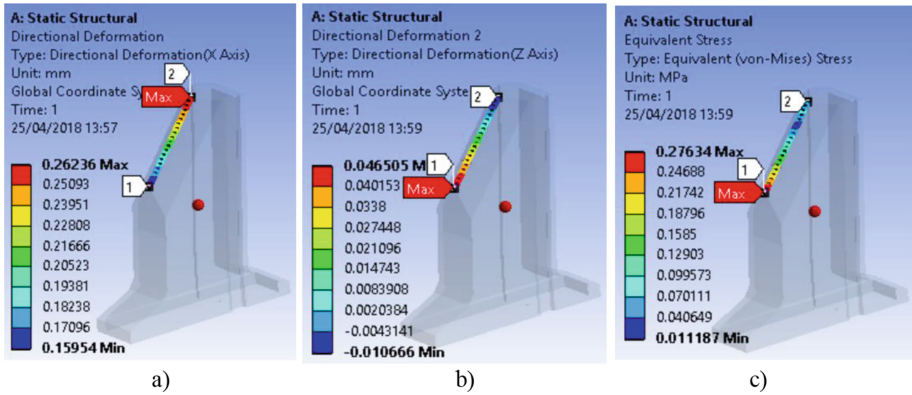


Fig. 8. Results of edge 1–2 with 9900 tetrahedral elements: (a) X-direction displacements, (b) Z-direction displacements, (c) von-Mises stress.

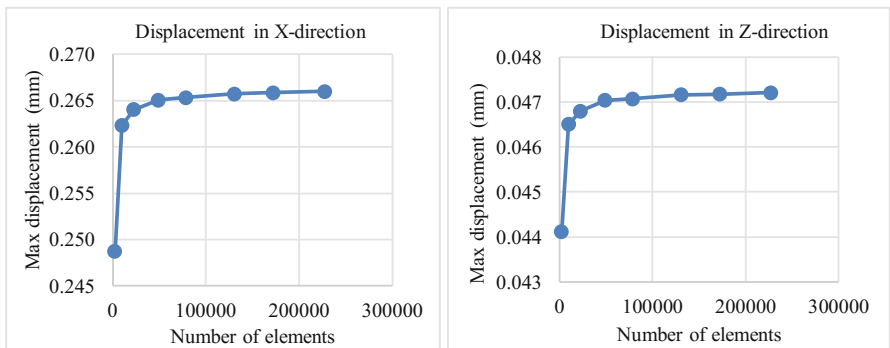


Fig. 9. Convergence of maximum displacement of edge 1–2: (a) X-direction displacement, (b) Z-direction displacement.

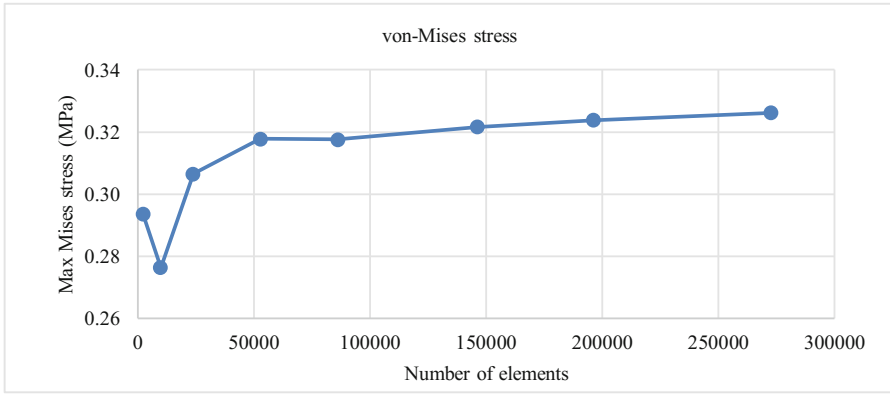


Fig. 10. Convergence of maximum equivalent von-Mises stress of edge 1–2.

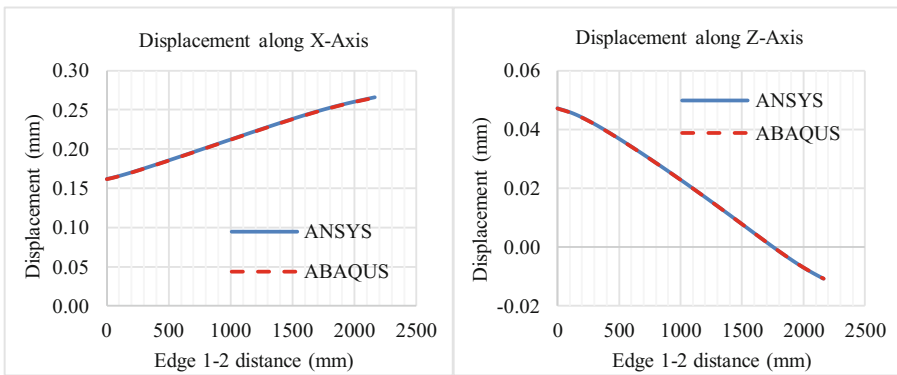


Fig. 11. Displacement along the edge 1–2: (a) X-direction displacement, (b) Z-direction displacement.

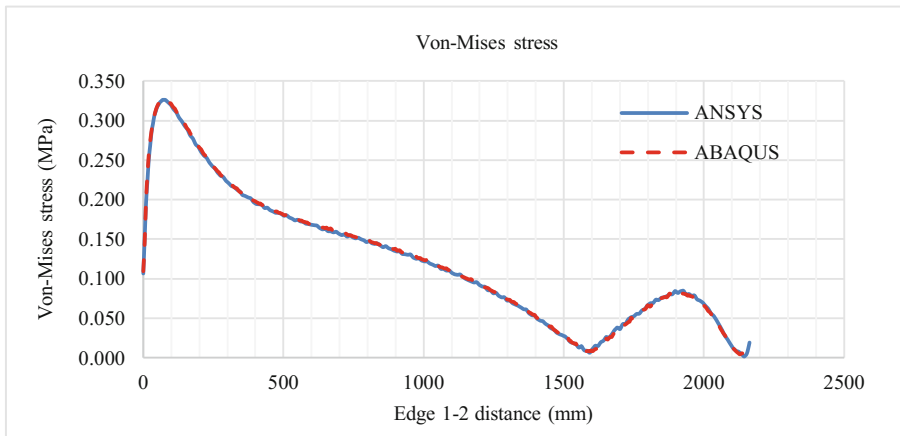


Fig. 12. Equivalent stress along edge 1–2.

Table 2. Convergence values of displacements and von-Mises stress of edge 1-2 according to the number of elements and nodes.

Number of elements	Number of nodes	Max displacement (mm)		Mises stress (MPa)	Percentage of difference (%)		
		X	Z		X	Z	Stress
2258	4438	0.2487	0.0441	0.2935			
9900	18348	0.2624	0.0465	0.2763	5.20	5.13	6.21
23915	44846	0.2640	0.0468	0.3065	0.62	0.67	9.84
52766	94674	0.2650	0.0470	0.3178	0.39	0.47	3.55
86124	147685	0.2654	0.0471	0.3176	0.12	0.10	0.05
146291	241381	0.2657	0.0472	0.3216	0.15	0.16	1.25
196242	319582	0.2659	0.0472	0.3238	0.04	0.03	0.67
272695	438754	0.2660	0.0472	0.3262	0.05	0.05	0.74

4 Conclusion

Interlocking revetment is an effective solution for coastline protection in Vietnam. The new shape of interlocking block is preliminary proposed. In this study, the authors calculate the innovative hollow concrete block for the static elastic case. To study the performance of the block model, the wave force is taken into account and is equalized as distributed load acting on the surface of the block. The results show that ANSYS can effectively determine the displacements of the models by just using 10-node tetrahedral meshes (type Tet10). However, the users must determine internal stresses with care because of stress singularities. The calculation of edge 1–2 is an example of determining stress that can avoid singularity points.

Acknowledgements. The authors acknowledge the financial support of VLIR-OUS TEAM Project, VN2017TEA454A103, ‘An innovative solution to protect Vietnamese coastal riverbanks from floods and erosion’, funded by the Flemish Government.

References

- Jayaratne, M.P.R., et al.: Failure mechanisms and local scour at coastal structures induced by tsunami. *Coast. Eng. J.* **58**(4), 1640017 (2016)
- Kato, F., Suwa, Y., Watanabe, K., Hatogai, S.: Mechanisms of coastal dike failure induced by the great east Japan earthquake tsunami. *Coast. Eng. Proc.* **1**(33), 1–9 (2012)
- Mori, N., Cox, D.T., Yasuda, T., Mase, H.: Overview of the 2011 Tohoku earthquake tsunami damage and its relation to coastal protection along the Sanriku coast. *Earthq. Spectra* **29**(SUPPL), 1 (2013)
- Jayaratne, R., et al.: Predictive model for scour depth of coastal structure failures due to tsunamis. *Coast. Eng. Proc.* **1**(34), 56 (2014)
- Kato, F., Inagaki, S., Fukuhama, M.: Wave force on coastal dike due to tsunami. *Coast. Eng.* **2006**, 5150–5161 (2006)

6. Timco, G.W.: On the stability criterion for fracture in dolos-armoured breakwaters. *Coast. Eng.* **8**, 161–170 (1984)
7. Guo, L., Latham, J.P., Xiang, J.: Numerical simulation of breakages of concrete armour units using a three-dimensional fracture model in the context of the combined finite-discrete element method. *Comput. Struct.* **146**, 117–142 (2015)
8. Burcharth, H.F.: Full-scale dynamic testing of Dolosse to destruction. *Coast. Eng.* **4(C)**, 229–251 (1980)
9. Myrick, G.B., Melby, J.A.: Monitoring of Dolos Armor Units at Crescent City, California (2005)
10. Latham, J.P., et al.: Modelling of massive particulates for breakwater engineering using coupled FEMDEM and CFD. *Particuology* **6(6)**, 572–583 (2008)
11. Guo, L., Xiang, J., Latham, J.P., Izzuddin, B.: A numerical investigation of mesh sensitivity for a new three-dimensional fracture model within the combined finite-discrete element method. *Eng. Fract. Mech.* **151**, 70–91 (2016)
12. Park, S.K., Dodaran, A.A., Han, C.S., Shahmirzadi, M.E.M.: Effects of vertical wall and tetrapod weights on wave overtopping in rubble mound breakwaters under irregular wave conditions. *Int. J. Naval Archit. Ocean Eng.* **6(4)**, 947–964 (2014)
13. Zhang, Y., et al.: Experimental study on mechanism of sea-dike failure due to wave overtopping. *Appl. Ocean Res.* **68**, 171–181 (2017)
14. Truong-Thi, P., Dang-Bao, L., Abdel Wahab, M., Duong-Ngoc, H., Hoang-Duc, T., Nguyen-Xuan, H.: Analysis of fluid–structures interaction problem of revetment slope thin-walled structure using abaqus. In: *Lecture Notes in Mechanical Engineering*, vol. PartF3, pp. 917–925 (2018)
15. ANSYS, Inc.: ANSYS FLUENT Theory Guide: Release 18.2 (2017)
16. U.S Army Corps Of Engineers: Coastal Engineering Manual. *Coast. Eng. Man.*, no. August 2001, pp. 1–62 (2002)



Effects of Construction Sequence on Reinforced Concrete Building Analysis

Mutlu Secer^(✉) and Tolga Arslan

Izmir Katip Celebi University, Izmir, Turkey
{mutlu.secer,tolga.arslan}@ikc.edu.tr

Abstract. Reinforced concrete frame structures are traditionally modelled by assuming that loads are applied after building construction is completed. However, this assumption overestimates column deflections and does not represent the realistic behavior. At the present time, it is possible to model reinforced concrete structures realistically due to the development of computing technology. In this study, building construction sequence and its effects are considered and loads are applied as each floor is constructed story by story. Moreover, time-dependent effects such as creep and shrinkage are considered for evaluating the whole structural behavior and analysis outcomes are compared with conventional analysis results. Furthermore, different design code approaches for creep and shrinkage are considered and their structural effects are also evaluated. In order to assess the differences in structural responses according to these approaches, 15 story reinforced concrete frame building is designed and analyzed according to design codes. Analysis results showed that the way of structural modelling and type of analysis considerably affected column deflections and behavior of members. Thus, this study reveals the importance of computational modelling and structural assumptions in building constructions.

Keywords: Reinforced concrete building · Construction sequence
Time-dependent analysis · Creep · Shrinkage

1 Introduction

Number of multi-story buildings is continuously increasing due to population increase and economizes on land area in metropolitans. Since these buildings are closely related to densely populated cities and directly affect the life of the city, they require precision and expertise in the design and construction stages. In order to model buildings and perform realistic behavior, computational modelling and detailed analysis become forward. In conventional reinforced concrete buildings analysis, loads are applied at the end of construction stage. In practice, various loads are applied to construction story-by-story. However, it is often neglected in reinforced concrete design and it leads to unrealistic results [1, 2]. Sequential application of dead loads has a great influence on the accuracy of the analysis results. Likewise, axial deformations may occur due to time-dependent effects such as creep and shrinkage of concrete in multi-story reinforced concrete buildings as well as elastic deformations. When differential axial shortenings that occur in vertical elements are ignored, it may lead to extreme deflections and unacceptable cracks.

In order to investigate construction sequence and time-dependent effects on buildings, Kwak and Kim [3] have worked on short term and long-term loading on a 10 story RC building with analytical and experimental studies considering construction sequences using ACI method. It is stated that greater bending moments and differential column shortenings are obtained when time-dependent effects and construction sequence are considered. For the purpose of developing a practical approach, Kim and Shin [4] have proposed a method in which stories are grouped and column shortening is considered with lumped construction sequences. Although this approach provides reduction in computing time it requires some limits about lumped story size. Flexible slab systems such as flat plates, slabs of average spans or long-span joist systems those are not usually susceptible to structural damage from differential shortening of columns. Pan et al. [5] have suggested a simple incremental superposition method for buildings lower than 30 stories with flexible slab. Besides, Kim and Abdelrazaq [6] have conducted a study that examines the long-term effects of high-performance concrete usage on flat plate/slab system behavior in multi-story buildings. For monitoring the time-dependent behavior in composite structural systems, Samarakkody et al. [7] have presented a technique to utilize the differential axial deformation in high rise buildings with composite concrete filled tube columns using a 60-story building.

In this study, construction sequence and time-dependent effects are investigated and numerical analyses are performed considering a multi-story reinforced concrete building. In the analysis, construction sequence is considered and results are compared with conventional analysis outcomes. Afterwards, time-dependent effects such as creep and shrinkage are considered in reinforced concrete building analysis due to FIB MC2010 [8] for several time periods. Also, time-dependent analyses are completed using other well-known approaches as Eurocode 2 [9] and AS 3600 [10].

2 Structural Modelling of Construction Sequence and Time-Dependent Behavior

Reinforced concrete buildings are usually analyzed in a single step in the conventional analysis based on the assumption that buildings are subjected to full load when the construction is completed. In practice, dead loads due to structural members are applied in separate stages as buildings are constructed story by story as shown in Fig. 1. There is a major difference in the building behavior between the conventional approach that the loads are applied in one step and the approach that the construction steps are taken into consideration. Hence, in order to simulate the actual condition during the construction of the building, construction sequence analysis is applied. Due to development in computing technology, construction stages and construction periods can be introduced to structural models using construction sequence analysis practically. In these analyses, each floor's construction period is considered, and loadings of each story are applied consequently. Thus, the actual situation up to the completion of the building can be modelled accurately.

Modelling of construction sequence in reinforced concrete buildings gives opportunity to determine column shortenings precisely. Column shortenings in a story may affect the partitions, cladding, piping, finishes and other non-structural building

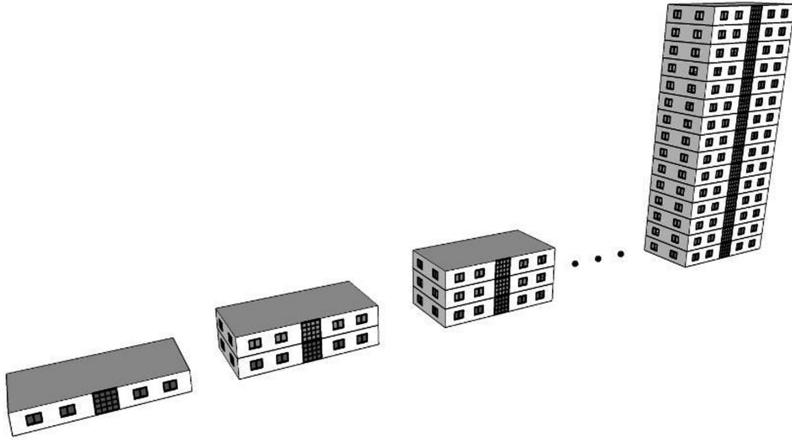


Fig. 1. Modelling of construction sequence.

components. Since these members are not generally designed to carry additional vertical loads, they should not be subjected to any shortening. On contrary, partitions can elongate from the moisture and claddings can be affected from solar radiation. Likewise, pipes can elongate if they contain hot liquids. Therefore, non-structural members and their movements relative to the reinforced concrete building should be controlled so that they should not introduce any additional problem.

On the other hand, differential shortening of columns may cause the horizontal building members to tilt with resulting rotation in walls and panels. Partitions made with modern dry-wall systems can be designed with acceptable flexibility along their edges and the vertical special joints may lead their distortions without noticeable problems. Conventional partitions such as plaster and masonry are comparatively rigid and brittle. These properties may cause substantial cracks when members undergo distortions due to shortenings in structural columns. For these reasons, building columns that have relatively high shortening values should be considered in the analysis and partitions should be designed to allow movements relative to the frames.

In addition, time-dependent effects in reinforced concrete buildings such as creep and shrinkage have remarkable influences on structural behavior. Long-term differential axial shortening of multi-story building's vertical members due to elastic deformations, shrinkage and creep may cause significant bending moments and shear forces in building floors.

Time-dependent effects can be calculated by different analysis methods according to several design codes and standards. In this study, FIB MC2010 [8], Eurocode 2 [9] and AS 3600 [10] and are considered for evaluations. Time-dependent analysis and its parameters that are influencing the behavior are summarized. Since creep parameter differs in each approach, different results may come out in calculating the time-dependent effects.

The creep coefficient for the FIB MC2010 [8] is calculated using Eq. 1.

$$\phi(t, t_0) = \phi_0 \cdot \beta_c(t, t_0) \quad (1)$$

where; $\beta_c(t, t_0)$ is the coefficient to describe the development of creep with time after loading, and ϕ_0 is the notional creep coefficient which takes in consideration the effect of relative humidity and the characteristic strength of the concrete with time [8].

Australian Standard AS 3600 [10] introduces a practical approach and the creep coefficient is calculated using Eq. 2.

$$\phi(t, t_0) = k_2 \cdot k_3 \cdot k_4 \cdot k_5 \cdot \phi_{basic} \quad (2)$$

where; ϕ_{basic} is the basic creep coefficient that is depend to compressive strength of concrete, k_2 describes the development of creep with time, k_3 depends on the age at first loading, k_4 accounts for the environmental effects and k_5 accounts for the reduced influence of both the relative humidity and the specimen size [10]. Parameters such as aggregate type, cement type and cement replacement materials are not directly accounted.

According to Eurocode 2 [9], creep coefficient $\phi(t, t_0)$ is calculated using Eq. 3.

$$\phi(t, t_0) = \phi_0 \cdot \beta_c(t, t_0) \quad (3)$$

where; ϕ_0 is the notional creep coefficient which takes in consideration relative humidity and the characteristic strength of the concrete with time and $\beta_c(t, t_0)$ is the coefficient to describe the development of creep with time after loading [9].

3 Numerical Analysis of a Reinforced Concrete Building

In order to evaluate modelling of construction sequence and time-dependent behavior in reinforced concrete buildings, a 15 story building is examined. Building is located in Turkey and it is designed according to relevant design standards and codes using STA4CAD [11] and ETABS [12]. Story height is accounted as 2.80 m and floor area is approximately 200 m². Three-dimensional model of the building model is presented in Fig. 2.

In the numerical analysis, dead loads are applied in two parts as the self-weight of the elements and permanent non-structural loads. Permanent non-structural loads are named as S-Dead load and the loads are considered as 2.5 kN/m². The floor thickness varies between 120 mm and 150 mm for the entire structure and bricks are used in partition walls. Concrete class of the reinforced concrete building is selected as C30/37 and rebar steel class is S420 as conventionally used in building region.

Formwork plan of a typical story of 15 story building and columns that are used in the analysis are shown in Fig. 3.

With the intention of investigating construction sequence and time-dependent effects on building columns, four columns are selected considering their numbers of beam connections. Two beams are connected to S1, three beams are connected to S12 and four beams are connected to S7 and S14 columns. Differences between S7 and S14

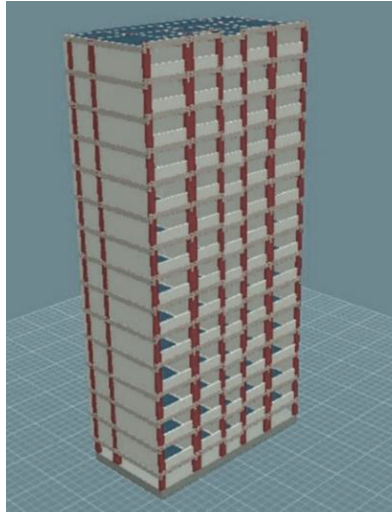


Fig. 2. Reinforced concrete building model.

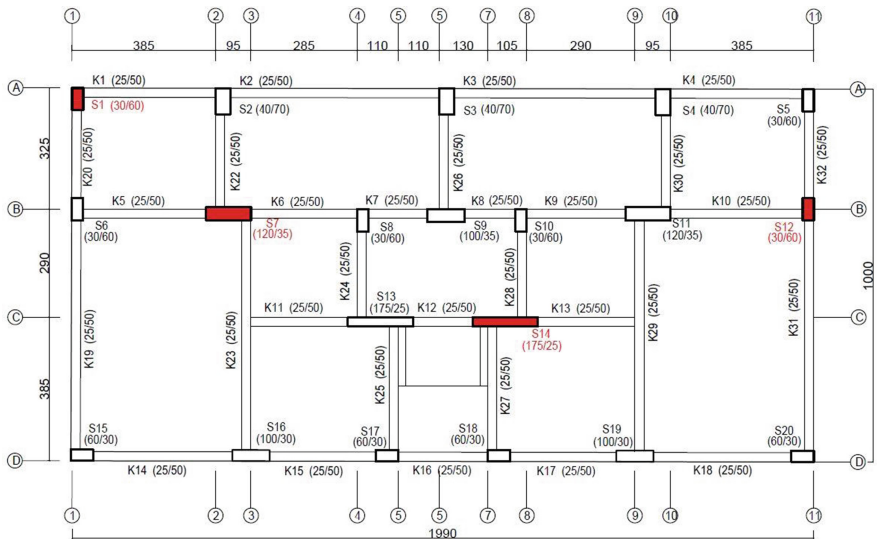


Fig. 3. Story formwork plan and selected columns.

columns are size and their structural models. S14 has greater area than S7. Also, shell elements are used in the modelling of S14 and frame elements are used in modelling of S7. In this manner, type of modelling and influence of geometric sizes are aimed to be monitored. For investigating the time-dependent effects, FIB MC2010 [8] is mainly considered in the time-dependent analysis. Different time periods are considered and the behaviors are monitored. In addition, Eurocode 2 [9] and AS 3600 [10] approaches

are used in time-dependent analysis for some time periods and analysis outcomes are used for evaluations.

3.1 Assessment of Column Displacements Considering Construction Sequence

For determining column displacements, three different calculation approaches are applied to the 15 story reinforced concrete building model and outcomes are compared. Building is analyzed considering conventional approach, construction sequence and construction sequence with time-dependent effects.

Four columns with different number of beam connections are selected for monitoring the structural behavior. Analysis results for the columns labeled as S1, S7, S12 and S14 are given in Figs. 4, 5, 6 and 7, respectively.

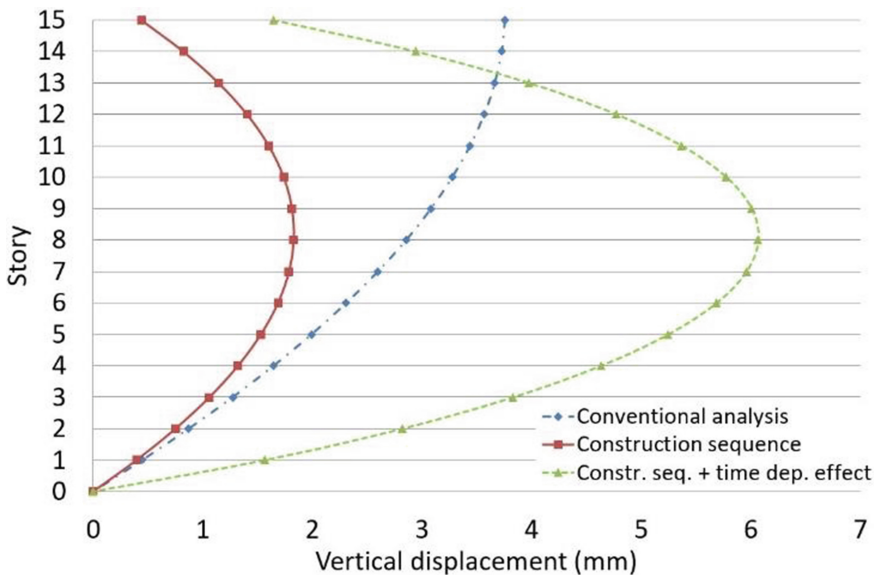


Fig. 4. Vertical displacements of S1 column.

Analysis results show that considering construction sequence give substantially different results than conventional approach. In conventional approach, vertical displacements increase with the increase in the number of the story. In construction sequence analysis, vertical displacements increase up to a story level and decrease after this level is passed. This is due to the fact that axial force levels are much higher in lower stories whereas member lengths are low and axial force levels are much lower in higher stories whereas total lengths are high. Considering construction sequence analysis provides more realistic results when the construction practice is targeted.

Moreover, time-dependent effects as creep and shrinkage are also considered in the construction sequence analysis. FIB MC2010 [8] is used in the analysis and 10 days of

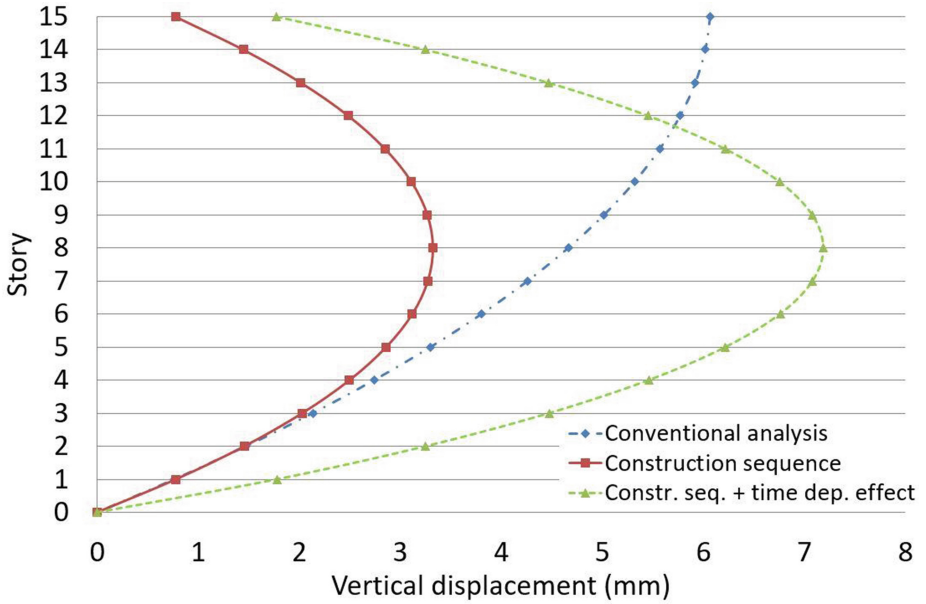


Fig. 5. Vertical displacements of S7 column.

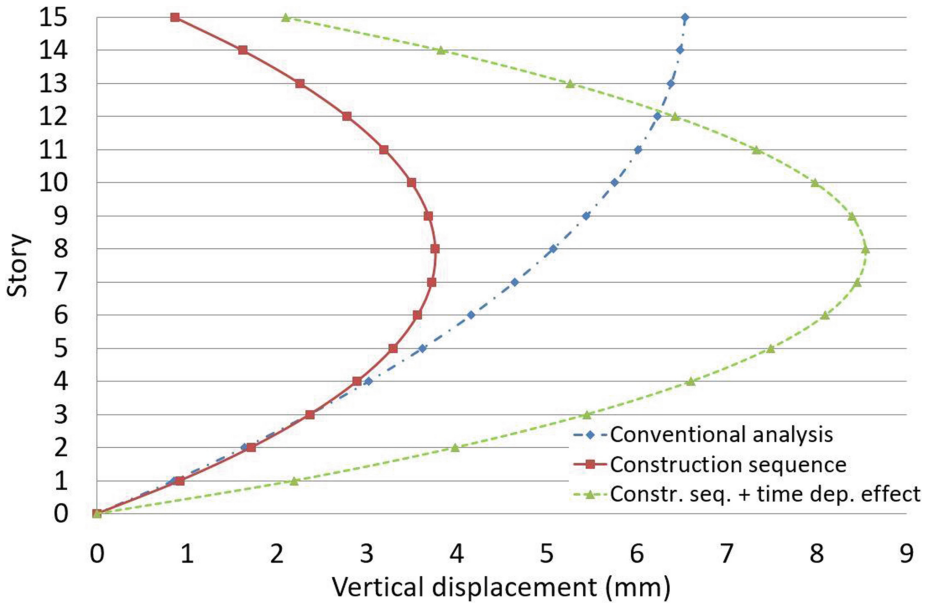


Fig. 6. Vertical displacements of S12 column.

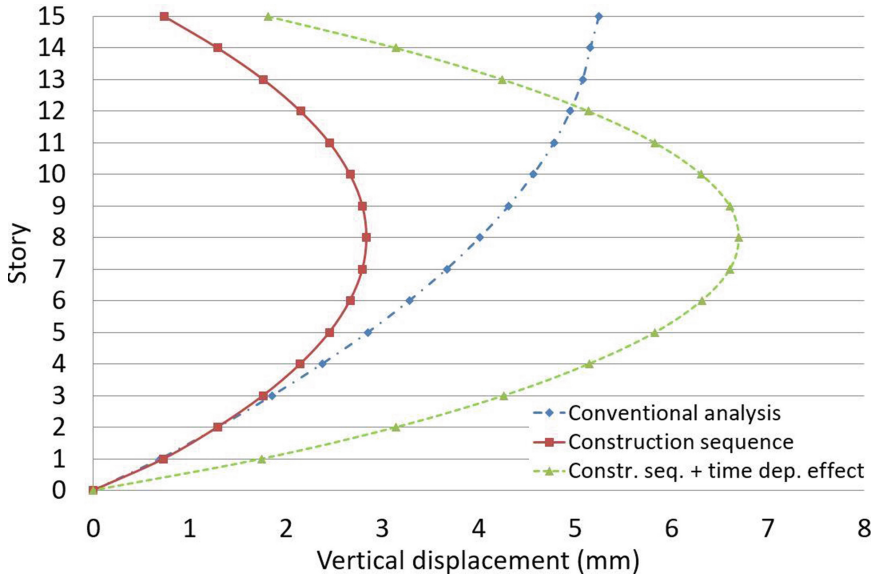


Fig. 7. Vertical displacements of S14 column.

time intervals are considered for completion of each story. Since it takes 150 days to finish the building construction, creep and shrinkage effects have influence on the column deflections as shown in the figures.

On the other hand, building columns that are selected have shown similar behavior for each analysis type.

3.2 Estimation of Time-Dependent Effects

Time-dependent effects are investigated in details for various time intervals using 15 story reinforced concrete building. Creep and shrinkage are modelled using FIB MC2010 [8] and time-dependents effects are accounted in construction sequence analysis. Time-dependent analyses are made up to 50 years considering the economic life of the reinforced concrete building. Since all investigated columns have shown similar behavior under construction sequence analysis, S7 column is selected and time-dependent analyses are performed. Vertical displacement of S7 column is presented in Fig. 8 for different time periods in terms of years.

Time-dependent analysis results of the reinforced concrete building column shows that during the initial period following the loading, the rate of creep is significant. The rate decreases due to time until it eventually approaches to a limit value. Vertical displacements of columns changed significantly and they are noticeably different than the conventional analysis.

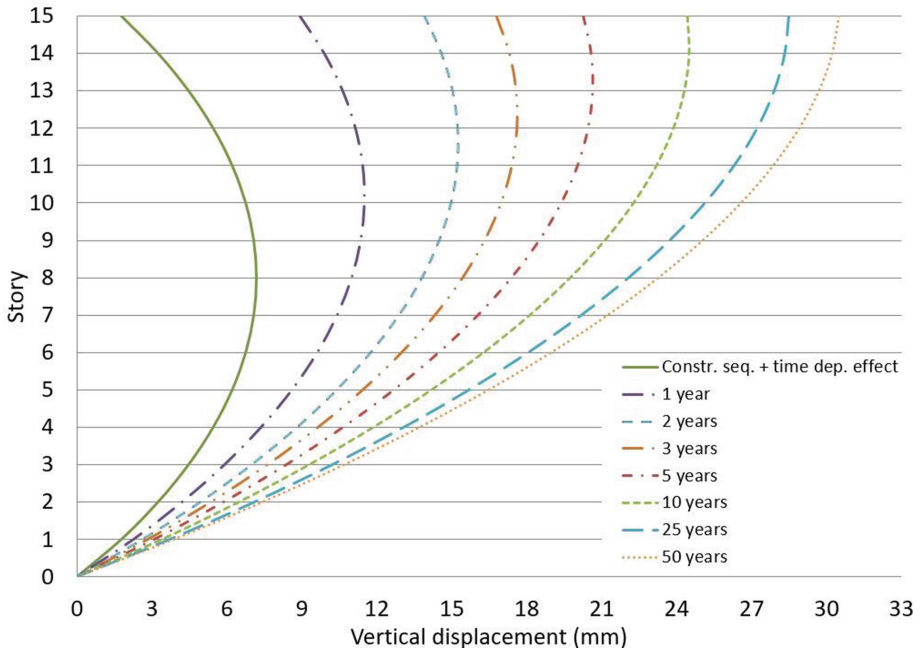


Fig. 8. Time-dependent vertical displacements of S7 column.

3.3 Evaluation of Standard and Codes for Time-Dependent Behavior

Time-dependent effects are investigated using different standard and codes considering same time periods. Eurocode 2 [9] and AS 3600 [10] approaches are also used to calculate time-dependent behavior of S7 column. Afterwards, these analyses outcomes are compared with the results of FIB MC2010 [8].

Parameters used in the numerical analysis for FIB MC2010 [8] are; 58% relative humidity, 3 days of curing, 30 MPa compression strength and 42.5R cement type. Likewise, almost same parameters are used in Eurocode 2 [9]. Besides, parameters that are used in AS 3600 [10] are 0.0006 basic drying shrinkage, 3 days of curing, 1.46 for k_3 , 0.65 for k_4 , 1 for k_5 , and 3.2 for ϕ_{basic} . Variation of creep coefficients with time is given in Fig. 9.

Time-dependent vertical displacements of column S7 are given in Figs. 10 and 11 considering Eurocode 2 [9] and AS 3600 [10] with FIB MC2010 [8] for same time periods.

Time-dependent analysis results considering FIB MC2010 [8], Eurocode 2 [9] and AS 3600 [10] show that all approaches can monitor time-dependent behavior precisely. All methods reveal that creep rate significantly affects the behavior and creep effects on the member decreases as time passes. The differences in between these methods are results of different input parameters and their influences on the creep coefficients.

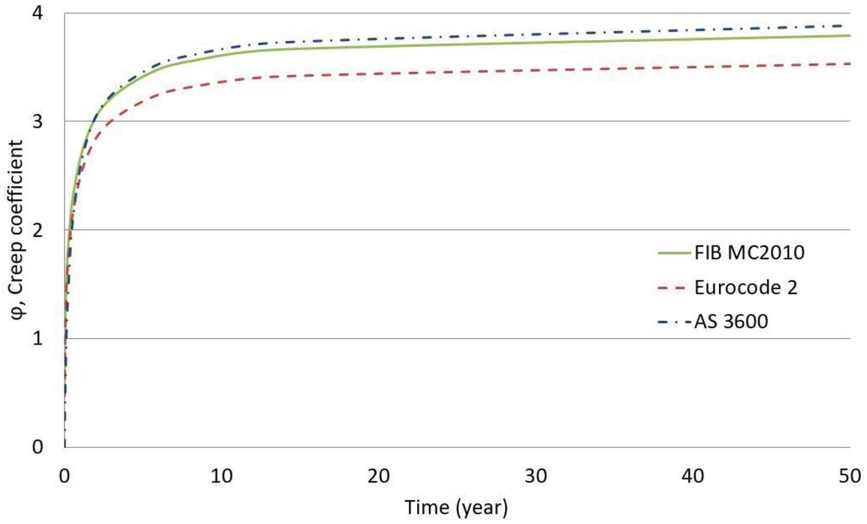


Fig. 9. Variation of creep coefficients with time.

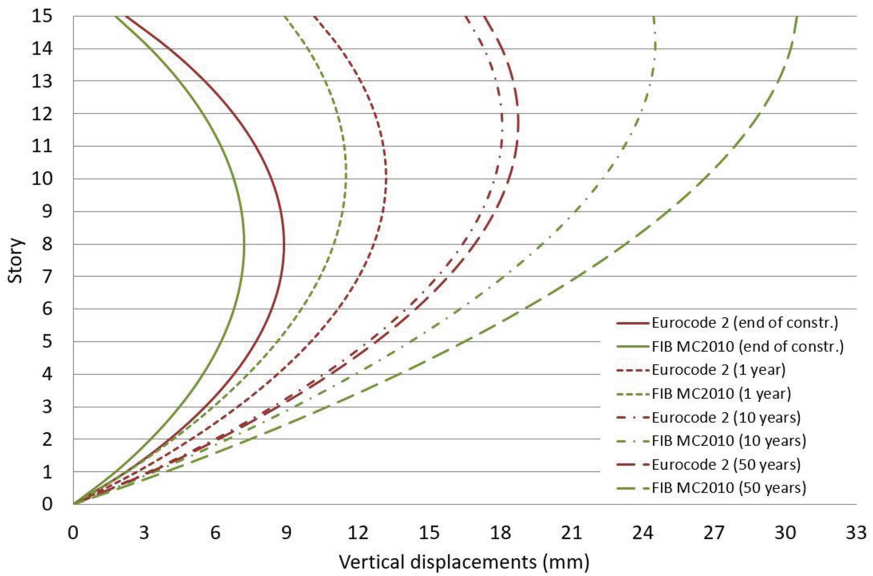


Fig. 10. Comparison between FIB MC2010 and Eurocode 2 for vertical displacements.

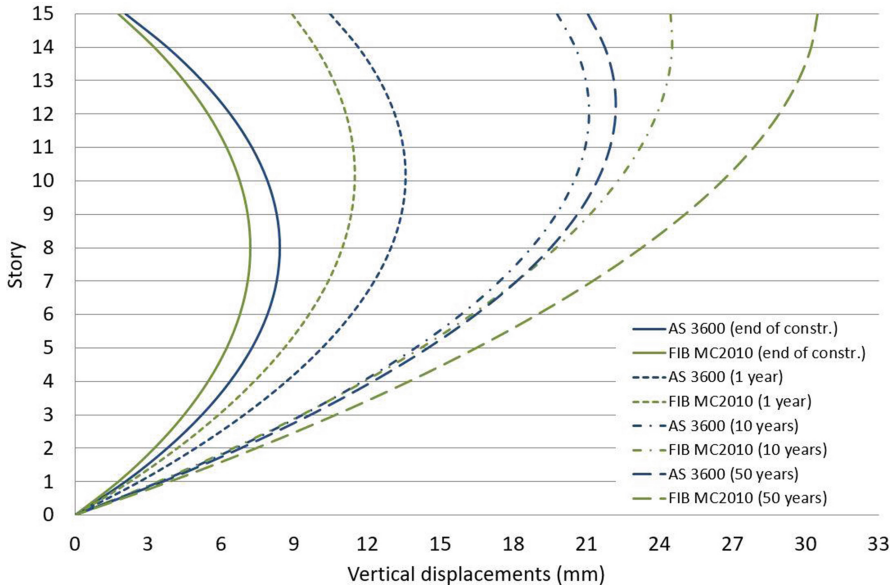


Fig. 11. Comparison between FIB MC2010 and AS 3600 for vertical displacements.

4 Conclusion

Modelling construction sequence and time-dependent effects in structural analysis plays an important role in determining realistic behavior due to the sequential and time-dependent nature of reinforced concrete building constructions. Numerical analyses of 15 story reinforced concrete building show that vertical displacements of columns have changed considerably when conventional analysis results and construction sequence analysis results are compared. Also, considering time-dependent behavior due to creep and shrinkage column shortenings increased significantly. This may cause serviceability problems in the nonstructural members located between columns that are induced by the differential column shortenings and should be considered in the design stage of these members. Additionally, time-dependent analyses are also performed for several time periods and results showed that creep rate is substantial at the initial period following the loading and it decreases due to time until it eventually approaches to a limit value. Moreover, time-dependent analyses using other well-known design standard and code approaches are performed and compared with the numerical results. Time-dependent analysis outcomes showed that results are strictly related with the input parameters and their effects on the creep behavior. Consequently, this study shows that it is necessary to consider the construction sequence and time-dependent effects in reinforced concrete building modelling if more realistic designs are desired.

References

1. Kurc, O., Lulec, A.: A comparative study on different analysis approaches for estimating the axial loads on columns and structural walls at tall buildings. *Struct. Des. Tall Spec. Build.* **22**, 485–493 (2013)
2. Au, F.T.K., Liu, C.H., Lee, P.K.K.: Creep and shrinkage analysis of reinforced concrete frames by history-adjusted and shrinkage-adjusted elasticity moduli. *Struct. Des. Tall Spec. Build.* **18**(1), 13–35 (2009)
3. Kwak, H.G., Kim, J.K.: Time-dependent analysis of RC frame structures considering construction sequences. *Build. Environ.* **41**(10), 1423–1434 (2006)
4. Kim, H.S., Shin, S.H.: Column shortening analysis with lumped construction sequences. *Procedia Eng.* **14**, 1791–1798 (2011)
5. Pan, L.B., Liu, P.C., Bakoss, S.L.: Long-term shortening of concrete columns in tall buildings. *J. Struct. Eng.* **119**(7), 2258–2262 (1993)
6. Kim, J.Y., Abdelrazaq, A.K.: Construction sequence analysis of the flat plate system in a high-rise building and its impact on the construction cycle. *Struct. Des. Tall Spec. Build.* **18**(3), 341–349 (2009)
7. Samarakkody, D.I., Thambiratnam, D.P., Chan, T.H., Moragasipitiya, P.H.: Differential axial shortening and its effects in high rise buildings with composite concrete filled tube columns. *Constr. Build. Mater.* **143**, 659–672 (2017)
8. FIB-Fédération Internationale du Béton: Model Code 2010 (first complete draft). Bulletin 55, 1(5) “Materials”, Lausanne (2010)
9. CEN, EN: Eurocode 2: Design of concrete structures. European Committee for Standardization (1992)
10. AS3600: AS3600-2009 Concrete Structures. Standards Australia (2009)
11. STA4CAD: Analysis and design manual of multi-story RC structures, V13.1. STA Computer Engineering and Consulting Company, Istanbul, Turkey (2010)
12. Computers and Structures Inc: CSI Analysis Reference Manual for ETABS. California, Berkeley (2009)



A Six-Variable Quasi-3D Model for Static Analysis of Laminated Composite Plates Using Isogeometric Analysis

Loc V. Tran¹(✉), Magd Abdel Wahab², and Jarkko Niiranen¹

¹ Department of Civil Engineering, School of Engineering,
Aalto University, Aalto, Finland
loc.tran@aalto.fi

² LaboSoete, Faculty of Engineering and Architecture,
Ghent University, Ghent, Belgium

Abstract. In this paper, a six-variable quasi-3D model is developed for laminated composite plate subjected to thermal and mechanical loadings. With higher-order terms in the displacement fields, the plate model can capture both shear deformation and thickness stretching effects. Consequently, it enables us to achieve more accurate results in deflection, shear stress distributions, which are satisfied with traction free and interlaminar continuity conditions. The governing equation is derived from Galerkin weak form and then discretized by isogeometric analysis (IGA), which utilized NURBS basis function to fulfill C^1 -continuity requirement without additional variables.

Keywords: Laminated composite plate · Isogeometric analysis
Thickness stretching effect and quasi-3D model

1 Introduction

Multi-layered structures stacked several lamina layers exhibit the distinguished properties, e.g., durability, high strength-to-weight and stiffness-to-weight ratios and so on. Thus, they are commonly used in aerospace, aircraft structures, high-speed vehicle frames, etc. due to lightweight and high stiffness characteristics. In their operations, friction between the vehicle surface and the atmosphere produces thermal loading. It leads to harmful effects due to stress concentration, cracking and de-bonding at the interface between two distinct layers or buckling, resulting in large deformation and reduction of structural stiffness. For this reason, thermal effect becomes a necessary consideration in design and analysis and has been addressed in the past few decades. For example, Noor and Burton [1] used three-dimensional (3D) elasticity to investigate the thermal buckling response of laminated composite and sandwich plates. Afterwards, Bhaskar et al. [2] extended 3D solutions for thermal bending of orthotropic and anisotropic composite laminates. However, the 3D elastic approach is a cumbersome object with highly computational cost, mathematical complexity and inability in modeling the complex geometries under arbitrary boundary conditions. In order to reduce the computational cost, the 3D theory can be simplified to 2D plate theories by

making suitable assumptions based on equivalent single layer (ESL) theory [3], which is classified as the following: the classical laminate plate theory (CLPT) [4] the first order shear deformation theory (FSDT) [5] and the higher order shear deformable theory (HSDT) [6]. In thermal environment, a constant, linear or nonlinear distributed temperature throughout the plate thickness generates a non-zero transverse normal strain. Thus, an assumption of $\sigma_z = 0$ and $\varepsilon_z = 0$ in the aforementioned 2D plate models is invalid and produces misleading results of thermal bending of composite plates. In fact, Fazzolari and Carrera [7] concluded that 3D effects cannot be neglected and accounting the transverse normal deformation is mandatory to accurately determine the thermal buckling parameter of thick plates. To remove the inconsistency completely in 2D plate model, quasi-3D theory, which accounts thickness stretching effect, is considered. Numerous quasi-3D theories have been exploited for composite plates by Carrera et al. [8] with 15 unknown variables, Ganapathi and Makhecha [9] with 13 variables, Kant and Shiyekar [10] and Matsunaga [11] based on M^{th} -order plate theory with 6 $M-1$ unknowns, Ferreira and his co-workers [12] using 9 variables and so on. Being different the aforementioned works, the present quasi-3D model is obtained by enhancing HSDT [13] with one additional variable in the transverse displacement. Consequently, this model considers shear deformation as well as thickness stretching effect. It helps to reduce the number of displacement variables to six but the model requires C^1 -continuity in approximation, an obstacle in the standard finite element formulations. Fortunately, Hughes and his co-worker, who proposed an efficient numerical method, so-called isogeometric analysis (IGA) [14], which utilizes the basis functions in geometric representation (e.g. B-Spline and non-uniform rational B-Spline (NURBS)) with higher-order smoothness and continuity, e.g., C^{p-1} continuity by using p^{th} degree. Hence, by incorporating IGA in the present quasi-3D plate model, C^1 -continuity requirement is naturally fulfilled without any additional variables.

2 The Plate Formulation Based on Quasi-3D Model in Conjunction with Isogeometric Analysis

2.1 Quasi-3D Model for Laminate Composite Plate Formulation

In 2D plate theory, the displacement components are represented as a combination of the unknown variables at mid-plane of plate, $\Omega \subset \mathbb{R}^2$ and the functions of thickness as follows

$$\begin{aligned} u(x, y, z) &= u_0 - zw_{0,x} + f(z)\phi_x \\ v(x, y, z) &= v_0 - zw_{0,x} + f(z)\phi_y, \\ w(x, y, z) &= w_0 + g(z)\phi_z \end{aligned} \quad \left(\frac{-h}{2} \leq z \leq \frac{h}{2} \right) \quad (1)$$

where $\{u_0, v_0, w_0\}$ denote the axial displacements at the middle-plane Ω and $\{\phi_x, \phi_y\}$ are the rotations of normal to middle-plane in the y - z , x - z planes, respectively. Meanwhile, an additional variable ϕ_z is introduced to account the stretching effect in the thickness direction. It makes sure of nonzero transverse normal strain ($\varepsilon_z \neq 0$). For sake of brevity, the distributed function $f(z)$ (listed in Ref. [13]) is chosen as an odd

function and $g(z) = f'(z)$ is an even function, which describes the distribution of thickness stretching effect through plate thickness.

$$\begin{aligned} \boldsymbol{\varepsilon} &= [\varepsilon_x \ \varepsilon_y \ \gamma_{xy} \ \varepsilon_z]^T = \begin{Bmatrix} \boldsymbol{\varepsilon}_1 \\ 0 \end{Bmatrix} + z \begin{Bmatrix} \boldsymbol{\varepsilon}_2 \\ 0 \end{Bmatrix} + f(z) \begin{Bmatrix} \boldsymbol{\varepsilon}_3 \\ 0 \end{Bmatrix} + g'(z) \begin{Bmatrix} \mathbf{0} \\ \phi_z \end{Bmatrix} \\ \boldsymbol{\gamma} &= [\gamma_{xz} \ \gamma_{yz}]^T = f'(z) \boldsymbol{\varepsilon}_s + g(z) \boldsymbol{\kappa}_s \end{aligned} \tag{2}$$

The constitutive equation for each lamina k^{th} in the structural reference system (x, y, z) can be described by Hooke's law as

$$\boldsymbol{\sigma}^{(k)} = \mathbf{Q}^{(k)} (\boldsymbol{\varepsilon} - \boldsymbol{\varepsilon}_{th})^{(k)} \quad \text{and} \quad \boldsymbol{\tau}^{(k)} = \mathbf{Q}_s^{(k)} \boldsymbol{\gamma}^{(k)} \tag{3}$$

where Q_{ij} are the fully transformed material constants in the structural coordinate [3] and thermal strain is given by

$$(\boldsymbol{\varepsilon}_{th})^T = [\alpha_x \ \alpha_y \ \alpha_{xy} \ \alpha_z] \Delta T \tag{4}$$

in which α_i is the thermal coefficient of expansion and ΔT is the temperature change.

The governing equation for the composite plate is derived from the principle of virtual displacement as [13]

$$\begin{aligned} &\int_{\Omega} \left(\begin{Bmatrix} \boldsymbol{\varepsilon}_1 \\ \boldsymbol{\varepsilon}_2 \\ \boldsymbol{\varepsilon}_3 \\ \phi_z \end{Bmatrix}^T \begin{bmatrix} \mathbf{A} & \mathbf{B} & \mathbf{E} & \mathbf{A}_3 \\ \mathbf{B} & \mathbf{D} & \mathbf{F} & \mathbf{B}_3 \\ \mathbf{E} & \mathbf{F} & \mathbf{H} & \mathbf{E}_3 \\ \mathbf{A}_3^T & \mathbf{B}_3^T & \mathbf{E}_3^T & H_3 \end{bmatrix} \delta \begin{Bmatrix} \boldsymbol{\varepsilon}_1 \\ \boldsymbol{\varepsilon}_2 \\ \boldsymbol{\varepsilon}_3 \\ \phi_z \end{Bmatrix} + \begin{Bmatrix} \boldsymbol{\varepsilon}_s \\ \boldsymbol{\kappa}_s \end{Bmatrix}^T \begin{bmatrix} \mathbf{A}^s & \mathbf{B}^s \\ \mathbf{B}^s & \mathbf{D}^s \end{bmatrix} \delta \begin{Bmatrix} \boldsymbol{\varepsilon}_s \\ \boldsymbol{\kappa}_s \end{Bmatrix} \right) d\Omega \\ &= \int_{\Omega} \left(\begin{Bmatrix} f_x \\ f_y \\ f_z \end{Bmatrix}^T \delta \begin{Bmatrix} u_0 \\ v_0 \\ w_0 \end{Bmatrix} + \begin{Bmatrix} \mathbf{N}_{th} \\ \mathbf{M}_{th} \\ \mathbf{P}_{th} \\ \mathbf{O}_{th} \end{Bmatrix}^T \delta \begin{Bmatrix} \boldsymbol{\varepsilon}_1 \\ \boldsymbol{\varepsilon}_2 \\ \boldsymbol{\varepsilon}_3 \\ \phi_z \end{Bmatrix} \right) d\Omega \end{aligned} \tag{5}$$

where f_i is the applied load according to i -direction and thermal stress resultants are expressed as

$$\begin{aligned} \{ \mathbf{N}_{th} \ \mathbf{M}_{th} \ \mathbf{P}_{th} \} &= \int_{-h/2}^{h/2} \mathbf{Q}(\boldsymbol{\varepsilon}_{th})^T \{ 1 \ z \ z^3 \} \Delta T dz, \\ \mathbf{O}_{th} &= \int_{-h/2}^{h/2} g'(z) \mathbf{Q}_{3i}(\boldsymbol{\varepsilon}_{th})^T \Delta T dz \end{aligned} \tag{6}$$



2.2 Isogeometric Finite Element for Plate Formulation

Let's start with the B-spline function, $N_i^p(\xi)$ which is a piecewise polynomial of degree p defined following to a recursive formula with a unit step function at beginning

$$\text{At } p \geq 1, \quad N_i^p(\xi) = \frac{\xi - \xi_i}{\xi_{i+p} - \xi_i} N_i^{p-1}(\xi) + \frac{\xi_{i+p+1} - \xi}{\xi_{i+p+1} - \xi_{i+1}} N_{i+1}^{p-1}(\xi) \quad (7)$$

A bivariate NURBS function is obtained by a tensor product of two univariate B-splines $N_i^p(\xi)$ and $M_j^q(\eta)$ with polynomial degrees of p and q , respectively in conjunction with the control weights ζ_{ij} corresponding to each individual control point.

$$R_{ij}^{pq}(\xi, \eta) = \frac{N_i^p(\xi)M_j^q(\eta)\zeta_{ij}}{\sum_i \sum_j N_i^p(\xi)M_j^q(\eta)\zeta_{ij}} \quad (8)$$

More importantly, B-Spline is a special case of NURBS with constant weight value, $\zeta_{ij} = \text{const}$. As pointed out in Ref. [14], NURBS has an important feature that is NURBS can achieve at least C^{p-1} continuity whole NURBS patch except its boundaries. Therefore, with higher-order degree, $p \geq 2$, NURBS-based isogeometric analysis naturally fulfils C^1 -continuity requirement of the present plate theory without any additional variables.

Using NURBS basis functions in Eq. (8), the displacement fields are approximated as

$$\mathbf{u}^h(\xi) = \sum_A R_A(\xi) \mathbf{q}_A \quad (9)$$

where $\mathbf{q}_A = [u_{0A} \ v_{0A} \ w_{0A} \ \phi_{xA} \ \phi_{yA} \ \phi_{zA}]^T$ denotes the vector of nodal degrees of freedom (DoF) associated with the control point A .

Substituting Eq. (9) into the strain-displacement relations Eq. (2), the in-plane and shear strains can be revealed as

$$\begin{aligned} \hat{\boldsymbol{\epsilon}}^T &= \sum_A \left[(\mathbf{B}_A^{b1})^T \ (\mathbf{B}_A^{b2})^T \ (\mathbf{B}_A^{b3})^T \ (\mathbf{B}_A^{b4})^T \right]^T \mathbf{q}_A, \\ \hat{\boldsymbol{\epsilon}}_s^T &= \sum_A \left[(\mathbf{B}_A^{s0})^T \ (\mathbf{B}_A^{s1})^T \right]^T \mathbf{q}_A \end{aligned} \quad (10)$$

Substituting Eq. (10) into the strain-displacement relations Eq. (5), the bending formulation of laminated composite plate can be described in form of the linear algebraic equation as follows

$$\mathbf{Kq} = \mathbf{F} \quad (11)$$



3 Numerical Results

In this section, we study the bending behavior of a three-layer $[0^\circ/90^\circ/0^\circ]$ square laminated composite plate with material properties for each lamina as: $E_L/E_T = 25$, $G_{LT}/E_T = 0.5$, $G_{TT}/E_T = 0.2$, $\nu_{LT} = \nu_{TT} = 0.25$. In which, L and T refer to the directions parallel and perpendicular, respectively, to the fiber orientation.

3.1 Plate Under Mechanical Load

Let us first consider a simply supported square laminated composite plate in the dimensions of $L \times W \times h$ subjected to a sinusoidally distributed load, $q = q_0 \sin(\frac{\pi x}{L}) \sin(\frac{\pi y}{W})$. First of all, the shear-locking test is studied through investigating the effect of length-to-thickness ratio, L/h on the central deflection, $\bar{w}(\frac{L}{2}, \frac{W}{2}, 0)$ and shear stress, $\bar{\tau}_{xz}(0, \frac{W}{2}, 0)$ plotted in Fig. 1. As seen, both of HSDT and quasi-3D models considerably overestimate the deflection and underestimate the stress as compared to the CLPT ones [16]. They all become unchanged as L/h increases. So, it can be concluded that they are free from shear locking. An important thing here is, the present model produces better shear stress as compared to the counterpart. For clearer observation, Fig. 2 plots the stress distributions of a thick composite plate ($L/h = 4$) via different plate theories. As seen, the present quasi-3D model seems to be an enhancement of HSDT [15] in achieving better shape of shear stresses with local continuity at the layer interfaces. While HSDT produces the piecewise stress distributions in whole plate thickness. It is worth noting that the maximum value of shear stress $\bar{\tau}_{xz}$ does not locate at $z = 0$ as mentioned in Ref. [15] using 5 unknown variables HSDT.

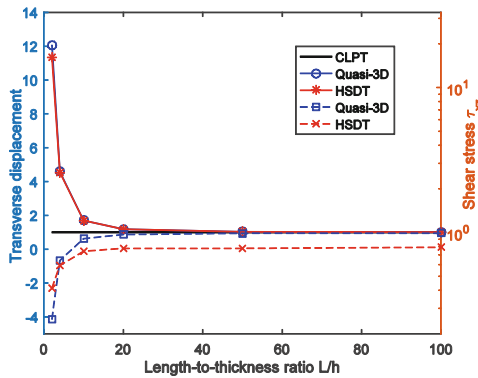


Fig. 1. Central deflection \bar{w} (solid lines) and shear stress $\bar{\tau}_{xz}$ (dash lines) of $[0^\circ/90^\circ/0^\circ]$ plate via L/h ratios.



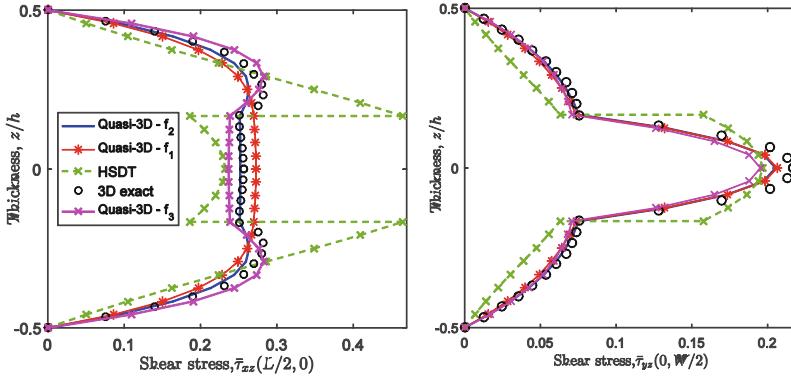


Fig. 2. Shear stress distribution with $L/h = 4$: $\bar{\tau}_{xz}$ (left) and $\bar{\tau}_{yz}$ (right) from 3D elastic solution, present quasi-3D (solid line) and HSDT (dash line).

3.2 Plate Under Sinusoidally Distributed Temperature

Next, thermal elastic bending of square composite plate subjected to gradient temperature $\Delta T(x, y, z) = \frac{2T_1}{h} z \sin(\frac{\pi}{L}x) \sin(\frac{\pi}{W}y)$ is investigated. The thermal anisotropy $\alpha_T/\alpha_L = 1125$ is set. Figure 3 shows the comparisons of u -displacement and deflection obtained from HSDT, quasi-3D and 3D elastic solution [2]. As observed, the transverse displacement is sensitive to change of length-to-thickness, L/h ratio. The quasi-3D present model produces the curves of displacements which are identical with 3D elastic theory while HSDT significantly underestimates results for thick plate ($L/h = 4$) with relative error up to 20% for $\bar{u}(\pm \frac{h}{2})$ and 39% for $\bar{w}(\pm \frac{h}{2})$. Regarding the shear stresses, the present model again achieves the better results with satisfaction of the traction free condition at the lateral surfaces and the inter-laminar continuity condition at the layer interfaces as shown in Fig. 4.

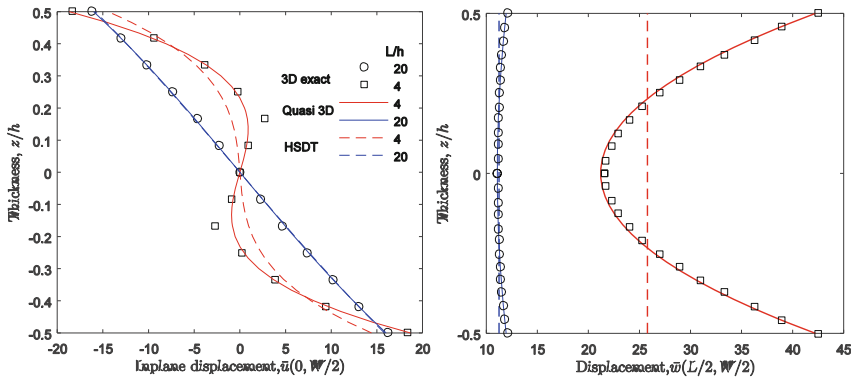


Fig. 3. Comparison of in-plane displacement \bar{u} (left) and transverse deflection \bar{w} (right) in three-layer $[0^\circ/90^\circ/0^\circ]$ plate subjected to gradient temperature with 3D elastic solution.

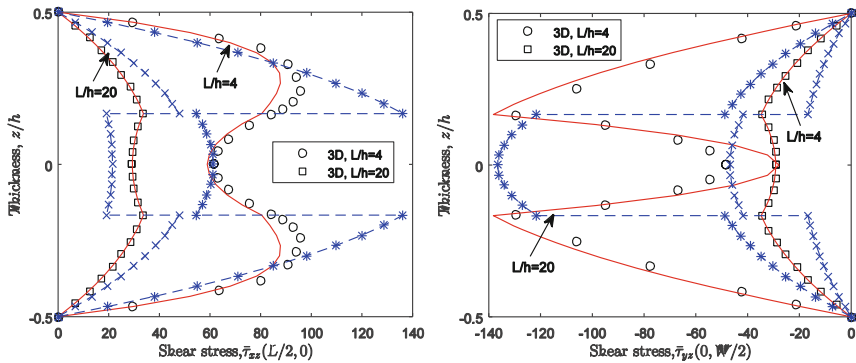


Fig. 4. Shear stress distribution of $\bar{\tau}_{xz}(L/2, 0)$ (left) and $\bar{\tau}_{yz}(0, W/2)$ (right) obtained from 3D elastic solution, present quasi-3D model (solid line) and HSDT model (dash line).

4 Conclusions

In this paper, the isogeometric finite element approach is developed to study bending behavior of laminated composite plates based on a six-variable quasi-3D plate model. With one more additional variable, the present model can capture both of shear deformation and thickness stretching effects. As a result, it is free with shear-locking and enhances the solution of HSDT [15] with more identical results to 3D exact solutions, especially for the shear stresses with satisfaction of traction free condition at the lateral surfaces and the continuity condition at the layer interfaces.

References

1. Noor, A.K., Burton, W.S.: Three-dimensional solutions for thermal buckling of multilayered anisotropic plates. *J. Eng. Mech.* **118**(4), 683–701 (1992)
2. Bhaskar, K., Varadan, T., Ali, J.: Thermoelastic solutions for orthotropic and anisotropic composite laminates. *Compos. Part B Eng.* **27**(5), 415–420 (1996)
3. Reddy, J.N.: *Mechanics of Laminated Composite Plates-Theory and Analysis*, 2nd edn. CRC Press, New York (2004)
4. Wu, C., Tauchert, T.: Thermoelastic analysis of laminated plates. I: Symmetric specially orthotropic laminates. *J. Therm. Stresses* **3**(2), 247–259 (1980)
5. Rolfes, R., Noor, A., Sparr, H.: Evaluation of transverse thermal stresses in composite plates based on first-order shear deformation theory. *Comput. Methods Appl. Mech. Eng.* **167**(3–4), 355–368 (1998)
6. Kant, T., Khare, R.: Finite element thermal stress analysis of composite laminates using a higher-order theory. *J. Therm. Stresses* **17**(2), 229–255 (1994)
7. Fazzolari, F.A., Carrera, E.: Thermo-mechanical buckling analysis of anisotropic multilayered composite and sandwich plates by using refined variable-kinematics theories. *J. Therm. Stresses* **36**(4), 321–350 (2013)
8. Carrera, E., Miglioretti, F., Petrolo, M.: Accuracy of refined finite elements for laminated plate analysis. *Compos. Struct.* **93**(5), 1311–1327 (2011)

9. Ganapathi, M., Makhecha, D.: Free vibration analysis of multi-layered composite laminates based on an accurate higher-order theory. *Compos. Part B Eng.* **32**(6), 535–543 (2001)
10. Kant, T., Shiyekar, S.: An assessment of a higher order theory for composite laminates subjected to thermal gradient. *Compos. Struct.* **96**, 698–707 (2013)
11. Matsunaga, H.: Thermal buckling of cross-ply laminated composite and sandwich plates according to a global higher-order deformation theory. *Compos. Struct.* **68**(4), 439–454 (2005)
12. Ferreira, A.J.M., Roque, C., Carrera, E., Cinefra, M., Polit, O.: Analysis of sandwich plates by radial basis functions collocation, according to Murakami's Zig-Zag theory. *J. Sandwich Struct. Mater.* **14**(5), 505–524 (2012)
13. Thai, C.H., Kulasegaram, S., Tran, L.V., Nguyen-Xuan, H.: Generalized shear deformation theory for functionally graded isotropic and sandwich plates based on isogeometric approach. *Comput. Struct.* **141**, 94–112 (2014)
14. Hughes, T.J.R., Cottrell, J.A., Bazilevs, Y.: Isogeometric analysis: CAD, finite elements, NURBS, exact geometry and mesh refinement. *Comput. Methods Appl. Mech. Eng.* **194** (39–41), 4135–4195 (2005)
15. Thai, C.H., Ferreira, A.J.M., Bordas, S.P.A., Rabczuk, T., Nguyen-Xuan, H.: Isogeometric analysis of laminated composite and sandwich plates using a new inverse trigonometric shear deformation theory. *Eur. J. Mech. A/Solids* **43**, 89–108 (2014)
16. Pagano, N.: Exact solutions for rectangular bidirectional composites and sandwich plates. *J. Compos. Mater.* **4**(1), 20–34 (1970)



The Rock Failure Behavior Analysis in Rock Cutting Using Finite Element Analysis

Weiji Liu^{1,2}, Xiaohua Zhu², Yunlai Zhou^{3(✉)}, Quanmin Liu⁴,
and Magd Abdel Wahab⁵

¹ The Key Laboratory of Well Stability and Fluid and Rock Mechanics in Oil and Gas Reservoir of Shaanxi Province, Xi'an Shiyou University, Xi'an, China

² School of Mechatronic Engineering,

Southwest Petroleum University, Chengdu, China

³ Department of Civil and Environmental Engineering,
National University of Singapore, Singapore, Singapore
zhouyunlail68168@gmail.com

⁴ Engineering Research Center of Railway Environmental Vibration and Noise of the Ministry of Education, East China Jiaotong University, Nanchang, China

⁵ Soete Laboratory, Faculty of Engineering and Architecture,
Ghent University, Ghent, Belgium

Abstract. Rock cutting in various forms is used in mining and civil engineering area such as oil & gas drilling, tunneling etc. The detailed understand of the rock cutting mechanism is quite essential to the bit design and parameters selection. This study constructed the finite element model of rock cutting to investigate the crack initiation and propagation, chips formation and cutting force, and the effect of cutting depth on rock breaking mechanism is also analyzed. The results show that cutting depth plays an important role in the rock failure behavior, when the cutting depth is shallow, the ductile failure mode is dominated and brittle failure mode is dominated at the larger depth of cut. The cutting force increases linearly with the depth increase of cut when cutting depth is shallow; however, the nonlinearity of cutting force increase appeared when the depth of cut exceeds the threshold value. The magnitude of MSE tends to decrease with the depth increase of cut and tends to stabilize when the depth of cut reaches a certain value. The results obtained in this study can lead to an enhanced understanding of rock breaking mechanisms in rock cutting.

Keywords: Rock cutting · FEM · Crack initiation · Chip formation
MSE

1 Introduction

Polycrystalline diamond compact (PDC) bit has been extensively used in the oil and gas exploitation, due to its advantages of higher efficiency of rock breaking, longer life and higher reliability and so on. According to statistics, the drill footage of PDC bit has accounted for the total length of 90% in the global scope [1, 2]. Therefore, it is

extremely important to study its rock breaking mechanism, which can offer a beneficial reference for the bit design and cutting parameters determination.

The direct way to study the rock cutting mechanism is experimental tests, because it can obtain the reliable results; however, the experimental tests must be conducted under the extremely strict environment, besides, it is also a waste of time and money. In contrast, the numerical simulation method offers a convenient way to study the rock cutting mechanism, and the numerical methods like discrete element method (DEM) [3–5], finite element method (FEM) [6, 7] and displacement discontinuity method (DDM) [8, 9] etc. are widely used. Among them, the FEM is the most commonly applied method. Menezes et al. [10] simulated the chip formation process during rock cutting by using an explicit finite element (FE) code, LS-DYNA. Chen et al. [11] studied the chip formation and force responses in two-dimensional orthogonal cutting of rock. Jaime et al. [12] developed a FE procedure to research the fracture process and propagation of quasi-brittle rock. Martinez et al. [13] carried out a series of numerical experiments to observe the cutting process under different geometrical conditions. Da Fontoura et al. [14] described one two-dimensional and one three-dimensional FE model of rock cutting to simulate the cutting process, and the confining pressure, large deformation and high strain rate are considered. Zhou and Li [15] first demonstrated that Bazant's simple size effect equation for quasi-brittle material fit rock cutting data well. Mohammadnejad et al. [16] predicted the crack initiation and propagation during rock cutting by using FEM, which takes into account the mix-mode I-II fracture criteria.

Many literature have been found to use FEM to investigate the rock cutting process above, however, the rock cutting mechanism is still not clear enough. The objective of this paper is revealing the crack initiation and propagation, chips formation and cutting force, and the effect of cutting depth on rock breaking mechanism. For this purpose, the numerical simulation model of rock cutting is developed, and a series of numerical simulation are carried out. This study leads to an enhanced understanding of rock breaking mechanisms in rock cutting.

2 FE Model of Rock Cutting

The numerical setup for rock cutting by a single cutter is shown in Fig. 1, the rock specimen has a length of 40 mm, a height of 20 mm and a thickness of 0.15 mm. The Drucker-Prager constitutive model with an isotropic damage model is used for the rock mode to study the rock failure modes. The cutter is treated as a rigid body. In order to better simulate the rock cutting process and rock chips formation process, those meshes contacting to cutter are enough fine with a size of 0.15 mm, in contrast, the meshes far away from the cutter are relatively coarse. The type of the meshes is C3D6 (6-node linear triangular prism). The cutter moves forward with a constant velocity, V , and the cutting depth is d , the rake angle of cutter is γ . All nodes at the bottom side of the rock sample are restricted in Y direction, and the left and right sides are restricted in X direction, the obverse and reverse of the specimen are restricted in Z direction.

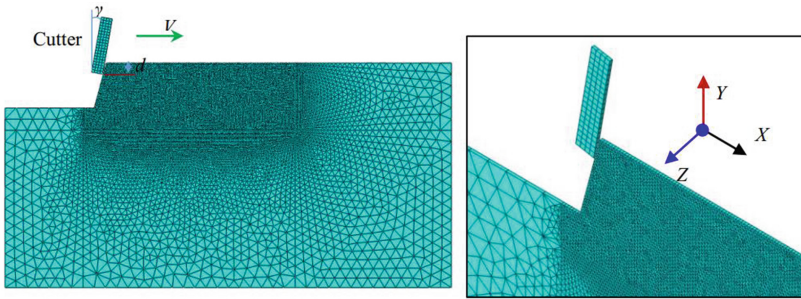


Fig. 1. The numerical simulation model of rock cutting

3 Results and Discussion

Figure 2 is the failure mode of rock under different cutting depth, the different colors in the figure represents the damage value of rock. The initiation and development of the damage rely on the plastic strain value of rock element. When the damage value equals to “0”, it indicates the rock sample is intact. When the damage value is “1”, the rock element will fully lost the strength and stiffness, and separate from the intact rock. It can be inferred from the figure that cutting depth plays an important role in chip formation. There has no chips formation when the cutting depth is shallow, and the ductile failure mode is dominated. As the increase of cutting depth, the larger chips will form and the ductile failure mode of rock transition to brittle failure mode. The larger the cutting depth the larger the chips would be.

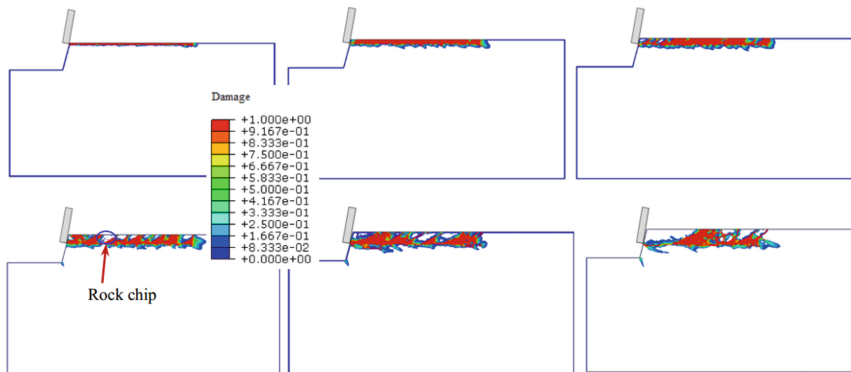


Fig. 2. The failure mode of rock under different cutting depth

Figure 3 shows the crack initiation and propagation, chip formation process in rock cutting. The crack initiates at the earlier stage of cutter-rock interaction, then the crack propagates with the cutter moving forward, at last, the crack propagates cross the free surface of rock sample with the chip formation, and the chip separates from the intact rock eventually.

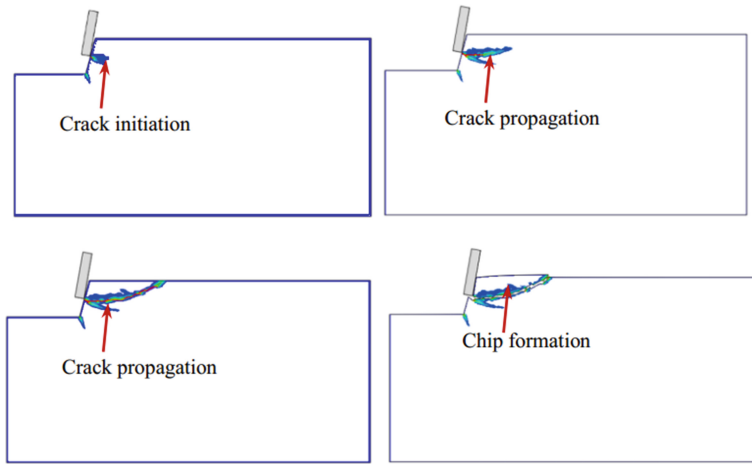


Fig. 3. The crack initiation and propagation process in rock cutting

Figure 4 illustrates the cutting force curve under two different cutting depths, when the cutting depth is shallow with a value of 0.1 mm, the cutting force has a high variation frequency and low amplitude. In contrast, the phenomenon of low variation frequency and high amplitude of cutting force is presented when the cutting depth is 2 mm. During the rock cutting process, the cutting force will significantly increase when the cutter crushes the rock, and then drops abruptly with the chip formation.

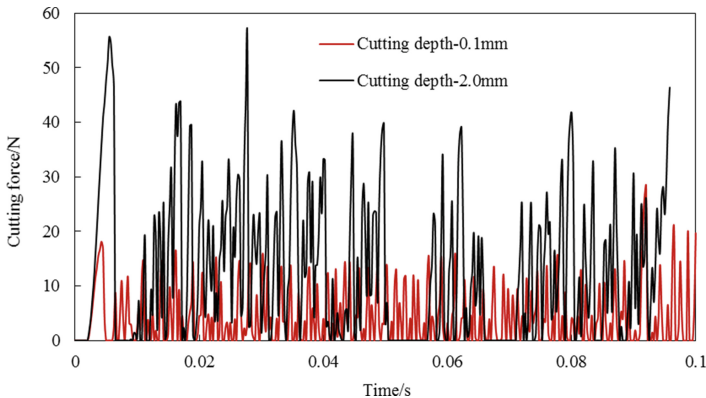


Fig. 4. The cutting force under different depth of cut

The average cutting force under different depth of cut are plotted in Fig. 5, it can be seen that the cutting force increases linearly with the increasing of depth of cut until the cutting depth exceeds a threshold value. However, the nonlinearity of cutting force increases is presented when the depth of cut exceeds the threshold value.

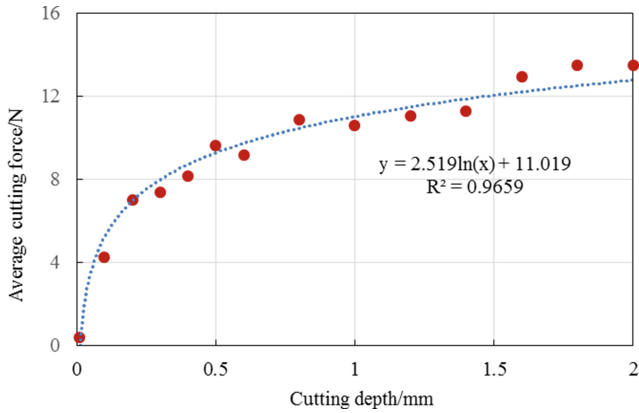


Fig. 5. The average cutting force under different depth of cut

The mechanical specific energy (MSE) is depicted in Fig. 6. It illustrates that the magnitude of MSE tends to decrease with the depth increase of cut and tends to stabilize when the depth of cut reaches a certain value. Although the cutting force and the volume of moved rock are increasing with the depth of cut increase, the MSE presents a totally different behavior, decreasing with the cutting depth increase. It indicates that the ductile failure mode without big chips formation of rock has a low rock breaking efficiency; on the contrary, the ductile failure mode with large chips formation will cause a low magnitude of MSE, as a result, the rock breaking efficiency is improved. In a word, the ductile failure mode of rock is what we expected during drilling.

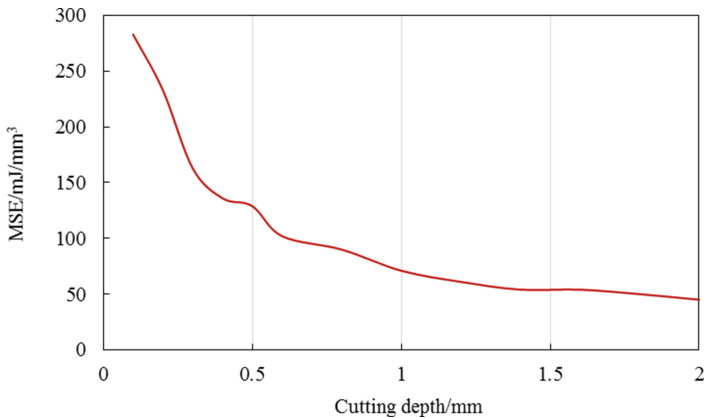


Fig. 6. The average cutting force under different depth of cut

4 Conclusions

This study used the FE model of rock cutting to investigate the crack initiation and propagation, chips formation and cutting force, and the effect of cutting depth on rock failure behavior as well. The following conclusions can be obtained:

Cutting depth plays an important role in the rock failure behavior. When the cutting depth is shallow, the ductile failure mode is dominated. As the cutting depth increases, the larger chips will be formed and the brittle failure mode is dominant. The larger the cutting depth is, the larger the chips would be.

The cutting force increases linearly with the depth increase of cut until the cutting depth exceeds a threshold value. However, the nonlinearity of cutting force increases appeared when the cut depth exceeds the threshold value.

The magnitude of MSE tends to decrease with the depth increase of cut and tends to stabilize when the depth of cut reaches a certain value.

Acknowledgment. This work reported in this paper was supported by key laboratory of well stability and fluid & rock mechanics in Oil and gas reservoir of Shaanxi Province, Xi'an Shiyou University (No. WSFRM20180102001), National Natural Science Foundation of China (Grant No. 51674214), Youth Science and Technology Innovation Research Team of Sichuan Province (2017TD0014). Such supports are greatly appreciated by the authors.

References

1. Yang, Y.X.: Research on Cutting Mechanics of PDC bit. Southwest Petroleum University (2003)
2. Zhu, R.Q.: International advancement of drilling bits for oil and gas well (3)—PDC bits progress and present trend. *Explor. Eng. Rock Soil Drill. Tunn.* **43**(3), 1–8 (2016)
3. Helmons, R.L.J., Miedema, S.A., van Rhee, C.: Modelling the effect of water depth on rock cutting processes with the use of discrete element method. *Terra et Aqua* **142**, 17–24 (2016)
4. He, X., Xu, C.: Discrete element modelling of rock cutting: from ductile to brittle transition. *Int. J. Numer. Anal. Meth. Geomech.* **39**(12), 1331–1351 (2015)
5. Liu, W., Zhu, X., Jing, J.: The analysis of ductile-brittle failure mode transition in rock cutting. *J. Petrol. Sci. Eng.* **163**, 311–319 (2018)
6. Labra, C., Rojek, J., Oñate, E.: Discrete/finite element modelling of rock cutting with a TBM disc cutter. *Rock Mech. Rock Eng.* **50**(3), 621–638 (2017)
7. Yari, N., Kapitaniak, M., Vaziri, V., et al.: Calibrated FEM modelling of rock cutting with PDC cutter. In: *MATEC Web of Conferences* (2018)
8. Wu, K., Olson, J.E.: A simplified three-dimensional displacement discontinuity method for multiple fracture simulations. *Int. J. Fract.* **193**(2), 191–204 (2015)
9. Marji, M.F.: Simulation of crack coalescence mechanism underneath single and double disc cutters by higher order displacement discontinuity method. *J. Cent. S. Univ.* **22**(3), 1045–1054 (2015)
10. Menezes, P.L., Lovell, M.R., Lin, J.S., et al.: Finite element modeling of discontinuous chip formation during rock cutting In: *ASME/STLE 2009 International Joint Tribology Conference*, pp. 463–465. American Society of Mechanical Engineers (2009)

11. Chen, D., et al.: Finite element study on chip formation and force response in two-dimensional orthogonal cutting of rock. In: ASME 2014 International Manufacturing Science and Engineering Conference collocated with the JSME 2014 International Conference on Materials and Processing and the 42nd North American Manufacturing Research Conference, pp. V002T02A038–V002T02A038. American Society of Mechanical Engineers (2014)
12. Jaime, M.C., Zhou, Y., Lin, J.S., et al.: Finite element modeling of rock cutting and its fragmentation process. *Int. J. Rock Mech. Min. Sci.* **80**, 137–146 (2015)
13. Martinez, I.M.R., Fontoura, S., Inoue, N., et al.: Simulation of single cutter experiments in evaporites through finite element method. In: SPE/IADC Drilling Conference and Exhibition held in Amsterdam, The Netherlands, pp. 5–7 (2013)
14. Da Fontoura, S.A.B., Inoue, N., Martinez, I.M.R, et al.: Rock mechanics aspects of drill bit rock interaction. In: 12th ISRM Congress, International Society for Rock Mechanics (2011)
15. Zhou, Y., Lin, J.S.: On the critical failure mode transition depth for rock cutting. *Int. J. Rock Mech. Min. Sci.* **62**, 131–137 (2013)
16. Mohammadnejad, M., Liu, H., Dehkoda, S., et al.: Numerical investigation of dynamic rock fragmentation in mechanical cutting using combined FEM/DEM. In: 3rd Nordic Rock Mechanics Symposium-NRMS 2017, International Society for Rock Mechanics and Rock Engineering (2017)



Coupled Thermal and Mechanical Analysis of Composite Cross Sections During Concrete Hydration Using Mathematical Optimization Strategies

Marcel Helmrich^(✉), Christopher Taube, and Guido Morgenthal

Department Simulation and Modelling of Structures, Bauhaus-Universität Weimar, 99421 Weimar, Germany

marcel.helmrich@uni-weimar.de

<http://www.uni-weimar.de/Bauing/MSK>

Abstract. The thermal and mechanical behavior of young concrete is highly nonlinear. In this article, a new simulation approach for the thermal and mechanical analysis of composite cross sections is shown, which uses energy principles and mathematical optimization algorithms as a consistent physical and methodical base. For the thermal analysis, an energy functional is developed by using the virtual source energy, while the mechanical analysis is performed by minimizing the potential energy. The changes in the thermal strain caused by the temperature differences are considered in the mechanical analysis as tension free pre-strain. By adding the maximum tensile strain to the mechanical material parameter evolution, the flip over of the residual stresses as well as cracking and its development over time can be represented. Furthermore, to reduce the number of unknowns without reducing the approximation order, numerical time integration methods of dynamics are applied to the thermal analysis.

Keywords: Composite cross sections · Hydration
Transient thermal analysis · Nonlinear mechanical analysis
Energy principles · Optimization task

1 Introduction

Structures are exposed to many different thermal effects, e.g. solar radiation, fire impact or the influence of internal energy sources such as the concrete hardening. These effects lead to mechanical deformations and, if such are prevented, they cause internal stresses, which can be significant for the bearing capacity or the durability of the structure. Especially cracks, which arise during the concrete hardening, can influence the durability of the structure before the structure is used, such that reinforcement is necessary in areas, where no structural reinforcement is needed. This is contrasted with a resource efficient and ecological

design approach, which is becoming more and more important. Since the hydration phase of the concrete is just a short stage of the whole life cycle of the structure, a precise calculation with more realistic results can impede an over design of the structure. The processing power of today's computer hardware allows to consider the nonlinear thermal and mechanical material behavior to achieve accurate results for the unequal temperature distribution in the cross section and the residual stresses.

The thermal as well as the mechanical material parameters are dependent on the degree of hydration, which can be described as a function of the released heat during the concrete hardening process. Since only the temperature field, but not the results of the mechanical analysis, influence the released hydration heat and the deformation are expected to be neglectable small, an one-dimensional coupling of the two analyses is chosen. On that basis, the workflow of the calculation process can be described with three main steps.

The first step is the determination of the temperature field in each point of the cross section at every time step. Since an analytical solution of the heat equation exists only for a few cases, numerical approximation has to be used. Besides the classical approaches such as the finite element method (FEM) or the finite difference method (FDM) [1], the temperature distribution can be calculated with the minimization of the total thermal energy. The energy functional Φ , which takes the nonlinear thermal material behavior, the boundary conditions and the internal energy sources into account, is developed by using the virtual source energy. The stability and efficiency of the optimization algorithm can be influenced by the number of unknowns, which, in turn, affect the approximation grade and the accuracy of the result. To keep the approximation grade while reducing the number of unknowns, different numerical time integration methods of dynamics, such as the Newton method or the Houbolt method, are used.

After the temperatures are calculated, the coupling with the mechanical analysis is done. For this, the thermal strains and mechanical material parameters are computed for each stage of the time interval from the temperature field and the hydration grade. Last but not least, the mechanical analysis can be performed. There exist many methods to consider the nonlinear mechanical material behavior. One is the energy method with integral material behavior (EIM) developed by Raue [2,3]. With the minimization of the total potential of the cross section and under the assumption of the Bernoulli hypothesis, the stress generating strain and with this the residual stress can be achieved. Since the mechanical material parameters, e.g. the young's modulus E or the maximum tensile strain ε_{ct} , vary with each time step, the flip over of the residual stresses as well as cracking of the cross section can be observed.

2 Thermal Analysis

2.1 Heat Transfer in Incompressible Materials

By applying the first law of thermodynamics and Fourier's law of heat transfer to incompressible materials, the heat flow inside the domain Ω can be described

with the general heat equation:

$$\varrho(\vartheta) c(\vartheta) \frac{\partial \vartheta}{\partial t} = \bar{\nabla} [\lambda(\vartheta) \nabla \vartheta] + W(\vartheta, \mathbf{x}, t) \text{ in } \Omega, \quad (1)$$

with the temperature field $\vartheta = f(\mathbf{x}, t)$, the density ϱ , the specific heat capacity c , the heat conductivity λ and the internal energy source W . In the following equations, the Nabla symbol ∇ represents the partial derivation operations for calculating the gradient of a function and $\bar{\nabla}$ the operations for obtaining the divergence of a vector field. Additional to Eq. 1, initial and boundary conditions are necessary to describe the heat flow problem completely. In most cases a constant temperature distribution is chosen for the initial condition:

$$\vartheta(\mathbf{x}, t = 0) = \vartheta_0(\mathbf{x}) = \text{const.} \quad (2)$$

For the description of the boundary conditions, the boundary $\Gamma = \Gamma_1 + \Gamma_2 + \Gamma_3$ of the domain Ω is divided into three parts with different thermal boundary conditions. A schematic distribution of the domain and its boundary is shown in Fig. 1. A boundary condition of first order, a Dirichlet condition, is applied with a given temperature to Γ_1 :

$$\vartheta_{\text{boundary}} = \Theta_{\text{boundary on } \Gamma_1}. \quad (3)$$

For most applications a given heat flow density is more common than a given temperature. In these cases the boundary condition of second order, a Neumann condition, is applied to Γ_2 :

$$-\lambda \left. \frac{\partial \vartheta}{\partial \mathbf{n}} \right|_{\text{boundary}} = q_{\text{boundary on } \Gamma_2}. \quad (4)$$

The third part of Γ is used for the heat transfer between two rigid bodies, where a temperature and a heat flow density is given, such that it can be expressed by a linear combination of Γ_1 and Γ_2 .

2.2 Development of the Optimization Task

To keep the following expressions for the development of the energy functional simple, the following terms are introduced:

$$\frac{\partial(\cdot)}{\partial t} = (\dot{\cdot}), \quad \frac{\partial(\cdot)}{\partial \vartheta} = (\cdot)', \quad \kappa(\vartheta) = \frac{1}{c(\vartheta) \varrho(\vartheta)}. \quad (5)$$

By multiplying Eq. 1 with a test function e and integration over the domain Ω and the time interval $T = [t_1, t_2]$, the heat equation changes to:

$$\int_T \int_{\Omega} \left(\dot{\vartheta} - \kappa(\vartheta) \bar{\nabla} [\lambda(\vartheta) \nabla \vartheta] - \kappa(\vartheta) W \right) \delta e \, d\Omega dt = 0, \quad (6)$$

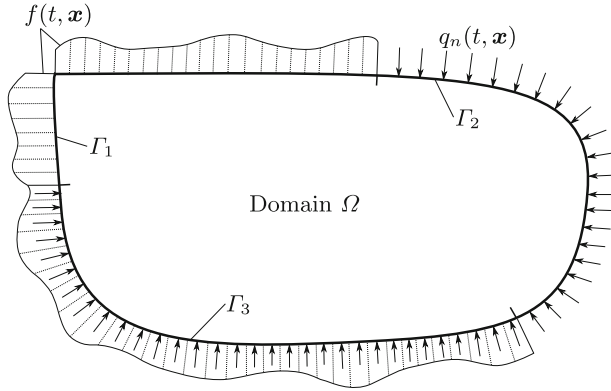


Fig. 1. Schematic domain distribution according to [4]

where the test function is defined as the virtual change of the specific thermal source energy:

$$e = \dot{\vartheta} - \kappa(\vartheta) \bar{\nabla} [\lambda(\vartheta) \nabla \vartheta]. \quad (7)$$

This expression is also called as principle of virtual source energy [4,5], which is a special form of the virtual energy transmission. With the transformation

$$\delta \int_T \int_{\Omega} \left(\frac{1}{2} e^2 - \kappa(\vartheta) W e \right) d\Omega dt = 0 \quad (8)$$

the functional can be obtained:

$$\Phi = \int_T \int_{\Omega} \left(\frac{1}{2} e^2 - \kappa(\vartheta) W e \right) d\Omega dt. \quad (9)$$

By using partial derivative and integration as well as the derivatives of the material parameters

$$\kappa'(\vartheta) = - \frac{c'(\vartheta) \varrho(\vartheta) + c(\vartheta) \varrho'(\vartheta)}{(c(\vartheta) \varrho(\vartheta))^2} \quad (10)$$

$$a'(\vartheta) = \frac{\lambda'(\vartheta) c(\vartheta) \varrho(\vartheta) - \lambda(\vartheta) c'(\vartheta) \varrho(\vartheta) - \lambda(\vartheta) c(\vartheta) \varrho'(\vartheta)}{(c(\vartheta) \varrho(\vartheta))^2}, \quad (11)$$

the energy functional can be obtained in its final form:

$$\begin{aligned}
\Phi = & - \int_T \int_{\Gamma_1} \kappa(\vartheta) \lambda(\vartheta) \dot{f}(t, \mathbf{x}) (\nabla \vartheta)^T \mathbf{n} \, d\Gamma dt + \int_T \int_{\Gamma_2} \kappa(\vartheta) q_n(t, \mathbf{x}) \dot{\vartheta} \, d\Gamma dt \\
& + \frac{1}{2} \int_{\Omega} \left(\left[\kappa(\vartheta) \lambda(\vartheta) (\nabla \vartheta)^T \nabla \vartheta \right]_{t=t_2} - \left[\kappa(\vartheta) \lambda(\vartheta) (\nabla \vartheta)^T \nabla \vartheta \right]_{t=t_1} \right) d\Omega \\
& + \int_T \int_{\Omega} \left(\frac{1}{2} \dot{\vartheta}^2 - \frac{1}{2} a'(\vartheta) \dot{\vartheta} (\nabla \vartheta)^T \nabla \vartheta + \kappa'(\vartheta) \lambda(\vartheta) \dot{\vartheta} (\nabla \vartheta)^T \nabla \vartheta \dots \right. \\
& \quad + \frac{1}{2} \kappa(\vartheta)^2 \lambda'(\vartheta)^2 \left((\nabla \vartheta)^T \nabla \vartheta \right)^2 + \frac{1}{2} \kappa(\vartheta)^2 \lambda(\vartheta)^2 (\bar{\nabla} \nabla \vartheta)^2 \dots \\
& \quad + \kappa(\vartheta)^2 \lambda'(\vartheta) \lambda(\vartheta) (\nabla \vartheta)^T \nabla \vartheta \bar{\nabla} \nabla \vartheta - \kappa(\vartheta) W \dot{\vartheta} \dots \\
& \quad \left. + \kappa(\vartheta)^2 \lambda'(\vartheta) W (\nabla \vartheta)^T \nabla \vartheta + \kappa(\vartheta)^2 \lambda(\vartheta) W \bar{\nabla} \nabla \vartheta \right) d\Omega dt. \tag{12}
\end{aligned}$$

The intermediate steps of the development of the energy functional can be taken from [6]. The functional represents the total thermal energy for the domain Ω in the time interval T with the unit $[\text{K}^2\text{m}^2/\text{s}]$ for a two-dimensional heat conduction. In order that the heat equation is satisfied, a temperature distribution has to be found, which minimizes the functional and fulfills the initial and boundary conditions. Since only one temperature field meets all these requirements, the optimization task is strictly convex [5] and has just one minimum, such that the solution can be found for any initial values of the optimization process. Normally, the optimization task can be done without additional constraints, which leads to the following optimization task:

$$\min_{\vartheta} \Phi(\vartheta). \tag{13}$$

However, additional constraints can be helpful or necessary for the optimization task, e.g. if the material parameters are only defined in a specific temperature range or if the boundary conditions should be exactly fulfilled without any tolerance. The constrained optimization task can be written as follows:

$$\min_{\vartheta} \Phi(\vartheta) \text{ with: } \begin{cases} \vartheta_{\min} \leq \vartheta \leq \vartheta_{\max} & \text{in } \Omega \\ \Theta_{\text{boundary}} = \vartheta_{\text{boundary}} & \text{on } \Gamma_1 \\ \dot{q}_{\text{boundary}} = -\lambda \frac{\partial \vartheta}{\partial \mathbf{n}} \Big|_{\text{boundary}} & \text{on } \Gamma_2. \end{cases} \tag{14}$$

2.3 Applying Time Integration Methods of Dynamics to the Thermal Analysis

For a good numerical approximation of the derivatives with respect to the Cartesian coordinates, the number of unknowns can increase rapidly, especially if the geometry is more complex. Since the discretization of the domain Ω has to be done for each point in time where the temperature field should be evaluated, the time interval is divided into sub intervals:

$$T = [t_0, t_{\text{end}}] = [t_0, t_1] \cup [t_1, t_2] \cup \dots \cup [t_{\text{end}-1}, t_{\text{end}}]. \tag{15}$$

Due to the division of the time interval, the number of unknowns can be reduced significantly, because each sub interval can be solved separately. Nevertheless, for an approximation grade of second or third order for the temperature trend over the time, more than one unknown is necessary in each point of the cross section. For this reason numerical time integration methods from dynamics are applied to the thermal analysis, such that with just one unknown in each point of the cross section a temperature trend of second or third order can be assumed. Two methods are especially numerical robust, the function value interpolation of the previous steps according to Houbolt and the acceleration approach according to Newmark. A schematic sketch for both methods is shown in Fig. 2.

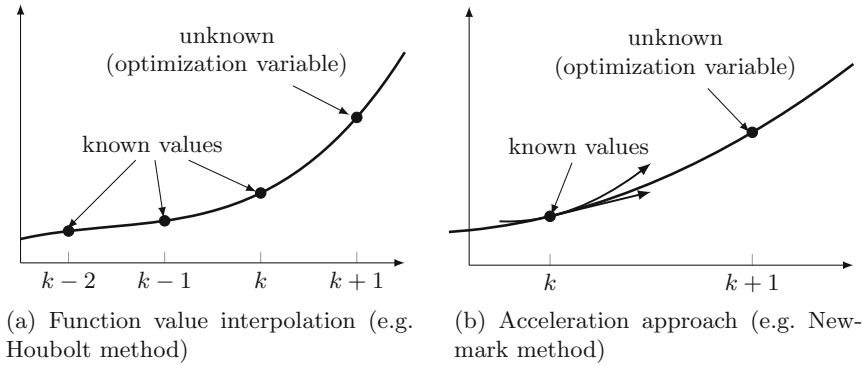


Fig. 2. Schematic sketch of the time integration methods

The Houbolt method is based on a backward Taylor series expansion, such that the function values and derivatives can be calculated as follows [7]:

$$\vartheta(\tau) = \vartheta_{t_{k+1}} - (\Delta t - \tau) \dot{\vartheta}_{t_{k+1}} + \frac{(\Delta t - \tau)^2}{2} \ddot{\vartheta}_{t_{k+1}} - \frac{(\Delta t - \tau)^3}{6} \dot{\ddot{\vartheta}}_{t_{k+1}} \quad (16)$$

$$\dot{\vartheta}(\tau) = \dot{\vartheta}_{t_{k+1}} - (\Delta t - \tau) \ddot{\vartheta}_{t_{k+1}} + \frac{(\Delta t - \tau)^2}{2} \dot{\ddot{\vartheta}}_{t_{k+1}}, \quad (17)$$

where

$$\tau \in [0, \Delta t] \quad (18)$$

$$\dot{\vartheta}_{t_{k+1}} = \frac{1}{6\Delta t} (11\vartheta_{t_{k+1}} - 18\vartheta_{t_k} + 9\vartheta_{t_{k-1}} - 2\vartheta_{t_{k-2}}) \quad (19)$$

$$\ddot{\vartheta}_{t_{k+1}} = \frac{1}{\Delta t^2} (2\vartheta_{t_{k+1}} - 5\vartheta_{t_k} + 4\vartheta_{t_{k-1}} - \vartheta_{t_{k-2}}). \quad (20)$$

The equations above are developed for a constant time step Δt , but can easily be modified for a variable one. While the Houbolt method uses the function values of the last three known time steps, the Newmark method uses only the function value and the two derivatives of the last time step and the assumption

of a constant mean acceleration for the whole time interval. With the interval variable from Eq. 18 the function value and derivatives are defined as:

$$\vartheta(\tau) = \left(1 - \frac{\tau^2}{\Delta t^2}\right) \vartheta_{t_k} + \frac{\tau^2}{\Delta t^2} \vartheta_{t_{k+1}} + \left(\tau - \frac{\tau^2}{\Delta t}\right) \dot{\vartheta}_{t_k} \tag{21}$$

$$\dot{\vartheta}(\tau) = -\frac{2\tau}{\Delta t^2} \vartheta_{t_k} + \frac{2\tau}{\Delta t^2} \vartheta_{t_{k+1}} + \left(1 - \frac{2\tau}{\Delta t}\right) \dot{\vartheta}_{t_k} \tag{22}$$

$$\ddot{\vartheta}(\tau) = -\frac{2}{\Delta t^2} \vartheta_{t_k} + \frac{2}{\Delta t^2} \vartheta_{t_{k+1}} - \frac{2}{\Delta t} \dot{\vartheta}_{t_k}. \tag{23}$$

2.4 Thermal Effect Due to the Concrete Hardening Process

To obtain a realistic result for the temperature distribution, the current temperature has to be considered for the calculation of the hydration heat, since the chemical reaction proceed faster, if the temperature is higher. The qualitative differences between isothermal and adiabatic conditions are shown in Fig. 3.

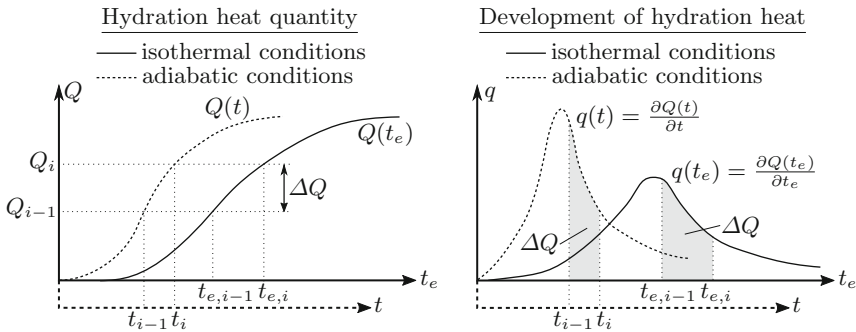


Fig. 3. Schematic comparison of the hydration process under isothermal and adiabatic experimental conditions according to [8,9]

The situation in a real structural element will always be between these two conditions. Hence, the measured heat in an experiment has to be converted to the actual temperature, which is done by using the effective age of the concrete according to Freiesleben [10]:

$$t_e = \int e^{\frac{E_A}{R} \left(\frac{1}{293} - \frac{1}{273+\vartheta}\right)} dt, \tag{24}$$

where E_A is a cement specific value and $R = 8.3143\text{J}/(\text{mol K})$. Other definitions for the effective age of the concrete can be found in [11,12]. Taking the effective concrete age into account, the hydration heat can be calculated as follows:

$$Q(t_e) = Q_0 + \alpha(t_e) Q_{\text{tot}}, \tag{25}$$

where Q_0 is the released heat directly at the beginning of the hydration process, Q_{tot} the total amount of the released heat of the whole process and α the degree of hydration with $0 \leq \alpha(t_e) \leq 1$. The function to determine the degree of hydration is obtained by curve fitting of experimental results, such as the evolution function I [13]:

$$\alpha(t_e) = \alpha_{max} \cdot e^{A \cdot \left(\frac{t_e}{t_k}\right)^B}, \tag{26}$$

with α_{max} as the the maximal possible degree of hydration based on the water-cement ratio and A, B, t_k as cement specific model parameters. Since the model parameters are approximated with experiments, which do not include all influencing factors, such as the grinding fineness of the cement, different curves for the same cement are obtained. The difference to each other in the time interval, where the temperature maximum is expected, can be up to 30% (see Fig. 4).

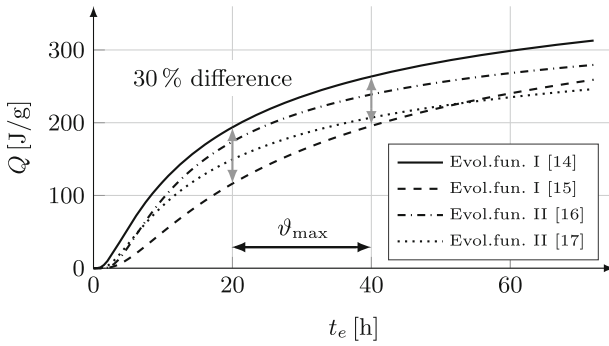


Fig. 4. Differences in the hydration heat for different evolution functions and model parameters for a CEM I 32.5 R

2.5 Evolution of the Thermal Material Parameter

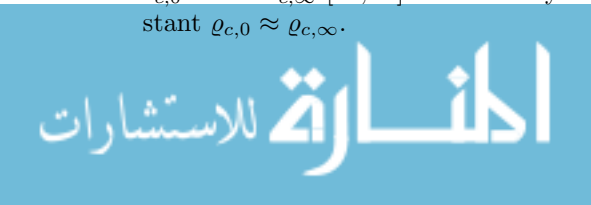
To solve the energy functional Φ , the thermal material behavior has to be described. The most used models set the material parameters in a linear relation to the degree of hydration α , such that the heat conductivity is defined as:

$$\lambda_c(\alpha) = \lambda_{c,0} - (\lambda_{c,0} - \lambda_{c,\infty}) \alpha, \tag{27}$$

where $\lambda_{c,0} = 1.4 \dots 1.5 \lambda_{c,\infty}$ [13, 18] is the heat conductivity at the begin of the concrete hardening and $\lambda_{c,\infty}$ the heat conductivity after the complete hydration. A similar relation can be found for the specific heat capacity:

$$c_c(\alpha) = c_{c,0} - (c_{c,0} - c_{c,\infty}) \alpha, \tag{28}$$

with the value for the specific heat capacity at the begin of hydration process $c_{c,0} = 1.15 c_{c,\infty}$ [13, 19]. The density is often assumed to be approximately constant $\rho_{c,0} \approx \rho_{c,\infty}$.



3 Coupling of Thermal and Mechanical Analysis

3.1 Coupling Method Employed

To choose the physically correct coupling, it is important to know in which way the two analyses influence each other. For the application, which is illustrated in this article, a one-dimensional coupling from the thermal to the mechanical analysis can be chosen. The influence of the mechanical analysis on the thermal one can be neglected, because the expected strains are small, such that the temperature field can be calculated for the initial geometry. Furthermore, the mechanical analysis does not have an impact on the hydration process within the chosen material models. The progress of the hydration depends only on the effective age of the concrete, which depends in turn on the temperature. For this reason the effective age of the concrete and the degree of hydration are just input parameters for the mechanical analysis.

3.2 Mechanical Analysis

The basic assumption for the mechanical analysis is the Bernoulli hypothesis, i.e. a linear strain distribution over the cross section area, such that the total strain of the cross section can be described as a function of the strain in the middle of the cross section and the two curvatures:

$$\varepsilon_{\text{tot}}(y, z) = \varepsilon_{\text{th}}(y, z) + \varepsilon_{\sigma}(y, z) = \varepsilon_0 + \kappa_z y + \kappa_y z, \quad (29)$$

where ε_{th} is the thermal strain and ε_{σ} the stress generating strain. With this assumption, the optimization task for the mechanical analysis can be written as:

$$\min_{\varepsilon} \Pi_{\text{tot}}(\varepsilon) \text{ with: } \Pi_{\text{tot}} = \Pi_i + \Pi_e, \varepsilon = (\varepsilon_0, \kappa_z, \kappa_y)^T. \quad (30)$$

A detailed explanation of the general principle can be found in [2,3,20]. The external potential is set for the application in this article to

$$\Pi_e = -(\varepsilon_0 N + \kappa_z M_y + \kappa_y M_z) = 0. \quad (31)$$

The internal potential Π_i , which is the integration of the internal work, is approximated based on the discretization of the thermal analysis with the fiber model:

$$\Pi_i = \int_{\Omega} W_i(\varepsilon) d\Omega \approx \sum_{(j)} W_{i,j} A_k. \quad (32)$$

Assuming a piecewise linear material behavior, the internal work for the point of time t_{k+1} in the fibre j can be calculated for the material concrete as follows:

$$W_{i,j}^{k+1} = W_{i,j}^k + \begin{cases} \sigma_{e,j}^k (\varepsilon_{\sigma,j}^{k+1} - \varepsilon_{\sigma,j}^k) \cdots & \text{for } \varepsilon_{\sigma,j}^{k+1} \leq \varepsilon_{ct,eff,j}^{k+1} \\ + \frac{1}{2} E_{\text{eff},j}^{k+1} (\varepsilon_{\sigma,j}^{k+1} - \varepsilon_{\sigma,j}^k)^2 & \\ \sigma_{e,j}^k (\varepsilon_{ct,eff,j}^{k+1} - \varepsilon_{\sigma,j}^k) \cdots & \text{for } \begin{cases} \varepsilon_{\sigma,j}^{k+1} > \varepsilon_{ct,eff,j}^{k+1} \\ \varepsilon_{\sigma,j}^k \leq \varepsilon_{ct,eff,j}^k \end{cases} \\ + \frac{1}{2} E_{\text{eff},j}^{k+1} (\varepsilon_{ct,eff,j}^{k+1} - \varepsilon_{\sigma,j}^k)^2 & \\ 0 & \text{for cracked fibres} \end{cases} \quad (33)$$

and for the material steel:

$$W_{i,j}^{k+1} = W_{i,j}^k + \sigma_{e,j}^k (\varepsilon_{\sigma,j}^{k+1} - \varepsilon_{\sigma,j}^k) + \frac{1}{2} E_{\text{eff},j}^{k+1} (\varepsilon_{\sigma,j}^{k+1} - \varepsilon_{\sigma,j}^k)^2. \quad (34)$$

Once a concrete fiber fulfills

$$\varepsilon_{\sigma,j}^{k+1} > \varepsilon_{ct,\text{eff},j}^{k+1}, \quad (35)$$

the fibre is considered as cracked. A reclosing of cracked fibers is not taken into account, such that the residual stresses are defined with the relation:

$$\sigma_{e,j}^{k+1} = \begin{cases} \sigma_{e,j}^k + E_{\text{eff},j}^{k+1} (\varepsilon_{\sigma,j}^{k+1} - \varepsilon_{\sigma,j}^k) & \text{fibre is not cracked} \\ 0 & \text{fibre is cracked.} \end{cases} \quad (36)$$

3.3 Evolution of the Mechanical Material Parameter

For the description of the mechanical material behavior, two approaches are considered. The first one takes the material parameter evolution according to the Eurocode 2 [21] into account. Since the effective age of the concrete and the degree of hydration are known from the thermal analysis, another approach without additional computational effort can be used, such that an arbitrary material parameter of the concrete X_{ci} is defined as follows [15]:

$$X_{ci}(\alpha) = \left(\frac{\alpha - \alpha_0}{1 - \alpha_0} \right)^n \cdot X_{ci}(\alpha = 1). \quad (37)$$

The exponent can be chosen as $n = 0.5$ for the young's modulus, $n = 1.0$ for the tensile strength and $n = 1.5$ for the compressive strength. The value for the degree of hydration for the begin of measurable strength can be estimated with the water-cement-ratio:

$$\alpha_0 = (0.35 \dots 0.4) \cdot w/c. \quad (38)$$

The maximum tensile strain can be calculated according to [15] either with the relation:

$$\varepsilon_{ctu,\text{eff}} = 0.03 + 0.04 f_{ct,\text{eff}} \quad (39)$$

or with the relation:

$$\varepsilon_{ctu,\text{eff}} = 1.01 \times 10^3 \frac{f_{ct,\text{eff}}}{E_{cm,\text{eff}}} + 8.4 \times 10^{-3} \quad (40)$$

or with taking the stress history into account with the relation:

$$\varepsilon_{ctu,\text{eff}}^{k+1} = \varepsilon_{\sigma}^k + \frac{f_{ct,\text{eff}}^{k+1} - \sigma_e^k}{E_{cm,\text{eff}}^{k+1}}. \quad (41)$$

4 Application

In this section an example is shown, which includes both the thermal as well as the mechanical analysis. For the example a 60 cm thick concrete wall with 2 cm wooden formwork at both sides is chosen. The concrete is set to a C20/25, CEM I 42.5 R with the following parameters: $C = 300 \text{ kg/m}^3$, $w/c = 0.6$ and $\vartheta_0 = \vartheta_{\text{air}} = 20^\circ\text{C}$. With these assumptions, the temperature distribution (see Fig. 5) can be calculated by evaluating the energy functional. For the presented results, the energy functional is approximated by a combination of finite differences, time integration methods (see Sect. 2.3) and numerical integration algorithms. Both optimization tasks, the thermal as well as the mechanical, are performed with a Quasi-Newton algorithm.

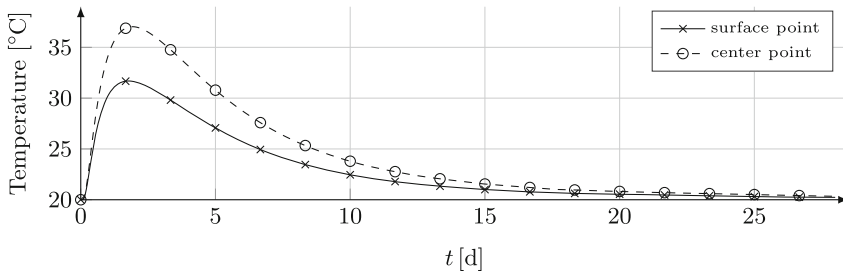


Fig. 5. Temperature distribution for the example calculated by minimizing the energy functional

Assuming that the concrete can not crack, the according residual stresses, which ensure the validity of the Bernoulli hypothesis, can be determined for different material parameter models as shown in Fig. 6.

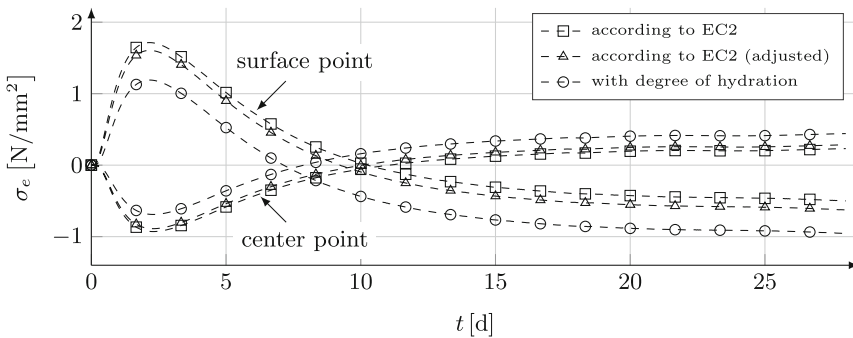


Fig. 6. Residual stresses for the example without cracking for different models of the mechanical material parameter evolution



For all material parameter models the flip over of the residual stresses is clearly recognizable. A more realistic calculation can be achieved, if cracking is added to the material parameter description. Even though the residual stresses before the flip over are smaller for the calculation of the material parameters with the degree of hydration, the cross section will crack earlier. This phenomenon is shown in Fig. 7 for the evaluation of the mechanical material parameter according to the Eurocode 2 (EC2) [21] and with the degree of hydration (DH). Furthermore, different approaches for the maximum tensile strain are applied to the analysis (Eqs. 39–41).

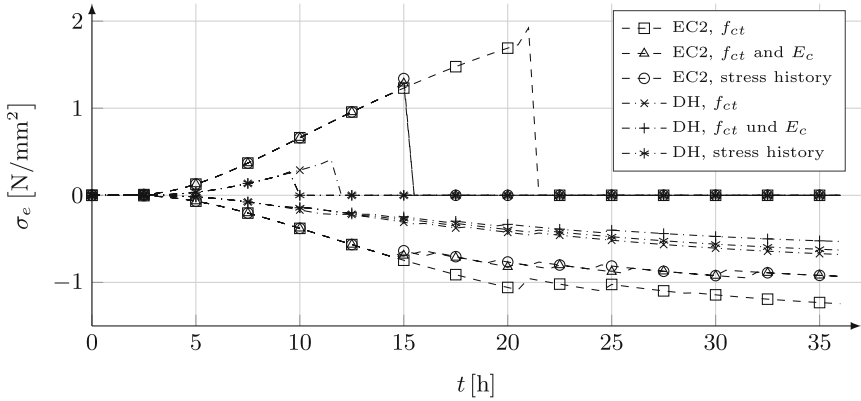


Fig. 7. Residual stresses for the example with cracking for different models for the maximum tensile strain

Because of the discretization of the cross section into fibers and the calculation of the total potential of the uncracked part of the cross section, the evolution and the total depth of a crack can be represented. Both, the evolution of the crack and its total depth, are significantly affected by the choice of the model for the mechanical material parameter evolution and for calculating the maximum tensile strain as shown in Fig. 8a. By adding reinforcement bars to the cross section, the evolution and depth of the crack can be influenced, but not the point when cracking begins (see Fig. 8b).

Since the temperature field is not significantly affected by the reinforcement bars, the thermal analysis has to be performed for each cross section just once, such that only the mechanical analysis has to be performed for the different reinforcement setups. With this procedure, the minimal required reinforcement during the concrete hardening process for the allowable crack depth and the location of the reinforcement bars can be determined. Varying both, the area and location of the reinforcement bars, the relation between the reinforcement parameters and the according crack depth can be obtained (see Fig. 9). It is further shown that results of the optimization algorithm match with required reinforcement according to the Eurocode 2 [21]. For one allowable crack width the obtained depths of the energy approach are approximately the same.

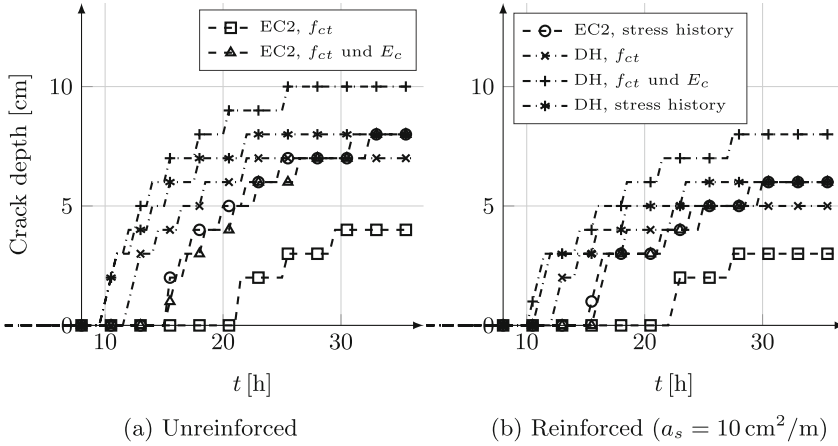


Fig. 8. Evolution of a crack for the example

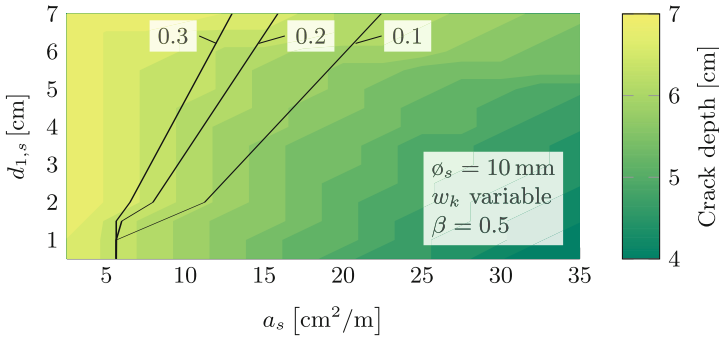


Fig. 9. Calculated crack depths with the optimization approach (area plot) compared with the required reinforcement according to the Eurocode 2 [21] (black)

5 Conclusions

This paper presents an alternative approach for a much demanded structural engineering application, the analysis of composite cross sections during the hydration phase of the concrete. By applying an energy principle to the thermal as well as to the mechanical analysis, the temperature field and residual stress distribution can be calculated using mathematical optimization strategies. The number of optimization variables for the mechanical analysis can be reduced significantly to only three unknowns by assuming the Bernoulli hypothesis. However, the number of unknowns for the thermal analysis must be kept larger, such that the temperature distribution and its derivatives can be approximated with an acceptable accuracy. Nevertheless, the number of variables for the thermal analysis can be reduced by using numerical time integration methods of dynamics and the computational effort can be minimized by guessing the

initial temperature distribution for each time step with a linear extrapolation of the previous results.

Even though this approach may require, especially for the thermal analysis, somewhat larger numerical and computational effort than traditional methods, arbitrary nonlinear parameters can be easily implemented, such that the time dependent evolution of the material parameters and cracks can be represented. Another advantage is that the introduced algorithms can be evaluated by using standard spreadsheet software for simple geometries or matrix computation software for more advanced problems.

As one application for the shown algorithm, the reinforcement design of a composite cross section for the concrete hardening process can be cross checked or the amount and location of the reinforcement bars can be optimized. Since the implemented algorithms are just for the analysis of cross sections of composite structures, further extensions to the method are required. To obtain the crack width, which is more meaningful than the calculated crack depth, an extension of the implemented algorithms is necessary, such that additional effects (e.g. tension stiffening) can be taken into account.

References

1. Baehr, H.D., Stephan, K.: Wärme- und Stoffübertragung, 8., aktualisierte Aufl. Springer Vieweg, Berlin (2013). ISBN 978-3-642-36557-7
2. Raue, E.: Nichtlineare Querschnittsanalyse als Optimierungsproblem. Ernst und Sohn Verlag, Bautechnik 82, Heft 11, pp. 796–809, Berlin (2005)
3. Raue, E., Timmler, H.-G.: Non-linear analysis of deformations of reinforced concrete elements by non-linear mathematical optimization. In: 9th International Conference “Modern building materials, structures and techniques”, Vilnius (2007). http://leidykla.vgtu.lt/conferences/MBM_2007/4pdf/Raue_Timmler2.pdf
4. Kaempf, B.: Mitteilungen aus dem Institut für Mechanik, Bd. Nr. 35: Ein Extremal-Variationsprinzip für die instationäre Wärmeleitung mit einer Anwendung auf thermoelastische Probleme unter Verwendung der finiten Elemente - Dissertation. Universität Bochum, Institut für Mechanik, Bochum (1983)
5. Mazilu, P.: Mitteilungen aus dem Institut für Mechanik, Bd. Nr. 33: Variationssprinzip der Thermoplastizität: 1. Wärmeausbreitung und Plastizität. Universität Bochum, Institut für Mechanik, Bochum (1982)
6. Taube, C., Timmler, H.-G., Helmrich, M., Morgenthal, G.: Coupled thermal and mechanical analysis of composite cross sections using mathematical optimization strategies. Eng. Struct. Technol. **9**(1), 41–51 (2017). <https://doi.org/10.3846/2029882X.2017.1299965>
7. Schwetlick, H., Kretzschmar, H.: Numerische Verfahren für Naturwissenschaftler und Ingenieure - eine computerorientierte Einführung. Fachbuchverl, Leipzig (1991). ISBN 978-3-343-00580-2
8. Laube, M.: Werkstoffmodell zur Berechnung von Temperaturspannungen in massigen Betonbauteilen im jungen Alter - Dissertation. Technische Universität Braunschweig, Braunschweig (1990)
9. Hamfler, H.: Berechnung von Temperatur-, Feuchte- und Verschiebungsfeldern in erhärtenden Betonbauteilen nach der Methode der finiten Elemente. Deutscher Ausschuss für Stahlbeton - Heft 395, Beuth Verlag GmbH, Frankfurt am Main (1988). ISBN 978-3-410-65595-4

10. Freiesleben, H., Hansen, P., Pedersen, E.J.: Maleinstrument til kontrol af betons haerding, no. 1, Nordisk Beton, Stockholm (1977)
11. Saul, A.G.A.: Principles Underlying the Steam Curing of Concrete at Atmospheric Pressure. Cement and Concrete Association, Magazine of Concrete Research (1951)
12. Springenschmid, R.: Thermal Cracking in Concrete at Early Ages - Proceedings of the International RILEM Symposium. Verlag E und FN Spon, London (1994)
13. Röhling, S.: Zwangsspannungen infolge Hydratationswärme, 2., durchgesehene und erweiterte Auflage. Edition beton, Verl. Bau und Technik, Düsseldorf (2009). ISBN 978-3-764-00500-9
14. Röhling, S.: Zwangsspannungen infolge Hydratationswärme. Edition beton, Verl. Bau und Technik, Düsseldorf (2005). ISBN 3-7640-0435-5
15. Röhling, S.: Betonbau. Band 2 - Hydratation - junger Beton - Festbeton. Fraunhofer Irb Stuttgart, Stuttgart (2012). ISBN 978-3-816-78645-0
16. Mangold, M.: Die Entwicklung von Zwang- und Eigenspannungen in Betonbauteilen während der Hydratation - Dissertation. Technische Universität München, Baustoffinst., München (1994)
17. Gutsch, A.-W.: Stoffeigenschaften jungen Betons: Versuche und Modelle - Dissertation. Bd. Heft 140, Institut für Baustoffe, Massivbau und Brandschutz, TU Braunschweig and Univ.-Bib, Braunschweig (1998). <http://www.digibib.tu-bs.de/?docid=00058591>. ISBN 3-89288-119-7
18. Bundesanstalt für Wasserbau: Rissmechanik in dicken Stahlbetonbauteilen bei abfließender Hydratationswärme - Mitteilungsblatt Nr. 92. Bundesanstalt für Wasserbau, Karlsruhe (2010). <https://www.baw.de/content/files/forschung-entwicklung/documents/A39510110124.pdf>
19. Eierle, B.: Berechnungsmodelle für rißgefährdete Betonbauteile unter frühem Temperaturzwang. Berichte aus dem Konstruktiven Ingenieurbau, Technische Universität München, Institut für Tragwerksbau, München (2000). ISSN 0941-925X
20. Schröter, H.: Nichtlineare Analyse von Verbundelementen auf der Grundlage von Energieprinzipien unter Anwendung der mathematischen Optimierung - Dissertation. Bauhaus-Universität Weimar, Weimar (2013)
21. European Committee for Standardization: EN 1992-1-1 Eurocode 2: Design of concrete structures - Part 1-1: General rules and rules for buildings. Brussels (2005)



Topology Optimization of an Interlocking Revetment Block

Hau Nguyen-Ngoc^{1,2(✉)}, Bao-Loi Dang^{1,4}, Hung Nguyen-Xuan³,
Hoang Duc Thao⁵, and Magd Abdel Wahab¹

¹ Laboratory Soete, Faculty of Engineering and Architecture,
Ghent University, Ghent, Belgium
Hau.NguyenNgoc@Ugent.be

² Faculty of Water Resources Engineering,
University of Science and Technology,
The University of Danang, Da Nang, Vietnam

³ Center for Interdisciplinary Research in Technology,
Ho Chi Minh City University of Technology (Hutech),
Ho Chi Minh City, Vietnam

⁴ Mien Trung University of Civil Engineering, Tuy Hòa, Vietnam

⁵ Ba Ria – Vung Tau Urban Sewerage and Development One Member Limited
Company (BUSADCO), Vung Tau, Vietnam

Abstract. Sea defenses are constructed to protect coastlines, embankments and artificial constructions from erosion and destruction of water actions such as wave, storm, tide and so on. However, these structures are destroyed yearly because the climate change and rising sea level induce storms, flood or even drought. The reasons of sea defense system failure can also be the out-of-date structure, which cannot withstand the rising level of water any more. Therefore, the aim of this study is to develop a new type of concrete block for interlocking revetment using topology optimization method in ANSYS 18.0, which saves about 70% of material compared to regular solid block. Topology optimization analysis cannot provide the exact solution of the concrete block shape for manufacturing, but it can be a great reference for engineering design practice.

Keywords: Interlocking revetment · Concrete block · Topology optimization
ANSYS 18.0

1 Introduction

Vietnam substantially suffers from storms and floods every year because the country totally locates in tropical climate region. Those climate actions are the most dangerous natural disasters, which not only take away properties but also human lives. In addition, Vietnam is the S-shape country with the coastline of more than 3000 km along the North to the South of the nation. Consequently, the effects of natural hazards are more severe, especially for the low-lying areas. The floods usually occur after heavy rain or during high flow river discharges. However, in Vietnam, the most dangerous disaster occurring every year is the combination of floods and winter storms. Storms arrive to Vietnamese coast around 5 times per year, which cause strong wind, high



waves and storm surges attacking severely coastal structure systems such as buildings, roads, bridges and even the protection sea dike systems. The accompanied heavy rain generating flash floods may cause landslide and wash away structures on low-land area, particularly for the delta regions. The noticeable low level of the protection of Vietnamese coastal defense systems was reported after the visit of two Dutch experts in 1996 [1]. Although the dikes in Vietnam are designed based on the boundary conditions with return period of 5% (once every 20 years), the reality failure probability is much higher than design frequency [2].

Revetment is a type of coastal defense structure, which is the armor layer protecting the land or dikes from erosion. The protection layer is usually made of rocks or prefabricated concrete blocks. Whereas, the latter are more preferable because many regions are lacking of stone supply or the materials are too far from the site. Other advantages of precast concrete blocks are that material quality, size, shape and strength of blocks are easily met through the precast process. However, revetments are damaged every year due to wave and current attack not only Vietnamese coasts but also other coasts around the world. The failure mechanisms are diverse and can be categorized into (1) the movement of armor blocks, (2) the erosion of soil of filter layer and/or cover layer, (3) the subsoil layer is unstable and (4) the revetment slides [3]. The armor concrete of the structure aims to resist the wave load, current load and internal load, which includes pore pressure, soil pressure, etc. Whereas, the protection strength is coming from block weight, friction, interlocking or tensile force. During normal cyclic wave, the damage of armor layer of revetment, which is placed on granular filter, is believed to be caused by negative pressure acting on the top of blocks. While water falls back, there is a large pressure gradient, which generated by simultaneous effect of run-down wave and current run-up wave. This pressure is dominant causing the uplift of revetment blocks [3, 4]. In the same manner, the failure mechanism of subsoil layer also leads to the damage of revetment. The total loading on the revetment induces by the wave action on cover layer and pore pressures, which corresponding to phreatic surface, in other layers of the revetment. During the wave attack, there is a fluctuated pressure acting outside the revetment, whereas deep down in the subsoil the internal force is hardly affected. In addition, while the wave runs down the pressure on the revetment reduces significantly, but somewhere in the subsoil, where the outside effects are damped, the pore pressure is kept nearly constant. This causes the pressure difference between subsoil and armor layer, which leads to uplift or slide parts of the structure. Failure mechanisms stated above are the main failure modes of placed blocks revetments, which are made of blocks placed close to each other to form an armor layer for slope.

Block mat revetment is found to be very efficient to resist those failure modes mentioned in the previous paragraph. It is made of connected blocks, which will form a "mat". The connections between blocks of the mat can consist of cables from block to block, or of interlocking parts (so-called arms and sockets) of the blocks, etc. The stability of interlocking blocks is more than that of the loose blocks revetment because the single concrete element cannot be uplifted without breaking the connection with others nearby or moving the large area of revetment. Therefore, the most popular failure mechanism of this type of structure is caused by the damage of subsoil layer, which leads to slide or collapse of armor parts. However, although the subsoil can be

seriously fail the interlocking blocks may still be reasonably connected. With this behavior, the armor layer is still able to provide a significant resistance from wave erosion, and then reduces the damage process of the whole revetment. Experiments have been carried out to study the failure mechanisms of interlocking blocks revetments due to instability [5–7]. The tested revetments consist of pattern concrete elements armor and a granular filter on top of the various subsoil embankment. Agreeing to the theory, when the wave runs down to the lowest point and the movement of water in the granular filter is relatively slow the uplift is believed to be maximum. In the case of revetment made of top layer, filter layer and subsoil core, whereas the top layer is less permeable than the filter, the uplift force acting on the armor would be high. Similarly, if the revetment has a geotextile mattress between the top layer and filter layer, the uplift force in the filter material increases significantly. Besides, the permeable capacity (filter material) of the filter layer is also a major parameter that proportionally affects the pressure beneath the armor blocks. Learning from those failure mechanisms, this study proposes a new shape of precast concrete block for interlocking revetment by using topology optimization in ANSYS software. Topology optimization is the process using mathematical formulation to optimize material inside a given domain under a specified applied loads, boundary conditions and set of constraints with the target of minimizing the material of the given structure [8].

2 Concrete Block Model

The interlocking revetment is designed to protect an estuary in Vietnam from erosion with the return period of 2%. The design water level is 4.25 m higher than the ground level. The revetment is constructed from interlocking concrete blocks. Each block is able to resist the forces generated by wave, soil pressure and not too heavy for construction managing. The details of the block subjected to topology optimization is described in Subsect. 2.2. In this case study, the interlocking revetment is working like a protection wall.

2.1 Theoretical Background

The development of topology optimization theory has been started over a century, and rapidly increased in recent decades. Besides, with the aids of modern computational methods and high performance computers, the applications of topology optimization widespread in various fields such as civil structure, solid mechanics, aerospace, etc.

The principle theory of topology optimization in ANSYS of this study is to minimize objective function of material distribution meeting the given constraints of concrete block volume. Indeed, the requirement of the problem is reached when the stiffness of the structure is maximized under given constraints. The problem is determined by using the density-based method which minimizes the objective function by identifying whether the material should be solid or void. The variable of objective function is material density

assigning to each finite element, ρ_e . Whereas, $0 \leq \rho_e \leq 1$, 0 corresponds to removed material and 1 to preserved material. The principle formulations are as follows [9]:

$$\begin{aligned} & \min : f(\rho, U) \\ & \text{subject to : } K(\rho)U = F(\rho); g_i(\rho, U) \leq 0; 0 \leq \rho \leq 1 \end{aligned} \quad (1)$$

where f is the objective function, ρ is the material density variables, K is the stiffness matrix, U is the displacement vector, F is the force vector and g_i is the specified constraints.

As can be seen from Figs. 1 and 2, the loads applying to the concrete block include wave pressure and soil pressure. However, the concrete block submerges in the design water level (DWL). Therefore, the static hydraulic pressure in the equilibrium state can be neglected. Besides, the block is submitted to optimize (not stability calculation) so that the uplift pressure is also not considered. The loads are calculated based on the Goda's formulations [10] as following:

$$P_1 = 0.5(1 + \cos \beta)(\alpha_1 + \alpha_* \cos^2 \beta)\gamma H_{design} \quad (2)$$

$$P_2 = \alpha_3 P_1 \quad (3)$$

$$\eta = 0.75(1 + \cos \beta)H_{design} \quad (4)$$

where H_{design} is determined at a distance of $5h_s$ seaward of the dike, $H_{design} = 3.1$ m; β is direction of waves with respect to dike normal, $\beta = 0$; h_b is water depth at $5h_s$ seaward of the dike; h_s is the water depth in front of the dike; α_1 is the effect of wave period on pressure distribution.

$$\alpha_1 = 0.6 + 0.5 \left(\frac{2kh_s}{\sinh 2kh_s} \right)^2 \quad (5)$$

α_* is the increase in wave pressure based on shallow mound

$$\alpha_* = \text{minimum} \left\{ \frac{h_b - d}{3h_b} \left(\frac{H_{design}}{d} \right)^2; \frac{2d}{H_{design}} \right\} \quad (6)$$

α_3 is linear pressure distribution

$$\alpha_3 = 1 - \frac{h_w - h_c}{h_s} \left(1 - \frac{1}{\cosh kh_s} \right) \quad (7)$$

The values of applied loads is calculated and showed in Fig. 3c.

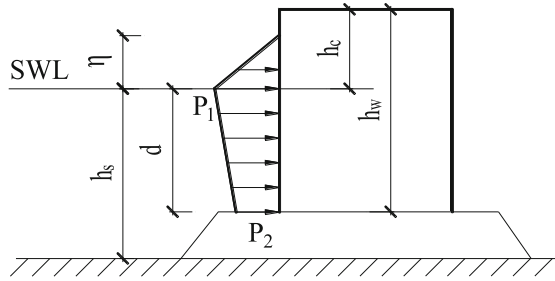


Fig. 1. Wave load acts on the vertical wall according to Goda's formulation.

In this study, we assume that the displacement of studied block under applied loads is very small, so that the lateral at-rest soil pressure is analyzed. The calculation of soil pressures acting on vertical wall is as following:

$$\sigma'_h = K_0 \sigma'_v \quad (8)$$

$$\sigma'_v = \gamma z \quad (9)$$

$$K_0 = 1 - \sin \varphi \quad (10)$$

where: γ is the unit weight of soil, z is the depth of soil layer, φ is angle of internal friction of soil, σ'_v is vertical geostatic stress, K_0 is coefficient of at-rest soil pressure.

In the case of inclined wall, the soil pressure is calculated as:

$$\sigma'_n = \sigma'_v (\sin^2 \alpha + K_0 \cos^2 \alpha) \quad (11)$$

where α is the angle of inclination of wall.

2.2 Topology Optimization Model in ANSYS

The concrete blocks are assembled to protect the seaward slope of the dike as showed in Fig. 2, in which, the hatched block is submitted to topology optimization in ANSYS. The block is solid with the boundary conditions and the applied loads are shown in Fig. 3. It is a part of interlocking revetment, which is constructed by connecting the concrete blocks into a row along the dike. Therefore, the lateral displacement (Z-Axis in Fig. 4a) of the model is restrained. The ground is modeled by elastic support with the stiffness of 20 N/mm^3 . In addition, the displacement in the direction perpendicular to the dike (X-Axis) is restrained at the bottom lines of the model (see Fig. 4).

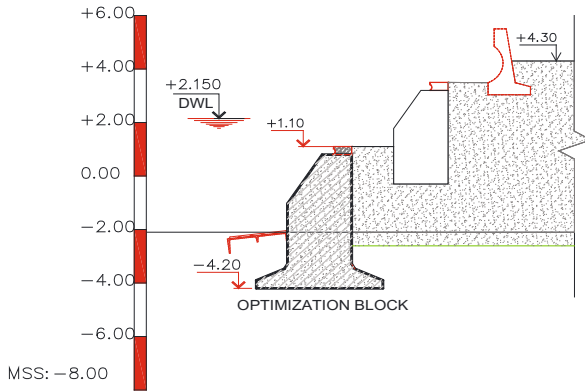


Fig. 2. Cross section of the dike with designed concrete blocks

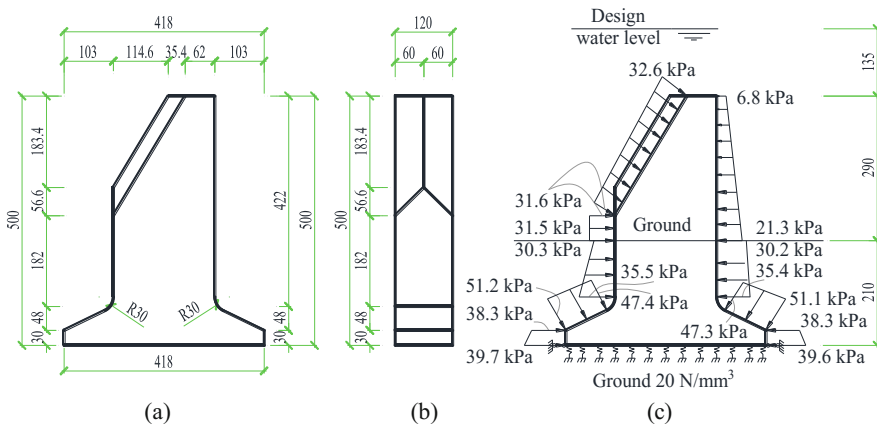


Fig. 3. Optimized concrete block: (a) side view, (b) front view, (c) boundary conditions of designed model. Length unit in cm.

The material properties of concrete block have Young’s modulus, E , of 30500 MPa; Poisson’s ratio, ν , of 0.2; Density, ρ , of 2500 kg/m³; Compressive strength, f'_c , of 22.9 MPa and tensile strength, f_t , of 2.15 MPa. After calculating the static results, the model is optimized with the target of about 30% retained volume.

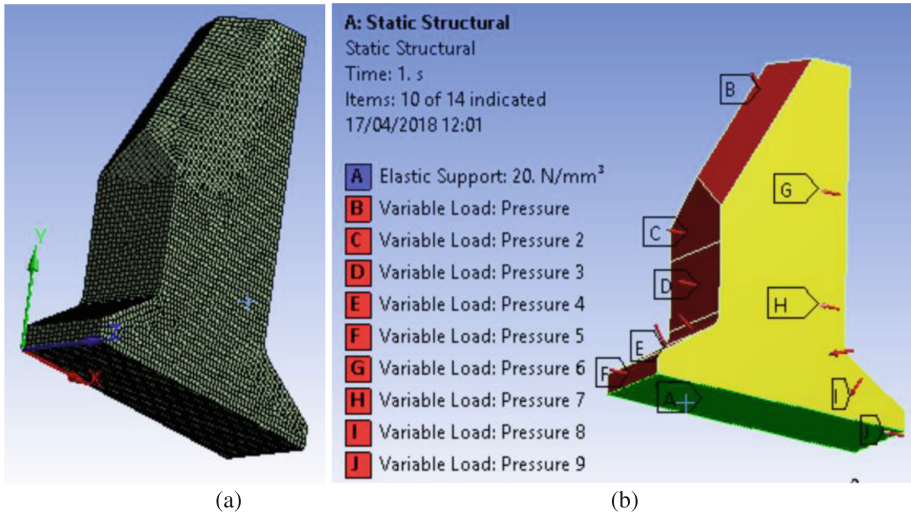


Fig. 4. Model in ANSYS: (a) 3D meshed model and the corresponding coordinate, (b) boundary conditions of designed model.

3 Results and Discussion

The output of ANSYS topology optimization is the shape of the concrete block (see Figs. 5 and 6) whereas the removed region corresponds to the density values of 0.0 to 0.4. The retained region of the block, which has density values from 0.6 to 1.0, can be submitted to shape design. The remaining density values represent the regions that need to be appropriately treated by the designer. Table 1 shows the results of volume and mass of the concrete block before and after running topology optimization. As can be seen from the table, the original volume is 12.56 m^3 corresponding to the original mass of 31.40 ton. After running the topology optimization, the remained volume of the design model is 3.59 m^3 corresponding to the final mass of 8.97 ton. The percentage of remained mass (volume) compared to original is 28.56% which is very close to the target. The static finite element calculation of proposed shape by BUSADCO is performed in Sect. 4.

Table 1. The results of topology optimization in ANSYS

Original volume	$1.2561 \times 10^{10} \text{ mm}^3$
Final volume	$3.5876 \times 10^9 \text{ mm}^3$
Percent volume of original	28.562
Original mass	31402 kg
Final mass	8969.1 kg
Percent mass of original	28.562



Fig. 5. The retained region of the concrete block

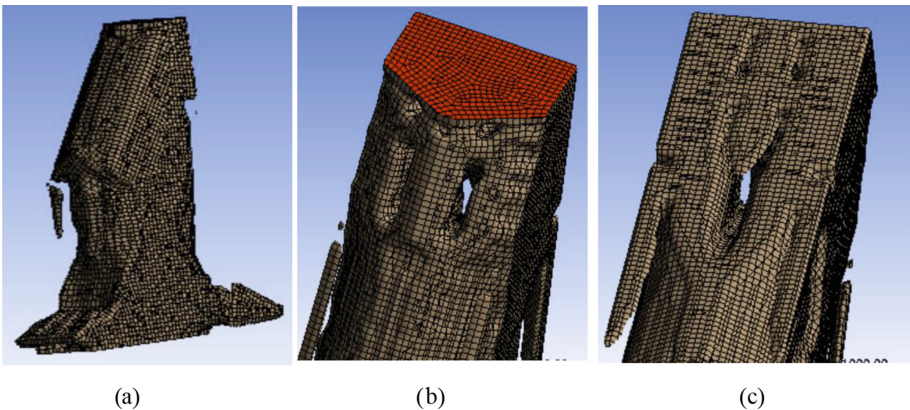


Fig. 6. The removed region of the concrete block: (a) the whole removed area, (b) the front upper part, (c) the back upper part

4 Proposed Concrete Block and FEM Analysis

Corresponding to the shape of concrete block after running topology optimization in Figs. 5 and 6, the interlocking block should be hollow inside. The retained region of structure, which has greatest effect on concrete block's stiffness, could guide the design of the block shape. It should be noted that there is small stiffener retained on the upper part of the block, which definitely increases the stiffness of the block against external pressures. However, we cannot apply directly the optimized solution for manufacturing because there are still some difficulties of casting activities in reality because of its complicated shape. BUSADCO uses a cap and sand filled inside the block, which can replace the stiffened parts of the optimized block. In additionally, the remained regions in the front and back of the body block are thicker than other parts. These regions will

be replaced by the stiffened pattern on the outside surfaces so that the casting work is more convenient. Besides, the stiffened patterns play an important role in strengthening the normal stiffness as well as increasing the connection with dike slope. The groove and tongue on the sides of the proposed block are for connecting with others forming the interlocking revetment (see Fig. 7).

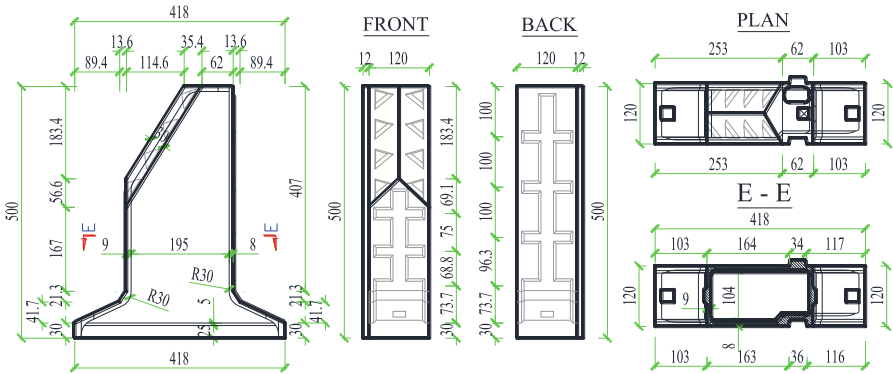


Fig. 7. Size and shape of proposed interlocking concrete block (BUSADCO)

The model of the concrete block in ANSYS is simulated with the same boundary conditions and applied load as the optimization block. However, the proposed block is hollow and will be filled by sand onsite so that there are additional sand pressures acting on the inside surfaces of the model (see Fig. 8a). The finite element model is showed in Fig. 8b and c, which has the volume of 3.57 m^3 corresponding to 8.93 ton in weight.

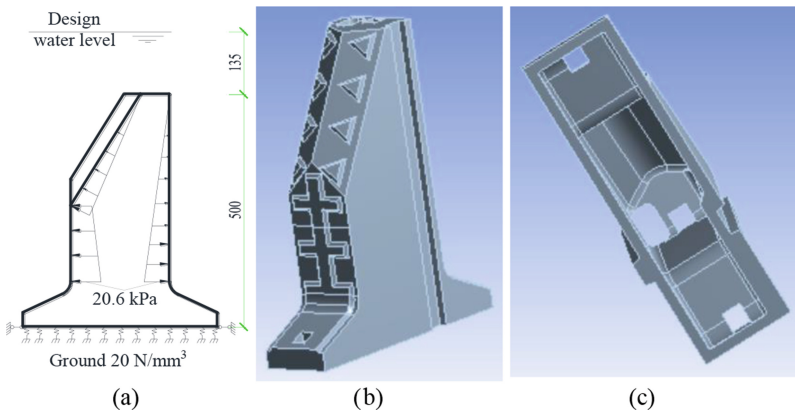


Fig. 8. The proposed model (BUSADCO): (a) additional load dues to filled sand where the pressures at the block foot are neglected because they are not sufficient; (b) 3D model, (c) bottom view of 3D model.

Table 2 shows the convergence history of the model according to the number of finite elements and nodes. In this study, the normal stresses of the block in Y-direction are considered. As presented in Table 2, the compressive stresses (negative values) are very small compared to concrete strength so that the tensile stresses attract more attention. The percentages of difference in values of positive stress are less than 1% whereas those of compressive stress fluctuated slightly. The maximum tensile stress is 0.844 MPa (see Fig. 9) corresponding to 225381 finite nodes, which is smaller than the tension limit of concrete material, 1.72 MPa ($0.8f_t$). Figure 10 shows the normal stresses of solid block after checking the convergence with 854074 nodes. As can be seen from the figure, the maximum tensile stress is very small (0.292 MPa), which means the original solid block is too conservative. Consequently, the proposed block based on optimized model should be constructed instead of the solid one.

Table 2. Convergence history of normal stress in Y-direction

Number of elements	Number of nodes	Normal stress		% difference in stress	
		Max	Min	Max	Min
17632	58171	0.830	-1.173		
29513	105931	0.835	-1.131	0.58%	-3.66%
42949	157376	0.840	-1.127	0.63%	-0.43%
56551	225381	0.844	-1.154	0.51%	2.38%

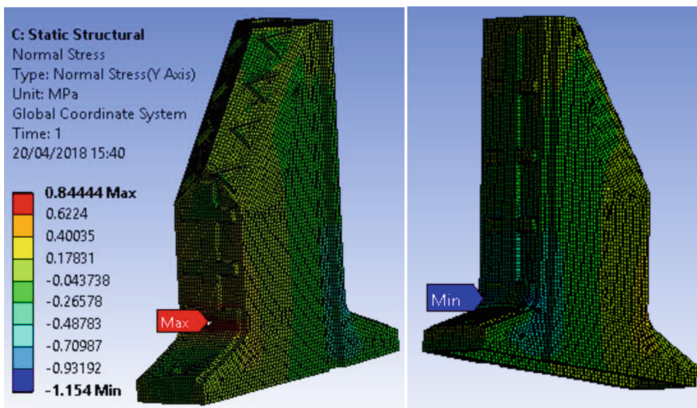


Fig. 9. Normal stress of the proposed block in Y-direction.

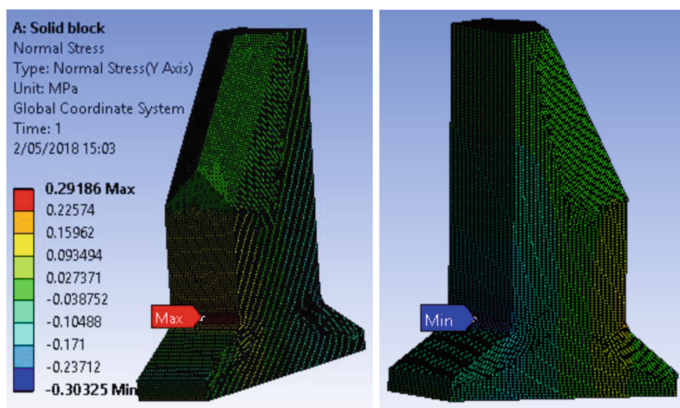


Fig. 10. Normal stress of the original solid block in Y-direction.

5 Conclusion

This paper makes use of ANSYS software to run topology optimization of a concrete block for interlocking revetment of a protection dike in Vietnam. The optimized model helps to achieve better condition of structure strength and stiffness as well as to reduce the usage of material while meeting the requirements of the structure about static stress resistance. However, the exact solution of the finite element model cannot be applied directly in manufacture because the formwork cannot be produced or the casting work is not able to be performed for the very complicated shape structure. The new concrete block is proposed by BUSADCO, which is hollow inside and will be filled by sand onsite. This saves about 70% concrete material compared to the solid block, while still satisfies the strength limits of structure.

Acknowledgements. The authors acknowledge the financial support of VLIR-OUS TEAM Project, VN2017TEA454A103, ‘An innovative solution to protect Vietnamese coastal riverbanks from floods and erosion’, funded by the Flemish Government.



References

1. Pilarczyk, K.W., Eversdijk, P.J., Kant, G.: Sea dikes northern part of Vietnam. Hydraulic Engineering Reports, Rijkswaterstaat, DWW (1996)
2. Mai, V.C., van Gelder, P.H.A.J.M., Vrijling, J.K., Mai, T.C.: Risk analysis of coastal flood defences- a vietnam case. In: 4th International Symposium on Flood Defence: Managing Flood Risk, Reliability and Vulnerability, pp. 93-1-93-8 (2008)

3. Pilarczyk, K.W., Klein Breteler, M., Bezuijen, A.: Wave forces and structure response of placed block revetments on inclined structures. In: International Conference on Coastal Engineering, ASCE (1995)
4. Burger, A.M., Breteler, M.K., Banach, L., Bezuijen, A.: Analytical method for closed block revetment. In: 21th International Conference on Coastal Engineering (1989)
5. Gier, F., Schüttrumpf, H., Mönnich, J., Van Der Meer, J.W., Kudella, M., Rubin, H.: Stability of interlocked pattern placed block revetments. In: ICCE, vol. 57 (2012)
6. Ju, L., Pan, J., Yang, F., Ren, Y.: Experimental study on the impact of filter layer permeability on revetment stability under wave action. *Procedia Eng.* **116**(1), 778–785 (2015)
7. Permana, M.S., Triatmodjo, B., Yuwono, N.: Wave-Induced pressure distribution on placed perforated revetment block. *Procedia Eng.* **170**, 443–450 (2017)
8. Li, X., Zhao, L., Liu, Z.: Topological optimization of continuum structure based on ANSYS. In: MATEC Web of Conferences, vol. 95, p. 7020 (2017)
9. Deaton, J.D., Grandhi, R.V.: A survey of structural and multidisciplinary continuum topology optimization: post 2000. *Struct. Multi. Optim.* **49**(1), 1–38 (2014)
10. N. U S Army Corps Of Engineers: Coastal Engineering Manual, pp. 1–62 (2002)



Damage Detection in Simply Supported Beam Using Transmissibility and Auto-Associative Neural Network

Huong Duong Nguyen¹(✉), Tien Thanh Bui², Guido De Roeck³,
and Magd Abdel Wahab⁴

¹ National University of Civil Engineering, Hanoi, Vietnam
duongnh2@nuce.edu.vn

² University of Transport and Communications, Hanoi, Vietnam

³ Department of Civil Engineering, Structural Mechanics,
KU Leuven, 3001 Leuven, Belgium

⁴ Soete Laboratory, Faculty of Engineering and Architecture,
Ghent University, Ghent, Belgium

Abstract. The first two steps in Structural Health Monitoring (SHM) are to detect and localize damage in a structure. Transmissibility uses only output signals to extract the structural dynamic parameter and very sensitive to damage. In this paper, a simply supported beam is analyzed using a transmissibility-based damage detection methodology combined with Auto-Associative Neural Network (AANN). Firstly, the transmissibility is calculated between two points in the examined beam. Then a transmissibility indicator is taken as input for the neural network, which accounts only for the response data and is sensitive to damage. The target of AANN is the location and the severity of the damage. It is found that the network, after being trained, show good results and can be used to detect and localize damage.

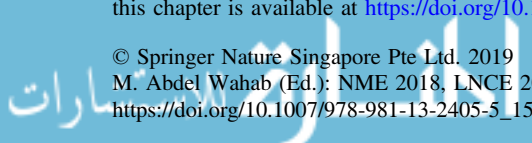
Keywords: Transmissibility · Damage detection
Auto-Associative Neural Network

1 Introduction

SHM is a technology to automate the inspection process in order to assess and evaluate the health condition of structures in real-time or at specified time intervals. SHM limits the number of collapsed structures, gives an opportunity to repair them, extends their lives and therefore it avoids demolishing them and constructing new structures. Thus, money will be saved, and the environment will be protected as well.

There are four different sequential levels: detection, identification, quantification and prediction. The higher levels of SHM are, the more complicated SHM technology is. SHM technology can be divided into two main categories, namely physical model-based and statistical/data model-based approaches. Physical model-based concentrates on the changes in vibration parameters such as frequency, mode shape and damping by

The original version of this chapter was revised: Incorrect term has been corrected. The correction to this chapter is available at https://doi.org/10.1007/978-981-13-2405-5_23



using Finite Element Analysis (FEA) with experiment data. The change of mode shape combined with Mac or Comac function are used to detect damage in [1, 2]. The frequency of a bridge can be extracted indirectly from a passing vehicle and then use for SHM [3, 4]. Statistical model-based methodology only considers the differences between two group of responses: responses under the intact condition and the responses under the damaged condition [5]. [6–8] success in using statistical analysis response measurement to detect damage in structure.

AANN is a statistical technique, which has been widely used in SHM during last decades. They proved that AANN is successfully used to detect damage [9–11]. In this paper, transmissibility is used incorporated with AANN to detect damage. The transmissibility in a single-degree-of-freedom system is defined as the ratio between the amplitude of the response displacement and the amplitude of the motion. The idea of transmissibility can be extended to a system with N degree-of-freedom. Transmissibility use output only response measurement, defined on output to output relationship. Transmissibility makes possible to detect damage without any assumption about the nature of excitations even though different loading conditions are applied during the experiments. In this paper, an indicator based on transmissibility function is used to get the input data for AANN.

2 Theoretical Derivation

2.1 Transmissibility of Motion

Firstly, we consider the relationship between responses and forces in term of receptance. If one has a vector F_A of magnitudes of applied forces at coordinates A, a vector X_U of unknown response amplitudes at coordinates U and vector X_K of known response amplitudes at coordinates K. The reader may find more information about transmissibility in reference [12].

One may establish the following relationship:

$$X_U = H_{UA}F_A \quad (1)$$

$$X_K = H_{KA}F_A \quad (2)$$

Where H_{UA} and H_{KA} are the receptance frequency response matrices related coordinates U and A, and K and A, respectively. Eliminating F_A in two equation, we have:

$$X_U = H_{UA}H_{KA}^+X_K \quad (3)$$

Or

$$X_U = T_{UK}X_K \quad (4)$$

Thus, the transmissibility matrix is defined as:

$$T_{UK} = H_{UA}H_{KA}^+ \quad (5)$$

The transmissibility matrix could be evaluated directly from the measurement of responses. From Eq. (4), we also have:

$$T_{UK} = X_U X_K^{-1} \quad (6)$$

If we consider a simply supported beam, the dynamic equilibrium equation can be written as:

$$M\ddot{x}(t) + C\dot{x}(t) + Kx(t) = f(t) \quad (7)$$

Where M , C and K are the mass, damping and stiffness matrices of the system, respectively.

$f(t)$ is the input vector and $x(t)$ contains the responses of each DOF of the system.

Solving this equation, we can calculate the displacement, velocity and the acceleration.

Herein, for a harmonic applied force at given coordinate, the transmissibility between point i and a reference to point j can be defined as:

$$T_{(i,j)}(\omega) = X_i(\omega)X_j^{-1}(\omega) \quad (8)$$

Where X_i and X_j are the complex amplitudes of the system response $x_i(t)$ and $x_j(t)$, respectively.

2.2 Auto-Associative Neural Network

The human brain has about 10^{12} neurons and about 10^{14} neural connections between them. This complex pairing system gives us the ability to analyze, process information, emotions, etc. The brain is able to organize and control its basic elements (single neurons) to perform tasks such as identification, control and analysis in much more effective way than the current computer. For example, the human brain is able to identify familiar faces in the crowd, estimating the distance of the observed object's moving velocities in the period from 100 ms to 200 ms, the speed at which the computer and computational software are still not available today. The ability to analyze handwriting, audio, and sound analysis, understand foreign languages and dialects is also a difficult task to simulate.

Artificial Neural Network (ANN) attempt to bring computer a little closer to brain's capacity by imitating certain aspects of information processing in the brain, in a highly simplified way. ANN investigates the capabilities of the human brain and reproduces those capabilities on machines, equipment or software. Once trained ANN is able to recognize similarities presented with a new input pattern, resulting in a predicted output pattern [13]. ANN has two basic processes: the learning process and the testing process.

Learning process is the process of creating knowledge from existing information. This

process is done for a set of sample data called metrics. Learning consists of three tasks; (a) compute output, (b) compare output with desired target then adjust weight and (c) repeat the process. The quality of the learning process is expressed by a target function or a function error. The learning process will reduce the error of this function. The learning process is usually learned on learning algorithms to optimize target functions. To evaluate the effectiveness of the learning process, one needs to use an additional testing process. A trained network is tested with a new set of data, called the test data set. The test variance will show the operability of ANN with new data, which has not appeared during the learning process. The low-test error corresponds to the ability to handle new good cases. AANN Application process consists of:

1. Collect data
2. Separate in to training and test Sets
3. Defined a network structure
4. Select a learning algorithm
5. Set parameters, values, initialize weights
6. Transform data to network Input
7. Start training, and determine and revise weights
8. Stop and test
9. Implementation: Use the network with new case

3 Numerical Example

A FE model of an experimentally tested simply supported beam, shown in Fig. 1, is divided in 18 elements as shown in Fig. 2. The beam is made of steel and has I100 cross-section. Young's modulus is 190.98 GPa, the density is 7800 kg/m^3 , and the length is 3 m. The beam is fitted with acceleration sensors in fixed positions. Based on the data of the accelerometers, we can calculate the experimental fundamental frequency as 34.26 Hz. Then, using the SAP2000 software to update the FE model, of the numerical fundamental frequency is determined as 34.26 Hz. The dynamic force is applied to the beam at node 3 and, in turn, the accelerations are obtained at the other nodes. To investigate the damage in the beam, we reduce the stiffness of each element in the beam. For each element, a stiffness reduction from 0% to 50% with an interval of 1% is recorded. For each single damage, there will be 51 scenarios, i.e. from D1 to D50 and D0 is for an intact case.



Fig. 1. Experimental beam

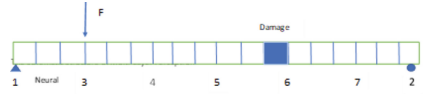


Fig. 2. FE model beam

3.1 Input for AANN

As discussed above, the transmissibility matrix T34, T35, T36, T37 could be evaluated directly from the measurement of the responses at nodes 3, 4, 5, 6 and 7 using Eq. (8). Zhou et al. [9], the indicator takes the sum of transmissibility along the specific frequency range that can be described as:

$$TI_i = \int_{f_{min}}^{f_{max}} T_{i,j} df \tag{9}$$

Where f_{min} and f_{max} are the low and high boundaries for the integration area as seen in Fig. 3.

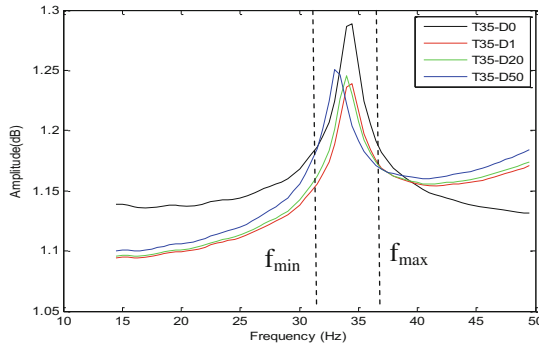


Fig. 3. A description of the frequency band

The choose of f_{min} and f_{max} greatly influences results and this is usually done by experience. With 4 functions T34, T35, T36, T37 we have 4 indicators TI1, TI2, TI3, TI4 can be used as input for the network. The intact beam natural frequency of mode 1 is 34.26 Hz. Survey Fig. 6, we saw the first peak of transmissibility function near the mode 1 most, then we used this peak to calculate.



As we know in advance, natural frequencies are important factors in assessing structural failure. There are also number of studies that make use of frequencies as damage indicators. However, in many cases, they are changing very slightly and then we don't have enough evidence to conclude that whether structure is damaged or not [14]. The natural frequencies of a simple beam can be determined using acceleration sensors located on the beam. In this paper, the natural frequencies are used as an input for the network.

3.2 Target for AANN

The first two levels of SHM are detection and localization of damage. This paper concentrates on those two indexes as the target for the network. The severity of damage is shown by the percentage decrease of the stiffness of damage section. Damages are introduced in four elements 4, 5, 6, 7. For each damage cases, we have 50 scenarios as explained earlier. All input parameters for the network are calculated based on the damaged position and the severity of the damage, respectively. The network diagram is shown in Fig. 4.

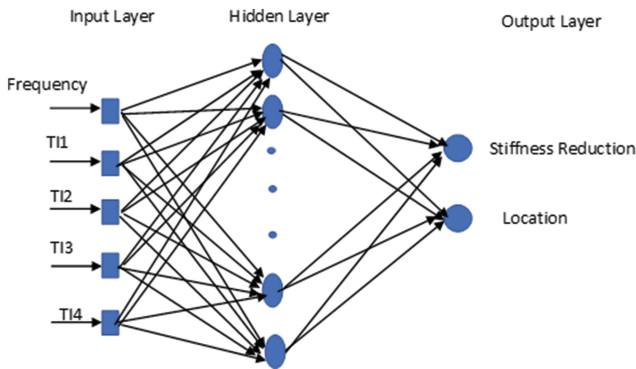


Fig. 4. The schematic structure of multi-layer perceptron neural networks model

3.3 Damage Detection Procedure

Step 1: Transmissibility is estimated from Eq. (4) for all measurements.

Step 2: The TI index is calculated based on the Eq. (9) and used as input data for AANN. This process is performed repeatedly with multiple defect locations and varying severity of damage (the stiffness reduces from 0% to 50%) as described above. Damage locations and deterioration levels are retained as a target for AANN.

Step 3: The AANN working as described in Sect. 2.2.

Step 4: Results analysis: Based on the objective function that evaluates whether the network is performing well or not. If the operation is not good, we can change the Norton number or change the frequency domain. If the result is satisfactory, the calculation is finished, and the network can be used.

3.4 Result Discussion

3.4.1 Intact Beam

We apply different forces to a beam position and measure the transmissibility function in the existing beam model. Because of symmetric, the T34 is almost the same with T36 and T37 is a horizontal line (Fig. 5). From the results shown in Figs. 5 and 6, we observe that although the applied force is different, the transmissibility function remains unchanged. This emphasizes that the transfer function can be determined from the response only, which can be characterized by the dynamic effect of the system and independent of the force. This makes it easier to apply it in practice cases because sometimes it is extremely difficult to measure the applied force on a structural in-service.

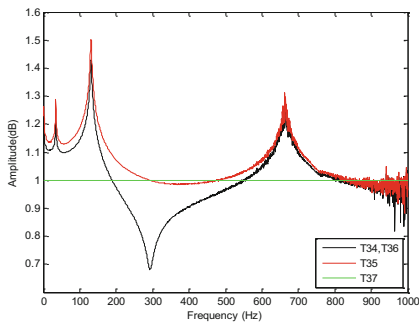


Fig. 5. The transmissibility with input 1

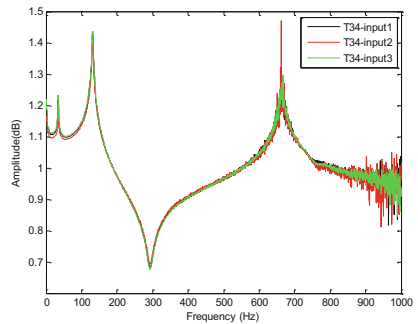


Fig. 6. The transmissibility T34 with difference inputs

3.4.2 Damaged Beam

The transmissibility's of damaged beam (the location of damage section is node 6) are shown in Figs. 7 and 8. It is easy to see that even when the damage is very small, the transmission function changes immediately. As the stiffness decreases, the peak of the transfer function moves slightly to the left Fig. 9. This suggests that the transfer function is more sensitive to the detection of damage than to the severity of the damage.

As discussed above, beams will be damaged at different levels by changing the stiffness of each element. This is done at positions close to points 4, 5, 6, 7. TI indicator is calculated and used as input data for AANN network. 70% sample of the data is used to train the network, which is adjusted according to its error. 15% sample is used to measure the network generalization, and to halt training when generalization stops improving. 15% sample is used to test the network, which has no effect on training and so provides an independent measure of network performance during and after training.

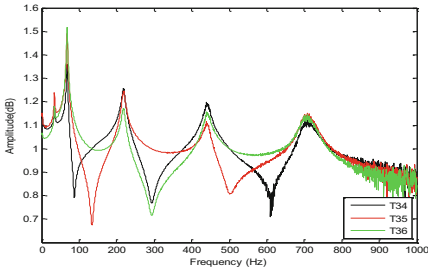


Fig. 7. The D1 transmissibility function damage in node 6

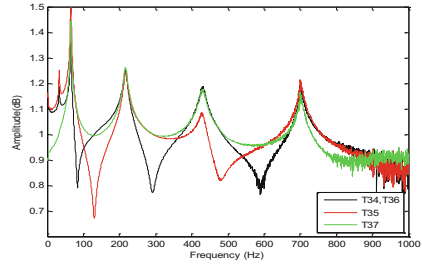


Fig. 8. The D50 transmissibility function damage in node 6

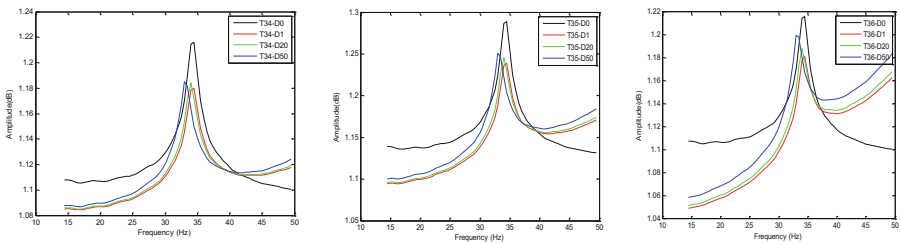


Fig. 9. Compared the first peak of the transmissibility with difference scenarios damage in node 6

Figure 10 shows the network outputs with respect to targets for training, validation and test sets. The results are perfectly fit, the data falls along 45-degree line, where network outputs are equal to the targets and with R value in each case of slightly above 0.99.

Figure 11 shows the predicted results of AANN function with 4 damage positions and 50 levels. The vertical axis indicates the location of the damage section (at 4 nodes 4, 5, 6, 7) and the horizontal axis is 50° of damage respectively (from D1 to D50). The graph shows that if the stiffness decreased by less than 5%, the results are less accurate. However, with more severity of damage, the network’s predicted results are relatively accurate. This is understandable because the structure needs enough changes to be identifiable and distinguishable. With the above results, we can confirm that after training the AANN network, we can completely detect the degree of damage and its location.

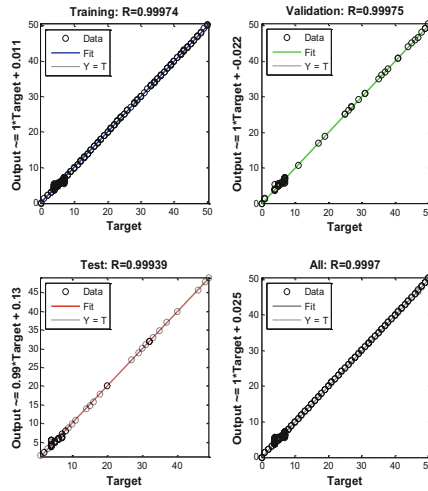


Fig. 10. Correlation between actual and predicted values in training phase, validation phase and test phase

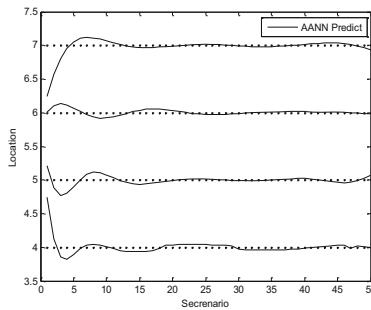


Fig. 11. Comparison between actual damage location and AANN prediction

4 Conclusion

This study proved that using transmissibility together with AANN could be used to detect and localize damage. It used response measurements only, and the use of AANN make it possible to detect damage once the base-line was defined.

The object of this study was simply supported beams that were simulated with various degrees of failure, i.e. damage positions and severities. Research has shown that, with the data collected, the network after learning was completely capable to identify damage. It should be noted, however, that the selection of input parameters greatly influences the results. Using this method requires large number of data sets to train and test the network, which is a drawback. In this paper, we analysis each of the single damage cases, however many cases may contain multiple damages. To solve this problem, we need a very large data sets. However, today with the development of

structural analysis software, the structure can be modeled using FEA and then get data to train the network, thus opening a new direction for SHM technology.

Acknowledgements. The authors acknowledge the financial support of VLIR-OUS TEAM Project, VN2018TEA479A103, ‘Damage assessment tools for Structural Health Monitoring of Vietnamese infrastructures’, funded by the Flemish Government.



References

1. Wang, T., Celik, O., Catbas, F.: Damage detection of a bridge model based on operational dynamic strain measurements. In: *Advances in Structural Engineering* (2016)
2. West, W.M.: Illustration of the use of modal assurance criterion to detect structural changes in an orbiter test specimen. In: *International Modal Analysis Conference, Los Angeles, vol. 4* (1986)
3. Yanga, Y.B., Chang, K.C.: Extracting the bridge frequencies indirectly from a passing vehicle: parametric study. *Eng. Struct.* **31**, 2448–2459 (2009)
4. Chang, F.K.: *Structural Health Monitoring*. Taylor & Francis, London (2000)
5. Sohn, H., Farrar, C., Hemez, F., Shunk, D., Stinemates, D., Nadler, B., Czarnecki, J.: A review of structural health monitoring literature: 1996–2001. Los Alamos National Laboratory Report, vol. LA-13976-MS (2004)
6. Sohn, H.: Applying the LANL statistical pattern recognition paradigm for structural health monitoring to data from a surface-effect fast patrol boat. Los Alamos National Lab., NM, USA (2001)
7. Catbas, F.N., Gokce, H.B., Gul, M.: Nonparametric analysis of structural health monitoring data for identification and localization of changes: concept, lab, and real-life studies. *Struct. Health Monit.* **11**(5), 613–626 (2012)
8. Nair, K.K., Kiremidjian, A.S., Law, K.H.: Time series-based damage detection and localization algorithm with application to the ASCE benchmark structure. *J. Sound Vib.* **291**(1), 349–368 (2006)
9. Zhou, Y.L., Wahab, M.A.: Damage detection using vibration data and dynamic transmissibility ensemble with auto-associative neural network. *Mechanika* **23**(5), 688–695 (2017)
10. Chen, Q., Chan, Y.W., Worden, K., Tomlinson, G.R.: Structural fault diagnosis and isolation using neural networks based on response-only data. *Comput. Struct.* **81**, 2165–2172 (2003)
11. Zapico, J.L., Gonzalez, M.P., Worden, K.: Damage assessment using neural network. *Mech. Syst. Signal Process.* **17**(1), 119–125 (2003)
12. Maia, N.M.M., Urgueira, A.P.V., R. Almeida, A.B.: Why and whereforces of transmissibility. In: *Vibration Analysis and Control - New Trends and Developments*, p. 364 (2011). ISBN 978-953-307-433-7
13. Tran, L.H.: *Neural Network and Application*. Bach Khoa, Hanoi (2014)
14. Wei, F., Pizhong, Q.: Vibration-based damage identification methods: a review and comparative study. *Struct. Health Monit.* **10**(1), 83–111 (2011)



A Coupled SPH-FEM for Fluid-Structures Interaction Problem with Free-Surface and Retment Slope Thin-Walled Structures

P. Truong-Thi^{1,2,3}✉, Hung Nguyen-Xuan²,
and Magd Abdel Wahab¹

¹ Laboratory Soete, Faculty of Engineering and Architecture,
Ghent University, Ghent, Belgium

{ThiPhuong. Truong, Magd. AbdelWahab}@UGent. be

² Center for Interdisciplinary Research, HUTECH University,
Ho Chi Minh City, Vietnam
ngx.hung@hutech.edu.vn

³ Institute of Mechanics, VAST, Hanoi, Vietnam

Abstract. Fluid-Structure Interaction (FSI) is one of the interesting subjects in coastal construction. In this study, Smoothed Particle Hydrodynamic (SPH) method is utilized to model the fluid domain. Finite Element Method (FEM) is used to model the solid structure. SPH is a mesh-free method, which is flexible to model and analyze complicated problem domains. The interaction between a thin-walled concrete block and wave under different initial conditions is modeled by ABAQUS. The SPH-FEM model is validated by interaction of elastic gate with water pressure, the results are compared with previous research and show very good agreement. It is found that SPH-FEM model can capture the entire FSI process deformation of a complex geometry. As expected, the present approach performs well with a suitable geometry for thin-walled concrete blocks to protect coastal areas from climate change.

Keywords: Smoothed Particle Hydrodynamic (SPH)
Finite Element Method (FEM) · Fluid-Structure interaction (FSI)
Retment Slope (RS) structure · Thin-walled structure

1 Introduction

Fluid-Structure Interaction (FSI) deals with the interaction between one or more deformable structures and a fluid flow. The structure can be exposed to either internal or external fluid flow. In this phenomenon, the deformable body suffers pressure from fluid flow to give rise to deformation, conversely, the fluid flow pressure field and velocity field are affected by the moveable or deformable structure [1, 2]. The fluid-structure interaction appears in wide variety problems. For instance, the classily basis aerodynamic problems such as the blade of wind turbine is bent due to aerodynamic loading [3], the plane will deform under aero-elastic forces [4], the pressure of blood affects heart valve [5] and the impact of flooding/landslide gives rise to collapse of construction [6].

SPH method is chosen for this FSI because SPH is a mesh-free Lagrangian method and is well suited for studying complex fluid dynamics. SPH was used the first times in late 1970s by Gingold and Monaghan [7]. During the four decades of this method existence, the SPH method was used effectively in wide branches of computational physic, especially in computation fluid dynamics. In addition, SPH method also can be combined with other methods to simulate of physical problems, which are difficult to handle individual solve. Some of these combinations are SPH-DEM [1] and SPH-SPH [8]. SPH model is applied to computational continuum mechanics with focus on the problems of interaction between hydrodynamics and elastic solid. The disadvantage of using SPH for both of fluid and solid domain is high computational costs. Therefore, in this study FEM is utilized to solve the solid domain. A typical example is the CFD-FEM model [9–11].

In this work, we presented a coupling SPH-FEM for FSI problems in ABAQUS in 3D. The combination between SPH and FEM is validated by a benchmark model and the obtained results are found to be in very good agreement with data from experiments and other numerical results. Then we apply this method to simulate an interaction of block with thin wall and free-surface. The simulation results show that a couple SPH-FEM can be used to solve FSI problems. The previous studies [12, 13] and this study will support the design of revetment slope structures based on fluid-structure interaction analysis.

2 Computational Methodology

2.1 Fluid Domain

2.1.1 SPH Method

The basic of SPH is based on an interpolation theory. The conservation laws of incompressible fluid dynamics are converted into integral equations. The value of a specific particle i is approximated from function values at surrounding particles in the influence domain of the particle i , is defined as [14, 15]:

$$\langle f(x_i) \rangle = \int_{\Omega} f(x_j) W(x_i - x_j, h) dx_j \approx \sum_{j=1}^n \frac{m_j}{\rho_j} f(x_j) W_{ij} \quad (1)$$

where $W_{ij} = W(x_i - x_j, h)$ is smooth kernel function satisfies two conditions:

$$\int_{\Omega} W_{ij} dx_j = 1, \quad \lim_{h \rightarrow 0} W_{ij} = \delta_{ij} \quad (2)$$

Equation (1) states the formulation at a particle i , in which m is the mass, ρ is the density, Ω is the volume of the integration that contain x_i and x_j . W is an interpolating kernel (kernel function), which has two properties as described in Eq. (2). The index i and j denotes the variables at particle i and j , respectively. The interpolating function W is defined so that its value monotonously decreases as the distance between particles

increases. This kernel has compact support domain, for which radius is defined by the smoothing length h . ABAQUS/Explicit computes a smoothing length at the beginning of the analysis so that the average number of particles associated with an element is roughly between 30 and 50. By default, the smoothing length is kept constant throughout the analysis, but this number can be modified and the maximum number of allowed particles associated with one element is 140 [16].

Many kernels were defined by Natanson [17]. In ABAQUS, by default, the kernel based on a cubic spline functions, which is post by Gingold and Monaghan, 1977 [7], is used. Alternatively, one may choose a quadratic kernel given by Johnson et al. [18] or quintic kernel given by Wendland [19]. In this study, Monaghan kernel is chosen in the interpolating function. If we define R as the relative distance between points x_i and x_j , $R = |x_i - x_j|/h$, then cubic spline function has the following form:

$$W(R, h) = \alpha_d \begin{cases} \frac{2}{3} - R^2 + \frac{1}{2}R^3 & 0 \leq R < 1 \\ \frac{1}{6}(2 - R)^3 & 1 \leq R < 2 \\ 0 & R \geq 2 \end{cases} \quad (3)$$

In one-, two- and three- dimensional respectively, $\alpha_d = 1/h$, $\alpha_d = 15/(7\pi h^2)$, $\alpha_d = 3/(2\pi h^3)$. The spatial derivative of the function at particle i is:

$$\langle \nabla \cdot f(x_i) \rangle = \sum_{j=1}^n \frac{m_j}{\rho_j} f(x_j) \nabla_i W_{ij} \quad (4)$$

where

$$\nabla_i W_{ij} = \frac{x_i - x_j}{r_{ij}} \frac{\partial W_{ij}}{\partial r_{ij}} = \frac{x_{ij}}{r_{ij}} \frac{\partial W_{ij}}{\partial r_{ij}}$$

In Eq. (4), a negative sign was already removed because $\nabla_i W_{ij}$ is taken with respect to particle i and not to particle j . More details of SPH method are given in [14, 20]. The shape of any kernel function is illustrated in Fig. 1, and the cubic spline kernel and its first derivative are shown in Fig. 2.

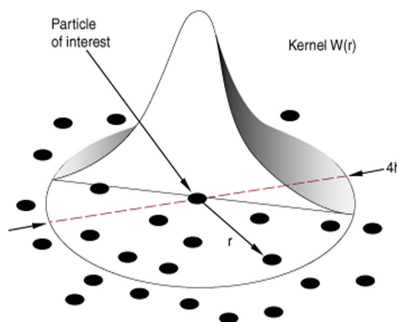


Fig. 1. Kernel function

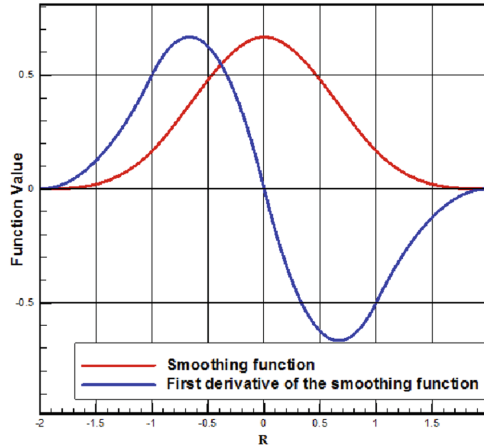


Fig. 2. The cubic spline kernel function and its derivative.

2.1.2 Governing Equations

Using SPH method, Navier-Stokes equations were transformed into ordinary differential equations through kernel function and its derivative [15].

Momentum equation

In SPH form, the momentum is described by the Navier-Stokes equation in the form:

$$\frac{D\mathbf{v}}{Dt} = \mathbf{g} - \frac{1}{\rho} \nabla \mathbf{P} + \frac{\mu}{\rho} \nabla^2 \mathbf{v} \tag{5}$$

where \mathbf{v} is the velocity vector, \mathbf{g} is the gravity acceleration vector, μ is the dynamic viscosity and ρ is the density of the fluid. For a single particle i , the conservation of momentum can be written as:

$$\frac{d\mathbf{v}_i}{dt} = \mathbf{g} - \frac{1}{\rho_i} \nabla \mathbf{P}_i + \frac{\mu}{\rho_i} \nabla^2 \mathbf{v}_i \tag{6}$$

In which the approximations to term of the Navier-Stokes equations are described through Eqs. (1) and (4). The pressure term is in the following form:

$$\frac{1}{\rho_i} \nabla \mathbf{P}_i = \sum_j m_j \left(\frac{p_i}{\rho_i^2} + \frac{p_j}{\rho_j^2} \right) \nabla_i W_{ij} \tag{7}$$

where p is the pressure. The term represents impact of viscous forces is approximated in the following form:

$$\frac{\mu}{\rho_i} \nabla^2 \mathbf{v}_i = \frac{\mu}{\rho_i} \sum_j m_j \left(\frac{\mathbf{v}_j - \mathbf{v}_i}{\rho_j} \right) \nabla_i^2 W_{ij} \tag{8}$$



Continuity equation

With a fluid like seawater, the conservation of mass satisfying the third Newton's law is obtained. In SPH formulation, the conservation for incompressible fluid is given by:

$$\frac{d\rho_i}{dt} = \sum_j m_j (\mathbf{v}_j - \mathbf{v}_i) \cdot \nabla_i W_{ij} \quad (9)$$

Equation of state

In order to solve the above Navier-Stokes equations for seawater, the dynamic pressure term must be calculated before. In SPH method, an equation of state is used to represent a pressure gradient for each particle, which is based on local density. Monaghan [14] applied the following from for incompressible fluid, it can be written by:

$$p = B \left[\left(\frac{\rho}{\rho_0} \right)^\gamma - 1 \right] \quad (10)$$

where γ is a constant often set equal to 7 [14]. However, there are some researches, who used other value such as $\gamma = 1$ has also been suggested. ρ_0 is initial density of fluid and B is the pressure constant, which sets a limit for the maximum change of the density. Assuming that the speed of sound is larger than 10 times of maximum velocity of the dynamic fluid flow, the constant will be calculated as:

$$B = \frac{100\rho_0 v_{\max}^2}{\lambda} \quad (11)$$

The equation of state at particle i is:

$$p_i = \frac{100\rho_0 v_{\max}^2}{\lambda} \left[\left(\frac{\rho_i}{\rho_0} \right)^\gamma - 1 \right] \quad (12)$$

2.2 Structure Domain

The dynamic equilibrium (for the discrete model in finite-element system) is defined in terms of the external applied forces (P), the internal element forces (I) and the nodal accelerations, as:

$$\mathbf{M} \frac{d^2 \mathbf{u}}{dt^2} = P - I \quad (13)$$

where \mathbf{M} is the mass matrix, \mathbf{u} is the displacement vector. From Eq. (13), we can solve displacements vector every time increment, i.e.:

$$\frac{d^2 \mathbf{u}}{dt^2} \Big|_n = \mathbf{M}^{-1} (P - I) \Big|_n \quad (14)$$

$$\left. \frac{d\mathbf{u}}{dt} \right|^{n+1/2} = \left. \frac{d\mathbf{u}}{dt} \right|^{n-1/2} + \frac{(\Delta t^{n+1} + \Delta t^n)}{2} \left. \frac{d^2\mathbf{u}}{dt^2} \right|^n \quad (15)$$

$$\mathbf{u}^{n+1} = \mathbf{u}^{n-1} + \Delta t^{n+1} \left. \frac{d\mathbf{u}}{dt} \right|^{n+1/2} \quad (16)$$

2.3 Coupled SPH-FEM

Coupling of fluid- and solid-portion is described by boundary conditions on the common interface. Kinematic condition means that the velocity of the fluid and the velocity of structure are continuous on the interface. Dynamic condition means that the normal stresses of fluid and solid are continuous on the interface and Geometric condition means that fluid- and solid-domain always match, no holes appears at the interface and the domains do not overlap [21]. In this study of fluid-structure interaction, the interaction force between SPH and FEM are coupled by using exchange velocity field and displacements field on the interface. On the interface (see Fig. 3) between the fluid domain and solid domain, two conditions are required:

$$\begin{aligned} v_f &= v_s \\ \sigma_f \cdot n_f + \sigma_s \cdot n_s &= 0 \end{aligned} \quad (17)$$

The framework of coupling SPH and FEM is schematically described in Fig. 4. The interaction between SPH particles and FEM elements follow Eq. (17).

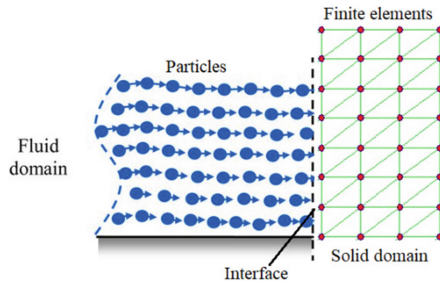


Fig. 3. Boundary conditions on the interface of fluid and solid

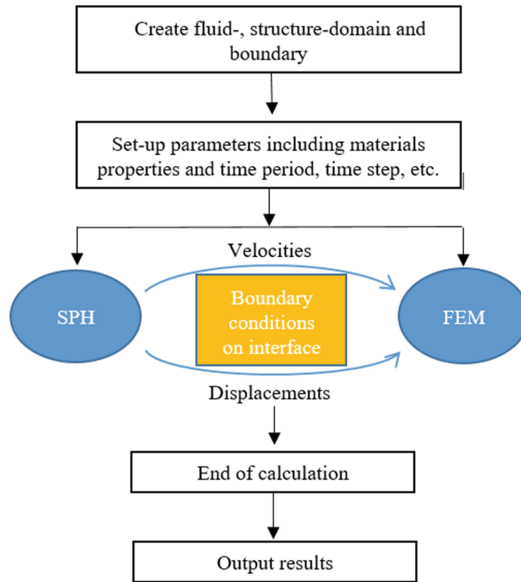


Fig. 4. Computation framework for coupling SPH and FEM.

3 Validation of the Coupled SPH-FEM Model

3.1 Numerical Simulation Set-up

The validation test for the coupled SPH-FEM model is carried out by simulating the water flow in elastic gate problem and comparing the results with experimental data and others numerical results using coupled SPH-SPH [8] and SPH-DEM [1] methods. The initial configuration is described in Fig. 5 and simulation parameters for this problem is shown in Table 1. The boundary conditions setup of gate are fixed at the top of elastic gate and the other end can be moveable. The gate is divided into finite elements and SPH for water is initialized with gravity as load. In particular, the parameters setup in numerical model are suitable due to requiring that the local Mach number is everywhere lower than 1.

3.2 Results and Discussion

The numerical results using the couple SPH-FEM model is in very good agreement with previous researches. Namely, comparison of numerical results from the present SPH-FEM model in ABAQUS software with experimental data, numerical results from SPH-SPH and SPH-DEM models, is shown in Fig. 6. The images are taken to compare at every 0.08 s. In these images, it is observed that the level of water behind the elastic gate of all of researches is the same. Additionally, plots of contour velocity obtained using SPH-DEM and SPH-FEM are shown in Fig. 7.

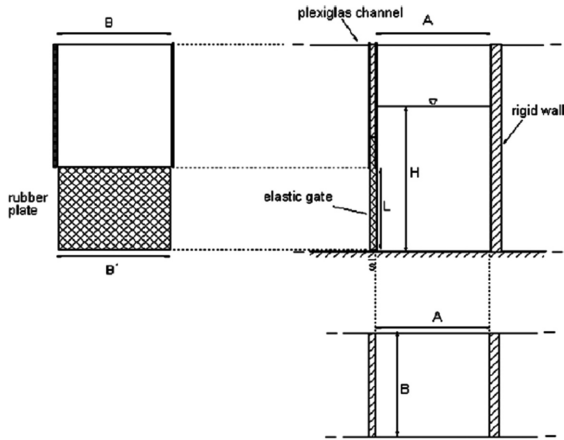


Fig. 5. Configuration of 3D elastic gate test in a coupled SPH-FEM model in ABAQUS software.

Table 1. Parameters for SPH-FEM modelling of elastic gate test.

Parameters	Values
A (m)	0.1
H (m)	0.14
L (m)	0.079
s (m)	0.005
B = A (m)	0.1
B' (m)	0.098
Thickness model (m)	0.1
Boundary mesh (m)	0.002
SPH mesh (m)	0.002
FEM mesh (m)	0.002
Kernel function type	Wendland
<i>Water</i>	
density (kg/m ³)	1000
viscosity (Pa. s)	8.9×10^{-4}
<i>Rubber gate</i>	
density (kg/m ³)	1100
elastic Modulus (Pa)	12×10^6
Poisson's ratio	0.4
Time step (s)	Auto
Time period (s)	0.4

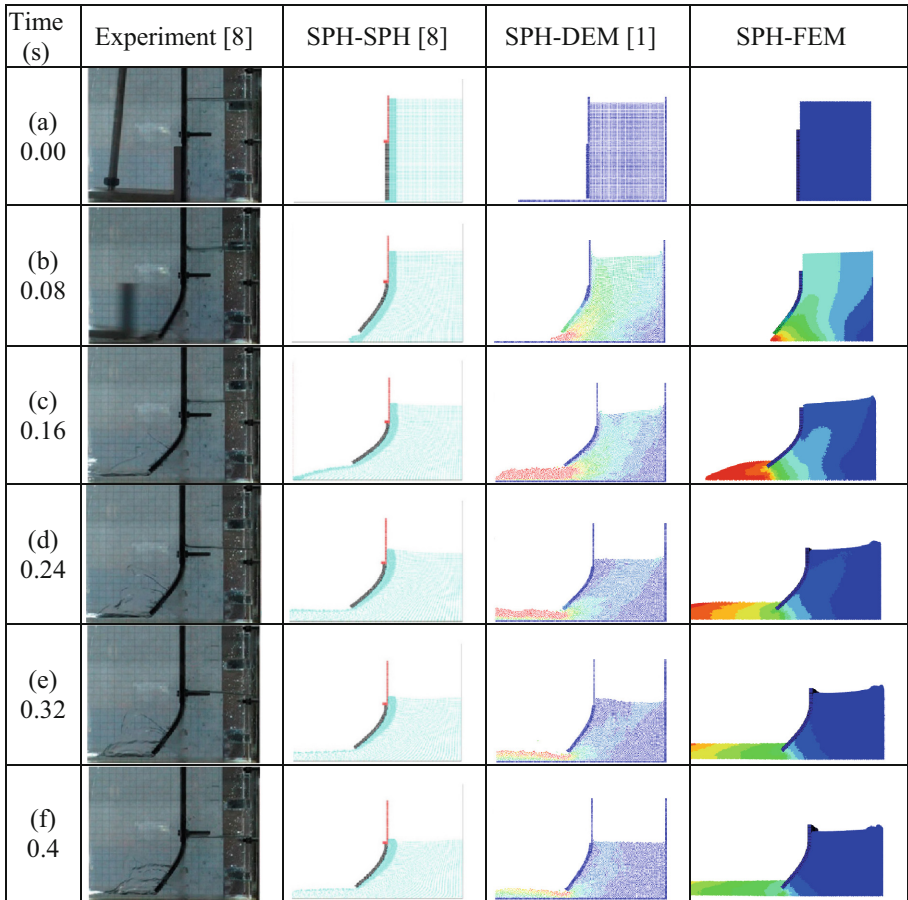


Fig. 6. Comparisons between experimental data, SPH-SPH, SPH-DEM and SPH-FEM results of elastic gate test at the same period of time (0.4 s).

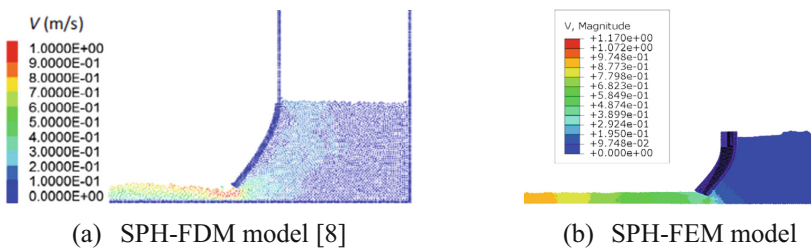


Fig. 7. Contour velocity of fluid flow at 0.4 s

Figure 8 presents the water levels behind the elastic gate and in Fig. 9 plots the horizontal and vertical displacements of the elastic gate versus time. Due to the water leakage in the experiment, the flow rates calculated from SPH-SPH, SPH-DEM and SPH-FEM models are slightly higher than the experimental data, which results in a faster decrease of water level.

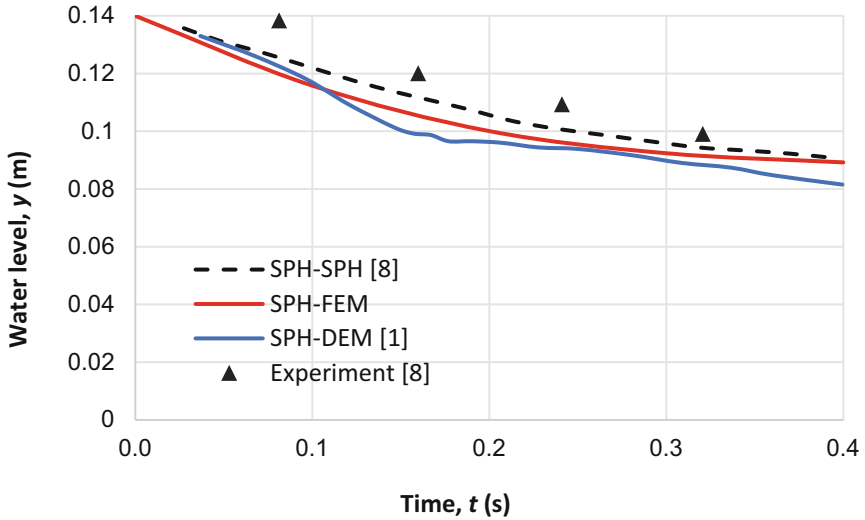


Fig. 8. Water level behind the rubber gate at different time

The comparison shows that between research results have a slight difference but can be considered. General, the coupled SPH-FEM model shows good agreement throughout the entire test process in term of elastic gate deformation and vertical displacement of free surface.

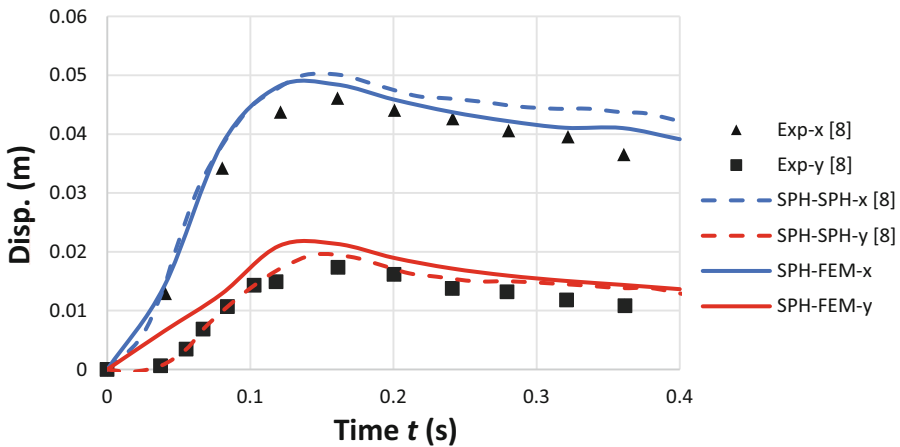


Fig. 9. Horizontal and vertical displacements of the free end of the rubber gate

4 Thin-Walled Revetment Slope Structure

4.1 Numerical Model

The previous model is an example to valid of our method for fluid-structure interaction problem. Now, we simulate the impact of water free surface on thin-walled revetment slope structure. The initial configuration of simulation model is shown in Fig. 10 and the parameters of model is described in Table 2. Height of column water is 7 m equivalent to 9 level storm. Simulating fluid-structure interaction at form wave is more difficult and needs high CPU time. This work will be the focus of our study in the future.

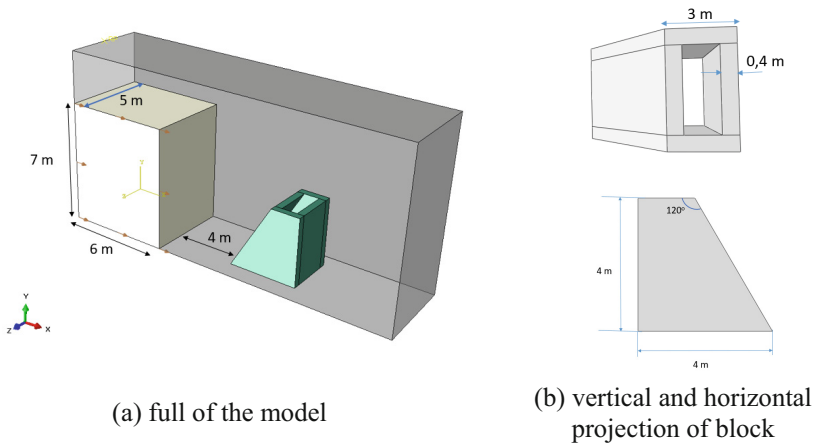


Fig. 10. Configuration of 3D coupled SPH-FEM of thin-walled block in ABAQUS software.

Table 2. Parameters for SPH-FEM modelling of revetment slope thin-walled block.

Parameters	Values
Water properties:	
Density (tonne/mm ³)	1×10^{-9}
Dynamic viscous (20-°C, MPa.s)	1×10^{-9}
Eos: $C_0 = 1.45 \times 10^6$, $S_0 = 0$, $\Gamma_0 = 0$	-
Thin-walled block	
Density (tonne/mm ³)	2.5×10^{-9}
Elastic Modulus (MPa)	2500
Poisson's ratio	0.2
SPH mesh (mm)	100
FEM mesh (mm)	100
Boundary mesh (mm)	100
Kernel function type	Cubic
Time step (s)	Auto
Time period (s)	3

The gravity acceleration is chosen equal 9.8 m/s^2 . The boundary condition of the revetment slope thin-walled structure is imposed as fixed at bottom face. The boundary of the model is set-up as discrete rigid. General contact is used in interaction module. The value of friction is set equal to 0.

4.2 Numerical Results

Figure 11 shows velocity contour distribution in the x -axis of fluid domain free fall-down at representative times. In this simulation, the water column falls down by its weight. From the simulation results, velocity contour distribution on fluid flow is reduced by about 30% (from 9 m/s to 6 m/s) after interacting with the thin-walled block. By this way, the energy wave is reduced due to interaction between flow and block. The displacements of the thin-walled block in the x -axis as shown in Fig. 12. The results of this simulation seem reasonable for both fluid and structure behaviors.

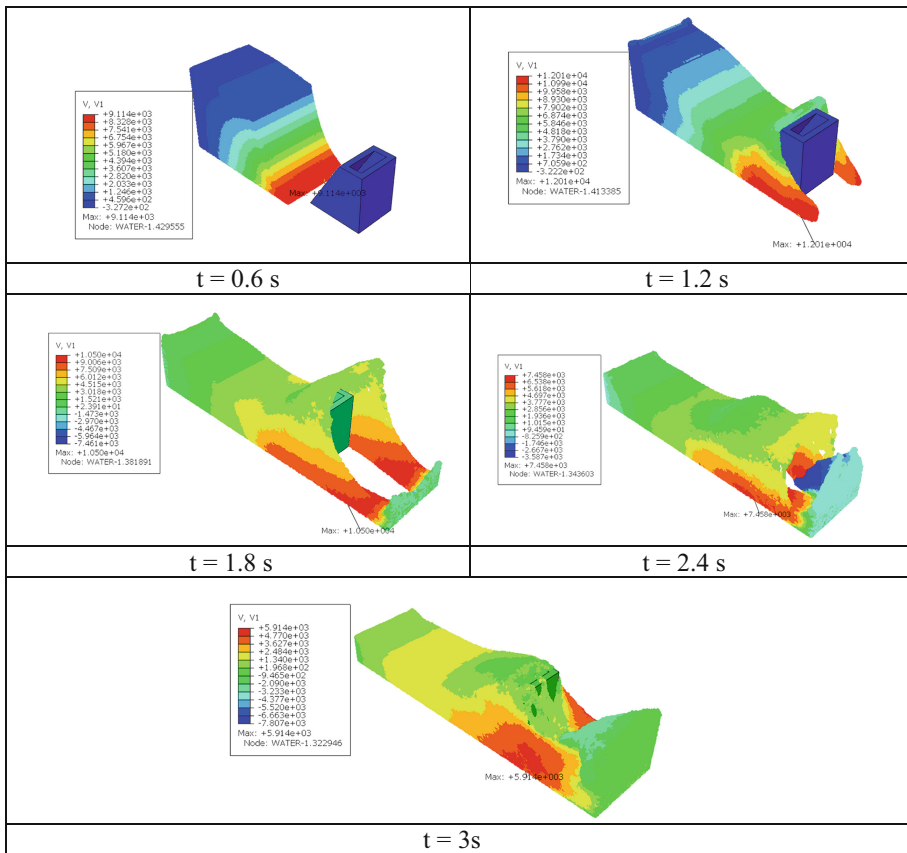


Fig. 11. Velocity contour distribution in the x -axis of fluid domain free fall-down at representative times

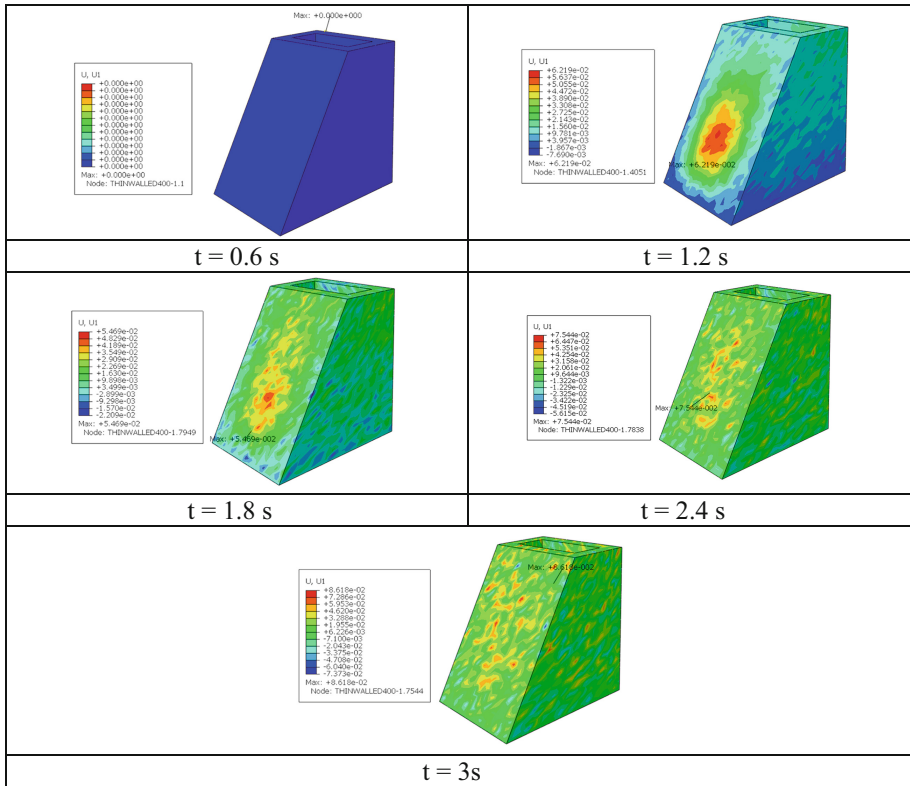


Fig. 12. Displacements distribution in the x-axis of structure domain at representative times

At early time $t = 0.6$ s, when the fluid flow has no yet contact with the structure, the structure is not deformed. After interaction between fluid flow and the thin-walled structure, the max displacement in the x-axis is 0.08 mm. We have performed a number of simulations using different velocities inlet of column water, respectively ($V = 5; 10; 15; 20$ m/s), the same phenomenon as the current simulation is obtained over a wide range of velocities inlet of water.

The fluid flow develops and affects the structure leading to structural deformation. Then structural deformation reacts the fluid flow somewhat reducing water velocity, which means wave energy is lost. A coupled SPH-FEM can be used to simulate fluid-structure interaction problems.

5 Conclusion

A 3D coupled SPH-FEM model to solve fluid-structure interaction problems has been presented. In this method, fluid domain was discretized into SPH particles and the structure domain was discretized by finite elements. This model is suitable for problems, which have a complex interface. The contact between SPH and FEM is automatic

in the range of two times the kernel smooth length. SPH model is based on Lagrangian method, hence it can solve the extremely large deformation, especially sloshing problems. It can be handled without any difficulties.

The coupled SPH-FEM model was validated through a test model and a comparison between the present method with experimental data and other numerical results. An application for this method is performed, which is the simulation of the interaction between a thin-walled block with free surface water. The obtained results have shown that both results of solid and fluid flow were accurate, e.g. displacements distribution and Mises's stress of solid and contour velocity of fluid flow, etc.

In the future, the coupled SPH-FEM model will be applied to predict the behavior of other more complex blocks, such as thin-walled block with holes. These studies aim to propose a new design block to protect embankments.

Acknowledgements. The authors acknowledge the financial support of VLIR-OUS TEAM Project, VN2017TEA454A103, 'An innovative solution to protect Vietnamese coastal riverbanks from floods and erosion', funded by the Flemish Government.



References

1. Wu, K., Yang, D., Wright, N.: A coupled SPH-DEM model for fluid-structure interaction problems with free-surface flow and structural failure. *Comput. Struct.* **177**, 141–161 (2016)
2. Hou, G., Wang, J., Layton, A.: Numerical methods for fluid-structure interaction - a review. *Commun. Comput. Phys.* **2**(12), 337–377 (2012)
3. Lee, Y.J., Jhan, Y.T., Chung, C.H.: Fluid-structure interaction of FRP wind turbine blades under aerodynamic effect. *Compos. Part B Eng.* **43**(5), 2180–2191 (2012)
4. Kamakoti, R., Shyy, W.: Fluid-structure interaction for aeroelastic applications. *Prog. Aerosp. Sci.* **40**(8), 535–558 (2004)
5. Peskin, C.: Numerical analysis of blood flow in the heart. *J. Comput. Phys.* **25**, 220–252 (1977)
6. Tang, C.L., et al.: The Tsaoling landslide triggered by the Chi-Chi earthquake, Taiwan: Insights from a discrete element simulation. *Eng. Geol.* **106**(1–2), 1–19 (2009)
7. Gingold, R.A., Monaghan, J.J.: Smoothed particle hydrodynamics-theory and application to non-spherical stars. *Mon. Not. R. Astron. Soc.* **181**, 375–389 (1977)
8. Antoci, C., Gallati, M., Sibilla, S.: Numerical simulation of fluid-structure interaction by SPH. *Comput. Struct.* **85**(11–14), 879–890 (2007)
9. Ahmed, S., Leithner, R., Kosyna, G., Wulff, D.: pump simulation: increasing reliability with FEM-CFD. *World Pumps* **2009**(509), 35–39 (2009)
10. Kim, S.H., Choi, J.B., Park, J.S., Choi, Y.H., Lee, J.H.: A coupled CFD-FEM analysis on the safety injection piping subjected to thermal stratification. *Nucl. Eng. Technol.* **45**(2), 237–248 (2013)
11. Peksen, M.: 3D transient multiphysics modelling of a complete high temperature fuel cell system using coupled CFD and FEM. *Int. J. Hydrogen Energy* **39**(10), 5137–5147 (2014)

12. Truong-Thi, P., Dang-Bao, L., Abdel Wahab, M., Duong-Ngoc, H., Hoang-Duc, T., Nguyen-Xuan, H.: Analysis of fluid–structures interaction problem of revetment slope thin-walled structure using abaqus. In: Nguyen-Xuan, H., Phung-Van, P., Rabczuk, T. (eds.) Proceedings of the International Conference on Advances in Computational Mechanics 2017, ACOME 2017. Lecture Notes in Mechanical Engineering, vol. PartF3, pp. 917–925. Springer, Singapore (2018)
13. Dang-Bao, L., Truong-Thi, P., Wahab, M.A., Nguyen-Xuan, H.: Numerical studies on contact problem of inter-locking concrete blocks forming revetment structure BT. In: Nguyen-Xuan, H., Phung-Van, P., Rabczuk, T. (eds.) Proceedings of the International Conference on Advances in Computational Mechanics 2017, ACOME 2017. Lecture Notes in Mechanical Engineering, vol. PartF3, pp. 143–154. Springer, Singapore (2018)
14. Monaghan, J.J.: Smoothed particle hydrodynamics. *ARAA* **30**, 543–574 (1992)
15. Bui, H.H., Sako, K., Fukagawa, R.: Numerical simulation of soil-water interaction using smoothed particle hydrodynamics (SPH) method. *J. Terramech.* **44**(5), 339–346 (2007)
16. ABAQUS version 6.14 Analysis User’s Manual, Dassault Systemes Simulia Corp (2011)
17. Natanson, I.P.: Theory of Functions of a Real Variable. Ungar, New York (1960)
18. Johnson, G.R., Stryk, R.A., Beissel, S.R.: SPH for high velocity impact computations. *Comput. Methods Appl. Mech. Eng.* **139**(1–4), 347–373 (1996)
19. Wendland, H.: Piecewise polynomial, positive definite and compactly supported radial functions of minimal degree. *Adv. Comput. Math.* **4**(1), 389–396 (1995)
20. Liu, G.G.-R. Liu, M.B.: Smoothed Particle Hydrodynamics: A Meshfree Particle Method, vol. 68 (2003)
21. Richter, T.: ALE formulation for fluid-structure interactions. In: Lecture Notes in Computational Science and Engineering, vol. 118, pp. 203–254 (2017)



Incompressible Fluid Computation Based on Polygonal Finite Element

T. Vu-Huu^{1(✉)}, C. Le-Thanh^{1,3}, Hung Nguyen-Xuan²,
and Magd Abdel Wahab¹

¹ Laboratory Soete, Faculty of Engineering and Architecture,
Ghent University, Ghent, Belgium

{huutruong.vu, le.thanhcuong, magd.abdelwahab}@ugent.be

² Center for Interdisciplinary Research in Technology, HUTECH University,
Ho Chi Minh City, Vietnam
ngx.hung@hutech.edu.vn

³ Faculty of Civil Engineering and Electricity, Ho Chi Minh City Open
University, Ho Chi Minh City, Vietnam

Abstract. This paper, instead of using the popular numerical methods such as Finite Element Method, Finite Volume Method, etc. that are applied for fluid computation with the advantages of simplicity, introduces a new method named Polygonal Finite Element Method (PFEM). Based on the stability of mixed finite element, discretization is governed by the so-called inf-sup condition, which, in this case, depends on the choice of the discrete velocity and pressure spaces. We put forward a new choice of these spaces defined over convex polygonal partitions of the domain. Within each element, the pressure field is represented by the polygonal basis functions and the velocity is controlled by richer polygonal bubble functions.

Keywords: Polygonal Finite Element Method · Inf-sub condition
Stoke equations · Polygonal bubble function

1 Introduction

The number of researches using finite element methods for incompressible fluid computation is vast and exhaustive [1–11]. For the stability of fluid computation problem, the inf-sup condition must be satisfied [1]. That condition depends on the discrete spaces for the approximation of the velocity and pressure fields. They cannot be chosen independently of one another. In general, the velocity space must be richer enough than the pressure space; otherwise, the discrete solution will be “over-constrained”. The poor convergence (or even non-convergence) can be obtained by larger pressure space than velocity one [12].

In this paper, a new polygonal element for incompressible fluid flow computation is presented, within each polygonal element, the pressure field is represented by the polygonal basics functions and the velocity is represented by polygonal basis functions with the enrichment of the bubble function. This element is named MINI Polygonal Finite Element (MINI-PFE). It is hopefully that the stability of MINI-PFE is obtained.

In the recent years, PFEM becomes a well-known numerical method occupying great flexibility and many other attractive features. For example, a number of mesh generation algorithms, harnessing the properties of Voronoi diagrams, have been developed recently [13–15]. A further advantage is the outperforming to their triangular and quadrilateral counterparts in terms of accuracy with the smaller overall system size. Thus, in this research the work of Wachspress [16–18] is proposed.

This paper is organized as follows. In the following section, the problem of incompressible fluid flow governed by Stoke equation system is introduced. Then, Sect. 3 presents the mixed finite element discretization of the problem. Next, in Sect. 4, we show the construction of the velocity and pressure space for MINI-PFE. Section 5 provides the basis and bubble functions for polygonal element. Numerical test showing the effectiveness of the MINI-PFE is presented in Sect. 6. Conclusions of the paper are reported in Sect. 7.

2 Stoke Equation Systems

The strong form of Stoke governing equation systems is normally presented as [1]:

$$\begin{aligned} \nabla p - \nu \nabla^2 \mathbf{u} &= 0 \\ \nabla \cdot \mathbf{u} &= 0 \end{aligned} \tag{1}$$

where ν is a constant of kinematic viscosity; \mathbf{u} is the fluid velocity in space $\mathbf{H}_E^1(\Omega)$ and p is the fluid pressure in space $\mathbf{L}_2(\Omega)$.

The domain of the Eq. (1) is Ω with the boundary conditions $\Gamma\Omega$ combining Dirichlet boundary, $\Gamma\Omega^D$, and Neumann boundary $\Gamma\Omega^N$, ($\Gamma\Omega = \Gamma\Omega^D \cup \Gamma\Omega^N$),

$$\begin{aligned} \mathbf{u} &= \bar{\mathbf{w}} \text{ on } \Gamma\Omega^D \\ \nu \frac{\partial \mathbf{u}}{\partial \mathbf{n}} - \mathbf{n}p &= \mathbf{s} \text{ on } \Gamma\Omega^N \end{aligned} \tag{2}$$

where \mathbf{n} denotes the outward-pointing normal to the fluid boundary.

The weak formulation of Eqs. (1) and (2) are

$$\begin{aligned} \nu \int_{\Omega} \nabla \mathbf{u} : \nabla \mathbf{v} d\Omega - \int_{\Omega} p(\nabla \cdot \mathbf{v}) d\Omega &= \int_{\Gamma\Omega^N} \mathbf{s} \cdot \mathbf{v} d\Gamma \quad \forall \mathbf{v} \in \mathbf{H}_{E0}^1 \\ \int_{\Omega} q(\nabla \cdot \mathbf{u}) d\Omega &= 0 \quad \forall q \in \mathbf{L}_2(\Omega) \end{aligned} \tag{3}$$

where \mathbf{v} and q are test functions; $\nu \int_{\Omega} \nabla \mathbf{u} : \nabla \mathbf{v} d\Omega$ is diffusive term; $\int_{\Omega} (\mathbf{u} \cdot \nabla \mathbf{u}) \cdot \mathbf{v} d\Omega$ is convective term.

3 Approximation Using Finite Elements

A discrete weak formulation uses finite-dimensional spaces $\mathbf{X}_0^h \subset \mathbf{H}_{E0}^1$ and $\mathbf{M}^h \subset \mathbf{L}_2(\Omega)$. They are approximated independently leading to the terminology mixed approximation. Specifically, given a velocity solution space \mathbf{X}_E^h , the discrete problem

is: find $\mathbf{u}_h \in \mathbf{X}_E^h$ and $p_h \in \mathbf{M}^h$ so that

$$\int_{\Omega} \nabla \mathbf{u}_h : \nabla \mathbf{v}_h d\Omega - \int_{\Omega} p_h (\nabla \cdot \mathbf{v}_h) d\Omega = \int_{\Gamma \Omega^N} \mathbf{s} \cdot \mathbf{v}_h d\Gamma \Omega^N \quad \forall \mathbf{v}_h \in \mathbf{H}_{E_0}^1, \tag{4}$$

$$\int_{\Omega} q_h (\nabla \cdot \mathbf{u}_h) d\Omega = 0 \quad \forall q_h \in \mathbf{L}_2(\Omega).$$

To identify the corresponding linear algebra problem, we introduce a set of vector-valued basis functions $\{\phi_j\}$ for velocity such as,

$$\mathbf{u}_h = \sum_{j=1}^{n_u} \mathbf{u}_j \phi_j + \sum_{j=n_u+1}^{n_u+n_{\Gamma}} \mathbf{u}_j \phi_j, \tag{5}$$

with $\sum_{j=1}^{n_u} \mathbf{u}_j \phi_j \in \mathbf{X}_0^h$. We fix the coefficients \mathbf{u}_j : $j = n_u + 1, \dots, n_u + n_{\Gamma}$ such that the second term interpolates the boundary data on $\Gamma \Omega^D$. Introducing a set of scalar basis functions $\{\psi_k\}$ for pressure

$$p_h = \sum_{k=1}^{n_p} \mathbf{p}_k \psi_k. \tag{6}$$

We find that the discrete formulation Eq. (4) can be expressed as a system of linear equations

$$\begin{bmatrix} \mathbf{A} & \mathbf{B}^T \\ \mathbf{B} & \mathbf{0} \end{bmatrix} \begin{bmatrix} \mathbf{u} \\ \mathbf{p} \end{bmatrix} = \begin{bmatrix} \mathbf{f} \\ \mathbf{g} \end{bmatrix}. \tag{7}$$

The matrix \mathbf{A} is called the vector-Laplacian matrix, and the matrix \mathbf{B} is called the divergence matrix. The entries are given by

$$\mathbf{A} = [a_{ij}], a_{ij} = \int_{\Omega} \nabla \phi_i : \nabla \phi_j d\Omega, \tag{8}$$

$$\mathbf{B} = [b_{kj}], b_{kj} = - \int_{\Omega} \nabla \psi_k \nabla \cdot \phi_j d\Omega, \tag{9}$$

For i and $j = 1, \dots, n_u$ and $k = 1, \dots, n_p$. The entries of the right-hand side vector are

$$\mathbf{f} = [f_i], f_i = \int_{\Gamma \Omega^N} \mathbf{s} \cdot \phi_i d\Omega - \sum_{j=n_u+1}^{n_u+n_{\Gamma}} \mathbf{u}_j \int_{\Omega} \nabla \phi_i : \nabla \phi_j d\Omega, \tag{10}$$

$$\mathbf{g} = [g_k], g_k = \sum_{j=n_u+1}^{n_u+n_{\Gamma}} \mathbf{u}_j \int_{\Omega} \psi_k \nabla \cdot \phi_j d\Omega, \tag{11}$$



and the function pair (\mathbf{u}_h, p_h) obtained by substituting the solution vectors $\mathbf{u} \in \mathbb{R}^{n_u}$ and $p \in \mathbb{R}^{n_p}$ into Eqs. (5) and (6) is the mixed finite element solution. The system Eqs. (7) to (11) is the discrete Stokes problem.

4 MINI Polygonal Finite Element

In this section, we illustrate a polygonal finite element (MINI-PFE) for incompressible fluid problem that enriched by basis bubble function so that inf-sup condition can be expectedly satisfied naturally. In detail, for each polygonal element, the velocity field is represented by the expansion of an appropriate set of barycentric basis functions with an enrichment of bubble function at the centroid node of element, see in Fig. 1.

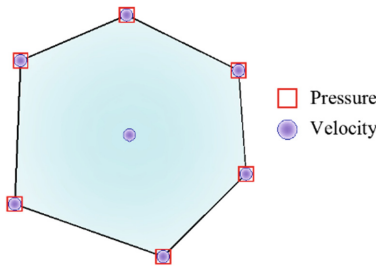


Fig. 1. MINI polygonal mixed finite element.

A finite element approximation space $\mathbb{V}^h \subset \mathbb{V}$ of velocity field is defined as [19, 20].

$$\mathbb{V}^h = \left\{ \mathbf{u}^h \in (\mathbf{H}_{E0}^1(\Omega))^2, \mathbf{u}^h|_{\Omega^e} \in \mathcal{P}, \mathbf{u}^h|_{\Gamma\Omega^e} \in C^0, \Omega^e \in \mathfrak{S} \right\}, \tag{12}$$

where \mathcal{P} refers to so-called generalized barycentric coordinates associated with $\Omega^e \in \mathfrak{S}$ (\mathfrak{S} is domain) of n_e polygons involving n_s edges and n_n nodes such that $\Omega \approx \Omega^h = \sum_{e=1}^{n_e} \Omega^e$.

Ideally, bubble functions whose values are zeros on the element boundaries are used for any interior point of finite elements. These are like bubble functions in the standard finite element literature. The supplementing space \mathbb{B}^h with a space of bubble functions is defined as

$$\mathbb{B}^h = \left\{ \phi_b^e = \frac{\mathcal{A}(\mathbf{x})}{\mathcal{A}(\mathbf{x}) + \mathcal{B}(\mathbf{x})}, \forall \Omega^e \in \mathfrak{S} \right\}, \tag{13}$$

where $\mathcal{A}(x)$ disappears on the boundary line, and $\mathcal{B}(x)$ is minimized at the centroid of element Ω^e and is smooth over the rest of the domain [20]. This velocity space, \mathbb{V}_b^h , now with the enrichment of bubble function is written as

$$\mathbb{V}_b^h = \mathbb{V}^h \oplus \mathbb{B}^h. \tag{14}$$

Then, the velocity $\mathbf{u}^h \in \mathbb{V}_b^h$ on $\Omega^e \in \mathfrak{S}$ is explicitly written as

$$\mathbf{u}^h(\mathbf{x}) = \sum_{i=1}^{n_{ne}} (\phi_i^e(\mathbf{x}) \mathbf{I}_2) \mathbf{d}_i^e + (\phi_b^e(\mathbf{x}) \mathbf{I}_2) \mathbf{d}_b^e, \tag{15}$$

where n_{ne} is the number of vertices of polygonal element, \mathbf{I}_2 is the unit matrix of 2nd rank, \mathbf{d}_i^e is DOFs of $\mathbf{u}^h(\mathbf{x})$ at the i th vertex, ϕ_i^e is the shape function at the i th vertex, \mathbf{d}_b^e is the unknown displacement associated with an extra centroid node $\mathbf{u}_b^h(\mathbf{x})$, and ϕ_b^e indicates the bubble shape function at the centroid node of the element. For pressure space \mathbb{Q}^h , over each polygonal element, the pressure field is represented by the expansion of an appropriate set of barycentric basis functions. A finite element approximation space \mathbb{Q}^h of pressure field is defined as [19, 20]

$$\mathbb{Q}^h = \left\{ q^h \in \mathbf{M}^h(\Omega), q^h|_{\Omega^e} \in \mathcal{P}, q^h|_{\Gamma\Omega^e} \in C^0, \Omega^e \in \mathfrak{S} \right\}, \tag{16}$$

where \mathcal{P} is the barycentric coordinates in $\Omega^e \in \mathfrak{S}$ (\mathfrak{S} is domain) of n_e polygons involving n_s edges and n_n nodes such that $\Omega \approx \Omega^h = \sum_{e=1}^{n_e} \Omega^e$. The pressure $q^h \in \mathbb{Q}^h$ on $\Omega^e \in \mathfrak{S}$ is explicitly written as

$$q^h(\mathbf{x}) = \sum_{i=1}^{n_{ne}} (\phi_i^e(\mathbf{x}) \mathbf{I}_2) \mathbf{d}_i^e, \tag{17}$$

where n_{ne} is the number of vertices of polygonal element, \mathbf{I}_2 is the unit matrix of 2nd rank, \mathbf{d}_i^e is DOFs of $q^h(\mathbf{x})$ at the i th vertex, ϕ_i^e is the shape function at the i th vertex.

5 Shape Functions on Convex Polygonal Elements

There are many methods to the construct the shape functions for polygonal elements [16, 21–23]. In this study, we focus on using Wachspress coordinates [16, 24] with iso-parametric mapping on a reference element to conform basis shape functions for polygonal finite element.

5.1 Wachspress Shape Functions

First, a polygon $\Omega^e \in \mathfrak{S}$ with n_{ne} vertices, $\mathbf{x}_1, \mathbf{x}_2, \dots, \mathbf{x}_{n_{ne}}$, ($n_{ne} \geq 3$) is considered in counter-clockwise ordering. For any interior point $\mathbf{v} \in \Omega^e$, Wachspress shape functions [12, 22, 25] can be defined as

$$\phi_i^e = \frac{\varphi_i}{\sum_{j=1}^{n_{ne}} \varphi_j} = \frac{\varphi_i}{\psi}, \text{ with } \varphi_i = \frac{A(\mathbf{x}_{i-1}, \mathbf{x}_i, \mathbf{x}_{i+1})}{A(\mathbf{v}, \mathbf{x}_{i-1}, \mathbf{x}_i)A(\mathbf{v}, \mathbf{x}_i, \mathbf{x}_{i+1})} \tag{18}$$

where $A(\mathbf{x}_a, \mathbf{x}_b, \mathbf{x}_c)$ is area of the triangle $[\mathbf{x}_a, \mathbf{x}_b, \mathbf{x}_c]$, see Fig. 2(a). An alternative to Wachspress coordinates is the perpendicular distances of the point \mathbf{v} to the edges of Ω^e ,

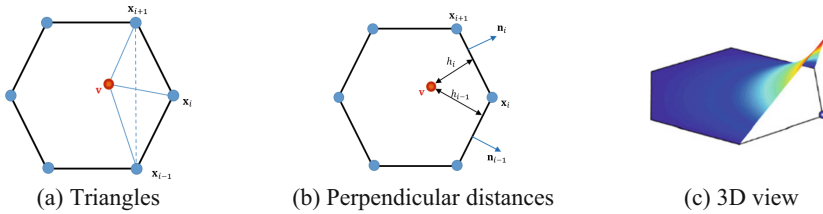


Fig. 2. Shape function for the boundary node of a hexagon using the Wachspress coordinates [17, 18, 26].

see Fig. 2(b) [19]. Let $h_i(\mathbf{x})$ denote the perpendicular distance of \mathbf{v} to the edge \mathbf{e}_i and define $\mathbf{p}_i(\mathbf{x}) = \mathbf{n}_i/h_i(\mathbf{x})$, where \mathbf{n}_i is the outward unit normal vector to the edge $\mathbf{e}_i = [\mathbf{x}_i, \mathbf{x}_{i+1}]$, with vertices indexed cyclically $\mathbf{x}_{n+1} = \mathbf{x}_1$. Then the Wachspress shape functions of polygonal element are

$$\phi_i^e = \frac{\varphi_i}{\psi} = \frac{\tilde{\varphi}_i}{\sum_{j=1}^{n_{ne}} \tilde{\varphi}_j}, \quad \text{with } \tilde{\varphi}_i = \det(\mathbf{p}_{i-1}, \mathbf{p}_i) \quad (19)$$

and their gradients are

$$\nabla \phi_i^e = \phi_i^e \left[\vartheta_i - \sum_{j=1}^{n_{ne}} \phi_j^e \vartheta_j \right] \quad \text{where } \vartheta_i = \mathbf{p}_{i-1} + \mathbf{p}_i. \quad (20)$$

5.2 Bubble Wachspress Shape Functions

The construction for bubble shape functions of an arbitrary convex polygons is proposed by Malsch and Dasgupta [20] with interior nodes by using square of a distance function and a function which vanishes on the boundary, see in Fig. 3. As presented in Sect. 4, a function $A(\mathbf{x})$ can be derived from the triangular simplex, the ratio of products of the Wachspress coordinate in Eq. (13) or Eq. (14) to establish $A(\mathbf{x})$ as

$$A(\mathbf{x}) = \frac{1}{\psi} = \frac{1}{\psi}. \quad (21)$$

In Eq. (10), $B(\mathbf{x})$ can be defined in a simple way as

$$B(\mathbf{x}) = \|\mathbf{x} - \mathbf{x}_b\|_{\Omega^e}^2, \quad (22)$$

where \mathbf{x}_b is the coordinates of the centroid of the polygonal element, Ω^e . As a result, a bubble shape function $\phi_b^e \in \mathbb{B}^h$ can be expressed as

$$\phi_b^e = \frac{1}{1 + \|\mathbf{x} - \mathbf{x}_b\|_{\Omega^e}^2 \tilde{\psi}} \quad (23)$$

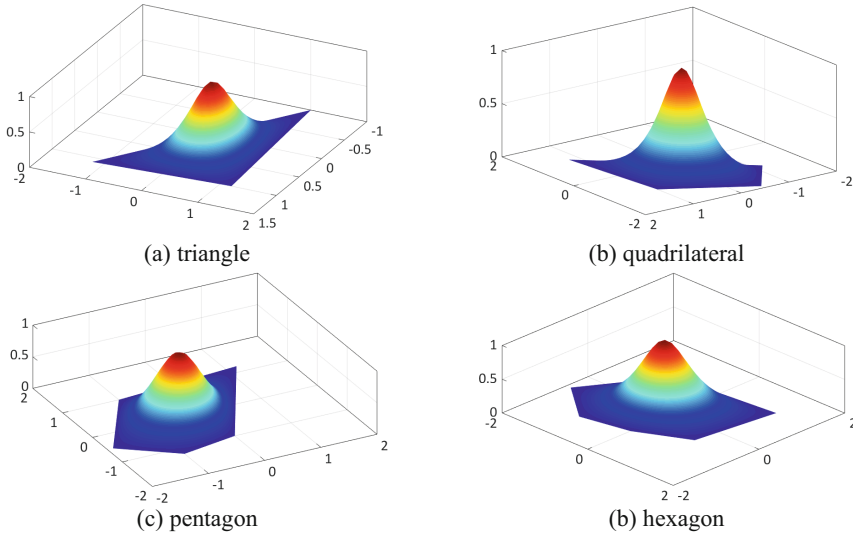


Fig. 3. The view of bubble shape function of triangle, quadrilateral, pentagon and hexagon. [17, 18, 26].

and its gradient is

$$\nabla \phi_b^e = \frac{\|\mathbf{x} - \mathbf{x}_b\|_{\Omega^e}^2 \nabla \tilde{\psi} + \nabla \|\mathbf{x} - \mathbf{x}_b\|_{\Omega^e}^2 \tilde{\psi}}{\left(\|\mathbf{x} - \mathbf{x}_b\|_{\Omega^e}^2 \tilde{\psi} + 1\right)^2}. \tag{24}$$

6 Numerical Test

In this section, the effectiveness of MINI-PFE is tested by a numerical example with a simple rectangular domain shown in Fig. 4(a). It has an inlet (4 m) on the left-hand side, an outlet (1.5 m) on the right-one and the rest is wall. At the inlet, the velocity components are set to $u_x = 10.0$ m/s and $u_y = 0$ m/s. The velocity at the wall boundary is zero, and the kinematic pressure at the outlet boundary is set zero. The fluid properties are: fluid density $\rho = 1000$ kg/m³, kinematic fluid viscosity $\nu = 1$ m²/s.

A polygonal mesh sample is presented in the Fig. 4(b) with 200 elements formed by 400 outer nodes and 200 bubble nodes. It means that the total number of DOFs for velocity is 1200 and for pressure is 800. The validated points of velocity and pressure are Node 1 (7,1.5) and Node 2(7,0.75) see in Fig. 4(b). In this section, ten polygonal meshes are created to check the convergence of the proposal MINI-PE for fluid computation.

The results of velocity and pressure field are introduced in the Fig. 5. It can be seen that the results of velocity field are normal. However, the abnormal thing is shown in

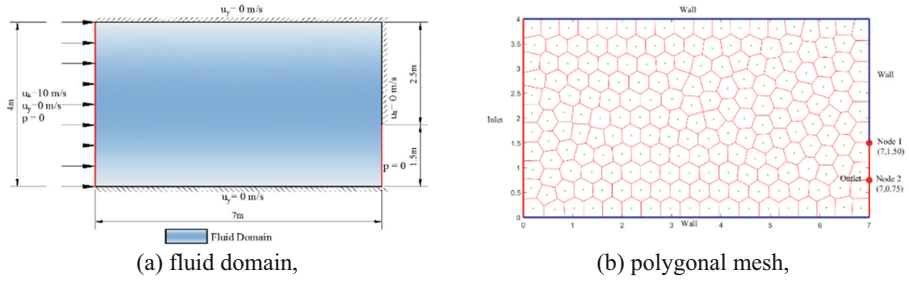


Fig. 4. The fluid domain (a) and its polygonal mesh (b).

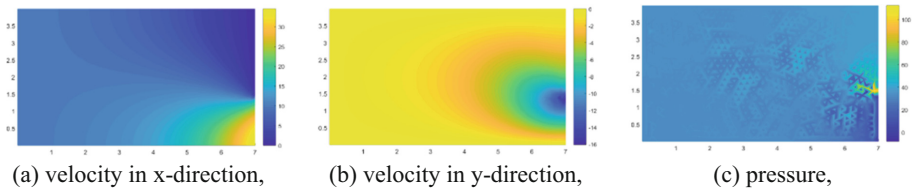


Fig. 5. The fluid domain (a) and its polygonal mesh (b).

the Fig. 5(c). It is the checkboard mode of pressure. It initially indicates that the MINI-PE for fluid computation cannot naturally satisfy the inf-sub condition.

The results at Node 1 and Node 2, shown in Table 1 and Fig. 6 demonstrate the convergence of the velocity and pressure.

Table 1. The velocity and pressure at validated points.

No.	Total Dofs of mesh	Velocity (m/s) at Node 2		Pressure (kPa) at Node 1
		v_x	v_y	p
1	166	29.7988	-15.6169	72.9956
2	326	31.9789	-14.9572	79.7571
3	563	31.1910	-14.0921	80.9511
4	806	32.8440	-13.7847	84.8782
5	1197	29.5146	-9.33240	84.7884
6	1603	29.6639	-9.02490	85.9124
7	1997	29.6254	-9.44350	87.1058
8	2397	29.3346	-9.13650	86.6133
9	3188	29.3785	-9.21540	86.3403
10	3979	29.4090	-9.09260	88.0629



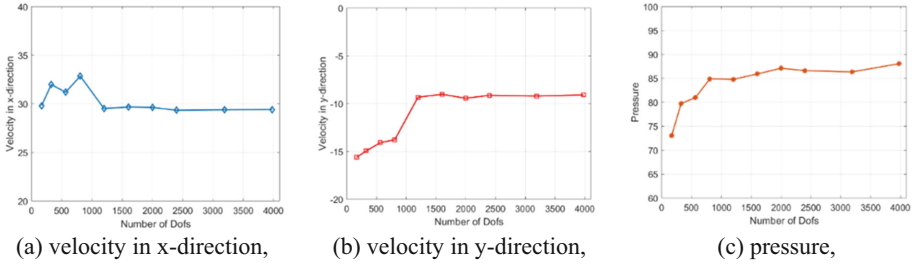


Fig. 6. The fluid domain (a) and its polygonal mesh (b).

It is clear that, the velocity of flow that is approximated by MINI-PE get quick convergence (around 1000 dofs), see in Fig. 6(a and b). However, it is not the same for pressure results that is unstable when velocity converged; see in Fig. 6(c).

7 Conclusions

As a conclusion, the proposal polygonal element, MINI-PE, purposing for the fluid computation is not as expectation, particularly, the pressure field of fluid flow has the checkboard mode. This is a inhibition of applying MINI-PE in the fluid problems. It means that in order to utilize the MINI-PE for fluid computation, a supplement method that improves the accuracy of MINI-PE is needed. That method stabilizes the pressure filed so that the solution is improved. Hence, the further goal of this research will develop a stabilization method to overcome the current problem of the using MINI-PE in the fluid computation.

Acknowledgement. The authors acknowledge the financial support of VLIR-OUS TEAM Project, VN2017TEA454A103, ‘An innovative solution to protect Vietnamese coastal riverbanks from floods and erosion’, funded by the Flemish Government.



References

1. Süli, A.S.E.: Numerical Mathematics and Scientific Computation. Oxford University Press, Oxford (2001)
2. Wendt, J.F.: Computational Fluid Dynamics. Springer, Heidelberg (2009)
3. Donea, J., Huerta, A.: Finite Element Methods for Flow Problems. Wiley, Chichester (2003)
4. Anderson, Jr., J.: Governing equations of fluid dynamics. In: Computational Fluid Dynamics, pp. 15–51. Springer, Heidelberg (2009)

5. Förste, J., Girault, V., Raviart, P.-A.: Finite Element Methods for Navier-Stokes Equations. Theory and Algorithms. Springer, Heidelberg (1986). ISBN 3-540-15796-4 (Springer Series in Computational Mathematics, vol. 5), ZAMM-Journal of Applied Mathematics and Mechanics/Zeitschrift für Angewandte Mathematik und Mechanik, vol. 67, no. 11, p. 579 (1987)
6. Brezzi, F., Fortin, M.: Mixed and Hybrid Finite Element Methods. Springer Series in Computational Mathematics, vol. 15. Springer, New York (1991)
7. Nguyen-Thoi, T., Phung-Van, P., Nguyen-Hoang, S., Lieu-Xuan, Q.: A smoothed coupled NS/nES-FEM for dynamic analysis of 2D fluid–solid interaction problems. In: Applied Mathematics and Computation, vol. 232, pp. 324–346, 4 January 2014
8. Vu-Huu, T., Phung-Van, P., Nguyen-Xan, H., Abdel-Wahab, M.: structure. Presented at the international conference on advances in computational mechanics - ACOME Phu Quoc, Vietnam, August 2017
9. Nguyen-Thoi, T., Phung-Van, P., Ho-Huu, V., Le-Anh, L.: An edge-based smoothed finite element method (ES-FEM) for dynamic analysis of 2D fluid-solid interaction problems. KSCE J. Civil Eng. **19**(3), 641–650 (2015)
10. Nguyen-Thoi, T., Phung-Van, P., Nguyen-Hoang, S., Lieu-Xuan, Q.: A coupled alpha-FEM for dynamic analyses of 2D fluid–solid interaction problems. J. Comput. Appl. Math. **271**, 130–149 (2014)
11. Nguyen-Thoi, T., Phung-van, P., Rabczuk, T., Nguyen-Xuan, H., Le-Van, C.: An application of the ES-FEM in solid domain for dynamic analysis of 2D fluid–solid interaction problems. Int. J. Comput. Methods **10**(01), 1340003 (2013)
12. Talischì, C., Pereira, A., Paulino, G.H., Menezes, I.F., Carvalho, M.S.: Polygonal finite elements for incompressible fluid flow. Int. J. Numer. Methods Fluids **74**(2), 134–151 (2014)
13. Talischì, C., Paulino, G.H., Pereira, A., Menezes, I.F.: PolyMesher: a general-purpose mesh generator for polygonal elements written in Matlab. Struct. Multidiscip. Optim. **45**(3), 309–328 (2012)
14. Sieger, D., Alliez, P., Botsch, M.: Optimizing voronoi diagrams for polygonal finite element computations. In: Proceedings of the 19th International Meshing Roundtable, pp. 335–350. Springer, Heidelberg (2010)
15. Ebeida, M.S., Mitchell, S.A.: Uniform random Voronoi meshes. In: Proceedings of the 20th International Meshing Roundtable, pp. 273–290. Springer (2011)
16. Wachspress, E.L.: A Rational Finite Element Basis. Elsevier, New York (1975)
17. Floater, M.S.: Wachspress and mean value coordinates. In: Approximation Theory XIV: San Antonio 2013, pp. 81–102. Springer (2014)
18. Floater, M., Gillette, A., Sukumar, N.: Gradient bounds for Wachspress coordinates on polytopes. SIAM J. Numer. Anal. **52**(1), 515–532 (2014)
19. Chau, K.N., Chau, K.N., Ngo, T., Hackl, K., Nguyen-Xuan, H.: A polytree-based adaptive polygonal finite element method for multi-material topology optimization. Comput. Methods Appl. Mech. Eng. **332**, 712–739 (2017)
20. Nguyen-Xuan, H., Nguyen-Hoang, S., Rabczuk, T., Hackl, K.: A polytree-based adaptive approach to limit analysis of cracked structures. Comput. Methods Appl. Mech. Eng. **313**, 1006–1039 (2017)
21. Malsch, E.A., Dasgupta, G.: Shape functions for polygonal domains with interior nodes. Int. J. Numer. Methods Eng. **61**(8), 1153–1172 (2004)
22. Warren, J.: Barycentric coordinates for convex polytopes. Adv. Comput. Math. **6**(1), 97–108 (1996)
23. Meyer, M., Barr, A., Lee, H., Desbrun, M.: Generalized barycentric coordinates on irregular polygons. J. Graph. Tools **7**(1), 13–22 (2002)

24. Hiyoshi, H., Sugihara, K.: Two generalizations of an interpolant based on Voronoi diagrams. *Int. J. Shape Model.* **5**(02), 219–231 (1999)
25. Sukumar, N., Tabarraei, A.: Conforming polygonal finite elements. *Int. J. Numer. Methods Eng.* **61**(12), 2045–2066 (2004)
26. Sukumar, N., Malsch, E.: Recent advances in the construction of polygonal finite element interpolants. *Arch. Comput. Methods Eng.* **13**(1), 129 (2006)



Investigation of Inclined Wellbore Stability Using Numerical Analysis

Weiwei Liu^{1,2}, Xiaohua Zhu², Yunlai Zhou^{3(✉)}, Xiangning Zhang^{4,5}, and Magd Abdel Wahab⁶

¹ The Key Laboratory of Well Stability and Fluid & Rock Mechanics in Oil and Gas Reservoir of Shaanxi Province, Xi'an Shiyou University, Xi'an, China

² School of Mechatronic Engineering, Southwest Petroleum University, Chengdu, China

³ Department of Civil and Environmental Engineering, National University of Singapore, Singapore, Singapore
zhouyunlail68168@gmail.com

⁴ Department of Materials Science and Engineering, The University of Tennessee, Knoxville, USA

⁵ State Key Laboratory of Mechanical Transmissions, Chongqing University, Chongqing, China

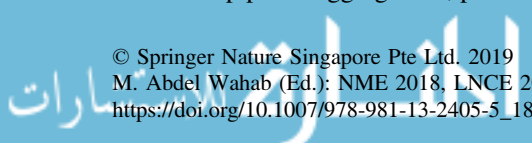
⁶ Soete Laboratory, Faculty of Engineering and Architecture, Ghent University, Ghent, Belgium

Abstract. Wellbore instability problem is one of the key problems in drilling highly deviated, extended reach wells, particularly in high temperature, high-pressure formations (HPHT). However, many researches are focus on the vertical wellbore, and few studies have investigated on the three-dimensional inclined wellbore instability analysis which considering the influence of thermo-oroelastoplasticity. In this paper, a three-dimensional fully coupled thermo-oroelastoplasticity inclined wellbore stability model is presented by using finite element method, besides, this model can be used for the wells with any deviation angle and azimuth angle just by changing the far field stresses and boundary conditions. The distribution of pore pressure, wellbore stresses under the conditions of various deviation angle, consolidation times and temperatures have been analyzed. The research results show that, the stability problems are generally serious in deviated wells. The wellbore has more instability while the consolidation time increases and it has more instability in the heating cases than in cooling cases. The conclusions achieved in this paper will help the drilling engineers to understand the inclined wellbore instability problems correctly.

Keywords: Inclined well · Finite element · Filter cake · Temperature Permeate · Fully coupled thermo-oroelastoplasticity model

1 Introduction

Wellbore instability problems may cause significant problems in drilling operations (including well completion, logging and cementing), such as increased drilling time, stuck drill pipe or logging tools, pore log quality, inadequate cement placement around



well casing [1–3]. According to the statistics, the annual expenditure to control the wellbore instability is as high as six billion dollars in the global petroleum industry and wellbore failures give rise to significant lost time accounting for over 40% of all non-productive time [4–7]. Stability problems are not only appear in vertical wells, they can also happened at deviated wells and the stability problems are generally more serious in deviated wells due to the unfavorable stress distribution, especially in high temperature and high pressure formations. Therefore, the need for deviated wellbore instability analysis is rising due to the increasing use of highly deviated, extended reach wells, it is vital to understand the mechanisms of inclined wellbore instability and analyze the reason of wellbore instability for insuring the safety during drilling and high rate of penetration and efficiency.

During the drilling process, the temperature difference between the drilling mud and formation has a great influence on the stress and pore pressure distributions of the borehole. Many researches have performed numerous studies about the wellbore stability while under the effect of coupled thermo-poroelastic. The research of Biot [8] theory for coupling thermal, hydraulic and mechanical processes in a fluid saturated porous media has attracted the attention of many scholars, among them, Rice and Cleary [9], Detournay and Cheng [10], Cui et al. [11, 12], Cui et al. [13], and Santarelli et al. [14]. The constitutive equation of thermo-poroelastic theory was first proposed by Palciauskas and Domenico [15] for the nonisothermal case. Subsequently, Aadnoy and Chenevert [16] have studied the general behavior of inclined boreholes based on the linear elastic and isotropic theory. Zhai et al. [17] established a new model and numerical scheme which take in account the effects of both thermal and hydraulic diffusion to reveal the influences of poro-elasticity and thermo-elasticity on wellbore stability. Jia et al. [18] studied the coupled process of wellbore and discussed its influence on pore pressure, temperature and stress. Gelet et al. [19] proposed a fully coupled finite element method which can be used to analyze the wellbore stability problem under non-isothermal conditions of thermo-elastic porous double porous media. Gaede et al. [20] have presented a strict verification of the analytical Amadei solution for the stress concentration around a random orientated wellbore in the anisotropic elastic medium. Goshtasbi [21] have researched the mechanical stability of three kinds of wells in seven different stress regimes and diverse orientations using FLAC3-D software, including vertical, directional and horizontal wellbores. Wang et al. [22] studied the variety of the temperature and pore pressure nearby the wellbore in the radial direction and calculated the tangential stress of wellbore while under-balanced drilling. Manshad et al. [23] have presented four different kinds of rock failure criteria, including Mohr-Coulomb, Mogi-Coulomb, Modified Lade and Tresca yield criterion and used them to optimize the drilling direction and mud pressure.

Most of the above literatures are focus on the vertical wellbore, and few studies have investigated on the three-dimensional inclined wellbore instability analysis, which considering the influence of thermo-poroelastoplasticity. In this present paper, a three-dimensional fully coupled thermo-poroelastoplasticity inclined wellbore stability model is established by using the finite element method, besides, this model can be used for the wells with any deviation angle and azimuth angle just by changing the far field stresses and boundary conditions. The distribution of pore pressure and wellbore

stress under the conditions of various deviation angle, consolidation times and temperatures has been discussed.

2 Numerical Analysis

The spatial position is determined by the wellbore deviation angle and azimuth angle of the borehole. For the isotropy formations without considering the tectonic stress, the behavior is not fully decided by the azimuth but the deviation angle. Figure 1 sketches a wellbore of general orientation in cross formation (with an arbitrary deviation angle ω) with respect to the orthogonal coordinate frame (x', y', z'), the figure also declares a cross-section orthogonal to the wellbore axis (z) and shows the far field stresses with respect to the local frame of reference (x, y, z). The borehole deviation causes a shear component stress σ_{zx} , the wellbore rock is in a three dimensional stress state under the action of principle stresses and shear stresses. The three-dimensional finite element of inclined well model, which takes into account the influence of thermo-poroelastoplasticity and filter cake, is established in this paper, it consists of 626 three-dimensional fully coupled temperature-pore pressure elements. The model has specified thickness in the z -direction with a single layer of 3D elements is used to accommodate the shear components. The thickness of the model is chosen as unit length for normalization, just as Fig. 2 shows. The wellbore stability problem becomes more complex with the coupled effects of pore pressure, in-situ stress, mud pressure and temperature. According to the theory of elastic-plastic mechanics, the length of the model sides is 10 times more than borehole diameter. The temperature at wellbore wall is equal to the drilling fluid and the pore pressure at wellbore wall is equal to the drilling mud pressure after the borehole generation. The properties of the rock are shown in Table 1.

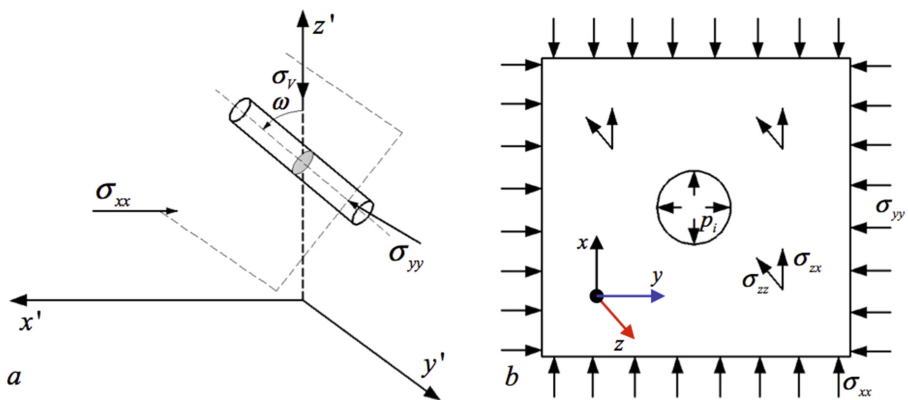


Fig. 1. The schematic of inclined wellbore in the orthogonal coordinate frame and the far field stresses in the local frame of reference

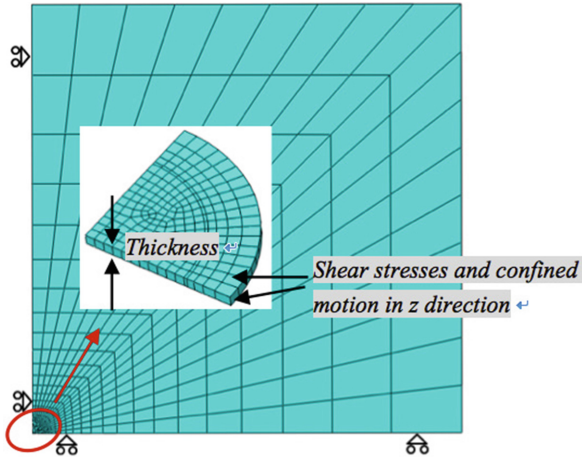


Fig. 2. Finite element model of inclined borehole

Table 1. Properties of the rock used in the computations

Young's modulus, E	16532 MPa
Poisson's ratio, ν	0.308
lame constant, λ	10137.6 MPa
Permeability coefficient, K	$1 \times 10^{-12} \text{m} \cdot \text{s}^{-1}$
Porosity, n	0.1
Solid mass density, ρ_m	2500kg/m^3
Solid mass thermal expansion coefficient, β_m	$1.5 \times 10^{-5}/^\circ\text{C}$
Solid mass thermal conductivity, k_m	$3.08 \text{J/m} \cdot \text{s} \cdot ^\circ\text{C}$
Solid mass specific heat, c_m	$896 \text{J/g} \cdot ^\circ\text{C}$
Biot coefficient, α	1
Pore fluid conductivity, k_f	$0.58 \text{J/m} \cdot \text{s} \cdot ^\circ\text{C}$
Pore fluid specific heat, c_f	$4200 \text{J/g} \cdot ^\circ\text{C}$
Pore fluid expansion, β_f	$2 \times 10^{-4}/^\circ\text{C}$
Pore fluid density, ρ_f	1000kg/m^3
Specific weight of pore fluid, γ_w	$1 \times 10^4 \cdot \text{N/m}^3$
Fluid viscosity, μ	$0.001 \text{Pa} \cdot \text{s}$
Friction angle, φ	46.4°
Cohesion stress, c	9.46 MPa
Mini horizontal principal stress, σ_h	32 MPa
Max horizontal principal stress, σ_H	32 MPa
Overburden pressure, σ_v	75 MPa
Initial pore pressure, p_p	30.3 MPa

The numerical simulation process can be divided into two steps. The first step is initial ground stress balance calculation; the rock suffers the principle stresses and shear stresses in this step. The second step is the fully coupled thermo-poroelastoplasticity analysis after the borehole generated by using birth-death element method, the wellbore will suffer the mud pressure and the temperature boundary and pore pressure boundary of wellbore wall will be changed.

3 Results and Analysis

When the borehole forms the drilled-out rocks are replaced by the drilling mud, then the drilling fluid will invasion into the wellbore wall or the pore fluid seep out, resulting in the pore pressure changes; besides, during the drilling process, there exist temperature difference between the drilling fluid and the formation. In the deeper formations the temperature of drilling mud is lower than the formation temperature. The wellbore rock matrix and pore medium will shrink due to the cooling effect on the wellbore wall. On the contrary, in the upper formations, the temperature of drilling mud is higher than the formation temperature, the rock matrix and porous medium will be expanded because of the heating effect on formation. Assuming that the initial formation temperature is $120\text{ }^{\circ}\text{C}$, the temperature gradients are $+50\text{ }^{\circ}\text{C}$ and $-50\text{ }^{\circ}\text{C}$, borehole radius is 108 mm , the drilling mud pressure is 30 MPa . For the convenience of analysis in the later sections, two paths along to the x -axis and y -axis directions are established, just as the red line shown in the Fig. 3.

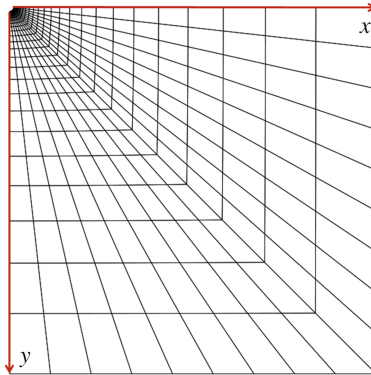


Fig. 3. The schematic of the two paths

3.1 The Effects of Temperature and Consolidation Time on Pore Pressure

The pore pressures around the wellbore in vertical well for various times (1 h, 10 h and 50 h) and temperatures (+50 °C, -50 °C) are shown in Fig. 4. For the heating cases, a significant increase of pressure is formed near the wellbore at early times in x-axis direction. With the time increasing the peak of the pore pressure is reduced and moves away from the wellbore. The pore pressure of the far away wellbore is approximately equal to the initial formation pore pressure. For the cooling cases, the negative peak of the pore pressure will be appeared in x-axis direction; with the time increasing the peak of the pore pressure is also reduced and equal to the initial formation pore pressure at the far away wellbore. In a word, heating increases the pore pressure and cooling reduces the pore pressure, with the time, increasing the peak of the pore pressure is reduced.

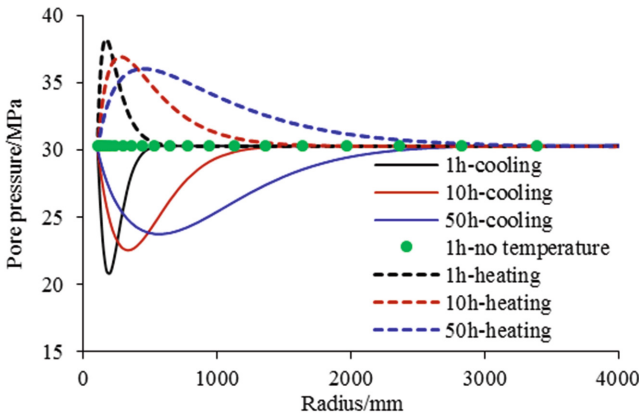


Fig. 4. The effects of temperature and consolidation time on pore pressure

3.2 The Effects of Deviation Angle on Pore Pressure

The effects of deviation angle on pore pressure are depicted in Fig. 5, a significant pressure decrease is generated near the wellbore, with the deviation angle increase the deviatoric component of geostatic stresses generate higher negative pore pressure in x-axis direction; the higher positive pore pressure will be generated with the deviation angle increase in the y-axis direction.

3.3 The Effects of Deviation Angle on Wellbore Stress

The stresses around the borehole under different deviation angles are shown in Figs. 6 and 7. Form Fig. 6(a) we know that the radial stress is decreasing to a certain value as far away from the wellbore, the radial stress is decreasing with the increasing of

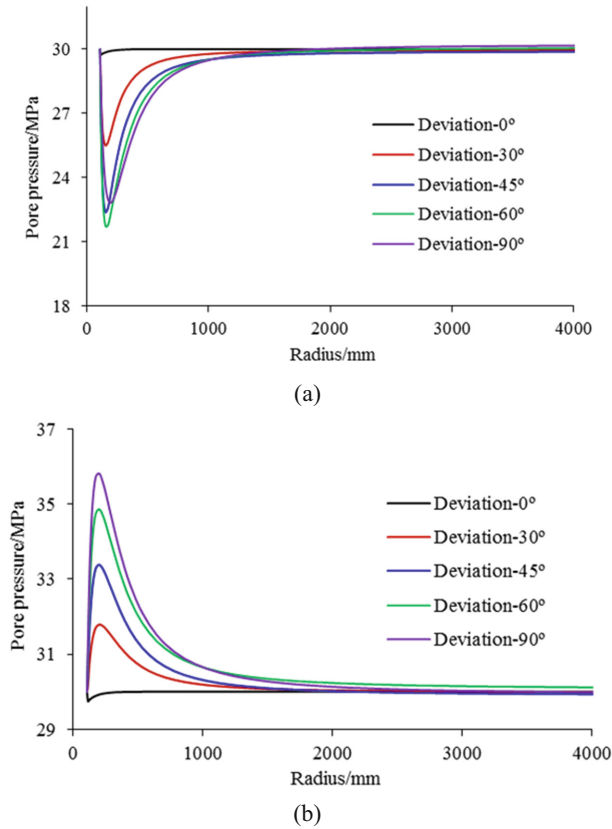


Fig. 5. The effects of deviation angle on pore pressure in (a) x-axis direction and (b) y-axis direction

deviation angle. In this paper, the negative stress is treating as compressive stress and the positive stress is treating as tensile stress. As Fig. 6(b) shows, a significant stress decrease is formed near the wellbore in the y-axis direction; with the deviation angle increases the peak of stress is increased. As Fig. 7(a) shows, the tangential stress near the wellbore in x-axis direction first decreases and then increases; while the deviation angle is 90° , the tangential stress at wellbore wall is larger than zero. It means that the tangential stress at the wall is changed from compressive stress to tensile stress; as a result, the tensile failure of wellbore is prone to occur. As Fig. 7(b) shows, the tangential stress near the wellbore in y-axis direction is decreasing with the increase of deviation angle.

The plastic deformations under various deviation angles are shown in Fig. 8. The wellbore is totally stability in vertical well while is instability in inclined well; it is mean that the stability problems are generally larger in deviated wells. As the deviation angle increases, the shear failure in x-axis direction is restrained while the tensile failure is more prone to happen and the shear failure in y-axis direction is promoted.

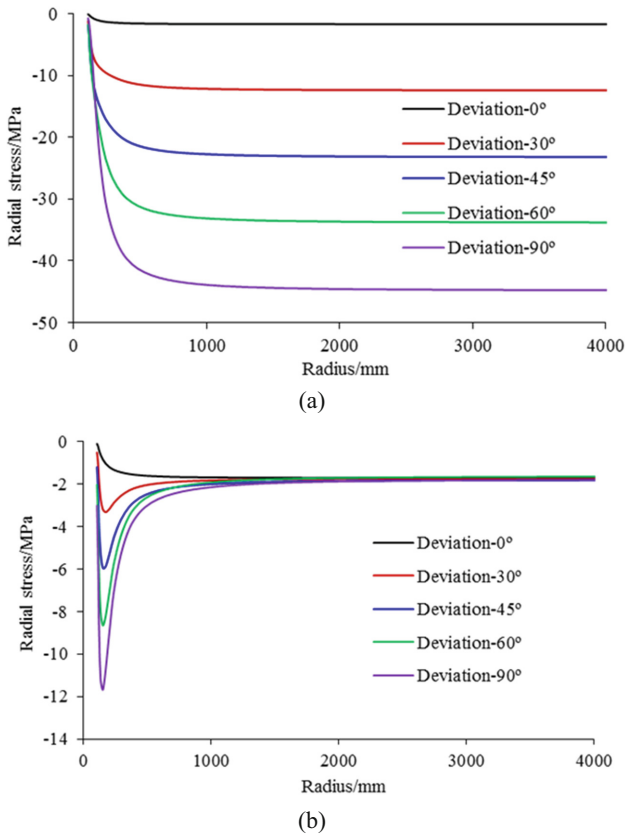


Fig. 6. The effect of deviation on radial stress in (a) x-axis direction and (b) y-axis direction

3.4 The Effects of Consolidation Time on Wellbore Stability

In order to make sure the consolidation time on borehole failure, the five inclined well (0°, 30°, 45°, 60°, 90°) are analyzed. The results show that the wellbore is more instability while the consolidation time increases. The calculated results with deviation angle 45° and 90° are shown in Fig. 9 and Fig. 10 respectively.

3.5 The Effects of Temperature Gradients on Wellbore Stability

The effects of temperature gradients on wellbore stability have been researched. The results show that the wellbore has more instability in the heating cases than in cooling cases. The reason for this phenomenon is that the borehole will expand then the borehole radius decreases, so the compressive stress will be increase causing wellbore instability. The calculated results with deviation angle 30° and 45° are shown in Fig. 11 and Fig. 12 respectively.



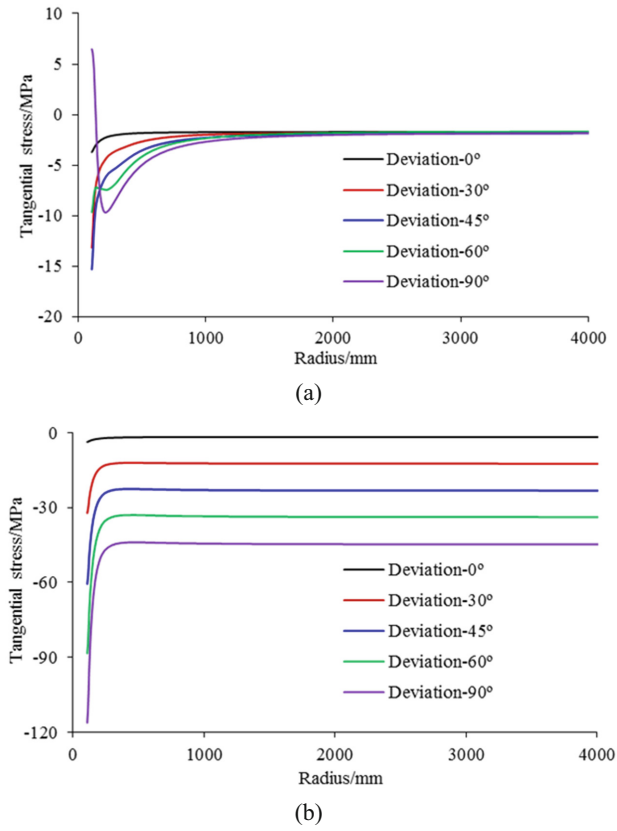


Fig. 7. The effect of deviation on tangential stress in (a) x-axis direction and (b) y-axis direction

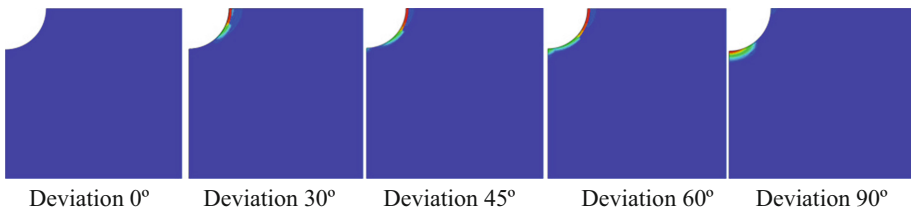


Fig. 8. Plastic deformation under various deviation angles

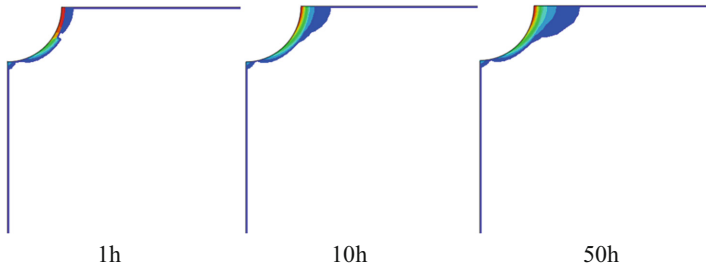


Fig. 9. Plastic deformation with deviation angle 45°

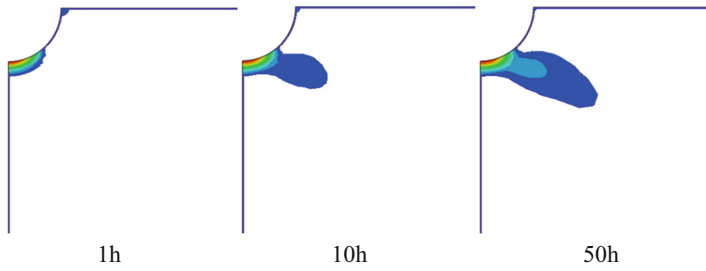


Fig. 10. Plastic deformation with deviation angle 90°

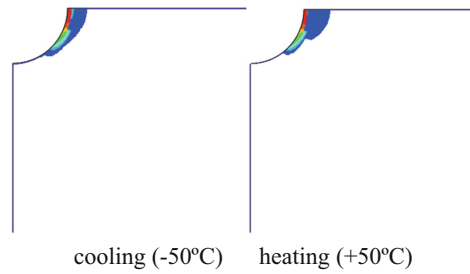


Fig. 11. The effect of temperature gradients on wellbore stability with deviation angle 30°

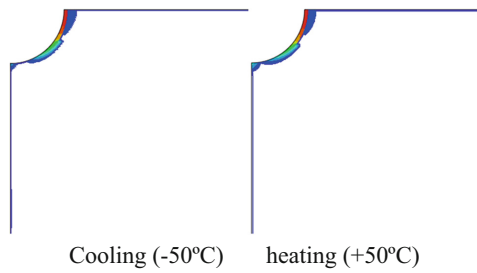


Fig. 12. The effect of temperature gradients on wellbore stability with deviation angle 45°

4 Conclusions

For the heating cases, a significant pressure increase is generated near the wellbore at early times. With the time increasing the peak of the pore pressure is reduced and moves away from the wellbore. The pore pressure of the far away wellbore is approximately equal to the initial formation pore pressure. For the cooling cases, the negative peak of the pore pressure will be appeared; with the time increasing the peak of the pore pressure is also reduced and equal to the initial formation pore pressure at the far away wellbore.

A significant pressure decrease is generated near the wellbore at early times, with the deviation angle increase the deviatoric component of geostatic stresses generate higher negative pore pressure in x-axis direction; in the y-axis direction, the higher positive pore pressure will be generated with the deviation angle increase.

The stability problems are generally serious in deviated wells. As the deviation angle increases, the shear failure in x-axis direction is restrained while the tensile failure is more prone to happen and the shear failure in y-axis direction is promoted.

The wellbore has more instability while the consolidation time increases. The wellbore has more instability in the heating cases than in cooling cases.

Acknowledgement. This work reported in this paper was supported by key laboratory of well stability and fluid & rock mechanics in Oil and gas reservoir of Shaanxi Province, Xi'an Shiyou University (WSFRM20180102001), National Natural Science Foundation of China (Grant No. 51674214).

References

1. Garrouch, A.A., Ebrahim, A.S.: Assessment of the Stability of Inclined Wells. SPE Western Regional Meeting (2001)
2. McLellan, P., Hawkes, C.: Borehole stability analysis for underbalanced drilling. *J. Can. Pet. Technol.* **40**(5), 31–38 (2001)
3. Ewy, R.T.: Yield and closure of directional and horizontal wells. *Int. J. Rock Mech. Min. Sci. Geomech. Abstr.* **30**(7), 1061–1067 (1993)
4. Wu, C., Chen, M., Jin, Y.: A prediction method of borehole stability based on seismic attribute technology. *J. Petrol. Sci. Eng.* **65**(3–4), 208–216 (2009)
5. Zhang, J.C., Lang, J., Standifird, W.: Stress, porosity, and failure-dependent compressional and shear velocity ratio and its application to wellbore stability. *J. Petrol. Sci. Eng.* **69**(3–4), 193–202 (2009)
6. Zhu, X., Liu, W.: The effects of drill string impacts on wellbore stability. *J. Petrol. Sci. Eng.* **109**, 217–229 (2013)
7. Zhu, X., Liu, W., Liu, Q.: The mechanism and law of wellbore instability due to drill string impact in air drilling. *Int. J. Oil Gas Coal Technol.* **8**(2), 153–181 (2014)
8. Biot, M.A.: General theory of three-dimensional consolidation. *J. Appl. Phys.* **12**(2), 155–164 (1941)
9. Rice, J.R., Cleary, M.P.: Some basic stress diffusion solutions for fluid-saturated elastic porous media with compressible constituents. *Rev. Geophys.* **14**(2), 227–241 (1976)

10. Detournay, E., Cheng, H.D.: Poroelastic response of a borehole in a non-hydrostatic stress field. *Int. J. Rock Mech. Min. Sci. Geomech. Abstr.* **25**(88), 171–182 (1988)
11. Cui, L., Cheng, A.H.D., Abousleiman, Y.: Poroelastic solution for an inclined borehole. *J. Appl. Mech.* **64**(1), 32–38 (1997)
12. Cui, L., Ekbote, S., Abousleiman, Y., et al.: Borehole stability analyses in fluid saturated formations with impermeable walls. *Int. J. Rock Mech. Min. Sci.* **35**(4), 582–583 (1998)
13. Cui, L., Abousleiman, Y., Cheng, A.H.D., et al.: Time-dependent failure analysis of inclined boreholes in fluid-saturated formations. *J. Energy Res. Technol.* **121**(1), 31–39 (1999)
14. Santarelli, F.J., Brown, E.T., Maury, V.: Analysis of borehole stresses using pressure-dependent, linear elasticity. *Int. J. Rock Mech. Min. Sci. Geomech. Abstr.* **23**(6), 445–449 (1986)
15. Palciauskas, V.V., Domenico, P.A.: Characterization of drained and undrained response of thermally loaded repository rocks. *Water Resour. Res.* **18**(2), 281–290 (1982)
16. Aadnoy, B.S., Chenevert, M.E.: Stability of highly inclined boreholes (includes associated papers 18596 and 18736). *SPE Drill. Eng.* **2**(4), 364–374 (1987)
17. Zhai, Z., Zaki, K.S., Marinello, S.A., et al.: Coupled thermoporoelastic effects on borehole stability. In: *SPE Annual Technical Conference and Exhibition*. Society of Petroleum Engineers (2009)
18. Jia, S., Ran, X., Wang, Y., et al.: Fully coupled thermal-hydraulic-mechanical model and finite element analysis for deformation porous media. *Chin. J. Rock Mech. Eng.* **31**(2), 3547–3556 (2012)
19. Gelet, R., Loret, B., Khalili, N.: Borehole stability analysis in a thermoporoelastic dual-porosity medium. *Int. J. Rock Mech. Min. Sci.* **50**, 65–76 (2012)
20. Gaede, O., Karpfinger, F., Jocker, J., et al.: Comparison between analytical and 3D finite element solutions for borehole stresses in anisotropic elastic rock. *Int. J. Rock Mech. Min. Sci.* **51**, 53–63 (2012)
21. Goshtasbi, K., Elyasi, A., Naeimipour, A.: Numerical assessment of the mechanical stability in vertical, directional and horizontal wellbores. *Int. J. Min. Sci. Technol.* **23**(6), 937–942 (2013)
22. Wang, M., Zhang, Z., Ma, Q.: Influence of thermo-seepage coupling effect on wellbore stress under the underbalanced condition. *Drill. Prod. Technol.* **37**(1), 1–3 (2014)
23. Manshad, A.K., Jalalifar, H., Aslannejad, M.: Analysis of vertical, horizontal and deviated wellbores stability by analytical and numerical methods. *J. Petrol. Explor. Prod. Technol.* **4**(4), 1–11 (2014)



Size-Dependent Analysis for FG-CNTRC Nanoplates Based on Refined Plate Theory and Modified Couple Stress

Cuong-Le Thanh^{1,2(✉)}, T. Vu-Huu¹, P. Phung-Van¹,
Hung Nguyen-Xuan³, and Magd Abdel Wahab¹

¹ Soete Laboratory, Faculty of Engineering and Architecture,
Ghent University, Ghent, Belgium
cuong.lt@ou.edu.vn

² Faculty of Civil Engineering and Electricity, Ho Chi Minh City Open
University, Ho Chi Minh City, Vietnam

³ Center for Interdisciplinary Research in Technology, Ho Chi Minh City
University of Technology (Hutech), Ho Chi Minh City, Vietnam

Abstract. This paper presents static bending behaviour of functionally graded carbon nanotube-reinforced composite (FG-CNTRC) nanoplates with four types of distribution of carbon nanotubes. The NURBS based isogeometric analysis (IGA) is associated with refined plate theory (RPT) with four unknowns, in which, there is no need to use shear correction factors. To capture the size-dependent effect of plate, the modified couple stress theory is used with only one material length scale parameter. The accuracy and efficiency of proposed method are demonstrated through comparison with reference solutions. A number of numerical examples are presented to demonstrate the influence of the length scale on the bending behaviors of FG-CNTRC nanoplates.

Keywords: NURBS · FG-CNTRC · RPT · Size-effect · Length scale ratio
Modified couple stress

1 Introduction

In recent year, the functionally graded carbon nanotube-reinforced composites (FG-CNTRC) have paid special attention to many researcher because of superior feature of carbon nanotubes (CNTs), such as high tensile strength, low density, advanced mechanical and electrical properties [2, 4, 8]. Due to the excellent properties of CNT, various applications of FG-CNTRC can be performed in engineering structures such as automobiles, submarine, fuel tanks, diesel engine pistons, aerospace equipment's, solar panels and so on.

To analyse the behaviour of FG-CNTRC beams and plates, many theories are developed to calculate the static bending, vibration and buckling. Based on Finite Element Method (FEM), Rashidifar and Ahmadi [16] investigated the free vibration response of FG nanocomposite beams reinforced single walled carbon nanotubes (SWCNTs). The material properties of FG-CNTRC beam were investigated by using the Eshelby-Mori-Tanaka method. Natural frequencies and critical buckling load of

FG-CNTRC nanocomposite Timoshenko beams were investigated by Yas and Samadi [24] with different boundary conditions. To analyse the nonlinear vibration of FG-CNTRC Timoshenko beams, Ke et al. [6] employed Ritz method to derive the governing equation from which the nonlinear frequencies of FG-CNTRC beam could be obtained. Alibeigloo [1] developed three-dimensional theory of elasticity for investigating the static bending problem of FG-CNTRC plate with piezoelectric layers under uniform load for simply supported boundary conditions. By using the first-order shear deformation theory and element-free IMLS-Ritz, Zhang et al. [25] investigated the free vibration behaviours of FG-CNTRC triangular plates reinforced SWCNTs. Lei et al. [9] proposed an approach for the buckling analysis of FG-CNTRC plates by using the element-free kp-Ritz method with a set of mesh-free kernel particle functions.

Using the classical mechanics theories, the size-effect of nanoplates is not taken into account in analysing the behaviour of nanoplates. For this reason, researchers developed higher order continuum theories for capturing the size-effect of nanoplates [7, 10, 21, 22]. Among these theories, the modified couple stress (MCS) proposed by Yang et al. [23] is considered as simplest theory to capture the size-effect, because it contains only one material length scale parameter.

Hughes et al. [5] introduced an advanced numerical method so-called IsoGeometric Analysis (IGA) which combine the Computer Aided Design (CAD) and Finite Element Analysis (FEA). The non-uniform rational B-spline (NURBS) basic functions are employed to describe the accurate geometry domain of structure. Moreover, it is easy to increase the order of NURBS functions with the smoothness through knot insertion [3, 13]. IGA has been applied for the solution of the linear and non-linear problems of FG-CNTRC nanoplates [14, 15, 20]. Furthermore, there are no publications on using the refined plate theories (RPT) [11] based on MCS theory and NURBS basic functions for the analysis the size effect behaviours of FG-CNTRC nanoplates. In this paper, the bending behaviours of FG-CNTRC nanoplates are investigated by using RPT theory and IGA, while the size effects are capture based MCS theory. The weak form of static bending is derived using the Hamilton's principle. By comparing the results with references solutions through the numerical examples, the proposed method proves its accuracy and dependability.

2 Main Theories

2.1 Refined Plated Theory

Based on Reddy's theory [17], which contains five unknowns, the four-variable RPT theory was proposed by Senthilnathan [11] such as:

$$\begin{aligned} u(x, y, z) &= u_0(x, y) - zw_{b,x}(x, y) + g(z)w_{s,x}(x, y) \\ v(x, y, z) &= v_0(x, y) + zw_{b,y}(x, y) + g(z)w_{s,y}(x, y) \\ w(x, y, z) &= w_b(x, y) + w_s(x, y) \end{aligned} \quad (1)$$

In Eq. (1), for depiction the spreading of transverse shear stress and strains across the thickness direction, the function $g(z) = f(z) - z$ is taken in the function $u(x, y, z)$

and $v(x, y, z)$, in which, the function $f(z) = -8z + 10z^3/h^2 + (6z^5)/(5h^4) + (8z^7)/(7h^6)$ [12] is satisfying the traction-free condition at the top and bottom surfaces ($z = \pm h/2$). Moreover, there is no requirement to use the shear correction factor for RPT theory.

From Eq. (1), the strain-displacement relations can be expressed as:

$$\begin{aligned} \epsilon_b &= \epsilon_o + z\kappa_1 + g\kappa_2 \\ \gamma &= f'\epsilon_s \end{aligned} \tag{2}$$

where

$$\begin{aligned} \epsilon_b &= \begin{Bmatrix} \epsilon_{xx} \\ \epsilon_{yy} \\ \gamma_{xy} \end{Bmatrix}; \epsilon_o = \begin{Bmatrix} u_{0,x} \\ v_{0,y} \\ u_{0,y} + v_{0,x} \end{Bmatrix}; \kappa_1 = - \begin{Bmatrix} w_{b,xx} \\ w_{b,yy} \\ 2w_{b,xy} \end{Bmatrix}; \\ \kappa_2 &= \begin{Bmatrix} w_{s,xx} \\ w_{s,yy} \\ 2w_{s,xy} \end{Bmatrix}; \gamma = \begin{Bmatrix} \gamma_{xz} \\ \gamma_{yz} \end{Bmatrix}; \epsilon_s = \begin{Bmatrix} w_{s,x} \\ w_{s,y} \end{Bmatrix} \end{aligned} \tag{3}$$

2.2 Modified Couple Stress Theory

To capture the size-effect of nano-plates, the modified couple stress theory proposed by Yang et al. [23] is used. The virtual strain energy contain not only the symmetric tensor σ_{ij} but also the deviatoric part of symmetric couple stress tensor m_{ij} such as:

$$\delta U = \int_V (\sigma_{ij}\delta\epsilon_{ij} + m_{ij}\delta\chi_{ij})dV \tag{4}$$

in which, ϵ_{ij} are components of Green-Lagrange strain tensor; χ_{ij} are the components of the symmetric curvature tensor m_{ij} .

According to Eq. (1), the components of the rotation vector are given by:

$$\begin{aligned} \theta_x &= \frac{1}{2} \left(\frac{\partial w}{\partial y} - \frac{\partial v}{\partial z} \right) = \frac{1}{2} (2w_{b,y} + 2w_{s,y} - f'(z)w_{s,y}) \\ \theta_y &= \frac{1}{2} \left(\frac{\partial u}{\partial z} - \frac{\partial w}{\partial x} \right) = \frac{1}{2} (-2w_{b,x} - 2w_{s,x} + f'(z)w_{s,x}) \\ \theta_z &= \frac{1}{2} \left(\frac{\partial v}{\partial x} - \frac{\partial u}{\partial y} \right) = \frac{1}{2} (v_{0,x} - u_{0,y}) \end{aligned} \tag{5}$$

and the components of curvature vector take the form as:

$$\begin{aligned} \chi^b &= \chi_1^b + f'(z)\chi_2^b \\ \chi_1^b &= \frac{1}{2} \left\{ \begin{array}{l} 2w_{b,xy} + 2w_{s,xy} \\ -2w_{b,xy} - 2w_{s,xy} \\ (w_{b,yy} - w_{b,xx}) + (w_{s,yy} - w_{s,xx}) \end{array} \right\}; \chi_2^b = \frac{1}{4} \left\{ \begin{array}{l} -4w_{s,xy} \\ 4w_{s,xy} \\ -2(w_{s,yy} - w_{s,xx}) \end{array} \right\} \\ \chi^s &= \chi_0^s + f''(z)\chi_1^s \\ \chi_0^s &= \frac{1}{4} \left\{ \begin{array}{l} v_{0,xx} - u_{0,xy} \\ v_{0,xy} - u_{0,yy} \end{array} \right\}; \chi_1^s = \frac{1}{4} \left\{ \begin{array}{l} -w_{s,y} \\ w_{s,x} \end{array} \right\} \end{aligned} \tag{6}$$

The components of the deviatoric part of symmetric couple stress tensor can be present in a form as:

$$m_{ij} = 2G\ell^2\chi_{ij} \tag{7}$$

where, G denotes the shear module and ℓ is the material length scale parameter which is considered as a material property measuring the effect of couple stress.

2.3 Functionally Graded Carbon Nanotube-Reinforced Composites Plates

Figure 1 show four types of distributions of carbon nanotube (CNT): Uniform (UD) and functionally graded in the thickness direction of composite plate which are denoted as FG-V, FG-O, FG-X. According to the distributions of uniaxially aligned single-walled CNTs, the volume fraction V_{CNT} can be expressed as:

$$V_{CNT} = \begin{cases} V_{CNT}^* & \text{(UD)} \\ \left(1 + \frac{2z}{h}\right)V_{CNT}^* & \text{(FG-V)} \\ 2\left(1 - \frac{2|z|}{h}\right)V_{CNT}^* & \text{(FG-O)} \\ \frac{4|z|}{h}V_{CNT}^* & \text{(FG-X)} \end{cases} \tag{8}$$

in which

$$V_{CNT}^* = \frac{w_{CNT}}{w_{CNT} + (\rho_{CNT}/\rho_m) - (\rho_{CNT}/\rho_m)w_{CNT}} \tag{9}$$

where w_{CNT} is the mass fraction of the CNTs, ρ_{CNT} and ρ_m are densities of the CNTs and the matrix, respectively. By using Mori-Tanaka scheme or the rule of mixtures [18]. The effective mechanical properties of the CNT-reinforced composites plates can be estimated as follows:

$$\begin{aligned} E_{11} &= \eta_1 V_{CNT} E_{11}^{CNT} + V_m E^m \\ \frac{\eta_2}{E_{22}} &= \frac{V_{CNT}}{E_{22}^{CNT}} + \frac{V_m}{E^m} \\ \frac{\eta_3}{G_{12}} &= \frac{V_{CNT}}{G_{12}^{CNT}} + \frac{V_m}{G^m} \\ \rho &= \rho_{CNT} V_{CNT} + \rho_m V_m \end{aligned} \tag{10}$$

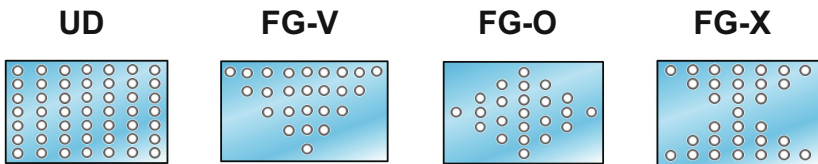


Fig. 1. Four distributions of CNT.

where the volume fraction of CNTs (V_{CNT}) and matrix (V_m) must satisfy the following equation: $V_{CNT} + V_m = 1$. E^m , G^m denote the Young's modulus and shear modulus of isotropic matrix, G_{12}^{CNT} corresponding to the shear modulus of CNT, material density is ρ ; E_{11}^{CNT} , E_{22}^{CNT} are the Young's modulus of CNTs. In addition, the efficiency parameters η_1 , η_2 and η_3 are introduced to account for the load transfer between CNTs and the matrix which are listed in Table 1 [18].

Table 1. The CNT efficiency parameters

V_{CNT}^*	η_1	η_2	η_3
0.110	0.149	0.934	0.934
0.140	0.150	0.941	0.941
0.170	0.140	1.381	1.381

In the same manner, the Poisson's ratio of the CNTRC nanoplate is defined as follow:

$$v_{12} = V_{CNT}^* v_{12}^{CNT} + V_m v^m \tag{11}$$

where v_{12}^{CNT} , v^m are the Poisson's ratio of CNT and the Poisson's ratio of matrix, respectively.

2.4 Weak Form of the Static Bending

By using the weak formulation, the weak form of the static bending analysis of CNTRC nanoplate subjected to transverse load q_0 based on MCS theory can be briefly expressed as:

$$\int_{\Omega_e} (\delta \varepsilon_b)^T \mathbf{D}_u^b \varepsilon_b d\Omega_e + \int_{\Omega_e} (\delta \varepsilon_s)^T \mathbf{D}_u^s \varepsilon_s d\Omega_e + \int_{\Omega_e} (\delta \chi^b)^T \mathbf{D}_c^b \text{diag}(\Gamma_\chi^1) \chi^b d\Omega_e + \int_{\Omega_e} (\delta \chi^s)^T \mathbf{D}_c^s \text{diag}(\Gamma_\chi^2) \chi^s d\Omega_e = \int_{\Omega_e} \delta w q_0 d\Omega_e \tag{12}$$

in which $\text{diag}(\Gamma_\chi^1) = \text{diag}(1, 1, 2)$ and $\text{diag}(\Gamma_\chi^2) = \text{diag}(2, 2)$, the material matrices \mathbf{D}_u^b , \mathbf{D}_u^s , \mathbf{D}_c^b and \mathbf{D}_c^s are taken in the form such as:

$$\mathbf{D}_u^b = \begin{bmatrix} \mathbf{A}^u & \mathbf{B}^u & \mathbf{E}^u \\ \mathbf{B}^u & \mathbf{D}^u & \mathbf{F}^u \\ \mathbf{E}^u & \mathbf{F}^u & \mathbf{H}^u \end{bmatrix}; \mathbf{D}_u^s = \int_{-h/2}^{h/2} (f'(z)^2) \begin{bmatrix} Q_{44} & 0 \\ 0 & Q_{55} \end{bmatrix} dz \tag{13}$$

$$\mathbf{D}_c^b = \begin{bmatrix} \mathbf{A}^c & \mathbf{B}^c \\ \mathbf{B}^c & \mathbf{E}^c \end{bmatrix}; \mathbf{D}_c^s = \begin{bmatrix} \mathbf{X}^c & \mathbf{Y}^c \\ \mathbf{Y}^c & \mathbf{Z}^c \end{bmatrix}$$



where the material matrices can be defined as:

$$\begin{aligned}
 (\mathbf{A}^u, \mathbf{B}^u, \mathbf{D}^u, \mathbf{E}^u, \mathbf{F}^u, \mathbf{H}^u) &= \int_{-h/2}^{h/2} \left(1, z, z^2, g(z), zg(z), g(z)^2 \right) \begin{bmatrix} Q_{11} & Q_{12} & 0 \\ Q_{21} & Q_{22} & 0 \\ 0 & 0 & Q_{66} \end{bmatrix} dz \\
 (\mathbf{A}^c, \mathbf{B}^c, \mathbf{E}^c) &= \int_{-h/2}^{h/2} \left(1, f'(z), [f'(z)]^2 \right) \begin{bmatrix} 2\mu\ell^2 & 0 & 0 \\ 0 & 2\mu\ell^2 & 0 \\ 0 & 0 & 2\mu\ell^2 \end{bmatrix} dz \\
 (\mathbf{X}^c, \mathbf{Y}^c, \mathbf{Z}^c) &= \int_{-h/2}^{h/2} \left(1, f''(z), [f''(z)]^2 \right) \begin{bmatrix} 2\mu\ell^2 & 0 \\ 0 & 2\mu\ell^2 \end{bmatrix} dz \\
 Q_{11} &= \frac{E_{11}}{1-\nu_{12}\nu_{21}}, \quad Q_{12} = \frac{\nu_{12}E_{22}}{1-\nu_{12}\nu_{21}}, \quad Q_{22} = \frac{E_{22}}{1-\nu_{12}\nu_{21}} \\
 Q_{66} &= G_{12}, \quad Q_{55} = G_{13}, \quad Q_{44} = G_{23}
 \end{aligned} \tag{14}$$

in which ν_{12}, ν_{21} are the effective Poisson’s ratio, defined as the ratio of transverse strain to the axial strain and E_{11}, E_{22}, E_{33} are the Young’s moduli of the CNTRC plates in the principal material coordinates and G_{12}, G_{13}, G_{23} are the effective shear moduli.

2.5 A Novel NURBS Formulation Based on Modified Couple Stress Theory

By using the NURBS basic function, the displacement field u of CNTRC nanoplate can be approximately expressed as:

$$\mathbf{u}^h(\xi, \eta) = \sum_{i=1}^{m \times n} N_I(\xi, \eta) \mathbf{d}_I \tag{15}$$

where N_I is the shape function and $\mathbf{d}_I = [u_{0I}, v_{0I}, w_{bI}, w_{sI}]$ denotes the vector of degree of freedom associated with the control point I . The in-plane and shear strains can be obtained as:

$$[\boldsymbol{\varepsilon}_0^T, \boldsymbol{\kappa}_1^T, \boldsymbol{\kappa}_2^T, \boldsymbol{\varepsilon}_s^T]^T = \sum_{i=1}^{m \times n} [(\mathbf{B}_I^m)^T, (\mathbf{B}_I^{b1})^T, (\mathbf{B}_I^{b2})^T, \mathbf{B}_I^s]^T \mathbf{d}_I \tag{16}$$

in which

$$\begin{aligned}
 \mathbf{B}_I^m &= \begin{bmatrix} N_{I,x} & 0 & 0 & 0 \\ 0 & N_{I,y} & 0 & 0 \\ N_{I,y} & N_{I,x} & 0 & 0 \end{bmatrix}; \quad \mathbf{B}_I^{b1} = - \begin{bmatrix} 0 & 0 & N_{I,xx} & 0 \\ 0 & 0 & N_{I,yy} & 0 \\ 0 & 0 & 2N_{I,xy} & 0 \end{bmatrix}; \\
 \mathbf{B}_I^{b2} &= \begin{bmatrix} 0 & 0 & 0 & N_{I,xx} \\ 0 & 0 & 0 & N_{I,yy} \\ 0 & 0 & 0 & 2N_{I,xy} \end{bmatrix}; \quad \mathbf{B}_I^{s0} = \begin{bmatrix} 0 & 0 & 0 & N_{I,x} \\ 0 & 0 & 0 & N_{I,y} \end{bmatrix}
 \end{aligned} \tag{17}$$



and the curvatures are

$$\left[(\chi_1^b)^T, (\chi_2^b)^T, (\chi_0^s)^T, (\chi_1^s)^T \right]^T = \sum_{i=1}^{m \times n} \left[(\mathbf{B}_i^{zb1})^T, (\mathbf{B}_i^{zb2})^T, (\mathbf{B}_i^{zs0})^T, (\mathbf{B}_i^{zs1})^T \right]^T dI \quad (18)$$

where

$$\begin{aligned} \mathbf{B}_i^{zb1} &= \frac{1}{2} \begin{bmatrix} 0 & 0 & 2N_{I,xy} & 2N_{I,xy} \\ 0 & 0 & -2N_{I,xy} & -2N_{I,xy} \\ 0 & 0 & (N_{I,yy} - N_{I,xx}) & (N_{I,yy} - N_{I,xx}) \\ 0 & 0 & 0 & -2N_{I,xy} \end{bmatrix}; \\ \mathbf{B}_i^{zb2} &= \frac{1}{4} \begin{bmatrix} 0 & 0 & 0 & 2N_{I,xy} \\ 0 & 0 & 0 & -2N_{I,xy} \\ 0 & 0 & 0 & -2N_{I,xy} \end{bmatrix} \\ \mathbf{B}_i^{zs0} &= \frac{1}{4} \begin{bmatrix} -N_{I,xy} & N_{I,xx} & 0 & 0 \\ -N_{I,xy} & N_{I,xy} & 0 & 0 \end{bmatrix}; \mathbf{B}_i^{zs1} = \frac{1}{4} \begin{bmatrix} 0 & 0 & 0 & N_{I,y} \\ 0 & 0 & 0 & N_{I,x} \end{bmatrix} \end{aligned} \quad (19)$$

Substituting Eqs. (16) and (18) into Eq. (12), the matrix form of the global equilibrium equations for static bending of CNTRC nanoplate can be written as follows

$$\mathbf{Kd} = \mathbf{F} \quad (20)$$

in which $\mathbf{K} = \mathbf{K}^u + \mathbf{K}^\theta$ is the global stiffness matrix; $\mathbf{K}^u, \mathbf{K}^\theta$ are the stiffness matrix corresponding to the classical mechanic theory and the couple stress theory. These matrix are computed by:

$$\begin{aligned} \mathbf{K}^u &= \int_{\Omega} \left[\begin{Bmatrix} \mathbf{B}^m \\ \mathbf{B}^{b1} \\ \mathbf{B}^{b2} \end{Bmatrix} \right]^T \begin{bmatrix} \mathbf{A}^u & \mathbf{B}^u & \mathbf{E}^u \\ \mathbf{B}^u & \mathbf{D}^u & \mathbf{F}^u \\ \mathbf{E}^u & \mathbf{F}^u & \mathbf{H}^u \end{bmatrix} \begin{Bmatrix} \mathbf{B}^m \\ \mathbf{B}^{b1} \\ \mathbf{B}^{b2} \end{Bmatrix} + (\mathbf{B}^s)^T \mathbf{D}_u^s \mathbf{B}^s \Big] d\Omega \\ \mathbf{K}^\theta &= \int_{\Omega} \left[\begin{Bmatrix} \chi_1^b \\ \chi_2^b \end{Bmatrix} \right]^T \begin{bmatrix} \mathbf{A}^c & \mathbf{B}^c \\ \mathbf{B}^c & \mathbf{E}^c \end{bmatrix} \begin{Bmatrix} \chi_1^b \\ \chi_2^b \end{Bmatrix} + \begin{Bmatrix} \chi_0^s \\ \chi_1^s \end{Bmatrix} \begin{bmatrix} \mathbf{X}^c & \mathbf{Y}^c \\ \mathbf{Y}^c & \mathbf{Z}^c \end{bmatrix} \begin{Bmatrix} \chi_0^s \\ \chi_1^s \end{Bmatrix} \Big] d\Omega \end{aligned} \quad (21)$$

and the load vector can be expressed as:

$$\mathbf{F} = \int_{\Omega} q_0 \mathbf{R} d\Omega; \quad \mathbf{R}_I = [0, 0, N_I, N_I]^T \quad (22)$$

3 Numerical Examples

In this section, several numerical examples are presented with the following aims:

- (1) Confirming the accuracy of the proposed approach presented in Sect. 2 by comparing its results with those in analytical solution [19].



(2) Investigating the size effect behaviours on the static bending of CNTRC nanoplate with difference thicknesses of plate by changing the material length scale parameter.

3.1 Example 1

The cubic NURBS function with the element mesh of 9×9 is sufficient for all numerical examples in this paper. For verification studies, the material properties of all edges simply support (SSSS) homogenous square plates are chosen as: $E = 1.44$ GPa, $\nu = 0.3$. The non-dimensional deflection of plates $\bar{w} = (10wEh^3)/(q_0a^4)$ under a sinusoidally distributed load $q_0 \sin(\pi x/a) \sin(\pi y/a)$ are compared with the Navie analytical solutions [19] and a numerical solution [21] with six different values of material length scale ratio ($\ell/h = 0, 0.2, 0.4, 0.6, 0.8, 1$) and the results match very well with reference solutions. It is clearly that, the length scale ratio $\ell/h = 0$ indicates the plates with no size-effect and the present model get back the classical model.

Further verification of accuracy of present model is performed on SSSS functionally graded (FG) square microplates with difference length-thickness ratio under sinusoidal load. The FG plate is made of alumina (Al - material 1), aluminium (Al2O3 - material 2) and the material properties are chosen such as: $E_1 = 380$ GPa; $\rho_1 = 3800$ kg/m³; $E_2 = 70$ GPa; $\rho_2 = 2702$ kg/m³, and Poisson’s ratio is constant through the thickness of plate with its value is equal to 0.3. In Tables 2 and 3, the non-dimensional deflections of thick plates are little bit smaller than analytical solution [19] (1.87% for $n = 0$ and 1.57% for $n = 5, 10$), and there is no difference between proposed model and other references solutions for thin plates. It clearly noticed that the two above examples prove the accuracy and conformability of proposed model.

Table 2. Non-dimensional central deflection of SSSS homogeneous plates

ℓ/h	$a/h = 5$			$a/h = 20$			$a/h = 100$		
	Ref. [19]	Ref. [21]	Present	Ref. [19]	Ref. [21]	Present	Ref. [19]	Ref. [21]	Present
0	0.3433	0.3433	0.3433	0.2842	0.2842	0.2842	0.2804	0.2804	0.2804
0.2	0.275	0.2875	0.2862	0.2430	0.243	0.2429	0.2401	0.2401	0.2401
0.4	0.1934	0.1934	0.1912	0.1693	0.1693	0.1691	0.1677	0.1677	0.1677
0.6	0.1251	0.1251	0.1232	0.1124	0.1124	0.1123	0.1116	0.1116	0.1116
0.8	0.0838	0.0838	0.0823	0.0765	0.0765	0.0764	0.0760	0.076	0.0760
1	0.0588	0.0588	0.0577	0.0542	0.0542	0.0541	0.0539	0.0539	0.0539

3.2 Example 2

The material properties of the matrix of FG-CNTRC nanoplates are assumed to be $E^m = 2.1$ GPa, $\nu^m = 0.34$, $\rho^m = 1160$ kg/m³ at the room temperature (300 K) and the material properties of single wall CNTs can be taken as follows: $E_{11}^{CNT} = 5.6466$ TPa, $E_{22}^{CNT} = 7.08$ TPa, $G_{12}^{CNT} = 1.9445$ TPa, $\alpha_{11}^{CNT} = 3.4584 \cdot 10^{-6}$ /K, $\alpha_{22}^{CNT} = 5.1682$



Table 3. Non-dementional deflection of SSSS AL/AL2O3 square microplates (rule of mixtures scheme)

a/h	ℓ/h	n = 0			n = 5			n = 10		
		Ref. [19]	Ref. [20]	Present	Ref. [19]	Ref. [20]	Present	Ref. [19]	Ref. [20]	Present
5	0	0.3433	0.3433	0.3433	1.0885	1.0885	1.0877	1.2276	1.2276	1.2270
	0.2	0.2875	0.2875	0.2862	0.8981	0.8981	0.8926	1.0247	1.0247	1.0184
	0.4	0.1934	0.1934	0.1912	0.5925	0.5925	0.5850	0.6908	0.6908	0.6818
	0.6	0.1251	0.1251	0.1232	0.3802	0.3802	0.3745	0.4514	0.4514	0.4443
	0.8	0.0838	0.0838	0.0823	0.2539	0.2539	0.2500	0.3052	0.3052	0.3003
	1	0.0588	0.0588	0.0577	0.1782	0.1782	0.1754	0.2158	0.2158	0.2124
10	0	0.2961	0.2961	0.2960	0.9114	0.9114	0.9111	1.0087	1.0087	1.0085
	0.2	0.2520	0.2520	0.2517	0.7743	0.7743	0.7730	0.8697	0.8697	0.8682
	0.4	0.1742	0.1742	0.1736	0.5349	0.5349	0.5331	0.6175	0.6175	0.6153
	0.6	0.1150	0.1150	0.1145	0.3538	0.3538	0.3524	0.4177	0.4177	0.4159
	0.8	0.0780	0.0780	0.0776	0.2403	0.2403	0.2393	0.2879	0.2879	0.2866
	1	0.0552	0.0552	0.0549	0.1702	0.1702	0.1695	0.2058	0.2058	0.2050
20	0	0.2842	0.2842	0.2842	0.8669	0.8669	0.8668	0.9538	0.9538	0.9537
	0.2	0.2430	0.2430	0.2429	0.7429	0.7429	0.7425	0.8303	0.8303	0.8299
	0.4	0.1693	0.1693	0.1691	0.5201	0.5201	0.5196	0.5986	0.5986	0.5980
	0.6	0.1124	0.1124	0.1123	0.3470	0.3470	0.3466	0.4090	0.4090	0.4085
	0.8	0.0765	0.0765	0.0764	0.2368	0.2368	0.2365	0.2834	0.2834	0.2831
	1	0.0542	0.0542	0.0541	0.1681	0.1681	0.1680	0.2033	0.2033	0.2030
100	0	0.2804	0.2804	0.2804	0.8527	0.8527	0.8526	0.9362	0.9362	0.9361
	0.2	0.2401	0.2401	0.2401	0.7327	0.7327	0.7327	0.8176	0.8176	0.8176
	0.4	0.1677	0.1677	0.1677	0.5153	0.5153	0.5153	0.5925	0.5925	0.5924
	0.6	0.1116	0.1116	0.1116	0.3448	0.3448	0.3448	0.4061	0.4061	0.4061
	0.8	0.0760	0.0760	0.0760	0.2357	0.2357	0.2356	0.2820	0.2820	0.2820
	1	0.0539	0.0539	0.0539	0.1675	0.1675	0.1675	0.2024	0.2024	0.2024

$10^{-6}/K$. The values of the CNT efficiency parameters for three case of V_{CNT}^* are taken in Table 1. Moreover, we assume that $G_{23} = G_{13} = G_{12}$ and $\eta_3 = \eta_2$.

In the Table 4, the non-dimensional central deflection of SSSS FG-CNTRC nanoplates under uniform loads for classical model are compare with the solutions obtained by the FE commercial package ANSYS [26] and the numerical method in Ref. [21]. It can be seen that the present results are in good agreement with those reference solutions. In addition, Table 4 shows that the deflection for FG-O plate is the largest but it is the smallest for FG-X plate in case for simply support boundary condition.



Table 4. Non-dimensional deflection of FG-CNTRC plates (SSSS)

V_{CNT}^*	a/h	Types	Ref. [26]	Ref. [20]	Present
0.11	50	UD	1.155	1.157	1.1417
		FG-V	1.652	1.654	1.6411
		FG-O	2.15	2.162	2.1477
		FG-X	0.792	0.792	0.7767
	20	UD	0.03629	0.0363	0.03395
		FG-V	0.04876	0.04882	0.04673
		FG-O	0.0613	0.06233	0.06006
		FG-X	0.02696	0.02696	0.02458
0.14	50	UD	0.918	0.916	0.9012
		FG-V	1.326	1.322	1.308
		FG-O	1.738	1.736	1.721
		FG-X	0.628	0.627	0.612
	20	UD	0.03001	0.02992	0.02760
		FG-V	0.04025	0.04015	0.03801
		FG-O	0.0507	0.0512	0.04887
		FG-X	0.02258	0.02256	0.02023
0.17	50	UD	0.752	0.753	0.744
		FG-V	1.081	1.083	1.075
		FG-O	1.411	1.417	1.410
		FG-X	0.514	0.516	0.506
	20	UD	0.02349	0.0235	0.02203
		FG-V	0.03171	0.03178	0.03048
		FG-O	0.04007	0.04054	0.03916
		FG-X	0.01738	0.01752	0.01599

In the next step, the effects of material length scale parameter on central deflection of FG-CNTRC nanoplates are studied by increasing the parameter. Tables 5, 6 and 7 present the non-dimensional deflection of FG-CNTRC nanoplates by changing length scale ratio. It is observed that the non-dimensional deflection decrease when the ratio increase. In the other words, the higher ratio is chosen, the lower nanoplate’s central deflection as well as the thinner the nanoplate, the higher nanoplate’s stiffness.

Table 5. Non-dimensional deflection of FG-CNTRC plates ($V_{CNT}^* = 0.11$)

a/h	Types	ℓ/h					
		0	0.2	0.4	0.6	0.8	1
20	UD	0.03395	0.03322	0.03126	0.02864	0.02578	0.02295
	FG-V	0.04673	0.04553	0.04231	0.03795	0.03328	0.02881
	FG-O	0.06006	0.05827	0.05339	0.04685	0.04005	0.03380
	FG-X	0.02458	0.02398	0.02255	0.02084	0.01909	0.01739
50	UD	1.14174	1.13206	1.09700	1.03384	0.95090	0.85917
	FG-V	1.64107	1.61482	1.53263	1.40304	1.24916	1.09243
	FG-O	2.14771	2.09937	1.95599	1.74495	1.51055	1.28598
	FG-X	0.77672	0.77297	0.75865	0.73046	0.69000	0.64157

Table 6. Non-dimensional deflection of FG-CNTRC plates ($V_{CNT}^* = 0.14$)

a/h	Types						
		0	0.2	0.4	0.6	0.8	1
20	UD	0.02760	0.02702	0.02550	0.02352	0.02139	0.01928
	FG-V	0.03801	0.03712	0.03474	0.03152	0.02803	0.02461
	FG-O	0.04887	0.04762	0.04414	0.03933	0.03418	0.02931
	FG-X	0.02023	0.01966	0.01840	0.01700	0.01565	0.01437
50	UD	0.90127	0.89615	0.87563	0.83550	0.77976	0.71539
	FG-V	1.30856	1.29281	1.24047	1.15292	1.04387	0.92823
	FG-O	1.72141	1.69178	1.59809	1.45139	1.28018	1.10920
	FG-X	0.61213	0.60965	0.60074	0.58311	0.55686	0.52422

Table 7. Non-dimensional deflection of FG-CNTRC plates ($V_{CNT}^* = 0.17$)

a/h	Types						
		0	0.2	0.4	0.6	0.8	1
20	UD	0.02203	0.02155	0.02027	0.01854	0.01665	0.01479
	FG-V	0.03048	0.02968	0.02751	0.02459	0.02148	0.01852
	FG-O	0.03916	0.03799	0.03476	0.03040	0.02587	0.02173
	FG-X	0.01599	0.01556	0.01457	0.01342	0.01227	0.01115
50	UD	0.74405	0.73736	0.71344	0.67085	0.61542	0.55455
	FG-V	1.07512	1.05669	0.99979	0.91137	0.80765	0.70314
	FG-O	1.40881	1.37575	1.27770	1.13431	0.97667	0.82723
	FG-X	0.50613	0.50307	0.49244	0.47279	0.44535	0.41294

4 Conclusions

In this paper, the refined plate theory (RPT) based the NURBS basic function has been developed to investigated the small scale effect behaviours on static bending of functionally graded carbon nanotube-reinforced composite nanoplates (FG-CNTRC) by using modified couple stress theory (MCT) with only one material length scale parameter. By using RPT theory with four unknowns, there no need to use shear correction factor and the proposed model is able to accurately capture the central deformations of FG-CNTRC nanoplates. Numerical examples show the exactness and efficiency of the proposed approach through comparison with the difference reference solutions. For studying the small scale effect of FG-CNTRC nanoplates, the deflections of plates are calculated for different small scale ratio's ℓ/h . The results also indicate that the thinner the FG-CNTRC nanoplate the higher nanoplate's stiffness.

Acknowledgement. The authors would like to acknowledge the MaDurOS project and the support from DeMoPreCI-MDT SIM SBO.

References

1. Alibeigloo, A.: Static analysis of functionally graded carbon nanotube-reinforced composite plate embedded in piezoelectric layers by using theory of elasticity. *Compos. Struct.* **95**, 612–622 (2013)
2. Khan, U., Coleman, J.N., Blau, W.J., Gun'ko, Y.K.: YK. Carbon Small but strong: a review of the mechanical properties of carbon nanotubepolymer composites **44**(9), 1624–1652 (2006)
3. Cottrell, J.A., Reali, A., Bazilevs, Y., Hughes, T.J.R.: Isogeometric analysis of structural vibrations. *Comput. Methods Appl. Mech. Eng.* **195**(41), 5257–5296 (2006)
4. Esawi, A.M.K., Farag, M.: Carbon nanotube reinforced composites: potential and current challenges. *Mater. Des.* **28**(9), 2394–2401 (2007)
5. Hughes, T.J.R., Cottrell, J.A., Bazilevs, Y.: Isogeometric analysis: CAD, finite elements, NURBS, exact geometry and mesh refinement. *Comput. Methods Appl. Mech. Eng.* **194**(39), 4135–4195 (2005)
6. Ke, Liao-Liang, Yang, Jie, Kitipornchai, Sritawat: Nonlinear free vibration of functionally graded carbon nanotube-reinforced composite beams. *Compos. Struct.* **92**(3), 676–683 (2010)
7. Koiter, W.T.: Couple stresses in the theory of elasticity, I and II *Nederl. Akad. Wetensch. Proc. Ser B* **67**, 17–44 (1964)
8. Gu, C., Lau, Kt: A critical review on nanotube and nanotube/nanoclay related polymer composite materials. *Compos. B Eng.* **37**(6), 425–436 (2006)
9. Lei, Z.X., Liew, K.M., Yu, J.L.: Buckling analysis of functionally graded carbon nanotube-reinforced composite plates using the element-free kp-Ritz method. *Compos. Struct.* **98**, 160–168 (2013)
10. Mindlin, R.D.: Influence of couple-stresses on stress concentrations. *Exp. Mech.* **3**(1), 1–7 (1963)
11. Lim, S.P., Senthilnathan, N.R., Lee, K.H., Chow, S.T.: Buckling of shear-deformable plates. *AIAA J.* **25**(9), 1268–1271 (1987)
12. Nguyen, Hoang X., Nguyen, Tuan N., Abdel-Wahab, M., Bordas, S.P.A., Nguyen-Xuan, H., Vo, T.P.: A refined quasi-3D isogeometric analysis for functionally graded microplates based on the modified couple stress theory. *Comput. Methods Appl. Mech. Eng.* **313**, 904–940 (2017)
13. Nguyen, V.P., Nguyen-Xuan, H.: High-order B-splines based finite elements for delamination analysis of laminated composites. *Compos. Struct.* **102**, 261–275 (2013)
14. Phung-Van, Phuc, Abdel-Wahab, Magd, Liew, K.M., Bordas, S.P.A., Nguyen-Xuan, H.: Isogeometric analysis of functionally graded carbon nanotube-reinforced composite plates using higher-order shear deformation theory. *Compos. Struct.* **123**, 137–149 (2015)
15. Phung-Van, Lieu, Phuc, Q.X., Nguyen-Xuan, H., Wahab, M.A.: Size-dependent isogeometric analysis of functionally graded carbon nanotube-reinforced composite nanoplates. *Compos. Struct.* **166**, 120–135 (2017)
16. Rashidifar, M.A., Ahmadi, D.: Vibration analysis of randomly oriented carbon nanotube based on FGM beam using timoshenko theory. *Adv. Mech. Eng.* **7**(2), 653950 (2015)
17. Reddy, J.N.: A simple higher-order theory for laminated composite plates. *J. Appl. Mech.* **51**(4), 745–752 (1984)
18. Shen, H.-S., Zhang, C.-L.: Thermal buckling and postbuckling behavior of functionally graded carbon nanotube-reinforced composite plates. *Mater. Des.* **31**(7), 3403–3411 (2010)
19. Thai, Huu-Tai, Kim, Seung-Eock: A size-dependent functionally graded Reddy plate model based on a modified couple stress theory. *Compos. B Eng.* **45**(1), 1636–1645 (2013)

20. Thanh, C.-L., Phung-Van, P., Thai, C.H., Nguyen-Xuan, H., Wahab, M.A.: Isogeometric analysis of functionally graded carbon nanotube reinforced composite nanoplates using modified couple stress theory. *Compos. Struct.* **184**, 633–649 (2018)
21. Richard, A.: Toupin, elastic materials with couple-stresses. *Arch. Ration. Mech. Anal.* **11**(1), 385–414 (1962)
22. Chong, A.C.M., Yang, F., Lam, D.C.C., Tong, P.: Couple stress based strain gradient theory for elasticity. *Int. J. Solids Struct.* **39**, 2731–2743 (2002)
23. Yang, F., Chong, A.C.M., Lam, D.C.C., Tong, P.: Couple stress based strain gradient theory for elasticity. *Int. J. Solids Struct.* **39**(10), 2731–2743 (2002)
24. Yas, M.H., Samadi, N.: Free vibrations and buckling analysis of carbon nanotube-reinforced composite Timoshenko beams on elastic foundation. *Int. J. Press. Vessels Pip.* **98**, 119–128 (2012)
25. Zhang, L.W., Lei, Z.X., Liew, K.M.: Free vibration analysis of functionally graded carbon nanotube-reinforced composite triangular plates using the FSDT and element-free IMLS-Ritz method. *Compos. Struct.* **120**, 189–199 (2015)
26. Zhu, P., Liew, K.M.: Static and free vibration analyses of carbon nanotube-reinforced composite plates using finite element method with first order shear deformation plate theory. *Compos. Struct.* **94**(4), 1450–1460 (2012)



Numerical Modelling of the Thermo-Mechanical Behavior of Concrete Arch Dams During the First Filling of the Reservoir

Noemi Schclar Leitão  and Eloísa Castilho  ^(✉)

Laboratório Nacional de Engenharia Civil, Lisbon, Portugal
emsantos@lnec.pt

Abstract. To understand the performance of the dam during the first filling, it is crucial to predict in real time the displacement and the stresses due to the water reservoir level and environmental conditions. Particular attention must be given to environmental actions which have a significant effect on arch dams. Hence, a correct simulation of the first filling should entail, amongst other, a proper transient heat transfer analysis to determine the temperature distribution in the dam.

The purpose of this paper is to describe the main issues concerning the structural and geotechnical modelling as well as the heat transfer and boundary conditions simulation necessary to obtain a representative behavior of the dam during the first filling.

An example of numerical simulation of the behavior of an arch concrete dam during the first filling of the reservoir is also given. The temperature distribution inside the dam was estimated using a finite element model which considered the effects associated with air temperature, water temperature and solar radiation. The structural response of the dam was assessed using the same finite element model. In this case, the contraction joints and the contact surface rock/concrete were included in the model and represented by zero thickness interface elements. The validation of the computed temperatures and the induced displacements was performed by comparison with the values measured with the monitoring system installed in the dam.

Keywords: Concrete arch dam · First filling · Thermo-mechanical FEA

1 Introduction

The first filling of a reservoir can be defined as the increase in water level behind the dam from the time the construction is complete until it reaches the desired operating level. The first filling of a reservoir should be planned, controlled, and closely monitored in order to reduce the risk of failure.

During the first filling, the reservoir is gradually risen in multiple stages. At each stage, the filling is paused to allow adequate time for monitoring and evaluating the performance of the dam and its foundation. In practice, the evaluation and assessment of project performance is usually based in design limits and threshold performance limits. However, these design limits are set for extreme conditions (e.g., empty/full

reservoir, coldest winter/hottest summer, etc.) which do not coincide with the actual state of the dam to be evaluated at each stage. Thus, it is difficult to assess if the dam presents a normal or abnormal behavior for the stage under evaluation.

To understand the performance of the dam during the first filling, it is crucial to predict, in real time, the displacements and the stresses due to the water reservoir level and environmental conditions. Particular attention must be given to environmental actions which have a significant effect on arch dams. Hence, a correct simulation of the first filling should entail, amongst other, a proper transient heat transfer analysis to determine the temperature distribution in the dam.

The purpose of this paper is to describe the main issues concerning the structural and geotechnical modelling, as well as the heat transfer and boundary conditions simulation necessary to obtain a representative behavior of the dam during the first filling.

An example of numerical simulation of the behavior of an arch concrete dam during the first filling of the reservoir is given. The validation of the computed temperatures and the induced displacements was performed by comparison with the values registered by the monitoring system installed in the dam.

2 Model Definition

2.1 Structural and Geotechnical Modelling Issues

In terms of modelling, it is evident that the geometry of the dam is well defined and reasonably easy to idealize. Also, in terms of concrete behavior, it is common practice to perform quality control of concrete that makes it possible to estimate the properties of the concrete placed into the dam body with sufficient accuracy.

In contrast, the modelling of the foundation usually involves much greater explicit uncertainties and complexities in idealizing both the geometry and the material properties.

Following the general criterion [1], an appropriate volume of the foundation rock should be included in the model to account for the effects of foundation flexibility on the static deflections and stresses of the dam. The foundation model must extend to a large enough distance beyond which its effects on deflections and stresses of the dam become negligible. Normally the site topography can be simplified by a prismatic foundation mesh constructed on semi-circular planes or developed by simple projection along the global coordinate axes, Fig. 1. It is worthwhile to mention that due to the degree of influence of the foundation in the total analysis, the element distortion resulting in the foundation mesh does not affect the accuracy of the results.

The rock mass elastic modulus is usually estimated using empirical correlations developed from *in-situ* test and rock mechanics index properties.

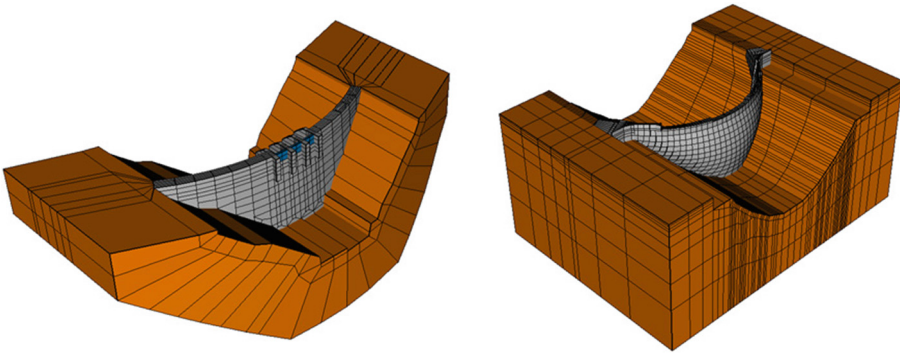


Fig. 1. Finite element models for dam and foundation.

2.2 Meshing

Although most mesh generation schemes are based on tetrahedral meshing algorithms, it is worthwhile to make an effort to construct meshes of hexahedron quadratic solid elements to represent the dam. They naturally suit the representation of vertical contraction joints and horizontal concreting lifts.

Mesh size is one of the key questions to be solved, a more refined mesh usually means more accurate results, but the computing time gets significantly higher as well. It is important to apply St Venant's principle whenever possible [2].

2.3 Contraction Joints

A concrete arch dam is constructed as a system of monolithic blocks separated by vertical contraction joints. The monoliths are constructed separately so that cooling and shrinkage may take place independently in each one. After the construction period, the contraction joints are grouted under high pressure with the aim to form a complete monolithic structure. At the end of the reservoir filling, it is usually assumed that the compressive arch stresses across the contraction joints will be further increased, such that the dam body behaves as a truly monolithic system with regard to static loads [3].

In fact, as grouted joints can take little or no tension even when a static analysis is performed, the use of linear-elastic numerical models can mislead the interpretation of the entire structure response [4].

During the filling of the reservoir, mainly when the water is still at low levels, joint openings can occur due to temperature variations. Therefore, to ensure that important aspects of the structural response are not missed, a nonlinear static analysis must be carried out. Fortunately, under normal conditions, the use of simple interface elements allowing the normal opening/closing of joints might be accurately enough to represent the actual behavior of the dam. Although more sophisticated interface elements, such as those developed for dynamic analysis [5], offer the possibility of including shear key properties, initial tensile stress, initial gap, etc., they have the drawback that the determination of these parameters remains a difficult task and cannot justify the increase in the complexity of the analysis at this stage.

2.4 Dam–Foundation Interface

High tensile stresses can be expected to occur mainly at the upstream heel due to the water load exerted by the reservoir, leading to crack formation. These cracks are usually stable, as long as shear stresses do not exceed the shear strength of mass concrete and rock. However, if the crack at the base of a dam opens, the deformations of the dam will increase resulting in a redistribution of the stresses, thus increasing the arch stresses [6].

To capture the influence of such disconnection between the dam heel and its foundation it is often represented in models by interface elements. Although this approach is accurate enough, one must bear in mind that cracks can also appear in joints of the rock mass located below the dam or even along a defective horizontal concreting lift of the dam itself [7].

On the other hand, interface elements between the dam and the rock mass foundation have to be defined if uplift load must be considered in the analysis.

3 Loads

3.1 Dead Load

Dead load is due to the weight of the concrete plus the appurtenant structures [1]. The weight of the appurtenances is normally negligible compared to the weight of the dam and may be neglected in the analysis. However, in the case of a massive overflow spillway it will be necessary to include this structure in the finite element model.

3.2 Hydrostatic Load

Regular time calculations following the water reservoir raising will allow a correct evaluation of the dam safety.

When the dam has controlled spillways equipped with gates, the use of elements with low stiffness allows transmitting the reservoir water force from the gates to the pillars of the dam. Since only resultant stresses are relevant for the safety overall analysis, the use of St Venant's principle avoids the highly mesh refinement of the pillars necessary for the representation of the gate reaction concentrated loads.

3.3 Seepage and Uplift Load

Interstitial water pressures develop within a concrete dam and its foundation as a result of preferential water penetration along discontinuities, *e.g.* joint planes, cracks and fine fissures, and also by seepage within the pore structure of rock and concrete. Uplift load is represented by the resultant effective vertical components of interstitial water pressure [8].

It is important to note that uplift pressure presents a distribution that change during the first filling of the reservoir, not only due to the level of the reservoir but also due to the progress of the hydraulic conductive process. Despite the advancements in seepage modeling that are available, experience suggests that it is difficult to model flow

through jointed rock and accurately predict foundation water pressure. Therefore, foundation pressures are normally determined using piezometric measurements [9].

3.4 Thermal Load

Concrete dams exhibit deformation from temperature changes within the concrete caused by conductive heat transfer from reservoir water, conductive heat transfer from the ambient air in contact with the dam, and radiative heat transfer from sunlight on the exposed concrete. In the presence of internal or external constraints this deformation will create thermal stresses.

Temperature distribution in the concrete is determined by thermal analysis considering the effects of transient air and water temperatures, reservoir level and solar radiation. The finite element and finite difference methods are the most commonly used numerical methods for solving the 1D to 3D thermal problem.

1D models have the advantage of saving computation time and the ability of reflecting the temperature distribution in sections far from the boundary of the dam. Therefore, they have been widely used in practice from the pre-computer era to today [10–12].

However, during the first filling of the reservoir the upstream-downstream deflection due to seasonal temperature variations dominates the response of the dam. Thus, at this stage, a 1D model is not accurate enough to simulate the actual behavior of the dam and a fully 3D analysis is required.

4 Example

As an example of the numerical simulation of the thermo-mechanical behavior of concrete arch dams during the first filling of the reservoir, the analysis of the Foz Tua dam will be presented. The Foz Tua Hydroelectric Project (owned by EDP) is located in the north region of Portugal, in the Tua River, an important right bank tributary of Douro River, close to its confluence into Douro River. The project includes a double curvature arch dam, which is 108 m high and 275 m long on its crest at elevation 272.00 m, Fig. 2. The dam is provided with a surface spillway over its crest designed for a 5500 m³/s flood, with four 15.7 m wide spans controlled by radial gates, and a downstream plunge pool. In the dam site, the valley is quite narrow and the rock foundation is sound granite. The dam was constructed between 2011 and 2016, and the first filling of the reservoir began in June 2016 and finished in June 2017.

In order to monitor the performance of Foz Tua dam during the first filling phase, a three stages filling was planned. In each stage, the rate of filling was controlled to allow the implementation of a predetermined surveillance program including the observation and analysis of instrumentation. The three stages, corresponding to water level at elevation 150.00, 168.00 and 170.00 m, stages P1, P2 and P3, respectively, were defined in order to obtain a hydrostatic pressure equal to 61%, 96% and 100% of the full storage level.



Fig. 2. Upstream view (under construction) and downstream view of Foz Tua dam.

4.1 Finite Element Model

The FE model represents the double-curvature arch concrete dam and an appropriate volume of the foundation rock. The dam includes the representation of the pillars, the surface spillway, the downstream central blocks extension up to the plunge pool and the gates, Fig. 3.

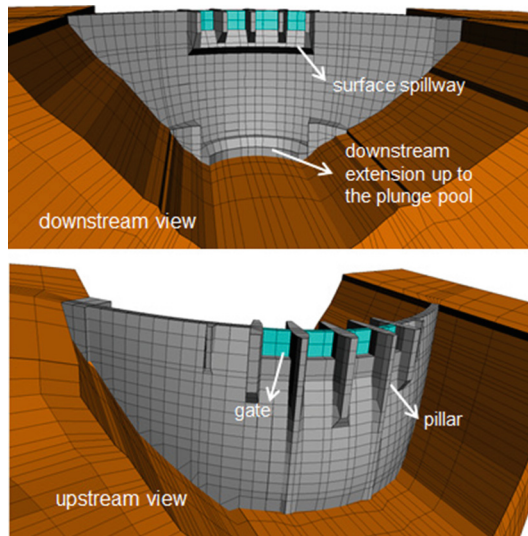


Fig. 3. Finite element model of Foz Tua dam.

The dam comprises four layers of 20 node solid elements through its thickness, except for the gravity block on the left abutment which has six layers of elements. For practical reasons, the same solid element mesh was used for both the thermal and the mechanical analysis.

For the mechanical analysis, the arch dam was divided into 18 monoliths separated by radial vertical contraction joints. The contraction joints and the dam-to-foundation contact surface were represented by 16 node zero thickness interface elements.

4.2 Thermal Analysis

The heat flowing inside a dam, and the heat entering and leaving the dam, are governed by different mechanisms. The heat inside the dam moves by conduction and it is treated as the governing equation expressed by the heat conduction equation. The heat entering or escaping the dam moves by convection, or radiation, or both, and it is usually considered as boundary conditions.

Boundary and Initial Conditions: Convection/radiation heat transfer and solar radiation flux absorption boundary conditions were applied in all air-exposed boundaries. Specified water temperature boundary conditions were applied at the upstream nodes below the water. Adiabatic boundary conditions were applied at the lateral boundary of the rock mass foundation. Bottom nodes of the foundation were prescribed with a temperature of 12 °C.

Convection/Radiation Boundary Condition: The external surface of the dam, which is not in contact with water, exchanges heat to the surroundings by means of convection and radiation calculated as follows:

$$\dot{q}_{conv.} + \dot{q}_r = h_t(T - T_a) \quad (1)$$

where the combined surface heat transfer coefficient h_t is the sum of the convective heat transfer coefficient h_c plus the radiative heat transfer coefficient h_r and T_a is the air temperature.

The convective heat transfer coefficient h_c was estimated using the expression given by Brown & Marco (1958) (as cited in Silveira [13]):

$$h_c = 0.055 \frac{k_f}{L} \left(\frac{LV\rho_f}{\mu_f} \right)^{0.75} \left[\frac{\text{W}}{\text{m}^2\text{K}} \right] \quad (2)$$

where k_f , ρ_f and μ_f are, respectively, the thermal conductivity, density and absolute viscosity of air, which correspond to the values of 0.026 W/(m K), 1.2 kg/m³ and 1.8 × 10⁻⁵ kg/(m s), V is the average wind speed in m/s and L represents the size of the considered flat surface, for which Silveira adopted the value of 0.60 m. Then, considering an average wind speed $V = 12$ km/h, the convection coefficient results $h_c = 60$ kJ/(h m² K).

Based on previous experience in Portuguese dams [13], the radiative heat transfer coefficient h_r was adopted as 18 kJ/(h m² K).

The air temperature T_a was introduced as hourly discrete data using the monitored values at the dam weather station. The intermediate values were obtained by interpolation.

Solar Radiation Boundary Condition: The solar radiation absorption is given by:

$$\dot{q}_s = \alpha I_x \quad (3)$$

where α is the absorptivity of concrete and I_x is the global irradiance incident on an arbitrary orientated surface.

For the analysis it was assumed that only the dam presented solar radiation boundary condition over its exposed surfaces with an absorption coefficient of 0.5.

The solar irradiance I_x incident on a plane oriented arbitrarily relative to the earth can be described in terms of several angles. These angles are illustrated in Fig. 4.

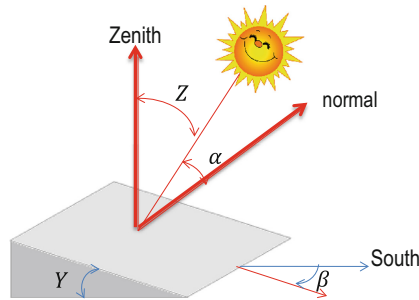


Fig. 4. Sun–earth angles for a tilted surfaces.

The solar elevation Z is the angle formed by the vertical line of the place (zenith) and the line connecting to the sun. It can be formulated in terms of the sun's declination δ , the earth's latitude ϕ , and the hour angle of the sun t :

$$\cos Z = \sin \phi \sin \delta + \cos \phi \cos \delta \cos t \quad (4)$$

The declination of the sun can be represented by the Spencer's formula, given by:

$$\delta = 0.006918 - 0.399912 \cos \gamma + 0.070257 \sin \gamma - 0.006758 \cos 2\gamma + 0.000907 \sin 2\gamma - 0.002697 \cos 3\gamma + 0.00148 \sin 3\gamma \quad (5)$$

where γ is the date expressed as an angle ($\gamma = \frac{2\pi}{365}(N - 1)$, $N =$ day number ranging from 1 on January 1st to 365 on December 31st), both δ and γ are in degrees.

The solar angle t is positive before noon and negative after noon:

$$t = -15^\circ(\text{hour} - 12) \quad (6)$$

The incidence angle α is the angle between the incident solar radiation and the normal to the surface. It can be formulated in terms of the angle of inclination of the surface, relative to the horizontal plane Y , the sun's declination δ , the earth's latitude ϕ , the hour angle of the sun t and the azimuth β :

with
$$\cos \alpha = A \sin \delta + B \cos t \cos \delta - C \sin t \cos \delta \tag{7}$$

$$\begin{aligned} A &= \cos Y \sin \phi - \sin Y \cos \phi \cos \beta \\ B &= \cos Y \cos \phi + \sin Y \sin \phi \cos \beta \\ C &= \sin Y \sin \beta \end{aligned} \tag{8}$$

The knowledge of the angle of solar elevation Z and the incident angle α allows the calculation of the solar radiation on an arbitrarily orientated surface:

$$I_x = \frac{I_h}{\cos Z} \cos \alpha \tag{9}$$

Where I_h is the global irradiance incident on a horizontal surface (oriented towards the zenith).

It is important to note that when $\cos \alpha < 0$ the solar radiation I_x must be set to zero, because in this case there is no incidence of sunlight to the considered surface. Another case in which is convenient to set the solar radiation I_x to zero is when the time of the day is close to sunrise or to sunset. In this case both the solar radiation I_h and the angle of solar elevation $\cos Z$ approach 0, creating an indeterminate limit.

Regarding the global irradiance I_h the monitored values obtained in the weather station were considered.

Water Temperature Boundary Condition: For the definition of the boundary conditions on the upstream surface of the dam, that is, for the definition of the elements above or below the water, a discretization of the level of the reservoir was adopted in bands compatible with the mesh adopted for the dam, Fig. 5. The water temperature of the reservoir was introduced as a prescribed temperature adopting the monitored upstream temperatures by the water thermometers.

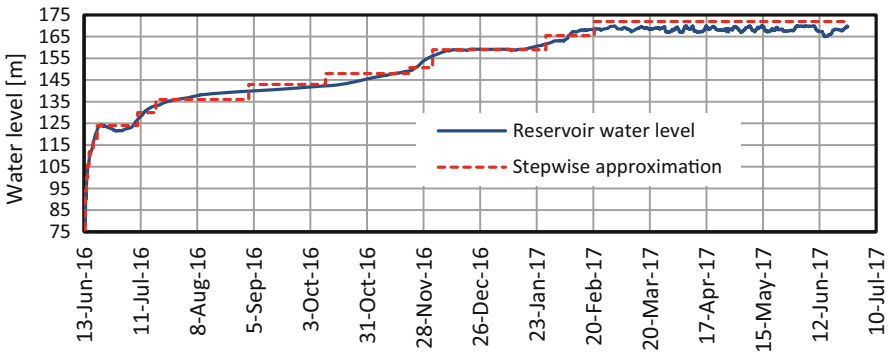


Fig. 5. Water level approximation considered in the thermal analysis.



Initial Condition: Cooling coils were placed on the top of the lift lines for circulation of cold water. At the end of the construction stage, refrigerated water was used to cool the dam sufficiently to contract the concrete and open the contraction joints for grouting. The grouting was performed in a stepwise fashion from the base to the crest of the dam. Accordingly, the artificial cooling was being deactivated once the grouting step was finished. Figure 6 shows the cooling ending dates for each level.

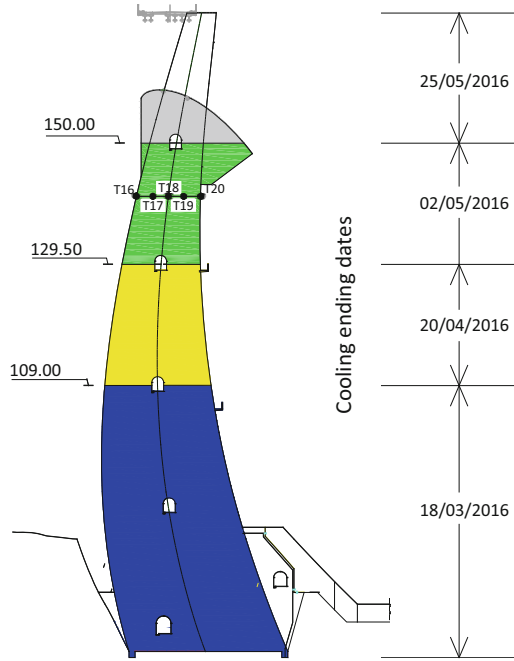


Fig. 6. Central block E1-E2 - Cooling ending dates and thermometers at elevation 141.00 m.

As a previous step, the thermal analysis was carried out considering only the foundation. After achieving convergence, the computed results were applied as initial temperatures at the mesh foundation nodes. For the dam mesh the adopted closure temperature of 10 °C was considered as initial temperature.

Analysis and Validation: The transient thermal analysis was performed with an in-house code which applies an implicit Euler backward finite difference scheme for the time discretization and a finite element scheme for the spatial discretization. Table 1 shows the values of the material properties used in the numerical simulations. The selected increment of time was 1 h.

To simulate the artificial cooling phase, a prescribed temperature of 10 °C was applied to the interior nodes of the dam mesh and removed at the cooling ending dates indicated in Fig. 6.



Table 1. Thermal properties.

Properties	Concrete	Rock mass
Conductivity coefficient k [kJ/(m h °C)]	8.4	8.4
Specific heat c [kJ/(kg °C)]	0.879	0.920
Density ρ [kg/m ³]	2400	2500

In order to validate the model, a comparison between predicted and measured temperatures was made. Figure 7 illustrates the comparison obtained by thermometers T16 to T20 located at elevation 141.00 m in block E1-E2, (see Fig. 6).

In all comparisons a good agreement between numerically calculated and measured quantities was achieved. This gave confidence that the thermal model was good enough to represent the temperature loads. Moreover, it is important to note that the numerical analysis provided more detailed information than that provided by the monitoring system.

Following the thermal analysis an input data file was prepared with the temperature loads ΔT resulted from the thermal difference between adopted reference temperature and concrete temperature for some selected dates.

4.3 Mechanical Analysis

Loads: The loads considered in the analysis were the gravity load of the dam, the hydrostatic pressure of the impounded water and the temperature load. The uplift pressure was not considered in the present analyses.

Material Properties: Since the tests performed on the concrete showed a low creep characteristic and the analysed period was short, linear elastic behaviour was adopted for the dam concrete.

For the rock mass foundation also a linear elastic behaviour was adopted. Due to the discontinuity persistence and weathering conditions of the right bank, it was assumed that the rock mass of that zone presented half of the elastic modulus considered for the foundation.

Figure 8 shows the different zones of material properties considered in the mechanical analysis.

The approach used for the interface elements is based in the penalty method and, because of that, the normal and tangential stiffness adopted for the interfaces elements have no physical meaning. For the analysis it was assumed a normal and tangential stiffness of 2×10^5 GPa/m and no tensile strength. No shear failure criteria were implemented, thus leading to an elastic behaviour when the joints were closed.

Analysis: The mechanical analysis started on June 14, 2016 corresponding to the first reading of the pendulums after the beginning of the first filling and conducted in intervals of time fitting the records of the pendulums reading.

Based on the material tests performed during construction, it was adopted for the concrete a modulus of elasticity $E_c = 30$ GPa. For the rock mass foundation the geomechanical characterization indicated a modulus of elasticity $E_f = 24$ or 12 GPa for

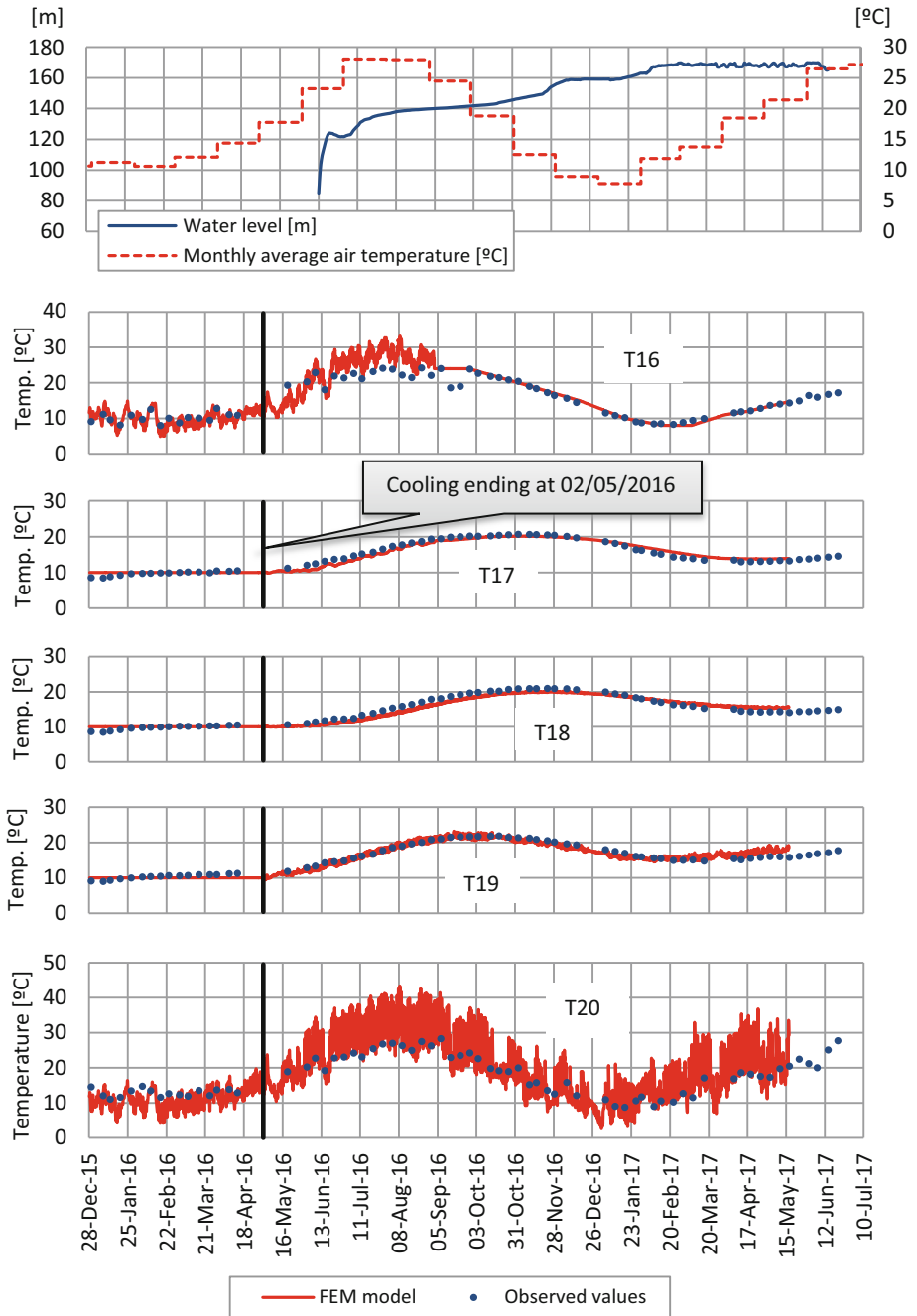


Fig. 7. Monthly average air temperatures, reservoir levels and comparison of predicted and observed temperatures at thermometers T16 to T20.



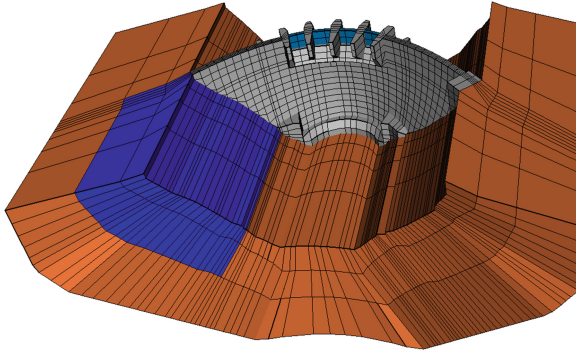


Fig. 8. Material properties zones.

the sound granite and the weathering rock of the right bank, respectively. For both materials the adopted Poisson's ratio was $\nu = 0.2$. The coefficient of linear thermal expansion adopted for the concrete was $\alpha_c = 1 \times 10^{-5} \text{ } 1/^{\circ}\text{C}$. On the contrary, the effect of thermal variation was neglected in the rock mass.

Figure 9 compares the results obtained with these properties, called Model 1, together with the values of the radial displacements observed with the pendulums at reading stations at elevation 150.35 m.

The analysis of Fig. 9 shows that Model 1 predicts results very close to the measured displacements from the beginning of the analysis to just after the end of November 2016 when the curves begin to separate.

As this behaviour was happening together with the decompression of the rock mass under the upstream base of the dam followed by an unexpectedly drainage flow increase, it was a clear evidence that the rock mass discontinuities had been opening. Consequently, there was a decrease of the stiffness of the rock mass due to the opening of the discontinuities. To approximate this new behavior of the rock mass, the rock mass modulus of elasticity was decreased to 15 GPa and 7.5 GPa for the sound granite and the weathering rock of the right bank, respectively. Model 2 represents the new obtained expected behavior.

Finally, a calibration of the concrete elasticity modulus was performed in order to obtain a better matching between the predicted and the observed behaviour. It is worthwhile to mention that at the beginning of the reservoir filling, free thermal deformation is preponderant in the dam response. Thus, during this time the induced displacements depend mostly on the adopted coefficient of linear thermal expansion. Only when the reservoir level reaches higher elevation, it is possible to analyse the correctness of the adopted concrete parameters. The adopted concrete modulus of elasticity was 20 GPa. This value was obtained by comparison between the strains measured with the Carlson extensometer and the stresses measured with the Carlson stress-meters located in nearby positions. The new behavior is represented by Model 3.

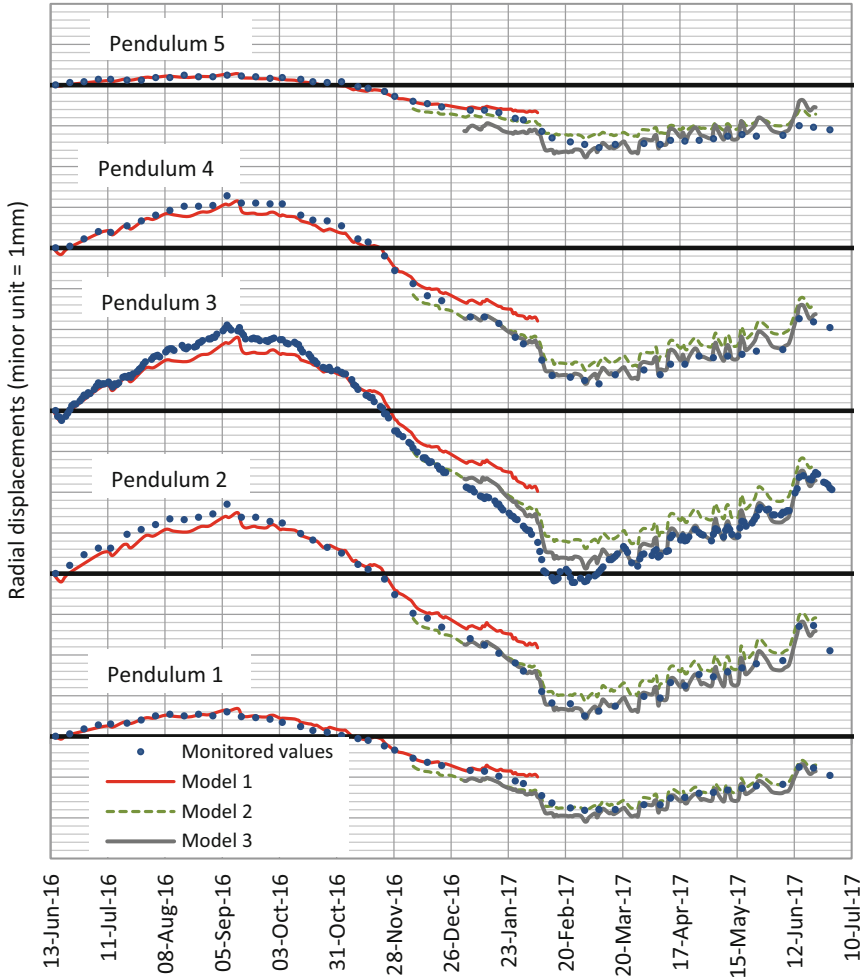
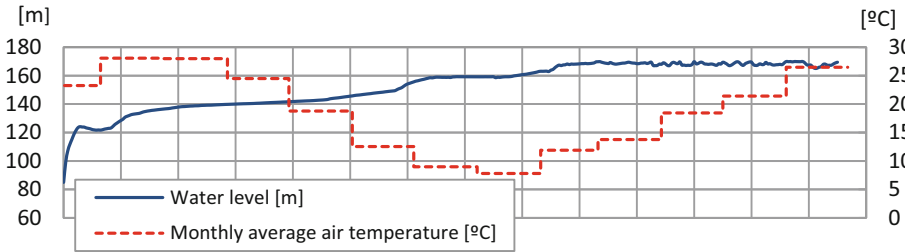


Fig. 9. Monthly average air temperatures, reservoir levels and comparison of calculated and measured radial displacements.

5 Conclusions

This paper deals with the numerical simulation of the thermo-mechanical behaviour of concrete arch dams during the first filling of the reservoir. The work has focused on the main issues concerning the structural and geotechnical modelling as well as the heat transfer and boundary conditions simulation needed to obtain a representative behaviour of the dam.

These topics were illustrated in the case study of Foz Tua dam in which the thermo-mechanical behaviour was analysed using a three-dimensional finite element model.

Due to the relevance of the environmental actions in the response of the dam, the boundary and initial conditions of the thermal analysis were thoroughly described. Time histories of calculated temperatures were compared with the corresponding thermometers. These comparisons showed that the thermal model can predict the temperature field with high accuracy.

The computed thermal load together with the gravity load and the hydrostatic pressure were applied to the mechanical model in order to obtain the expected behaviour of the dam. The results were compared with the displacement measured by the pendulums.

The main conclusion is that, during the beginning of the reservoir filling, the free thermal deformation is preponderant in the dam response. Thus, at this stage, the relevant concrete property is the coefficient of linear thermal expansion. As the reservoir level reaches higher elevation, the stiffness of the concrete becomes more important in the response of the dam and a better calibration of the adopted elastic modulus can be performed.

It is worth mentioning that numerous factors affect the dam behaviour during the first filling and special attention should be given to all monitoring values in order to adequate the model. In the case of Foz Tua dam, when the drainage flow increases unexpectedly the adopted stiffness of the rock mass had to be decreased to conveniently model the opening of the rock mass discontinuities.

Acknowledgments. The authors would like to acknowledge EDP – Energias de Portugal, S.A. for permission to publish data relative to Foz Tua dam.

References

1. USACE: Arch dam design. Engineer Manual 1110-2-2201. U.S. Army Corps of Engineers, Washington (1994)
2. MacLeod, I.A.: Modern Structural Analysis – Modelling Process and Guidance. Thomas Telford, London (2005)
3. Shaw-Han Kuo, J.: Joint Opening Nonlinear Mechanism: Interface Smeared Crack Model. Earthquake Engineering Research Center, Berkeley (1982)
4. Boggs, H.L., Jansen, R.B., Tabox, G.S.: Arch dam design and analysis. In: Jansen, R.B. (ed.) Van Nostrand Reinhold, Ney York, USA (1988)
5. Guerra, A.: Shear Key Research Project – Literature Review and Finite Element Analysis. Bureau of Reclamation, Denver (2007)

6. Wiedland, W., Malla, S.: Investigating stress concentration. *Int. Water Power Dam Constr.* 28–33 (2007)
7. Carrère, A.: Arch dams uplift and design criteria: are heel base joints useful? *Hydropower Dams* 78–86 (1994)
8. Novak, P., Moffat, A., Nalluri, C., Narayanan, R.: *Hydraulic Structures*. 4th edn. Taylor & Francis (2007)
9. USBR, USACE: Foundation risk for concrete dams. In: *Best Practices in Dam and Levee Safety Risk Analysis*. U.S Department of the Interior, Bureau of Reclamation and U.S. Army Corps of Engineers, USA (2015)
10. Stucky, A., Derron, M.: Problèmes thermiques posés par la construction des barrages-réservoirs. École Polytechnique de l'Université de Lausanne, Switzerland (1957)
11. Léger, P., Leclerc, M.: Hydrostatic, temperature, time-displacement model for concrete dams. *J. Eng. Mech.* **133**(3), 267–277 (2007)
12. Santillán, D., Salet, E., Toledo, M.: A new 1D analytical model for computing the thermal field of concrete dams due to the environmental actions. *Appl. Therm. Eng.* **85**, 160–171 (2015)
13. Silveira, A.: Temperatures variations in dams. LNEC Memória n° 177. Lisbon, Portugal (1961). (in Portuguese)



System Identification Based on Vibration Testing of a Steel I-Beam

Viet Long Ho^{1(✉)}, Ngoc Hoa Tran², Guido De Roeck³,
Tien Thanh Bui², and Magd Abdel Wahab⁴

¹ University of Transport and Communications,
Campus in Ho Chi Minh City, Ho Chi Minh, Vietnam
hvlong@utc2.edu.vn

² University of Transport and Communications, Hanoi, Vietnam

³ Department of Civil Engineering, KU Leuven, 3001 Leuven, Belgium

⁴ Soete Laboratory, Faculty of Engineering and Architecture,
Ghent University, Ghent, Belgium

Abstract. Vibration testing is a crucial approach for identifying modal properties of a structure, e.g. natural frequencies, mode shapes and damping ratios. Based on these model properties, optimization methods can be employed to detect, locate damage and assess the status of structures. These are important goals of Structural Health Monitoring (SHM) in formulating nondestructive assessment tools. The paper focuses on system identification of a simply supported steel I-beam and its modal parameters, under forced excitation. Therefore, output-only system identification methods for instance: nonparametric PSD + estimation, data-driven and covariance-driven stochastic subspace identification, will be introduced in the paper. Then modal analysis techniques using peak picking and stabilization diagram, are applied. Moreover, measurement results are verified with those obtained from Finite Element (FE) model using ANSYS. The discrepancy of outcomes with regard to eigenfrequencies, mode shapes between measurements and simulations is compared and interpreted.

Keywords: System identification · Modal analysis
Finite Element Method (FEM)

1 Introduction

Nowadays, application of Structural Health Monitoring (SHM) in civil and bridge structures, has been obtaining significantly achievement. The most remarkable advantages of SHM is the formulation of an effective damage assessment tool without destruction [7]. By means of the tool, the authority can make a timely and suitable maintenance plan in order to reduce the risk and maintenance costs. Therefore, SHM has been studying and applying worldwide.

SHM techniques can involve static-based SHM and vibration-based SHM [11]. The first is a local study based on the change of static properties such as displacement, rotation when damage occurs. This approach needs an exact location of damage before placing the instrumentation at an adjacent region. In addition, a large number of static

forces is necessary to identify a significant deformation in detecting damage. Visual inspection, dye penetration test, magnetic particle test, eddy current test and acoustic emission test are involved in this technique. While, the latter is based on premise that the dynamic properties such as eigenfrequencies, mode shapes and damping ratios when damage exists on a structure. Change of local stiffness can lead to a shift of overall dynamic parameters of a structure. Vibration measurements play an important role in the second approach because with data from some measurement points can assess the whole behavior of a structure, even these points are not located at damage position. Measurement data can be collected periodically or continuously by a limited number of sensors and a data acquisition system. After that, a process of finding a match mathematical model of a dynamic system based on measured data is called system identification [6, 7, 10]. Many vibration-based studies proved promising potential and effectiveness in structural assessment using system identification [2, 3, 7].

There are some techniques in system identification, such as [2]: physical model-based, data-based (e.g. neural network and genetic algorithm), signal processing-based, chaos theory or multi-paradigm. Two techniques are involved in this paper, namely physical model-based and signal processing-based. By utilizing FEM software's such as ANSYS, physical model-based approach is used to determine the dynamic system and modal parameters of I-beam for comparison purpose. In the next signal processing-based approach, classification of system identification as deterministic and stochastic method, can depend on the input-output or output-only information from experiments [1]. In principle, when control inputs e.g. measurable force, digitized wave signal, are applied on a structure, the output will be measured. System identification algorithm uses the data so-called deterministic method. Ahmed [2], Ros et al. [6] and de Abreu et al. [3] studied and applied the approach. However, it is not always possible to control, create or measure the artificial force, especially in huge structures such as cable-stayed bridges, in which ambient excitation is the input whereas the output is the only available information. Stochastic system identification was generated and applied effectively for output-only measurement data in comparison with deterministic method via studies [1, 4, 5]. From the practical reasons above, this paper focuses on stochastic system identification problem.

For a comprehensible dynamic behavior of structure, some output-only modal analysis techniques are employed to estimate modal parameters e.g. eigenfrequencies, mode shapes and damping ratios from the identified system model. A procedure of vibration-based test of a steel I-beam in laboratory is presented as follows [9]:

- Collecting measurement data
- System identification with stochastics methods
- Estimation of modal parameters

2 System Identification and Modal Parameters Estimation Techniques

As stated above, the aim of this section is to present some techniques of output-only system identification, as well as, modal parameters estimation based on identified system model for linear discrete-time systems.

2.1 System Identification Methods

This section reviews basic system identification methods that use output-only vibration data. To facilitate the system identification of a linear system like a steel I-beam, MACEC¹ software is recommended for processing and analyzing data.

Nonparametric PSD+ Estimation Using Correlogram and Periodogram²: In this approach, a Positive power spectral density (PSD+) matrix is used to describe the system model. Therefore, estimation of Positive power spectral density, mathematically denoted as $S_{yy}^+(w)$, is necessary for system identification. In general, the first N_w positive lags of the correlation function will be utilized to calculate the $S_{yy}^+(w)$ and its variance using discrete Fourier transform:

$$S_{yy}^+(w) = \sum_{n=0}^{N_w-1} r_n z_k^{-n} \quad (1)$$

Where $z_k = e^{i2\pi k/N_w}$, r_n correlation function is given as follows:

$$r_n = \sum_{r=1}^{N_m} \phi_r K_r^T \lambda_r^n + \phi_r^* K_r^H \lambda_r^n \text{ for } n \geq 0 \quad (2)$$

And the variance of positive power spectral density is described as:

$$\text{var}\left(S_{yy}^+(w)\right) = \text{var}\left(S_{yy}^+(w_{mk})\right) \quad (3)$$

To solve the problem, there are two approaches, one using the correlogram method, the other using periodogram method.

In the correlogram method, a correlation function between the response signals and the reference output signals will be estimated by averaging at the first step, shown in Eq. (4):

¹ MACEC is a MATLAB toolbox and developed by many authors at the Civil Engineering department of K.U. Leuven University, Belgium. Many identification algorithms are introduced into MACEC to deal with every step in the modal analysis procedure [9].

² For more specific of nonparametric PSD+ estimation, interested reader may consult Refs. [8, 9].

$$\begin{cases} r_n = \frac{1}{N-n} \sum_{k=0}^{N-n-1} y_k + n y_k^{ref T} & \text{with } 0 \leq n \leq N-1 \\ r_n = \frac{1}{N-|n|} \sum_{k=|n|}^{N-1} y_k + |n| y_n^{ref T} & \text{with } -(N-1) \leq n \leq 0 \end{cases} \quad (4)$$

In the next step of this method, the power spectra will be obtained by using the discrete Fourier transform of the estimated correlation function above.

$$S_{yy}(w_k) = \sum_{n=-N}^N w_n r_n z_k^{-n} \quad (5)$$

Note: When to use this method in processing measurement data, the first positive lags need to be determined for obtaining a suitable Number of time lags in MACEC.

In periodogram method, the process starts with dividing the raw response data into N_b block of equal length. The length of each block after that is doubled by using zero padding. Then, each block is transformed to frequency domain by discrete Fourier transform with a time window w_n . The response spectra of each block will be achieved:

$$Y_b(w_k) = \sum_{n=0}^{N-1} w_n y_{b,n} z_k^{-n} \quad (6)$$

Next step is to average all response spectra from overall divided blocks. The outcome of this step is the power spectra:

$$S_{yy}^{ref}(w_k) = \frac{1}{N_b} \sum_{b=1}^{N_b} Y_{b,k} Y_{b,k}^{refH} \quad (7)$$

However, for reduction purpose of variance error of this method, inverse discrete Fourier transform of the obtained power spectra will be taken with a time window N_w for a new correlation estimation. The discrete Fourier transform once again is taken to achieve the Positive power spectra.

The Procedure of Method and Notes: In MACEC, two parameters need to be identified in processing the data including the number of data blocks N_b and time window factor m . Where, factor m can be calculated by dividing the length of one block by the length of time window. The noise or spike reduction in PSD+ estimation plot is influenced by the value of m . However, a higher value than 2 needs to be considered.

Data-Driven Stochastic Subspace Identification³ (SSI-DATA): The method is based on the projection of the row space of the future outputs into the row space of all past outputs. The purpose is to use the past information to estimate future outputs [4]. The execution of this method starts by taking the QR factorization of the block Hankel matrix H that contains the past and future outputs:

³ For details on Data-driven stochastic subspace identification, interested reader may consults Refs. [4, 7-9].

$$H \equiv (Y_p/Y_f) = RQ^T \tag{8}$$

The next step is to implement a projection of the row space of future outputs into the row space of the past outputs, the projection P_i is shown as:

$$P_i \equiv Y_f/Y_p \equiv Y_f Y_p^T (Y_p Y_p^T)^* Y_p \tag{9}$$

Where “*” implies the pseudo-inverse of a matrix.

In addition, the projection P_i equals the observability matrix and the Kalman⁴ filter state sequence [4], thus:

$$P_i = \begin{pmatrix} C \\ CA \\ CA^2 \\ \dots \\ CA^{i-1} \end{pmatrix} (\hat{x}_i \hat{x}_{i+1} \dots \hat{x}_{i+j-1}) \equiv O_i \hat{X}_i \tag{10}$$

When the SVD is applied to the projection matrix, the order of the system n is determined from:

$$P_i = U_1 S_1 V_1^T \tag{11}$$

In the next step for obtaining the system matrices, a new projection is created by using the shifted past and future outputs of Hankel matrix:

$$P_{i-1} = (Y_f^-/Y_p^+) = O_{i-1} \hat{X}_{i+1} \tag{12}$$

Meanwhile, extending the stochastic state-space model equation⁵ and calculating the Kalman state sequence with only output data, the system matrices can be obtained:

$$\begin{pmatrix} \hat{X}_{i+1} \\ Y_{ij} \end{pmatrix} = \begin{pmatrix} A \\ C \end{pmatrix} (\hat{X}_i) + \begin{pmatrix} \rho_w \\ \rho_v \end{pmatrix} \tag{13}$$

Where Y_{ij} is a block of Hankel matrix with only one row of outputs.

To transfer A, C, Q, R, S into the system matrices $A, G, C, \Lambda o$, Lyapunov equation is solved for Σ :

$$\Sigma = A \Sigma A^T + Q \tag{14}$$

Where: $\Lambda o = C \Sigma C^T + R; \quad G = A \Sigma C^T + S.$

⁴ The theory of the Kalman filter states is not explained in this paper, please consult ref. [4] for more information.

⁵ Please consult [4] for details of the stochastic state-space model.

The Procedure of Method and Notes: The expected system order i , can be calculated at two times of the expected number of modes that can be identified. However, this factor should be chosen as a higher value during processing data for an accurate system estimation. However, this factor is also chosen based on the memory usages of the computer. After this step, a calculation of QR-factorization and Singular Value Decomposition (SVD) has to be implemented. Based on the singular value can extract the system order n by looking for the non-zero singular values or looking at a discrete between two adjacent singular values.

Covariance-Driven Stochastic Subspace Identification⁶ (SSI-COV): Based on the determining the covariances between all outputs. In order to solve the identification problem, we need covariance matrices $\Lambda_i = E[y_{k+1}y_k^T]$ and system matrices A , G and C . The covariance matrices compose a block Toeplitz matrix T as:

$$T_{1|i} = \begin{pmatrix} \Lambda_i & \Lambda_{i-1} & \dots & \Lambda_1 \\ \Lambda_{i+1} & \Lambda_i & \dots & \Lambda_2 \\ \dots & \dots & \dots & \dots \\ \Lambda_{2i-1} & \Lambda_{2i-2} & \dots & \Lambda_i \end{pmatrix} \tag{15}$$

And

$$T_{2|i+1} = \begin{pmatrix} \Lambda_{i+1} & \Lambda_i & \dots & \Lambda_2 \\ \Lambda_i & \Lambda_{i+1} & \dots & \Lambda_3 \\ \dots & \dots & \dots & \dots \\ \Lambda_{2i} & \Lambda_{2i-1} & \dots & \Lambda_{i+1} \end{pmatrix} \tag{16}$$

In addition, from a comparison between the output covariance matrices and the next state-output covariance matrices, have:

$$\Lambda_i = C \cdot A^{i-1}G \tag{17}$$

Therefore, the block Toeplitz matrix can be decomposed as:

$$T_{1|i} = \begin{pmatrix} C \\ CA \\ CA^2 \\ \dots \\ CA^{i-1} \end{pmatrix} (A^{i-1}GA^{i-2}G \dots AGG) = O_i C_i \tag{18}$$

With O_i and C_i are observability and reference-reversed controllability matrix, respectively.

⁶ For details of Data-driven stochastic subspace identification, interested reader may consult Refs. [4, 7-9].

When SVD is applied, the block Toeplitz matrix can be rewritten as:

$$T_{1|i} = USV^T = (U_1 \ U_2) \begin{pmatrix} S_i & 0 \\ 0 & 0 \end{pmatrix} \begin{pmatrix} V_1^T \\ V_2^T \end{pmatrix} = U_1 S_1 V_1^T \quad (19)$$

To obtain the system matrix A , we can decompose a shifted block Toeplitz matrix, the result is shown in Eq. (20):

$$T_{2|i+1} = O_i A C_i \quad (20)$$

From Eq. (20), system matrix A is identified as follows:

$$A = O_i^* T_{2|i+1} C_i = S_i^{-1/2} U_1^T T_{2|i+1} V_1 S_1^{-1/2} \quad (21)$$

The Procedure of Method and Notes: when identifying the expected system order by using i factor – implying the half of the number of block rows of the block Toeplitz matrix, in MACEC i can be calculated at two times of the expected number of modes that can be identified. This factor does not increase during processing data. After estimating the covariances, the calculation of QR-factorization and SVD (singular value decomposition) also has to be implemented. Similar to data-driven stochastic subspace identification, the system order n can be determined by looking for the non-zero singular values or looking at a discrete between two adjacent singular values. Choosing the factor i and order model should be considered because this method needs a longer computation time than other methods.

2.2 Modal Parameters Estimation Techniques

The next following step of system identification is to estimate modal parameters of structure. The simplest technique will be introduced first, followed by the more complex technique.

The Peak Picking Technique (PP): This technique often applied in estimating the modal parameters of the structures that suffered ambient load. The main idea of the technique is to identify the eigenfrequencies of structures by picking the peaks of a spectrum plot. Felber proposed that based on the diagonal elements of the identified spectrum matrix, an averaged normalized power spectral density (ANPSD) could be calculated. In MACEC, the ANPSD values are computed and plotted in screen. The modal parameters are estimated by picking the highest peaks. This technique is highlighted by simplicity and speed. However, its accurate estimation is not as good as other techniques.

A vibration experiment of a steel I-beam was conducted. The peak picking technique is used to determine the modal parameters. The specific description of the experiment is presented in Sect. 3. The illustration of the peak picking technique is shown in Fig. 1.

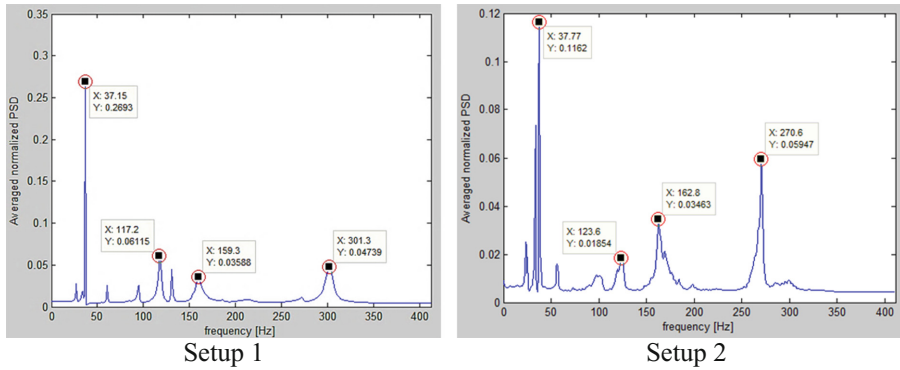


Fig. 1. Peak picking technique in ANPSD plot under unmeasured force

The Stabilization Diagram: for a more accurate estimation of modal parameters, the stabilization diagram is created by realizing the state-space models for system orders $n = 2, 3, 4, \dots$, [7]. The system matrices A and C are used to identify the modal parameters, with:

$$A = \Psi \cdot \Lambda_d \cdot \Psi^{-1}; \quad V = C \cdot \Psi \tag{22}$$

Where Λ_d : discrete poles and V : observed mode shapes.

In the stabilization diagram, the trace of the spectrum matrix also is plotted for visualization purpose, and to facilitate the selection of the stable poles. There three stabilization criteria: frequency, damping and mode shape vectors. For a clear stabilization diagram, presetting criteria is necessary: 1% for frequency, 5% for damping and 1–2% for mode shape vectors. The used symbols are: \oplus for stable pole, $(.v)$ for a stable frequency and mode shape vectors pole, $(.d)$ for a stable frequency and damping pole and $(.f)$ for a stable frequency pole. The stable poles are selected first.

Stabilization diagram is utilized to estimate the modal parameters of I-beam in the experiment that is mentioned above. The specific description of the experiment is shown in Sect. 3. Details of stabilization diagram are illustrated in Fig. 2.

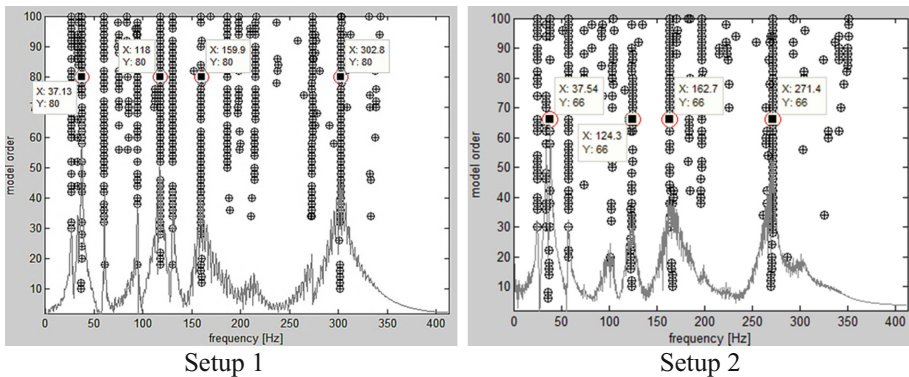
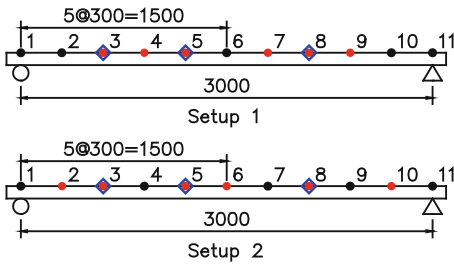


Fig. 2. Stabilization diagram of system identification results under unmeasured force, with $i = 50$ and model order 100

3 Experimental Set-Up

3.1 Sensor Placement

An experiment of a 3-m simply supported steel I-beam is arranged, as shown in Fig. 3b, for collecting the output-only data for system identification. Six accelerometers with sensitivity from 1.054–1.083 V/m/s² are deployed in the top flange of the girder. There are 6 vertical measurement points for each setup, with 3 roving points and 3 points as reference. Altogether there are 9 measurement points in 2 setups as illustrated in Fig. 3a.



a. Measurement points in each setup

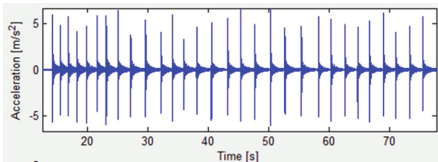


b. Placing sensors in field

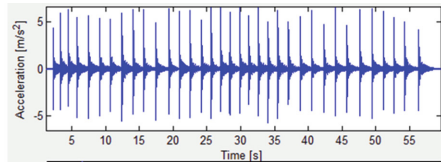
Fig. 3. Sensor placement along the girder; red: measurement points and blue: reference points.

3.2 Collecting Vibration Data

Excitation Source: In order to collect impulse response of beam, a rubber hammer is employed to generate an unmeasured force on the top flange at node 3. The signal variation during excitation is shown in Fig. 4 and corresponding frequency domain is shown in Fig. 5.



a. Setup 1



b. Setup 2

Fig. 4. Time history under excitation.

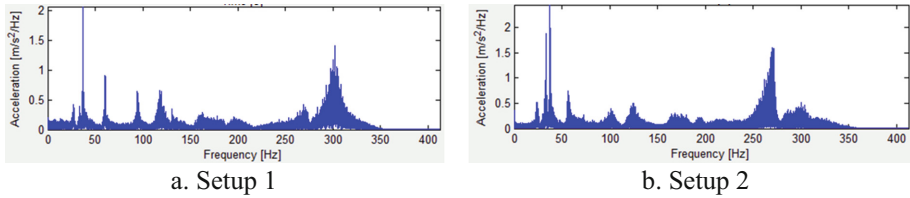


Fig. 5. Frequency domain

Data Acquisition: In each setup, after 5 min for an operational stability of accelerometers, the process of collecting data takes place during 10 min under impact of rubber hammer, then the beam vibrates freely. The chosen sampling rate is 1651 Hz. The analog signals in accelerometers are transferred to digital signals by a data acquisition system (cDAS). All data is recorded on a laptop for next processing step. Field measurement instrumentations are shown in Fig. 6.



Fig. 6. Measurement equipment in laboratory

3.3 Data Processing

MACEC software is employed to process the measured data. However, all recorded data must be converted into MCSIGNAL file with sample frequency same as sampling rate in the experiment, before processing data. Estimating Positive power spectral density (PSD+) is used for system identification. Some mentioned techniques above are utilized for determining the modal parameters. A procedure of processing data using MACEC, including:

- Convert measured file (*.TDMS) to file (*.mat)
- Convert file (*.mat) to MCSIGNAL file
- Process the MCSIGNAL file
- Choose a system identification method
- Choose a modal parameters estimation technique.

4 Experimental Results

This section introduces the obtained results of eigenfrequencies as well as the corresponding mode shapes. With sample frequency 1651 Hz, the impact of rubber hammer on beam surface during a 10-min time is processed. The two SSI methods and one nonparametric PSD+ method are employed to identify system models and estimate the modal parameters. Estimated eigenfrequencies of each method are given in Table 1 and the corresponding mode shapes with eigenfrequency values is presented in Fig. 7. Because there is a similarity about mode shapes between the system identification methods, the mode shapes using SSI-COV are plotted for visualization.

Table 1. Eigenfrequency of the beam under the impact of hammer in Hz

Method	Measured eigenfrequency values (Hz)			
Nonparametric PSD+	37.46	120.84	161.46	286.37
SSI-COV	36.75	120.06	162.11	287.08
SSI-DATA	37.34	121.11	161.31	287.12
Averaged value	37.18	120.67	161.63	286.86

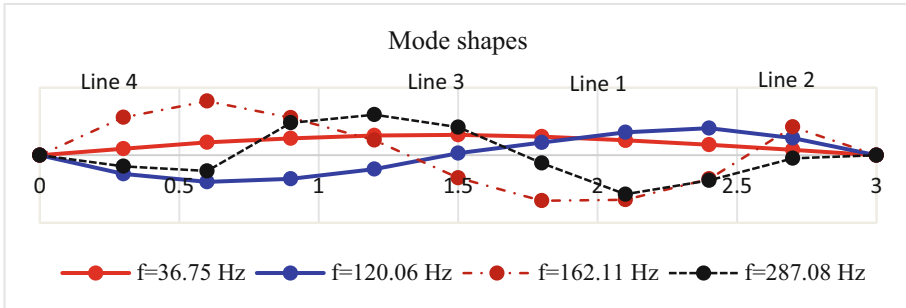


Fig. 7. Bending mode shapes with SSI-COV

From the obtained results in Table 1, averaged values of identified eigenfrequency are taken for comparison purpose. The discrepancies between three methods are quite negligible, just around 0.078% to 1.615% as shown in Table 2. This means the accuracy of system identification and model parameters estimation are warranted by using MACEC in case of output-only measured data.

Based on the Fig. 7, two identified bending modes are 1st mode and 2nd mode with regard to line 1 and line 2. Although line 3 and line 4 perform a similar shape as 3rd mode, the third mode still does not identify in the experiment. This can be due to not enough amplitude of forced excitation.



Table 2. The deviation of eigenfrequency values in comparison with an averaged eigenfrequency

Method	Deviation			
Nonparametric PSD+	0.744%	0.141%	0.103%	0.170%
SSI-COV	1.165%	0.506%	0.299%	0.078%
SSI-DATA	0.421%	0.365%	0.196%	0.092%

5 Numerical Model

5.1 Data Input

In this section, a simply supported steel I-beam is modelled, the beam is divided into 100 elements as in Fig. 9. The element type in modelling is BEAM 3 as shown in Fig. 8. BEAM 3 is a uniaxial element with bending, compression, and tension capacities. The element has 3-degrees of freedom at each node: translational displacement in x, y directions and rotating displacement in z-direction [12].

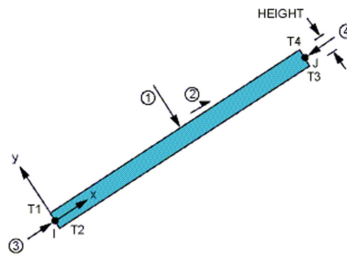


Fig. 8. Element type

The length of the beam is 3.1 m, two supports placed at 0.05 m from the edge of the beam and the cross-section of the beam is I- beam 100 × 52 mm as shown in Fig. 9. Young modulus is 200000 MPa, density is 7800 kg/m³, and Poisson’s ratio is 0.3. ANSYS 17, is used to calculate the natural frequencies of the I-beam.

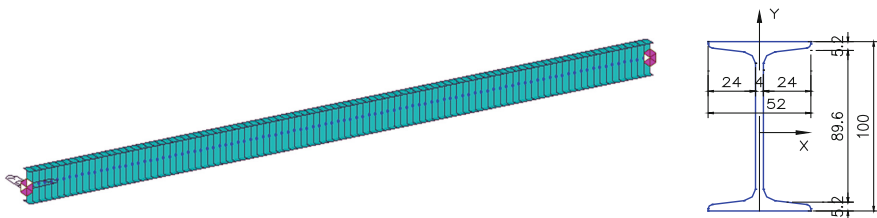


Fig. 9. Finite element model and details of cross-section of the I-beam

5.2 Numerical Results and Comparison

Mode Shapes: The FE model identifies five bending modes with corresponding eigenfrequency values are shown in Table 3. Due to the limit in measurement points on the beam and forced excitation, only two first bending modes are identified by measurement. Therefore, these mode shapes are presented for comparison purpose with FE model in Fig. 10.

Eigenfrequencies: by using ANSYS 17 to model, values of eigenfrequency are determined with corresponding mode shapes as listed in Table 3.

Table 3. Frequencies obtained by FE model in Hz

FEM Software	Mode 1	Mode 2	Mode 3	Mode 4	Mode 5
Ansys	35.46	141.49	317.10	560.59	871.77

In order to get a global picture of the eigenfrequencies, all values are described in Fig. 11. Obviously, eigenfrequencies of the first modes determined by Finite Element Method and experimental method are a quite good match, with slight deviation around 4.85%. Meanwhile, the second mode shows a significant discrepancy between modelling and measurement, approximately 14.71%.

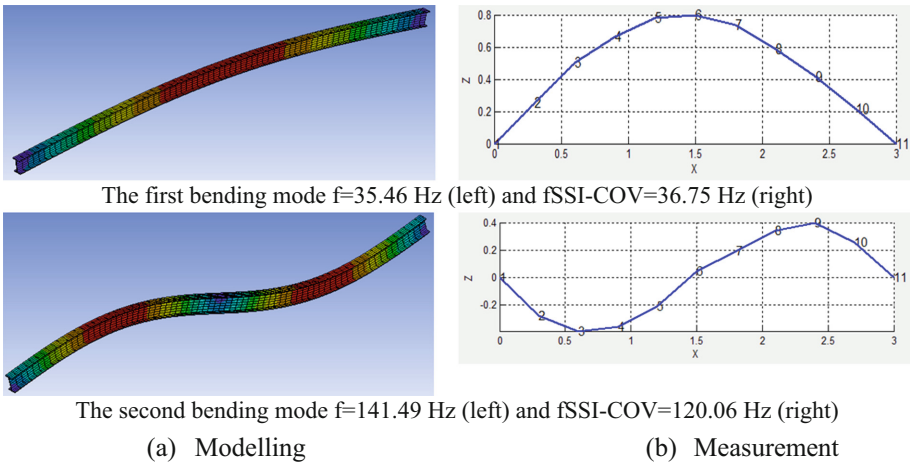


Fig. 10. Mode shapes of steel I-Beam

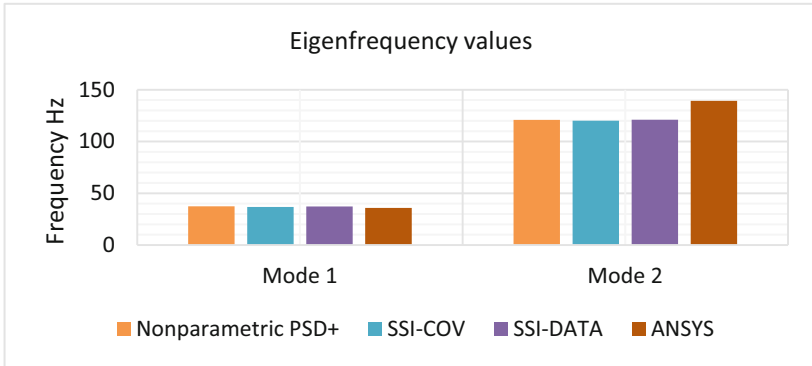


Fig. 11. Summary of eigenfrequencies obtained by measurements and modelling

6 Conclusions

The paper has described the system identification and modal parameters estimation of a steel I-beam based on output-only measurement data. From the obtained results, initially, there is a comparison between system identification methods. Based on the comparison, a promising application of MACEC in the model analysis is confirmed.

Although there is a similarity in mode shapes between the experimental results and modelling results, the discrepancy of eigenfrequency values is still considerable. The differences can be due to unideal boundary conditions, the effect of the mass of accelerometers and the size of wires, mesh discretization, unsuitable assumed physical properties of the material in FE model.

The next research will be to focus on finding out the main reason leads to the discrepancies, e.g. using the “free-free” boundary conditions, modelling the mass of accelerometers in the FE model, etc. The model updating also is applied for reducing the gap between the experimental and modelling results.

Acknowledgements. The authors acknowledge the financial support of VLIR-OUS TEAM Project, VN2018TEA479A103, ‘Damage assessment tools for Structural Health Monitoring of Vietnamese infrastructures’, funded by the Flemish Government.

References

1. Peeters, B., De Roeck, G.: Stochastic system identification for operational modal analysis: a review. *J. Dyn. Syst. Meas. Control* **123**(4), 659–667 (2001)
2. Ahmed, A.: System identification of a beam using frequency response analysis. In: International Conference on Inter Disciplinary Research in Engineering and Technology, pp. 101–105 (2016)
3. de Abreu, G.L.C.M., da Conceição, S.M., Lopes Jr., V., Brennan, M.J., Alves, M.T.S.: System identification and active vibration control of a flexible structure. Special Issue **XXXIV**, 386–392 (2012)
4. Peeters, B., De Roeck, G.: Reference-based stochastic subspace identification for output-only modal analysis. *Mech. Syst. Signal Process.* **13**, 855–878 (1999). Article No. mssp.1999.1249
5. Reynders, E., De Roeck, G.: Reference-based combined deterministic-stochastic subspace identification for experimental and operational model analysis. *Mech. Syst. Signal Process.* **22**(3), 617–637 (2008)
6. Ros, N.F.M., Saad, M.S., Zakaria, M.Z., Darus, I.Z.M.: Modeling of flexible beam using system identification approach. In: 2nd International Conference on Advances in Engineering and Technology (RTET-2017) (2017)
7. Peeters, B.: System identification and damage detection in civil engineering. Ph.D. thesis, Department of Civil Engineering, K.U. Leuven (2000)
8. Cauberghe, B.: Applied frequency-domain system identification in the field of experimental and operational modal analysis. Ph.D. thesis, Vrije Universiteit Brussel (2004)
9. Reynders, E., Schevenels, M., De Roeck, G.: MACEC 3.2: A MATLAB toolbox for experimental and operational modal analysis. User's manual. Report BWM-2011-XX (2011)
10. Aarts, R.G.K.M.: Course: System Identification and Parameter Estimation. University of Twente. Edition 2011/2012
11. Roy, K., Mukhopadhyay, S.: Structural Health Monitoring. Workshop on Earthquake Resistance of Low-Cost Engineered Housing in North-East India, 24–25 June 2016, IIT Guwahati (2016)
12. Ansys 17 manual



Numerical Calibration of a Simplified Model for FRP Confinement of Columns

Marinella Fossetti¹(✉), Alfio Francesco Siciliano¹,
Francesco Basone¹, and Giovanni Minafò²

¹ Facoltà di Ingegneria e Architettura, Università degli Studi di Enna “Kore”,
Cittadella Universitaria, 92100 Enna, Italy
marinella.fossetti@unikore.it

² Dipartimento di Ingegneria Civile, Ambientale, Aerospaziale, dei Materiali
DICAM, Viale delle Scienze Ed. 8, 90128 Palermo, Italy

Abstract. This paper presents the calibration of a simplified analytical model for concrete columns confined by fiber reinforced polymer (FRP) jackets. The model allows evaluating the increase of strength, ductility and dissipated energy without defining the lateral confinement pressure and it can be easily extended for the assessment of FRP confinement in design applications. This model was obtained by a simplified procedure based on the best fit of experimental data available in the literature and the coefficient of determination (R^2) was evaluated in order to estimate the accuracy of the regression analysis. A numerical database resulting from finite element (FE) analyses was compiled and reported for integrating the model's calibration obtained by the few experimental data. The FE models are built based on results of experimental tests available in the literature and several FE simulations are carried out. The experimental results are then integrated with numerical results and new forms of the simplified expressions are obtained by new best fit. The new values of R^2 confirm an improvement of the accuracy of the regression analysis. Finally, the performance of the simplified model is compared with existing formulas available in the literature.

Keywords: FRP jackets · Concrete columns · Non-linear FE model
Simplified analytical model

1 Introduction

In the last years, the need of upgrading existing structures proved to be of fundamental importance. In this context, the retrofit of existing reinforced concrete (RC) structures represents a key target to be addressed, due to the widespread presence of design or construction errors, change of use and hence different design loads, damages due to seismic events or environmental factors. In existing RC structures, columns always need to be strengthened according to the performance-based design philosophy adopted by almost all national seismic codes. The most common techniques to upgrade column performances provide the adoption of external jackets made by different materials, such as RC, steel or Fiber-Reinforced Polymers (FRP). The use of FRP jackets has shown an

increasing popularity [1–9] due to different reasons: high strength-to-weight ratio of the composite, corrosion resistance and ease and speed of application. For these reasons, the structural behavior and effectiveness of FRP jackets has been widely investigated and as a results of some studies, guidelines have been drawn up [10–12].

Results of earlier research conducted on columns wrapped with FRP jackets demonstrated that confinement effectiveness is significantly affected by several parameters: type of fiber and resin, fiber volume and orientation, jacket thickness, concrete strength, shape and corner radius of the cross-section, length-to diameter (slenderness) ratio and the bond at the interface between the concrete core and the jacket. For example, the corner radius influence was investigated in [7] and it was found that when the corner radius is zero no confinement effect is provided by FRP jackets. In [13] the influence of the shape of the cross-section was studied and the results showed that for fixed number of FRP layers the confinement effect is strongly dependent on the shape of the cross-section of the column. In [14] it was shown that a small corner radius of the cross-section significantly reduces the ultimate strength of the FRP jackets due to stress concentration in the corner area.

Many mechanical models have been proposed in the literature to describe the behavior of compressed concrete columns wrapped with FRP jackets; most of these models are based on the confinement model of Mander et al. [15] originally developed for steel confinement; it correlates the increase in strength and ultimate strain with the lateral confinement pressure. Several confinement models based on the formulation in [15] have been proposed in the literature [16–24] for the FRP system; in all these works the evaluation of the lateral confinement pressure is calibrated on compression tests on concrete columns wrapped by FRP fiber sheets. The accuracy of predictions provided by these models is strictly related to correct definition of the lateral confinement pressure, which is strictly related with the hoop strain in the jacket. It is difficult to evaluate the lateral confinement pressure experimentally as it depends on various parameters. Consequently, many empirical or semi-empirical models given in the literature are affected by experimental calibration and then only applicable to specific cases.

In order to overcome this drawback recently the present authors proposed a simplified model for FRP systems that relates the increase in strength, ultimate strain and energy absorption capacity directly to a single parameter dependent on the relative stiffness of the jacket and the concrete column [25]; in this way definition of the lateral confinement pressure is avoided. In [25], the analytical functions are obtained from the best fitting of several experimental results [29, 30] and therefore they can be used for each kind of FRP jacketing.

The mathematical models for the strength, ductility and dissipated energy enhancement in [25] are obtained by a best fit of experimental data with the least squares method and the coefficient of determination R^2 is evaluated in order to estimate the accuracy of the regression procedure. These values of R^2 are small because the data are taken from different experimental campaigns and then very different stress-strain curves were considered for the construction of the database.

In order to compensate for the lack of experimental results, in this paper a numerical investigation is carried out. Following the strategy adopted in [31, 32], finite element (FE) models are calibrated on results of experimental tests available in the literature and FE simulations of compression tests with configurations that have not yet

been tested are performed. The experimental results are then integrated with the FE simulations results, and following the approach adopted in [25] the analytical models of strength, ductility and dissipated energy variation due to the FRP system are again obtained by a new best fit.

Finally, by means of comparison with available experimental data it is shown that the proposed approach provides predictions in good agreement with available mechanical models.

2 Simplified Expressions for Assessing the Effect of FRP Confinement on the Compressive Behaviour of Concrete Columns

In this section the analytical model considered in this paper is briefly presented, postponing the detailed discussion in [25].

The characteristic parameters considered were: f_{co} , f_{cc} unconfined and confined maximum compressive stress; $\mu_{\epsilon o}$, μ_{ϵ} unconfined and confined ductility; E_o , E unconfined and confined energy absorption capacity.

The objective of this study was to provide a simplified procedure for assessing the performance in terms of strength (f_{cc}/f_{co}), ductility ($\mu_{\epsilon}/\mu_{\epsilon o}$) and dissipated energy (E/E_o) of FRP confined concrete columns, which have square or circular cross-sections with side ℓ or diameter ℓ , respectively.

The simplified procedure was developed for columns with $f_{co} \leq 40$ MPa, without steel reinforcement and with FRP reinforcing laminates with fibers only in the direction normal to the axis.

Considering the following parameters:

$\rho = 2r/\ell$ Corner radius ratio of the square cross-sections

E_c Elastic modulus of the unconfined specimens;

$\rho_f = 4 n t_f / \ell$ Fiber volumetric ratio (n number of fiber layers; t_f nominal thickness of the reinforcing system);

E_f Elastic modulus of the fibers;

it was possible to define an analytical law for evaluate f_{cc}/f_{co} , $\mu_{\epsilon}/\mu_{\epsilon o}$ and E/E_o for FRP wrapped columns by evaluating a parameter η defined as:

$$\eta = \frac{\ell}{4 n t_f} \cdot \frac{E_c}{E_f} = \frac{E_c}{\rho_f E_f} \quad (1)$$

The parameter η depends on the mechanical and geometrical characteristics of the system, made by the original concrete core and external FRP jacket.

The analytical expressions that give the strength, ductility and dissipated energy enhancement as a function of the corner radius ratio and the fiber volumetric ratio is provided by Eq. (2), Eq. (3) and Eq. (4) respectively.

$$\frac{f_{cc}}{f_{co}} = a \eta^b \rho + c \eta^d \quad (2)$$

$$\frac{\mu_\varepsilon}{\mu_{\varepsilon o}} = a \eta^b \rho^c \eta^d \quad (3)$$

$$\frac{E}{E_o} = a \eta^b \rho + c \eta^d \quad (4)$$

It is observed that in general, the evaluation of f_{cc}/f_{co} , $\mu_\varepsilon/\mu_{\varepsilon o}$ and E/E_o ratio requires the definition of the lateral confinement pressure. By contrast, the proposed procedure allows to evaluate the enhancement of the mechanical properties mentioned without knowing the lateral confinement pressure.

The coefficients a , b , and c in Eqs. (2), (3) and (4) were defined by means of best fitting of experimental data with the least square method. For this purpose an experimental database was reported considering some characteristic values of stress-strain curves, collected from different experimental campaigns.

The coefficients of determination R^2 , considered to evaluate the accuracy of the models provided in Eqs. (2), (3) and (4) were: $R^2 = 0.77$ for strength; $R^2 = 0.53$ for ductility and $R^2 = 0.43$ for dissipated energy. This values were small because of the large dispersion in the experimental data available in the literature.

In this paper, in order to improve the accuracy of the analytical these models, a new best fit of the experimental data reported in [25] and the numerical data evaluated in next section was carried out with the least square method. The new coefficients of determination R^2 , reported in Sect. 4, highlights an improvement of the accuracy of the models proposed in [25].

3 Non-linear FE Analyses

3.1 Numerical Models

The code ATENA Engineering - 3D [33] was used to carry out non-linear FE analyses. ATENA software uses Finite Element Method during solution procedures and the Updated Lagrange formulation to calculate the deformed shape of the member. In fact, the volume change depend on a loading level applied and the weak governing equations are written with respect to the most recent deformed configuration.

The FE discretization of columns was obtained by means of solid 3D isoparametric elements with a mesh of four node. These elements are codified as CCIsoTetra with linear Gauss interpolation. Furthermore, the size of the mesh of the external contact surface of the column was more refined than core to ensure compatibility with the jacket's mesh. The constitutive law of the concrete is "CC3DNonLinCementitious2" and it was chosen because combines the tensile (fracturing) and compressive (plastic)

behavior of the concrete is simulated with very refined numerical methods. Therefore, it allows complete modelling of the member, taking account of progressive damage of the concrete. This constitutive law decomposes the strain into elastic, plastic and fracturing component [34]. The fracture model is based on the classical orthotropic smeared crack formulation and the crack band model. It employs the Rankine failure criterion and exponential softening, and it can be used as a rotated or fixed crack model. Figure 1 shows crack opening law according to this criterion. The crack opening w is computed multiplying fracturing strain by the characteristic length. The latter is calculated as a size of the element projected into the crack direction [35]. In Fig. 1, f'_t is the uniaxial tensile strength and G_f is the fracture energy. It is worth to specify that this fracturing criterion assume that crack direction is given by the principal stress direction.

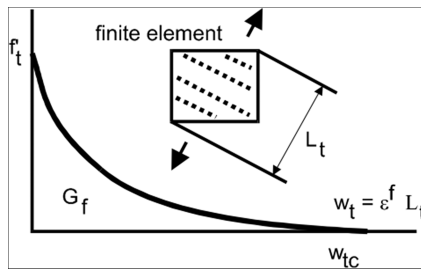


Fig. 1. Exponential crack opening law [33].

Figure 2 shows the hardening/softening law used in the plasticity model and is based on the uniaxial compressive test. The ascending branch law is elliptical and is based on strains. It is worth to note that the formulation of constitutive material is considered in the plan stress state so, the strength of concrete is calculated by biaxial stress failure criterion according to Kupfer et al. [36] under the assumption of a proportional stress path. Additionally, in order to eliminate the Poisson’s effect, is introduced the equivalent uniaxial strain ϵ_{eq} , obtained as the ratio between uniaxial stress and stiffness modulus associated with the considered direction.

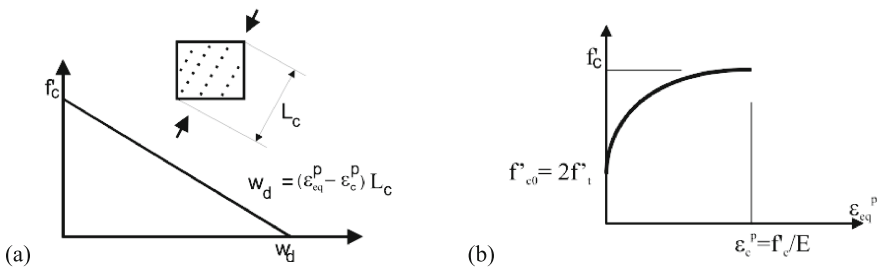


Fig. 2. Uniaxial compressive law of the concrete: (a) hardening; (b) softening [33].

In the hardening nonlinear branch the plastic strain ε_{cp} , the uniaxial cylinder strength of the concrete f'_c and f'_{co} are input parameters. In order to obtain a real deformed mesh, descending branch is based on displacements of the FE [37]. The latter transformation, from plastic deformation to displacement, is defined by means length scale parameter L_c .

Similarly, of the fracture model, L_c is the projection of element size into the direction of minimal principal stresses. This plasticity model is based on the Men etrey-Willam failure surface and uses return mapping algorithm to integrate the constitutive equation. The latter algorithm provides for the definition of “ β ” parameter: if $\beta < 0$ the material is being compacted during crushing, if $\beta = 0$ the material volume is being preserved, and if $\beta > 0$ the material is dilating.

At this point an iterative algorithm is used by ATENA 3D to combine the two above models so that Rankine Fracture model is used for cracking and the plasticity model for crushing. From field theory, after concrete cracking, the compressive strength decrease in perpendicular direction [38]. Hence, uniaxial cylinder strength of the concrete f'_c is limited by a coefficient r_c . The compressive strength reduction implemented in ATENA 3D is based on the previous formula.

Furthermore, the algorithm ensures that tensile strength should decrease when concrete crushing occurs.

The concrete parameters used for FE simulations are: Poisson’s ratio $\nu_c = 0.2$; modulus of elasticity $E_c = 29450$ MPa and $\beta = 0.5$.

The FE discretization of FRP jacket was obtained with a mesh of Ahmad shell elements. These elements were reduced from a quadratic 3D brick element with 20 nodes. The element had 9 integration points in the shell plane and six layers in the direction normal to its plane. The total number of integration points was 9×6 . This element has nodal points in vertexes and in the middle of element sides; so, quadratic displacement shape function was adopted with quadratic Gauss interpolation. The size of the mesh of FRP jacketing was equal to that of external contact surface of the column to ensure compatibility.

The contact surface between the FRP and concrete was modelled so that no slip occurs at interface. Moreover, FRP wrap was modelled as a smeared reinforcement layer. In particular, the matrix material constitutive law was assumed linear-elastic, and the fibers are replaced by a linear-elastic layer of smeared reinforcement in the transverse direction. Such a layer was placed at half the jacket’s thickness and the thickness of the smeared reinforcement layer was calculated so that sum of cross sectional area of the carbon fibers and the replacing smeared reinforcement layer was the same. The linear-elastic law of the carbon fibers was defined by an elasticity modulus of 240 GPa, a strain at failure of 15.5% and a thickness of 0.117 mm.

All specimens were subjected to a monotonic axial compressive load in displacement control mode. The displacements were applied concentrically by means of a steel plate, which was also modelled with the same kind of brick element, taking also care in ensuring compatibility with the topmost face of the column.

As an example, Fig. 3 shows a model of unconfined column, the FE model with the stress distribution at intermediate load and the crack pattern at peak load.

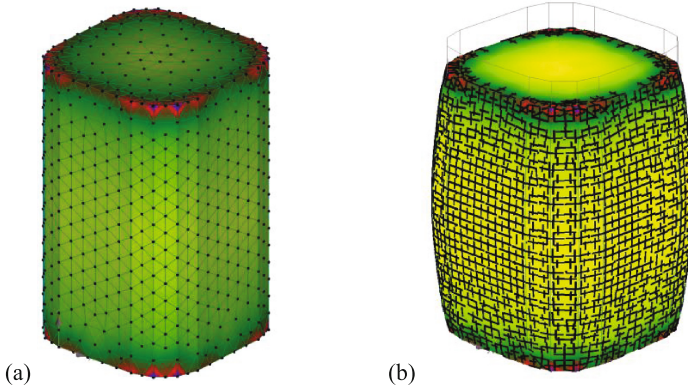


Fig. 3. Unconfined concrete columns: (a) Stress distribution at intermediate loads; (a) Crack patterns and deformed mesh at peak load.

3.2 FE Analysis and Numerical Database

The experimental results by Rousakis et al. [28] were considered in order to calibrate the FE models.

In particular, the specimens wrapped with one layer of carbon fiber were considered with the following details and experimental key results: square cross-section with side of 200×200 mm, height of 320 mm and corner radius of 30 mm; $\rho = 0.30$; $\rho_f = 0.234\%$; $f_{co} = 33.04$ MPa; $f_{cc} = 38.44$ MPa; $\epsilon_{cou} = 1.71\%$; $\epsilon_{ccu} = 4.50\%$.

For confined and unconfined concrete columns, the above values of f_{co} , f_{cc} , ϵ_{cou} and ϵ_{ccu} are obtained as average values of three test results.

The stress–strain numerical curves were obtained just like the experimental curves by dividing the axial load by the cross-section area and the imposed displacement by the height of the specimens.

Figures 4 and 5 show the comparisons between the stress–strain curves determined with the FE model and the experimental results of Rousakis et al. [28] for unconfined and confined columns respectively. As can be noted, good agreement is observed between the two results, highlighting the fact that the derived FE model is verified with good accuracy. In particular, the FE model is able to predict the axial capacity, the onset stiffness and the softening branch of the columns with and without FRP jacket.

It is observed that the numerical stress–strain curves were clipped at the axial strain of 0.4%. In fact, as indicated in [10], for higher axial strains FRP-confined RC members lose their functionality.

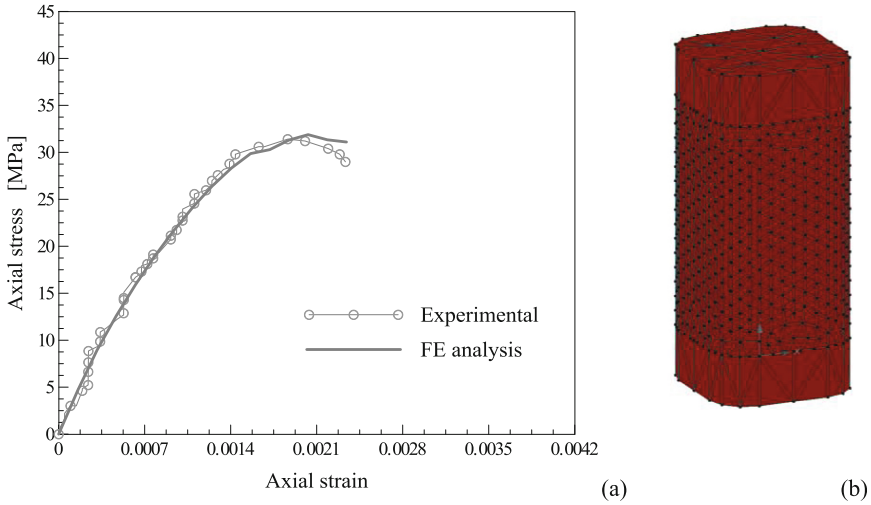


Fig. 4. Unconfined columns: (a) Comparisons between experimental results of Rousakis et al. [25] and numerical results; (b) FE model.

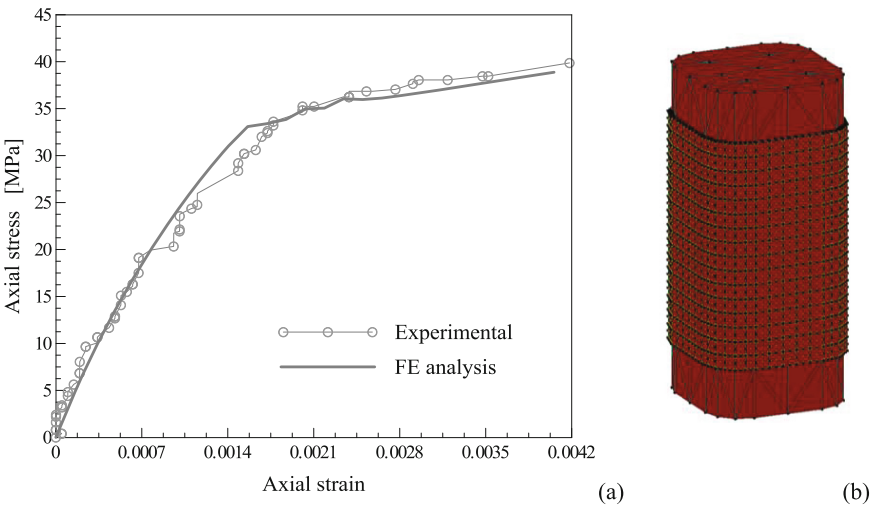


Fig. 5. Confined columns: (a) Comparisons between experimental results of Rousakis et al. [25] and numerical results; (b) FE model.

The numerical database was built with three series of non-linear FE analyses that were carried out for t_f equal to 0.117 mm, 0.125 mm, and 0.187 mm. For each values of t_f , the corner radius r was varied at the values of 30 mm, 50 mm, 60 mm, 70 mm and 90 mm.

The parameters unchanged in the FE simulations are: height of columns 320 mm; $\ell = 200$ mm; $E_c = 29450$ MPa; $E_f = 240$ GPa; $n = 1$.

The FE numerical results are summarized in Table 1. The symbols used in the table were previously described.

Table 1. Details of FE models for FRP confined columns and numerical key results.

t_f [mm]	ρ	ρ_f [%]	f_{co} [MPa]	f_{cc}/f_{co}	E_o [MJ/m ³]	E/E_o	ε_{cou} [%]	$\mu_{\varepsilon o}$	$\mu_{\varepsilon}/\mu_{\varepsilon o}$
0.117	0.3	0.234	31.88	1.219	0.052	2.306	0.23	1.77	1.608
	0.5	0.234	32.10	1.260	0.052	2.385	0.23	1.77	1.554
	0.6	0.234	31.02	1.259	0.051	2.364	0.23	1.79	1.572
	0.7	0.234	31.68	1.285	0.051	2.389	0.23	1.85	1.469
	0.9	0.234	31.20	1.280	0.051	2.382	0.23	1.87	1.474
0.187	0.3	0.375	31.88	1.224	0.052	2.335	0.23	1.77	1.584
	0.5	0.375	32.10	1.272	0.052	2.405	0.23	1.77	1.539
	0.6	0.375	31.02	1.264	0.051	2.382	0.23	1.79	1.555
	0.7	0.375	31.68	1.309	0.051	2.414	0.23	1.85	1.450
	0.9	0.375	31.20	1.296	0.051	2.413	0.23	1.87	1.478
0.125	0.3	0.250	31.88	1.211	0.052	2.308	0.23	1.77	1.608
	0.5	0.250	32.10	1.259	0.052	2.387	0.23	1.77	1.552
	0.6	0.250	31.02	1.249	0.051	2.366	0.23	1.79	1.570
	0.7	0.250	31.68	1.267	0.051	2.390	0.23	1.85	1.467
	0.9	0.250	31.20	1.269	0.051	2.385	0.23	1.87	1.473

Figure 6 shows the stress distribution in the transverse cross-sections of the some specimens analyzed at the peak load. The stress distribution was consistent with the theoretical assumption for the in-plane efficiency coefficient (Fig. 6. Stress distribution in MPa at peak loads in square columns with different corner radii. (a) Theoretical model. (b) $r = 30$ mm. (c) $r = 50$ mm. (d) $r = 60$ mm. (e) $r = 70$ mm. (f) $r = 90$ mm. A commonly adopted in most analytical models [10, 16, 17, 19–24], for considering confinement effects.

In particular, an effectively confined core was highlighted and delimited by variation of concrete lateral stress in the cross-section. The latter started from the edges of rounded corners and developed with a parabolic shape in the section, evidencing the effectively and ineffectively confined zones. Furthermore, it is observed that decreasing the corner radius decreases the effective confined area of the cross-section while the confining pressure at the corners increases with consequential decrease in FRP efficiency.

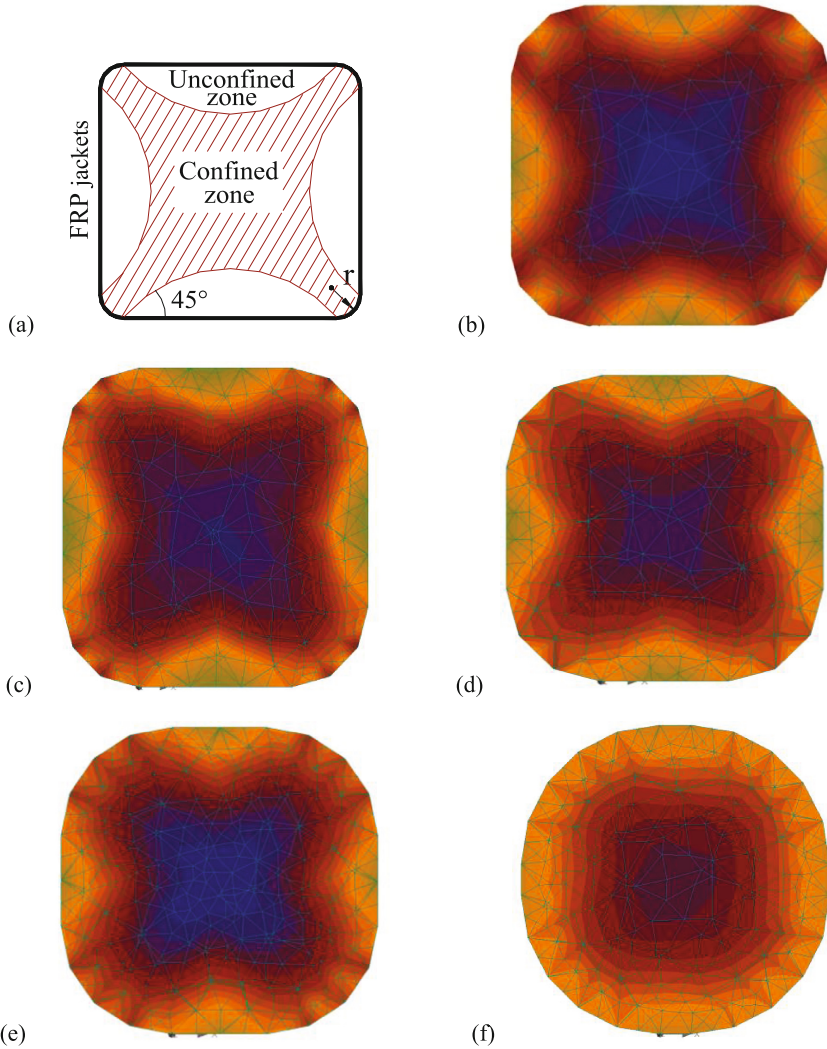


Fig. 6. Stress distribution in MPa at peak loads in square columns with different corner radii. (a) Theoretical model. (b) $r = 30$ mm. (c) $r = 50$ mm. (d) $r = 60$ mm. (e) $r = 70$ mm. (f) $r = 90$ mm.

4 New Calibration of the Simplified Analytical Models [25]

This section shows the improvement of the empirical model [25] by a new calibration of the coefficient of Eqs. 2, 3 and 4 using the experimental data presented in [25] and the numerical data of Sect. 3. The calibration was carried out by using a general regression analysis based on minimizing an error function.

The new best fit leads to the following values of the coefficients for the analytical expressions that give the increase/decrease in strength, ductility and dissipated energy:

$$\frac{f_{cc}}{f_{co}} = 1629.4 \eta^{-2.55} \rho + 2.21 \eta^{-0.17} \quad (5)$$

$$\frac{\mu_e}{\mu_{e0}} = 0.020 \eta^{1.11} \rho^{-14.07} \eta^{-0.95} \quad (6)$$

$$\frac{E}{E_o} = 161.03 \eta^{-1.20} \rho + 25.20 \eta^{-0.59} \quad (7)$$

In order to evaluate the performance of the new expressions provided by Eqs. (5), (6) and (7), two indices are considered: the coefficient of determination (R^2) and the Root Mean Square Error (RMSE).

R^2 is the square of the correlation coefficient that defines the relationship between predicted and experimental values as it follows:

$$R^2 = \left(\frac{\sum (x - \bar{x})(y - \bar{y})}{\sqrt{\sum (x - \bar{x})^2 \sum (y - \bar{y})^2}} \right)^2 \quad (8)$$

where x and y are the experimental and predicted values, respectively, while \bar{x} and \bar{y} are the mean experimental and predicted values, respectively. R^2 equal to one indicate perfect correlation between experimental and predicted values, whereas R^2 equal to zero indicate zero correlation.

Because the coefficient R^2 only indicates a linear correlation between predicted and experimental values in the present paper also the RMSE is evaluated. It is defined as follows:

$$RMSE = \sqrt{\frac{\sum (x - y)^2}{N}} \quad (9)$$

where N is the number of data points. Such value shows the closeness of predicted values to experimental data. Lower values of RMSE indicate a better fit, with zero indicating a perfect prediction. Therefore, the R^2 provides a relative measure of the fit whereas RMSE is an absolute measure of fit without any upper limit.

The values of f_{cc}/f_{co} for varying ρ and η and for number of layer $n = 1$ are shown in 3D Fig. 7. In the picture the experimental data (black points) and numerical data (red points) are also shown. The good agreement between analytical results and experimental and numerical ones is confirmed by the value of the coefficient of determination $R^2 = 0.85$ and the coefficient $RMSE = 0.14$.

The values of μ_e/μ_{e0} for varying ρ and η and for number of layer $n = 1$ are shown in Fig. 8. Experimental data (black points) and numerical data (red points) are also shown in the picture. The good correlation between analytical results and experimental and numerical ones is confirmed by the value of the coefficient of determination

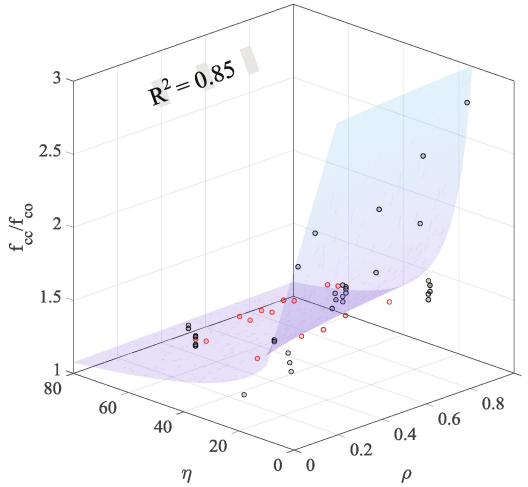


Fig. 7. 3D figure of Eq. 5 in terms of f_{cc}/f_{co} for $n = 1$.

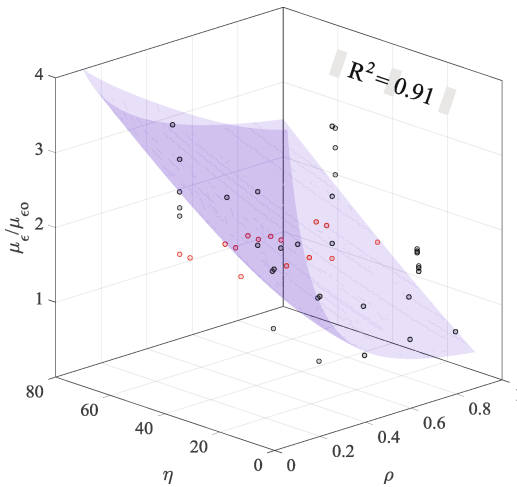


Fig. 8. 3D figure of Eq. 6 in terms of μ_e/μ_{co} for $n = 1$.

$R^2 = 0.91$. In this case, the coefficient $RMSE = 1.19$ shows a greater dispersion of ductility predictions respect to the strength predictions. This is due to the fact that different stress-strain curves are considered and the post-elastic behavior is not easy to capture with a simple bilinear curve.

The values of E/E_0 for varying ρ and η and for number of layer $n = 1$ are shown in 3D Fig. 9. Experimental (black points) and numerical data (red points) are also reported in the picture. In this case the values coefficient are $R^2 = 0.47$ and $RMSE = 1.82$. These results show that the predictions of energy dissipation capacity do not show a significant increase of accuracy with respect to the model reported in [25]. This is due to the fact that E is strongly dependent on the post-elastic branch regarding

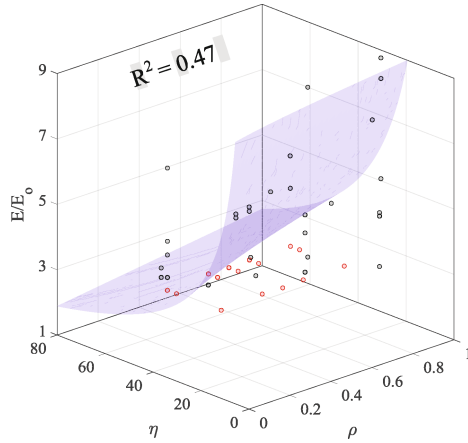


Fig. 9. 3D figure of Eq. 7 in terms of E/E_o for $n = 1$.

strength and ductility, being the latter only influenced by elastic and ultimate strain values. In the FE analyses, the slope of the post-elastic branch is not easy to reproduce accurately and consequently there is only a small improvement in the coefficient of determination.

Figure 10 shows the values of f_{cc}/f_{co} , μ_e/μ_{e0} , E/E_o for varying ρ and for number of layers two and five. For fixed η , it is observed that:

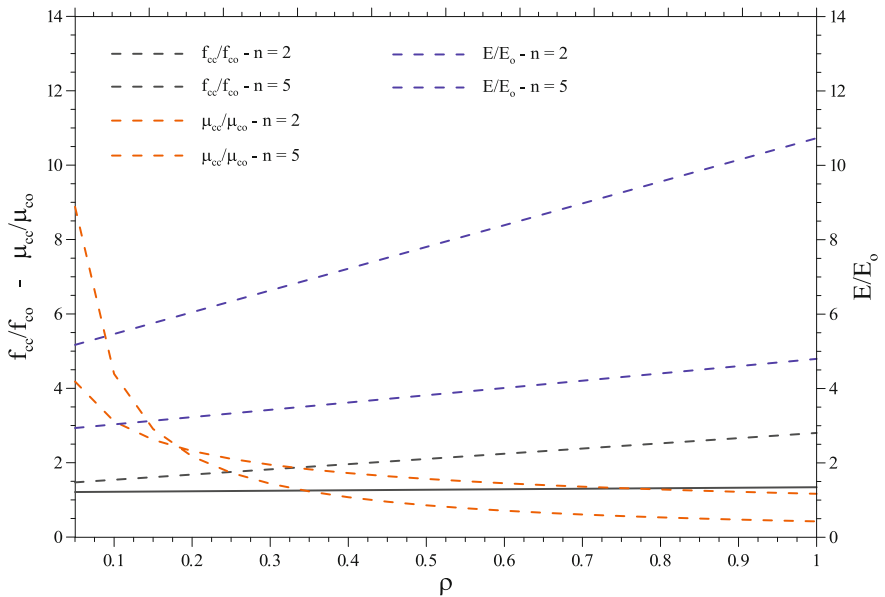


Fig. 10. $f_{cc}/f_{co} - \rho$ curves, $\mu_e/\mu_{e0} - \rho$ curves and $E/E_o - \rho$ curves of columns confined by FRP system for $n = 2$ and $n = 5$.

- the enhanced strength depends linearly on the corner radius ratio and increases with the corner radius ratio and with the fiber volumetric ratio;
- the enhanced ductility is related to the corner radius ratio with a power law and decreases with the corner radius ratio and with the fiber volumetric ratio.
- the enhanced dissipated energy is related to the corner radius ratio with an almost linear power law and increases with the corner radius ratio and with the fiber volumetric ratio.

The proposed procedure can easily be extended for evaluating the performance of FRP confined concrete columns in design applications (see details in [25]).

Assuming the following parameters: ℓ , E_c , t_f and E_f , two procedures can be used for designing the FRP jacket. The first procedure can be resumed as it follows: - the desired increase of ductility ($\mu_\varepsilon/\mu_{\varepsilon 0}$) is chosen at first step; the increase of strength (f_{cc}/f_{co}) and dissipated energy (E/E_0) are subsequently calculated. Conversely, the second procedure requires to choose the strength increase (f_{cc}/f_{co}) and afterwards to evaluate the increase of ductility ($\mu_\varepsilon/\mu_{\varepsilon 0}$) and dissipated energy (E/E_0).

Once that the increase ductility or strength has been chosen, the volumetric ratio ρ_f of fiber and the parameter η have to be evaluated as described in detail in [25] for different values of the number of layers n .

5 Comparisons with Literature Models

Since existing models do not provide expressions for evaluating the enhancement of ductility and energy absorption capacity, the reliability check of the proposed model was carried out by a comparisons in terms of strength increase (f_{cc}/f_{co}).

Usually, models available in the literature express the value of f_{cc}/f_{co} as a function of the confinement pressure ($f_{l,e}$), by means of the following expression:

$$\frac{f_{cc}}{f_{co}} = \alpha + k_1 \left(\frac{f_{l,e}}{f_{co}} \right)^m \quad (8)$$

where:

$$f_{l,e} = \frac{1}{2} \rho_f E_f \varepsilon_f k_e \quad (9)$$

Equation 8 involves the non-dimensional parameters α , k_1 and m , all experimentally assessable, while $k_1 = \alpha k_{1,R}$ is a coefficient which depend by each models.

In Eq. 9 E_f is the elastic modulus in the lateral direction, ε_f is the strain of the jackets in the same direction and k_e is a coefficient that counts the variation in the confinement pressure in square and rectangular cross-section specimens compared to the circular ones. This coefficient is calibrated by the authors of each model.

The selected models for the comparisons are: Pellegrino et al. [16], Campione et al. [17], Triantafillou et al. [19], Mirmiran et al. [20], Di Ludovico et al. [21], Karbhari and Gao [22], Lam and Teng [23], Samaan et al. [24].

Two series of calculations were carried out, for two different values of ρ (0.13 and 0.17). Each series of calculations are replicated for three values of f_{co} (20 Mpa, 25 Mpa and 30 MPa) while the square and circular section are assumed always with $\ell = 300$ mm.

Moreover, the comparison was carried out considering two kind of fibers (Fiber#1 and Fiber#2) with mechanical properties shows in Table 2. For Fiber#1 was assumed $\rho_f = 0.156\%$, 0.312% and 0.468% while, for Fiber#2 was assumed $\rho_f = 0.220\%$, 0.440% and 0.660% .

Table 2. Mechanical properties of FRP jacketing system.

Fiber	Nominal thickness [mm]	Ultimate tensile strength [MPa]	Ultimate tensile strain [%]	Elastic modulus [GPa]	Primary fiber direction
#1	0.117	3700	1.54	240	Unidirectional
#2	0.165	4364	2.00	219	Unidirectional

In all evaluations, the values f_{cc}/f_{co} predicted by the proposed models are compared with existing models values by the determinations of the two coefficient R^2 and RMSE.

R^2 and RMSE are determined in the same way as already shows in the Sect. 4, with the difference that the variable x and y are referring to the existing models values and to the proposed model values, respectively.

In Figs. 11, 12, 13, 14, 15, 16, 17 and 18 are presented the “existing models vs. proposed model” values together the confinement parameters for each available models considered.

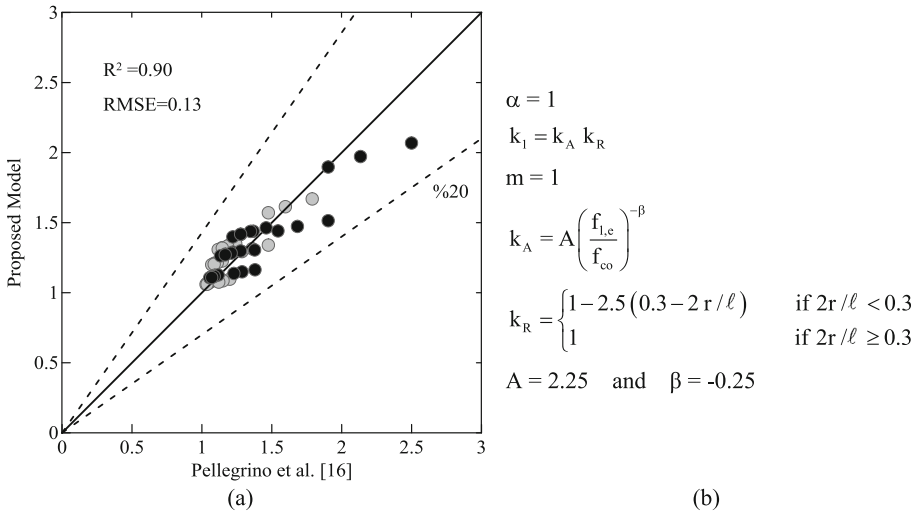
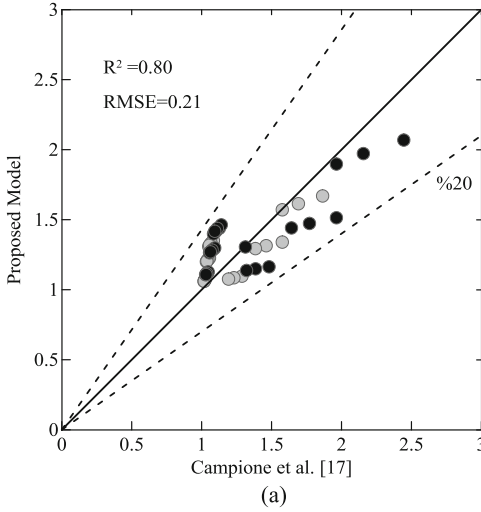


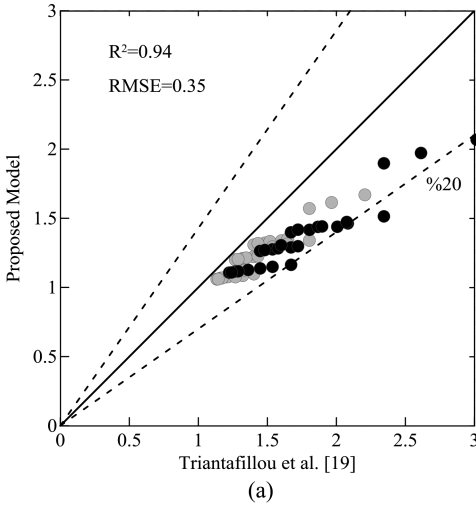
Fig. 11. Pellegrino et al. [16] model: (a) Comparison (f_{cc}/f_{co}) with the proposed model; (b) Parameters and coefficients.



$\alpha = 1$
 $k_1 = 2$
 $m = 1$
 $f_{lc} = \frac{2 n t_f f_r}{\ell}$
 $f_r = f_{fu} \left[\left(1 - \frac{\sqrt{2}}{2} k_i \right) \frac{2r}{\ell} + k_i \frac{\sqrt{2}}{2} \right]$
 $f_{fu} =$ ultimate strength of the fiber
 $k_i = 0.2121$

(b)

Fig. 12. Campione et al. [17] model: (a) Comparison (f_{cc}/f_{co}) with the proposed model; (b) Parameters and coefficients.



$\alpha = 1$
 $k_1 = 2.79$
 $m = 1$
 $f_r = f_{fu} \left[\left(1 - \frac{\sqrt{2}}{2} k_i \right) \frac{2r}{\ell} + k_i \frac{\sqrt{2}}{2} \right]$
 $k_e = k_H k_V k_\alpha$
 $k_H = 1 - \frac{2(\ell - r)^2}{3A_g}$
 $k_v = k_\alpha = 1$ for continuous jackets with fibers \perp to the member axis

(b)

Fig. 13. Triantafyllou et al. [19] model: (a) Comparison (f_{cc}/f_{co}) with the proposed model; (b) Parameters and coefficients.

As an example, Figs. 19 and 20 present the comparison in a different form, which shows the performance of the proposed model with respect to the models available in literature. In these pictures the values were deduced for columns with square section ($\ell = 300$ mm) and $\rho = 0.13$.

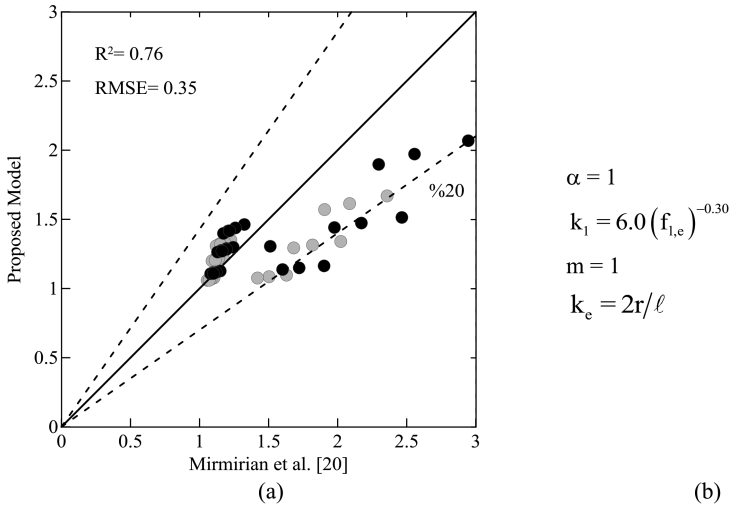


Fig. 14. Mirmirian et al. [20] model: (a) Comparison (f_{cc}/f_{co}) with the proposed model; (b) Parameters and coefficients.

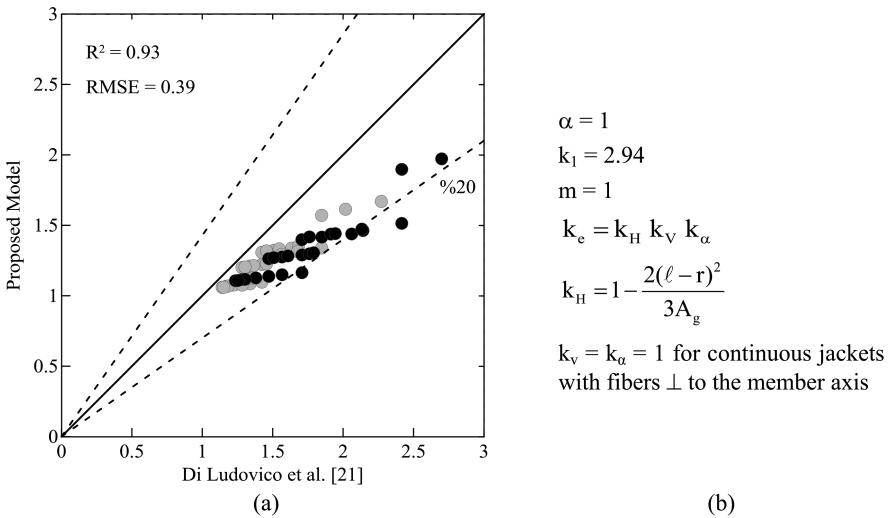


Fig. 15. Di Ludovico et al. [21] model: (a) Comparison (f_{cc}/f_{co}) with the proposed model; (b) Parameters and coefficients.

Good agreements were obtained between the proposed model and the models of Campione et al. [17], Pellegrino et al. [16], Mirmirian et al. [20] and Karbhari and Gao [22]. The best agreement was obtained with the models of Pellegrino et al. [16] for which the RMSE is very low and equal to 0.13. A greater overestimations of the



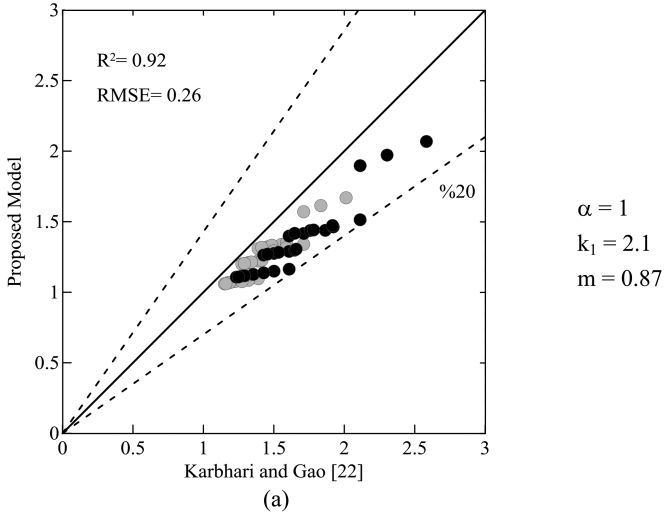


Fig. 16. Karbhari and Gao [22] model: (a) Comparison (f_{cc}/f_{co}) with the proposed model; (b) Parameters and coefficients.

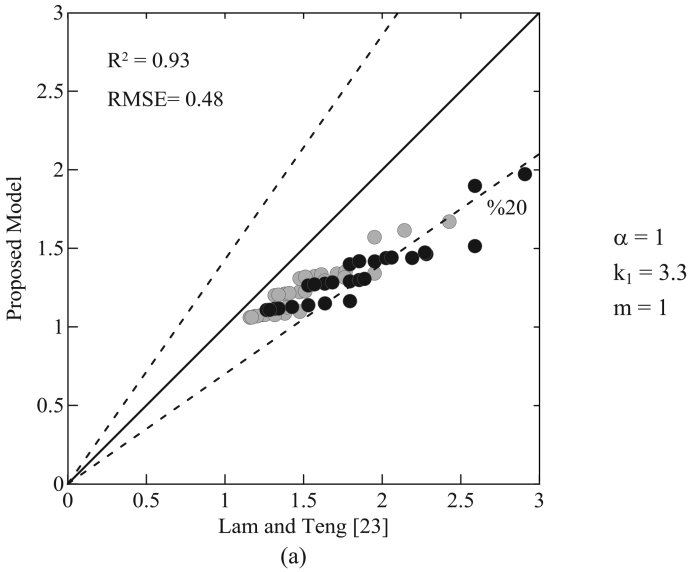


Fig. 17. Lam and Teng [23] model: (a) Comparison (f_{cc}/f_{co}) with the proposed model; (b) Parameters and coefficients.

strength prediction can be observed for the models of Lam and Teng [23] and Samaan et al. [24] with respect to the proposed one. By and large, the proposed model gives suitable results for evaluating the performance of square and circular columns wrapped with FRP jackets.



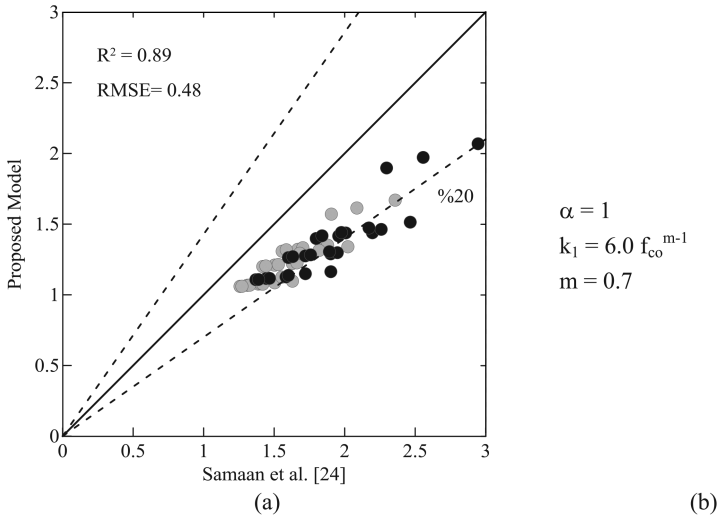


Fig. 18. Samaan et al. [24] model: (a) Comparison (f_{cc}/f_{co}) with the proposed model; (b) Parameters and coefficients.

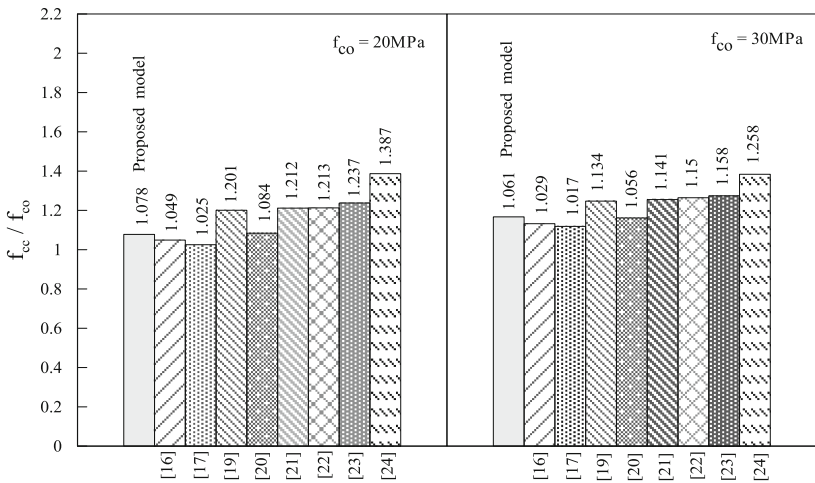


Fig. 19. Comparison (f_{cc}/f_{co}) between the proposed model and existing models for Fiber#1 and $\rho_f = 0.156\%$.

Finally, it is pointed out again that existing analytical expressions available in literature, the accuracy of the predictions is strongly dependent on the definition of the effective confinement pressure and coefficients of effectiveness. The proposed model overcomes this drawback and provide a simplified estimation, which allows to calculate strength and also ductility and energy absorption capacity.



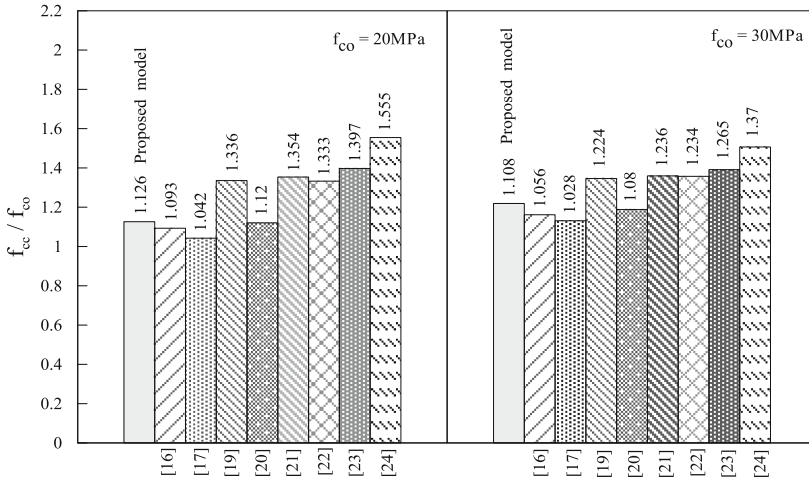


Fig. 20. Comparison (f_{cc}/f_{co}) between the proposed model and existing models for fiber#2 and $\rho_f = 0.22\%$.

6 Conclusions

This paper presented the calibration of simplified analytical expressions for the FRP confinement of concrete columns through a large dataset of numerical analyses.

The numerical database was compiled by advanced non-linear FE analyses performed by the code ATENA Engineering - 3D. The new calibration of the empirical model was carried out by means of a general regression analysis and the coefficients of determination (R^2) and the Root Mean Square Error (RMSE) were evaluated in order to estimate the accuracy of the new expressions.

The performance of the improved model was verified by means a comparison with results of some confinement models available in literature.

This model allows the evaluation of strength, ductility and dissipated energy increase without calculating the lateral confinement pressure, but only taking into account the mechanical and geometrical properties of columns and FRP jacket. Furthermore, it is particularly remarkable that this simplified model was developed by fitting the experimental data coming from different experimental campaigns and numerical data derived from FE analyses, meaning that it can be used in general applications.

References

1. Xiao, Y., Wu, H.: Compressive behavior of concrete confined by carbon fiber composite jackets. *J. Mater. Civil Eng.* **2**, 139–146 (2000)
2. Pessiki, S., Harries, K.A., Kestner, J.T., Sause, R., Ricles, J.M.: Axial behavior of reinforced concrete columns confined with FRP jackets. *J. Compos. Constr.* **4**, 237–245 (2001)

3. Lam, L., Teng, J.G.: Design-oriented stress–strain model for FRP-confined concrete. *Constr. Build. Mater.* **6–7**, 471–489 (2003)
4. Lam, L., Teng, J.G.: Ultimate condition of fiber reinforced polymer-confined concrete. *J. Compos. Constr.* **6**, 539–548 (2004)
5. Lam, L., Teng, J.G., Cheung, C.H., Xiao, Y.: FRP-confined concrete under cyclic axial compression. *Cem. Concr. Compos.* **10**, 948–958 (2006)
6. Campione, G., Colajanni, P., La Mendola, L., Spinella, N.: Ductility of R.C. members externally wrapped with FRP sheets. *J. Compos. Constr.* **3**, 279–290 (2007)
7. Wang, L.M., Wu, Y.F.: Effect of corner radius on the performance of CFRP-confined square concrete column: test. *Eng. Struct.* **2**, 493–505 (2008)
8. Jiang, T., Teng, J.G.: Analysis-oriented stress–strain models for FRP-confined concrete. *Eng. Struct.* **11**, 2968–2986 (2007)
9. Wu, Y.F., Tao, L., Oehlers, D.J.: Fundamental principles that govern retrofitting of reinforced concrete columns by steel and FRP jacketing. *Adv. Struct. Eng.* **4**, 507–533 (2006)
10. CNR-DT200: Guide for the design and construction of externally bonded FRP systems for strengthening existing structures. CNR, National Research Council, Rome, Italy (2004)
11. ACI Committee 440: Guide for the design and construction of externally bonded FRP systems for strengthening concrete structures, ACI 440.2R-08. American Concrete Institute, Farmington Hills (2008)
12. Fédération internationale du Béton (fib): Externally bonded FRP reinforcement for RC structures. Bulletin no. 14, technical rep. Lausanne, Switzerland (2001)
13. Rochette, P., Labossiere, P.: Axial testing of rectangular column models confined with composites. *J. Compos. Constr.* **3**, 129–136 (2000)
14. Yang, X., Wei, J., Nanni, A., Dharani, L.R.: Shape effect on the performance of carbon fiber reinforcement polymer wraps. *J. Compos. Constr.* **5**, 444–451 (2004)
15. Mander, J.B., Priestley, M.J.N., Park, R.: Theoretical stress–strain model for confined concrete. *ASCE J. Struct. Div.* **ST11**, 2227–2244 (1988)
16. Pellegrino, C., Modena, C.: Analytical model for FRP confinement of concrete columns with and without internal steel reinforcement. *J. Compos. Constr.* **6**, 693–705 (2010)
17. Campione, G., Miraglia, N.: Strength and strain capacities of concrete compression members reinforced with FRP. *Cem. Concr. Compos.* **1**, 31–41 (2003)
18. Mostofinejad, D., Moshiri, N., Mortazavi, N.: Effect of corner radius and aspect ratio on compressive behavior of rectangular concrete columns confined with CFRP. *Mater. Struct.* **1–2**, 107–122 (2015)
19. Triantafillo, T.C., Papanicolaou, C.G., Zissimopoulos, P., Laourdekis, T.: Concrete confinement with textile-reinforced mortar jackets. *ACI Struct. J.* **1**, 28–37 (2006)
20. Mirmiran, A., Shahawy, M., Samaan, M., El-Echary, H.: Effect of column parameters on FRP confined concrete. *J. Compos. Constr.* **4**, 175–185 (1998)
21. Di Ludovico, M., Prota, A., Manfredi, G.: Structural upgrade using basalt fibers for concrete confinement. *J. Compos. Constr.* **5**, 541–552 (2010)
22. Karbhari, V.M., Gao, Y.: Composite jacketed concrete under uniaxial compression–verification of simple design equations. *J. Mater. Civil Eng.* **9**(4), 185–193 (1997)
23. Lam, L., Teng, J.G.: Design-oriented stress–strain model for FRP-confined concrete. *Constr. Build. Mater.* **17**(6–7), 471–489 (2003)
24. Samaan, M., Mirmiran, A., Shahawy, M.: Model of concrete confined by fiber composites. *J. Struct. Eng.* **124**(9), 1025–1031 (1998)
25. Fossetti, M., Alotta, G., Basone, F., Macaluso, G.: Simplified analytical models for compressed concrete columns confined by FRP and FRCM system. *Mater. Struct.* **6**, 1–20 (2017)

26. Bournas, D.A., Lontou, P.V., Papanicolaou, C.G., Triantafillou, T.C.: Textile-reinforced mortar versus fiber-reinforced polymer confinement in reinforced concrete columns. *ACI Struct. J.* **6**, 740–748 (2007)
27. Karabinis, A., Rousakis, T.C.: Carbon FRP confined concrete elements under axial load. In: *FRP Composites in Civil Engineering Conference*, pp. 309–316 (2001)
28. Rousakis, T.C., Karabinis, A.I., Kioussis, P.D.: FRP-confined concrete members: axial compression experiments and plasticity modelling. *Eng. Struct.* **7**, 1343–1353 (2007)
29. Wu, Y.F., Wei, Y.Y.: Effect of cross-sectional aspect ratio on the strength of CFRP-confined rectangular concrete columns. *Eng. Struct.* **1**, 32–45 (2010)
30. Matthys, S., Taerwe, L., Audenaert, K.: Tests on axially loaded concrete columns confined by fiber reinforced polymer sheet wrapping. In: *Proceedings of the Fourth International Symposium on Fiber Reinforced Polymer Reinforcement For Reinforced Concrete Structures*, ACI SP-188, Michigan, USA (1999)
31. Yeh, F.Y., Chang, K.C.: Size and shape effects on strength and ultimate strain in FRP confined rectangular concrete columns. *J. Mech.* **4**, 677–690 (2012)
32. Mostofinejad, D., Mortazavi, N., Ilia, E.: Fibre-reinforced polymer efficiency in square columns with different corner radii. In: *Proceedings of the Institution of Civil Engineers: Structures and Buildings*, vol. 3 (2017)
33. ATENA Program Documentation, Part 1, ATENA Theory Manual, CERVENKA CONSULTING, 2000–2014
34. De Borst, R.: Non-linear analysis of frictional materials, Ph.D. thesis, Delft University of Technology (1986)
35. Cervenka, V., Pukl, R., Ozbolt, J., Eligehausen, R.: Mesh sensitivity effects in smeared finite element analysis of concrete structures. In: *Proceedings of the FRAMCOS 2*, pp. 1387–1396 (1995)
36. Kupfer, H., Hilsdorf, H.K., Rüschi, H.: Behavior of concrete under biaxial stress. In: *Journal ACI Proceedings*, vol. 66, no. 8, pp. 656–666, August 1969
37. Van Mier, J.G.M.: Multi-axial strain-softening of concrete, part I: fracture, materials and structures. In: *RILEM 1986*, vol. 19, no. 111, (1986)
38. Vecchio, F.J., Collins, M.P.: Modified compression-field theory for reinforced concrete beams subjected to shear. In: *ACI Journal Proceedings*, vol. 83, no. 2, pp. 219–231, March-April 1986



Correction to: Damage Detection in Simply Supported Beam Using Transmissibility and Auto-Associative Neural Network

Huong Duong Nguyen, Tien Thanh Bui, Guido De Roeck,
and Magd Abdel Wahab

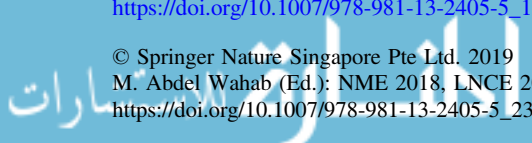
Correction to:

Chapter “Damage Detection in Simply Supported Beam Using Transmissibility and Auto-Associative Neural Network”
in: M. Abdel Wahab (Ed.): *Proceedings of the 1st International Conference on Numerical Modelling in Engineering*, LNCE 20,
https://doi.org/10.1007/978-981-13-2405-5_15

In the original version of the book, the word “neutral” in the term “neutral network” is corrected as “neural” and the term should read as “neural network” in chapter “Damage Detection in Simply Supported Beam Using Transmissibility and Auto-Associative Neural Network” throughout. The correction chapter and the book have been updated with the change.

The updated online version of this chapter can be found at
https://doi.org/10.1007/978-981-13-2405-5_15

© Springer Nature Singapore Pte Ltd. 2019
M. Abdel Wahab (Ed.): NME 2018, LNCE 20, p. E1, 2019.
https://doi.org/10.1007/978-981-13-2405-5_23



Author Index

A

Abdel Wahab, Magd, [67](#), [112](#), [135](#), [143](#), [165](#),
[177](#), [187](#), [202](#), [213](#), [225](#), [254](#)
Agoudjil, B., [81](#)
Alioua, T., [81](#)
Arslan, Tolga, [123](#)

B

Basone, Francesco, [269](#)
Boudenne, A., [81](#)
Bui, Tien Thanh, [177](#), [254](#)

C

Castilho, Eloísa, [238](#)

D

Dang, Bao-Loi, [67](#), [112](#), [165](#)
De Roeck, Guido, [177](#), [254](#)
Djamel, Nedjar, [14](#)

F

Fossetti, Marinella, [90](#), [269](#)

H

Helmrich, Marcel, [150](#)
Ho, Viet Long, [254](#)

I

Ishii, Ken, [30](#)

K

Kikuchi, Masaru, [30](#)
Kong, Suk-Min, [44](#)
Krajníková, Katarína, [54](#)

L

Lee, Yong-Joo, [44](#)
Leitão, Noemi Schclar, [238](#)
Le-Thanh, C., [202](#)
Liu, Quanmin, [143](#)
Liu, Weiji, [143](#), [213](#)

M

Meriem, Seguini, [14](#)
Minafò, Giovanni, [90](#), [269](#)
Morgenthal, Guido, [150](#)

N

Nagy, Balázs, [1](#)
Ngoc, Hau Nguyen, [67](#)
Nguyen, Huong Duong, [177](#)
Nguyen-Ngoc, Hau, [112](#), [165](#)
Nguyen-Xuan, Hung, [67](#), [112](#), [165](#), [187](#),
[202](#), [225](#)
Niiranen, Jarkko, [135](#)

O

Oh, Dong-Wook, [44](#)

P

Phung-Van, P., 225

S

Secer, Mutlu, 123

Siciliano, Alfio Francesco, 90, 269

T

Taube, Christopher, 150

Thanh, Cuong-Le, 225

Thao, Hoang Duc, 67, 112, 165

Tran, Loc V., 135

Tran, Ngoc Hoa, 254

Truong-Thi, P., 187

V

Vodička, Roman, 54

Vu-Huu, T., 202, 225

Z

Zhang, Xiangning, 213

Zhou, Yunlai, 143, 213

Zhu, Xiaohua, 143, 213